TÉCNICO LISBOA

Study of the brain's dynamic functional connectivity with simultaneous fMRI-EEG: a network science approach

Francisca Ayres Basto Soares Ribeiro

Thesis to obtain the Master of Science Degree in

Information Systems and Computer Engineering

Supervisors: Prof. Alexandre Paulo Lourenço Francisco
Prof. Patrícia Margarida Piedade Figueiredo

Examination Committee

Chairperson: Prof. João António Madeiras Pereira
Supervisor: Prof. Patrícia Margarida Piedade Figueiredo
Member of the Committee: Prof. Arlindo Manuel Limede de Oliveira

January 2021

Declaration

I declare that this document is an original work of my own authorship and that it fulfils all the requirements of the Code of Conduct and Good Practices of the Universidade de Lisboa.

Acknowledgments

First and foremost, I want to thank my supervisors, who guided me through this journey. They were always available to discuss new ideas, even when the pandemic made things more difficult. I am really grateful for the freedom they gave me and for joining together to allow me to take on this challenge. To professor Alexandre Francisco, I would like to thank in particular for always finding the time to answer my many questions and to help me stay grounded throughout this thesis. To professor Patricia, I would like to thank for being as much as a dreamer as I am and for always asking new questions, making me think even more. I feel very lucky to have such an amazing pair of supervisors, complementing one another and each giving me great tools to start my path as a researcher.

Secondly, I want to give a special thanks to Sofia Teixeira, for all the extra help and support she gave, especially towards the end of this work. She was really essential to gain confidence in my work and to guide me as a young researcher in my first presentation in the CCS2020 conference. Also, I would like to thank Jonathan Wirsich for providing me the dataset for this work and for always being available to answer any question I had.

Also, I want to thank my office colleagues in INESC, for keeping a light mood and loads of plants around, helping everyone to stay motivated. In particular, I would like to thank David Calhas for all the kindness and camping trips that help me keep going throughout this year. To Marta Xavier, I want to send a BIG thank you, for discussing ideas with me and sometimes even working together to overcome some difficulties. You were truly one of a kind, as a colleague but specially as a friend. In addition, I want to thank my dear friend Sofia Navalho who, despite all the distance, helped me at all times, to grow and to believe in myself. Also, I would like to thank Francisco Pombal for all the technical and hardware help, especially when everything seemed literally lost.

To my friends, that accompanied me through my journey in Técnico and outside of it (they know who they are), I am extremely thankful. All of them helped, inspired and taught me so much. I would not be able to have come to this point without them. I would like to send a special thanks to Marta Cuxart for always being there, when things are full of light but also when things get darker.

Last but definitely not least, to my family, I am really grateful for supporting and believing in me at all times, in particular, during this tough year, when things never went as expected. I feel very blessed to have such amazing and patient parents, always there for me.

Resumo

A organização intrínsica do cérebro em redes funcionais pode ser avaliada recorrendo a diversas técnicas de neuroimagem, maioritariamente ressonância magnética functional (fMRI) e electroencefalografia (EEG). Apesar de estudos recentes terem sugerido uma ligação entre a conectividade funcional dinâmica detectada por estas duas modalidades, a relação exacta entre a organização espaço-temporal das redes funcionais de fMRI e de EEG é ainda pouco clara. Para além disso, visto que estas redes estão incorporadas no espaço do cérebro, levanta-se a questão se as características topológicas capturadas são explicadas exclusivamente pelas restrições espaciais. Estas duas questões são abordadas investigando as redes funcionais obtidas com dados de fMRI e EEG adquiridos simultaneamente durante repouso, usando análise de comunidades e de motivos. Para tal foram usados vários métodos já estabelecidos, como o algoritmo de Louvain, bem como a versão multiplex, aqui aplicada para encontrar partições combinando fMRI e EEG pela primeira vez, e ainda a estrutura de dados g-tries para a contagem eficiente de subgrafos. Para explorar a influência do espaço na topologia observada foram aplicadas novas abordagens, como uma versão modificada do algoritmo de Louvain que inclui um modelo nulo espacial na definição de modularidade, mas também uma análise de motivos em que os subgrafos são testados estatisticamente contra este modelo nulo espacial. É mostrado que, apesar dos conectomas funcionais de fMRI e EEG estarem um pouco correlacionados, as duas modalidades parecem capturar informação diferente, com a maior parte, mas não toda a topologia a ser explicada pelas restrições espaciais.

Palavras-chave: fMRI-EEG; redes complexas; análise de comunidades; análise de motivos; embedding espacial

Abstract

The brain's intrinsic organization into functional networks can be assessed using several imaging techniques, mainly functional magnetic resonance imaging (fMRI) and electroencephalography (EEG). While recent studies have suggested a link between the dynamic functional connectivity captured by these two modalities, the exact relationship between the fMRI and EEG functional networks spatiotemporal organization is still unclear. Furthermore, since these networks are spatially embedded, the question arises whether the topological features captured can be explained exclusively by the spatial constraints. We address these two questions by investigating functional brain networks measured by fMRI and EEG data acquired simultaneously during resting-state, using a community and motif analysis. For this purpose, several established approaches were used, such as the Louvain algorithm as well as its multiplex version, here applied to find partitions combining fMRI and EEG for the first time, and also g-tries data structure to efficiently count the occurrence of subgraphs. To explore the influence of space in the topology captured, new approaches were applied, such as a modified version of the Louvain algorithm, including a degree constrained spatial null model in the modularity definition, but also a motif analysis where the subgraphs are statistically tested against this spatial null model. We show that even though fMRI and EEG functional connectomes are slightly linked, the two modalities seem to capture different information, with most topology, but not entirely, being explained by the spatial constraints.

Keywords: fMRI-EEG; network science; community analysis; motif analysis; spatial embedding

Contents

List of Tables

List of Figures

Nomenclature

AAL Automated Anatomical Parcellation

AAS Average Template Subtraction

BEM Boundary Element Method

BOLD Blood Oxygen Level Dependent

CSF Cerebrospinal Fluid

DAM Dorsal Attention Network

dFC Dynamic Functional Connectivity

DMN Default Mode Network

ECG Electrocardiogram

EEG Electroencephalography

EPI Echo Planar Imaging

EPSP Excitatory Postsynaptic Potential

FMRI Functional Magnetic Resonance Imaging

FWHM Full-Width at Half Maximum

HRF Hemodynamic Response Function

ICA Independent Component Analysis

IPSP Inhibitory Postsynaptic Potential

LTI Linear Time Invariant

MNE Minimum Norm Estimates

NMI Normalized Mutual Information

PC Phase Coherence

PCA Principal Components Analysis

PLV Phase Locking Value

ROI Region of Interest

RSN Resting State Network

TR Repetition Time

SNR Signal-to-Noise Ration

TTP Time-to-Peak

WM White Matter

Chapter 1

Introduction

1.1 Motivation and Problem Statement

Brain activity is believed to be organized into functional networks, reflecting the dynamic coupling between remote brain regions and the continuous exchange of information throughout the whole brain [1]. These systems can be studied to characterize the spatiotemporal organization of the brain. Several studies have focused on spontaneous fluctuations, that reflect the coordinated activity between the different regions in a context with no specific stimulus, also known as the resting-state [1–3]. Understanding the dynamic behaviour of these networks and their topology might be the key to increase the understanding of brain's complex activity and, possibly, provide biomarkers for neurological and psychiatric diseases [4, 5].

Both functional Magnetic Resonance Imaging (fMRI) and electroencephalography (EEG) have been used to study brain function in humans. The fMRI is a non-invasive imaging technique that measures the neuronal activity in an indirect way, currently being the most widely used technique to explore functional connectivity. It measures a blood-oxygen-level-dependent (BOLD) signal, that reflects variations in the blood oxygenation ratio as a result of synaptic activity and is known for its high spatial resolution [6]. On the other hand, the EEG has been thoroughly exploited for its high temporal resolution and also for allowing a direct measure of electric activity generated by synchronized brain regions [7], albeit with much poorer localization power. Even though both these techniques reveal the dynamic behaviour associated with functional networks, it is still not entirely known how the two measures are correlated with each other, i.e., what is the relationship between the hemodynamic response and electric activity, and whether they capture the same information or not [8].

In recent years, several studies have analyzed functional connectivity by combining simultaneously acquired fMRI-EEG recordings with the objective of investigating the relationship between the two and also to take advantage of the complementarity between the two signals [8–10]. Moreover, this type of analysis can provide a richer characterization of the spatiotemporal brain dynamics and also help establish the relationship between time-varying electrical and hemodynamic activity. However, no study to date has performed a comparative analysis between these two modalities functional networks by

investigating their topology over time.

The analysis of the functional networks, defined using these two techniques, can be done considering a graph theory framework that allows the brain functional systems to be modeled as complex networks [4]. In this context, the networks and their time-varying topology can be studied in several ways already established, such as by analyzing the global properties, like the community structure [11–13], or by exploring how these networks are organized on a local perspective, using motif analysis [14, 15].

Therefore, this work consists in the first study to our knowledge to perform a comparative network analysis of fMRI and EEG functional connectivity data, both on a macro- and meso-scale, by means of a community and a motif analysis, respectively. For this work, several established approaches were used, such as the Louvain algorithm [16] for the extraction of large groups of coordinated activity, as well as its multiplex version [17], here applied to find partitions combining fMRI and EEG for the first time. Also the g-tries data structure [18] was used to efficiently count the occurrence of subgraphs in these functional networks, while determining if they are statistically significant.

Furthermore, since these networks are spatially embedded, the question arises whether the topological features captured can be explained by the impositions determined by the brain's underlying structure [19] or if there is still some functional synchronization deviating from these proximity constraints. Some studies have already explored this space effect in structural networks [19, 20] and, more recently, in the community structure of functional networks, considering only long-distance connections [21].

As such, with hopes of exploring the influence of space in the global and local topology, the fMRI and EEG functional networks' topology beyond these spatial constraints was investigated. With this objective, new approaches were applied, such as a modified version of the Louvain algorithm [22], that includes a degree constrained spatial null model in the modularity definition, and also a motif analysis where the subgraphs were statistically tested against this spatial null model.

1.2 Objectives

The objectives of this thesis are the following:

1. Characterize and compare the connected components structure across time between fMRI and EEG functional networks;
2. Characterize and compare the community structure arising from dynamic functional connectivity detected by fMRI and EEG data;
3. Examine the effect of spatial proximity in the community structure retrieved for each modality as well as in their correlation;
4. Investigate the potential of combining both modalities to analyze the modular configuration of functional connectivity;
5. Characterize and compare the local structure of fMRI and EEG functional networks by means of motif analysis;

6. Examine the effect of spatial proximity in the motif characterization of both fMRI and EEG functional connectivity;

1.3 Thesis Outline

This thesis is organized in several chapters, in the following way: Chapter 2 (Background and Related Work) presents the main theoretical concepts within the framework of this work, as well as a review of the related studies with respect to the analysis of brain networks. Subsequently, Chapter 3 (Data Processing and Initial Analysis) includes the data acquisition and processing steps, as well as the definition of these functional networks. It also integrates the estimation of the hemodynamic response delay and threshold and even an initial connected component analysis. Afterwards, Chapter 4 (Community Structure Analysis) describes the methods and results regarding the analysis of the global structure of these networks, including the comparison with two null models, community analysis with and without the spatial influence and also a brief multilayer community analysis. Chapter 5 (Motif Analysis), in turn, presents the motif analysis with respect to the same two null models used in the community analysis for the characterization of the functional networks on a local perspective. Finally, Chapter 6 (Conclusions) includes the final conclusions referring to both analysis and comparison between fMRI and EEG functional networks, as well as the limitations associated to this work and future possibilities for further analysis considering the results obtained.

1.3.1 Publications

A portion of the work developed in this thesis led to the publication of an abstract and subsequent presentation in the Conference of Complex Systems (CCS) 2020 occurring from 7th to 10th of December, with the title ”Space-Independent Modular Structure of Brain Functional Networks”. As the title suggests, this publication was relative to the community analysis and the effect of space in the global organization of fMRI functional networks, exclusively.

Chapter 2

Background and Related Work

2.1 fMRI and EEG

2.1.1 Functional Magnetic Resonance Imaging (fMRI)

Functional Magnetic Resonance Imaging (fMRI) is one of the most widely used imaging techniques since it allows a noninvasive whole-brain analysis. It measures brain activity based on changes in the blood flow, tightly correlated with neuronal activity [23]. This method is typically used for the detection and delineation of brain regions whose activity changes in response to specific experimental conditions [24], having a relatively high spatial resolution. In the next sections, the principles behind this imaging technique are further described, as well as several approaches to study brain's dynamic behaviour.

2.1.1.1 Basic Principles of fMRI

Magnetic resonance imaging is based on the interaction of atomic nuclei with an applied magnetic field. Some nuclei, composed by protons and neutrons, possess an inherent angular momentum called spin, which will be associated with a magnetic dipole moment. In particular, the hydrogen nucleus (composed by a single proton and present in water molecules and brain tissues) will behave like a small magnet and, when placed in a magnetic field, it will precess at a frequency proportional to the field so as to align parallel or antiparallel with this field [6]. However, due to the spins associated with these protons, they will precess around the magnetic field's longitudinal axis and at a certain angle to the transverse plane, instead of simply align to it.

In absence of a magnetic field, the spins of the nuclei are randomly oriented, so the net magnetization vector M is zero. When an external magnetic field is applied, the alignment of the nuclei will create a net magnetization across all spins, composing a parallel vector to the static magnetic field [6]. Nonetheless, applying an oscillating electromagnetic pulse - denoted as RF pulse - will excite part of the protons at the resonant frequency, resulting in a flip from the longitudinal direction towards the transverse plane. The protons' spins will be in phase together, making the net magnetization to change over time in the transverse plane, precessing around the resulting field composed by the sum of the static field and the

oscillating one [25]. Therefore, there will be a longitudinal magnetization due to the static field and a transversal magnetization due to the applied pulse.

After the RF pulse, a relaxation of the spins will occur so as to return to the alignment with the static magnetic field, i.e., a lower energy state. The energy emitted through the process of relaxation is then captured by the MRI scan. This longitudinal relaxation, consisting in the recovery of the longitudinal net magnetization, is controlled by time constant T1, that depends on the tissue composition and structure (as interactions between spins and with their surroundings will vary) [23, 25]. Besides this, an exponential decay of the transversal magnetization will occur in the absence of the pulse, due to a loss of phase coherence between spins, as they interact randomly with each other. This is called transverse relaxation and its decay is controlled by time constant T2, also depending on the physiological tissue [25].

It is important to notice that due to magnetic field inhomogeneities, water molecules move into regions with different local fields, and thus the present protons will have a range of precession rates. This results in a decrease of the coherence of the nuclear spins, which will accelerate the decay of the net signal, a rate controlled by T2* time constant instead of T2 [23]. In the brain, these inhomogeneities depend on the neuronal activity affecting the composition of the local blood supply, which results in a change its magnetic susceptibility. Deoxyhemoglobin, present at high concentrations in deoxygenated blood, is paramagnetic, so it will create field distortions which lead to a decrease of local signal, unlike to oxyhemoglobin that has a diamagnetic behaviour [6]. In the presence of synaptic activity, there is an increase in cerebral blood flow larger than the rate of consumption of oxygen, which results in an overall increase of blood oxygenation [26]. This way, the degree of attenuation of the signal caused by deoxyhemoglobin is reduced and, therefore, the MR signal increases. As such, arising from the blood-oxygen-level-dependent (BOLD) contrast, the fMRI signal corresponds to a time-series for each voxel, that indirectly describes the variations in brain activity for each location. This allows the production of a T2*-weighted map representing the brain activation patterns across the different regions [6], obtained at a reasonably high resolution.

A key aspect about this technique is the increase of blood flow, together with a rise in blood volume and oxygenation, known as the hemodynamic response, that occurs following brief neural activation. However, these changes come slow and with a significant delay, which will impact the temporal resolution of this imaging technique [27]. Besides this, the BOLD signal response can be described by the hemodynamic response function (HRF), whose shape is characterized by three properties: a response height, time-to-peak and full-width at half maximum (FWHM) (see figure 2.1). Since, in many cases, the BOLD signal can be assumed to behave linearly, displaying Linear Time Invariant (LTI) properties, it can be modeled by convolving the HRF with the given neuronal signal [27]. This can be useful to compare the signals obtained from fMRI with other imaging techniques that capture the neural activity directly.

2.1.1.2 FMRI Functional Connectivity and Related Techniques

Functional communication between brain regions is expected to have a major role in complex cognitive processes, by means of continuous integration of information across different areas of the brain [1]. Therefore, the study of how these regions interact and correlate is fundamental for the understanding of

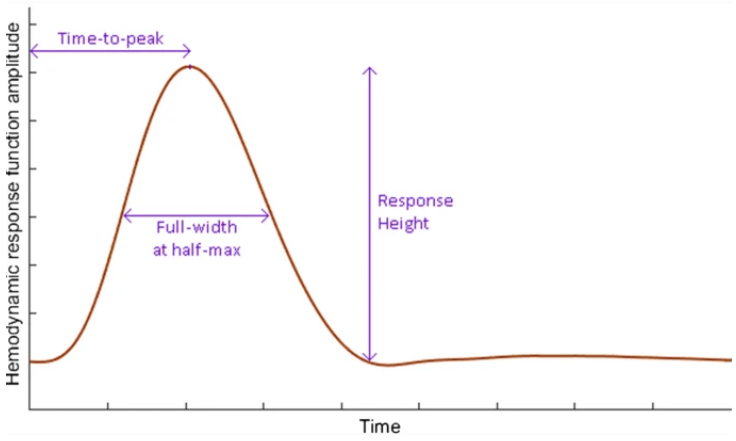

Figure 2.1: Hemodynamic response function (HRF) canonical representation in time (s) with its three parameters: response height, time-to-peak and full-width at half maximum, adapted from [28].

the spatiotemporal organization of the brain.

Besides detecting and mapping regions of the brain regarding to their activity, fMRI can unravel information about how neural systems are functionally coupled together [24]. This is done through functional connectivity analysis of the fMRI data. Functional connectivity is defined as the temporal dependency of BOLD activation patterns, i.e, the similarity between the activity of anatomically separated brain regions, reflecting the level of functional interaction between them [1]. It can be examined through the study of spontaneous changes in the BOLD signal, i.e., using resting-state fMRI. Opposed to the standard task-based fMRI paradigm, in resting-state studies there is no specific stimulus and the activation of the different brain areas occurs during rest, possibly revealing the baseline activity of the brain [6]. It is even speculated that the functional connectivity observed during rest may help keep functional systems ready, improving their performance when they are needed [1].

Measures to examine brain connectivity with fMRI data are usually time independent, assuming stationarity over a scanning session, with the Pearson correlation coefficient being the most commonly applied measure of functional connectivity [5]. Other methods to examine this connectivity in a resting-state context include seed-based methods, independent component analysis (ICA) and clustering techniques, with the last two being the more adequate to analyze whole-brain connectivity patterns [1, 29], as they are data-driven methods. The ICA can be used to detect networks of coherent activity, i.e., functionally connected regions, by searching for a mixture of underlying spatial sources that explains the measured spatiotemporal fMRI data. It relies on the assumption that the spatial components obtained are statistically independent and separates the data into spatial components with similar temporal coordinated activity [29], that correspond to different networks. The clustering involves grouping voxels into subsets for which BOLD time-series have a higher level of similarity than with ones in different groups (clusters) [29]. In contrast with the previous one, it allows a characterization of functional connectivity without relying on any assumptions and it is a more intuitive approach to find activity patterns. The most common clustering approach in this context is the k-means, that splits the voxels into k non-overlapping clusters, being necessary to define the number of partitions *a priori*.

Unfortunately, these methods provide a rather simplistic view of resting-state activity, specially con-

sidering that it has been shown the existence of fluctuations in functional connectivity over time [30]. This dynamic behaviour, denoted as dynamic functional connectivity (dFC), can then be characterized using a sliding window approach. This approach consists in segmenting the BOLD time-series from the brain regions (or voxels) into a set of temporal windows, within each the pairwise correlation is examined [5]. This way, all connections between brain regions are represented by a connectivity matrix per time window, allowing the study of the temporal evolution of functional connectivity. As mentioned before, the Pearson correlation coefficient represents the most direct measure to assess this, particularly within this approach. Nevertheless, other possibilities have been proposed, such as the sliding-window ICA [31], where the BOLD time courses are decomposed with ICA and the spatial components for each time frame are obtained.

By computing correlation measures using sliding time windows, although providing a simple approach able to capture features of the dynamic functional connectivity, these methods compromise the temporal resolution by averaging the correlation over the time frame [32]. For these approaches, there is a trade-off between the size of the window, so as to be short enough for detection of temporal variations of interest (sensitivity), but long enough to provide reliable computation of correlation (specificity). Additionally, choosing a fixed window length constraints the analysis of dynamic functional connectivity changes to frequencies equal or below to the one imposed by the window period [5].

To not lose temporal resolution and to solve the reliability trade-off, dFC can be measured instantaneously using phase synchronization, also known as phase coherence (PC), across brain regions. Two signals are said to be coherent if they have a constant relative phase, i.e., being synchronous, while the associated amplitudes may vary [33]. Consequently, the idea behind this phase synchronization approach is to compare two regions' signals regarding the instantaneous phase information of the time-series [32] and to use the degree of synchronization of these BOLD fluctuations as a measure of connectivity. To compare any two time-series, it is necessary to separate their instantaneous amplitude from the instantaneous phase, which can be achieved using the Hilbert transform while guaranteeing that the signal is periodic or narrowband. As such, the first step of this approach is to bandpass filter the BOLD signal to a frequency band of interest, and then compute the analytic representation of the BOLD signal ($x(t)$), which corresponds to a complex signal $x_a(t)$, using the Hilbert transform $H[.]$:

$$x_a(t) = x(t) + jH[x(t)], \tag{2.1}$$

where *j* is the imaginary unit. Considering that the bandpass filtered BOLD time-series is a narrowband signal, it can be written as an amplitude-modulated low-pass signal $a(t)$ with a sinusoidal carrier frequency $\phi(t)$, such that:

$$x(t) = a(t)cos[\phi(t)]. \tag{2.2}$$

If the Bedrosian's theorem [34] is respected, the Hilbert transform of the BOLD signal is $H[x(t)] = a(t)sin[\phi(t)]$, leading to, according Euler's formula:

$$x_a(t) = a(t)e^{i\phi(t)}, \tag{2.3}$$

with $a(t)$ as the instantaneous envelope and $\phi(t)$ the instantaneous phase [32]. Then, given the phases of the BOLD signals, the phase coherence between two brain regions n and p at each time point t can be computed using:

$$PC(n, p, t) = cos[\phi(n, t) - \phi(p, t)], \tag{2.4}$$

having $cos(0) = 1$, i.e, $PC(n, p, t) = 1$, if the two regions have synchronous BOLD signals at time t. Computing for all brain regions will result in a phase coherence matrix for each time point [35].

The PC has the advantage of being computationally faster than temporal correlations, since it obtains the phase value for each time point and the whole brain with one transform, allowing maximal temporal resolution [32]. However, it has the disadvantage of being more susceptible to noise than the sliding window approaches. A similar approach, also not using sliding-windows, is based on the Wavelet Transform Coherence, performing a time-frequency decomposition analysis, allowing the study of the temporal variability in the amplitude and phase relationships between brain regions [30].

Finally, an additional approach to analyze dFC is through a graph theoretical framework, which allows the time-varying characterization of the architecture of brain networks as well as the information flow, by analyzing the resulting connectivity networks represented through graphs [5]. These networks can be built using any of the connectivity measures presented above, as it will be further described in section 2.2.

2.1.2 Electroencephalography (EEG)

The electrophysiological methods measure the underlying neuronal events in real time. In particular, electroencephalography (EEG) allows the direct measurement of the propagation of transient brain electrical dipoles generated by neuronal activity [23]. With the use of scalp electrodes, this constitutes a non-invasive method to record synchronous electrical activity of neuronal populations, either associated to spontaneous or event-related activities, having a high temporal precision [36]. In the next sections, the principles behind this imaging technique are further described, as well as several approaches to study dynamic connectivity between brain regions.

2.1.2.1 Basic Principles of EEG

The neurons (composing brain tissues) are cells susceptible to excitation, being able to generate electrical time-varying currents when activated. These currents correspond to changes in ionic concentration at the membrane level, resulting in voltage fluctuations that can be measured through EEG [7].

Neuronal activation can be a result of two different mechanisms. On one hand, it can correspond to a fast depolarisation of the neuronal membranes, resulting in an action potential. This consists in a sudden change of the membrane potential, due to in and out flow of sodium and potassium ions, propagating along the neuron's axon. The second form of activation is through slower changes in the

potential of neuronal membranes, due to synaptic activity. This can lead to excitatory postsynaptic potentials (EPSPs), where the transmembrane current is carried by positive ions inwards, or to inhibitory postsynaptic potentials (IPSPs), where the transmembrane current is carried by negative ions inwards or positive ions outwards, exciting and inhibiting the postsynaptic neuron, respectively.

The charge created by these local intracellular currents is compensated in the opposite direction, by extracellular current flow along the neuronal membrane, allowed by volume conduction. This creates a sink-source configuration generating a current dipole. This dipole will be oriented along the dendrite and it is in the origin of the electrical signal measured at the scalp recording electrodes [7, 37]. More precisely, the signal arises from the summation of individual dipoles, generated mainly by synchronous pyramidal neurons of the cortex, since their dendrites are aligned and perpendicular to the cortical surface and these cells have open-fields, i.e., dendrites are aligned with each other leading to a large measurable dipole [38].

The EEG signal corresponds to a time-series associated to each electrode, but can also be represented in the frequency domain:

$$X(f,t) = A(f,t)e^{i\phi(f,t)}, \tag{2.5}$$

where $A(f,t)$ represents the amplitude and $\phi(f,t)$ the phase of the signal. Besides this, is important to notice that the signal measured by EEG can reflect both spontaneous and event-related activity. In this work, the spontaneous EEG is more interesting as it reflects neuronal responses that occur in the absence of a particular stimulus, unraveling patterns of intrinsic functional connectivity across brain regions [36].

Also, the EEG recordings are conventionally decomposed into five main frequency components: delta (1-4 Hz); theta (4-8 Hz); alpha (8-12 Hz); beta (12-30 Hz); gamma ($>$ 30 Hz), each frequency band associated with different functions and activated regions. In fact, low-frequency oscillations tend to represent coordinated activity of large-scale neuronal networks, whereas high-frequency oscillations mostly reflect synchronization between nearby cortical regions [39]. Nevertheless, the alpha band is by far the most studied brain rhythm, being induced by relaxation and closing the eyes [38].

2.1.2.2 EEG connectivity and Related Techniques

As mentioned before, neuronal oscillations reflect synchronized rhythmic fluctuations and allow the flow of neural information between the different synchronized brain regions [40]. The fMRI is widely used for exploring functional connectivity, as shown in the previous section, however, it is an indirect measure of neuronal activity, with particularly limited temporal resolution. Therefore, the high temporal precision of EEG makes this imaging technique fitting to study the brain as dynamic system, by describing rhythmic EEG activity in terms of functional connectivity [41]. Identically to fMRI, resting-state EEG data is also known to exhibit fluctuations, reflecting changes in connectivity between and within brain networks.

Functional networks can be characterized using EEG with a variety of connectivity metrics such as Pearson correlation coefficient, the simplest measure of the linear relationship between time series, or with cross-correlation (R^2), a classical measure of interdependence between two time series that ac-

counts for possible shifts between signals [42], being both methods done in the time domain. However, in order to detect individual rhythmic components, it is usually better to represent the signals in the frequency domain. This can be done applying Fourier decomposition for the whole time period or using windowed short-term Fourier transform where the global observation window is partitioned into several segments and the spectrum is estimated for each time-frame [40, 43]. For non-stationary signals, which is the case for the study of dynamic functional connectivity, this approach is not adequate. As an alternative, the representation of these signals in the frequency domain can be done through the Hilbert transform, requiring the bandpass filtering the signal [40].

As such, most connectivity metrics are computed from the frequency domain representation, which characterizes an estimate of amplitude and phase of the neural oscillations captured in the data, across time points [40]. Some of these connectivity metrics include coherency, phase synchronization by means of the phase locking value (PLV) and imaginary part of coherency. Coherency is the simplest and most popular metric to assess interaction at a specific frequency, corresponding to a generalization of correlation in the frequency domain. It is given by:

$$C(f,t) = \frac{S_{xy}(f,t)}{\sqrt{S_{xx}(f,t)S_{yy}(f,t)}}, \tag{2.6}$$

where $S_{xx}(f,t)$ and $S_{yy}(f,t)$ are the power spectral densities of two signals $x(t)$ and $y(t)$, and $S_{xy}(f,t)$ the cross-spectral density. Being defined as the normalized cross-spectrum, i.e, the normalized value of similarity between the two signals spectra, it assesses how the phases of the two signals are coupled to each other, weighted with the product of the amplitudes, thus, quantifying the linear relationship between two time-series at a specific frequency [41]. Coherency's phase indicates the average phase difference between those time-series, within each time-window (non-stationary, using Welch's method) or the whole scan period (stationary) [43], while its absolute value, defined as coherence, reflects the stability of that phase delay [44].

Phase Locking Value (PLV) is a connectivity metric that measures phase synchronization in a stricter manner, by only considering phase as relevant to assess the coupling of neuronal oscillations. It requires the extraction of the instantaneous phase of both signals at each time point through a Wavelet transform or, equivalently, with a Hilbert transform, as previously mentioned. This measure is given by:

$$PLV_{xy}(f,n) = \left| \frac{1}{n} \sum_{t=1}^{n} e^{i(\phi_x(f,t) - \phi_y(f,t)))} \right|, \tag{2.7}$$

where $\phi(f,t)$ corresponds to the instantaneous phase of a signal for the time point t at frequency f and n the number of time points in the trail. This can be computed over the whole time of the trial or for each time frame, corresponding to an average of the phase differences in the chosen window [40].

It is important to note that these connectivity metrics, and other metrics not mentioned here, are susceptible to the volume conduction effect, meaning that they can yield spurious connectivity when applied directly with EEG signals measured with electrodes placed at the scalp. In fact, there is an inevitable mixing in the EEG sensors of overlapping signals arising from distinct brain sources [42, 44]. This constitutes the volume conduction problem, i.e, the source mixing due to the conductivity of the

electrical signals spreading into the surroundings tissues through the brain, skull and scalp, resulting in the sensors picking up activity of multiple regions. In practice, this can create misleading coherence or phase-locking, not representing a true neuronal interaction, but instead corresponding to the activity from the same underlying source detected in two different channels [40].

Considering the quasi-static approximation for EEG [45], i.e, the assumption that there is no time-lag between the underlying source activity (propagated through volume conduction until the scalp) and the observed EEG signal, there is a zero-phase shift between two signals if they arise from the same source. For an actual interaction, on the other hand, there will be a delay in phase that corresponds to the period of time it takes for one source to synchronize with another. Thus, it is possible to have connectivity measures which are robust against volume conduction by ignoring zero-lag synchronizations between signals [41]. This is the case for the imaginary part of coherency. This connectivity metric isolates the part of coherency that reflects the actual interaction between two signals (coherency value projected in the imaginary axis), since the amplitude components of the underlying sources (corresponding to contributions along the real axis) are propagated through volume conduction to the electrodes, being obviously sensitive to its effects [41]. Even though it removes interactions that might not represent real functional connectivity being only sensitive to coupling of signals that are time-shifted from each other [40], this measure can fail to detect some brain interactions when the time-lag between those regions is very small or close to 180 degrees [41].

Another possibility to reduce the effects of volume conduction is establishing functional connectivity directly at the source level, as it was done in [46]. The transition from the electrode space into the source space can be done through source reconstruction, i.e., the localization of the underlying sources and reconstruction of the associated time series, within the brain [47]. The source reconstruction and its methods will be further described in section 2.1.3.1. Having established the underlying sources and their activity, it is possible to use connectivity metrics that are not robust against volume conduction, avoiding having to resort to more complex measures. However, even though connectivity analysis at the source level has been shown to lower volume conduction effects, the problem of spurious connectivity can also be present [42], as a result of source mixing in EEG reconstruction solutions [44]. Therefore, it might be more cautious to employ metrics which are, in theory, insensitive to volume conduction when using the estimated sources and their time-series.

Finally, as for fMRI, it is possible to use graph theory approaches to analyze EEG time-varying connectivity, by means of the characterization of the topology of brain networks and other metrics that reveal the efficiency of information processing throughout the whole-brain [42]. This will be further explored in section 2.2.

2.1.3 Multimodal fMRI-EEG Integration

Both fMRI and EEG are non-invasive techniques that allow the study of whole-brain dynamic functional connectivity in resting-state, by probing neuronal activity through distinct biophysical processes and with different spatial and temporal resolutions. As such, it increased the interest of integrating these two techniques by taking advantage of the complementary between the two signals in terms of resolution: EEG's

excellent temporal resolution in the milliseconds scale to adequately capture the fast changing dynamics and fMRI's spatial resolution providing a map of the local neuronal activity. This multimodal integration can also be done to potentially overcome the intrinsic limitations of these two imaging techniques [48].

Even though these two techniques depend on the underlying neuronal activity, the signals captured compose a complex and biased representation of only part of that activity, which will only be partially overlapping between the two [49]. Having the interest to unravel the neuronal coupling of EEG and fMRI, i.e, the relationship between the hemodynamic response and neuronal activity for which there is still no ground truth, the simultaneous acquisition of these signals seems fundamental to evaluate the correlation between the spontaneous BOLD signals and electrical activity in the same time period and experimental conditions [8]. The use of simultaneous fMRI-EEG recordings is of particular interest considering that the fMRI and EEG activity may show local discrepancy or decoupling. There can be brain regions generating EEG signal that is not necessarily placed in the same localization of the blood supply for these neurons, leading to an EEG and BOLD signal local discrepancy. Additionally, it may occur physiological activity requiring energetic support (provided by increase of blood flow) causing hemodynamic BOLD changes without EEG correlates as there was no electric activity generation [50]. This means that, by using simultaneous information from both EEG and fMRI, we might obtain more reliable results by reciprocally cross-validating both signals.

It is important to mention that this simultaneous acquisition gives rise to many artifacts that can completely compromise the signal of interest by having a signal-to-noise ratio quite inferior to the uni-modal paradigms. This is due to electromagnetic perturbations originated from both systems and their interaction, such as contamination of EEG acquisition in the presence of the strong magnetic field of the MRI system [50]. Therefore, it is necessary to apply denoising techniques and removal of artifacts that appear specifically in this multi-modal acquisition, besides all the other preprocessing methods that remove the individual artifacts affecting each modality separately. These techniques are enumerated in section 3.1.1.2 and 3.1.1.3, for fMRI and EEG respectively.

To analyze the simultaneous fMRI-EEG data and establish a parallel or correlation of dynamic connectivity between the two, it is convenient to define a spatial mapping between the two signals, having an equivalency between the brain regions defined for fMRI and the sources that lead to the EEG signals detected by the electrodes. This is further described in the following section.

2.1.3.1 EEG Source Reconstruction

To analyze concurrent fMRI and EEG data is necessary to map the regions of interest (ROIs) resulting from the segmentation of the whole-brain three-dimensional structure obtained with MRI to the EEG electrodes placed in the scalp. This mapping is required to have a correspondence between the BOLD activity measured and averaged within these regions and the electric activity time-courses. For this mapping, source reconstruction can be applied to localize the underlying sources of the electric potentials measured at the scalp and reconstruct their times series. This provides a direct correspondence between EEG and fMRI activity to the same locations in the brain volume, resorting to the same whole-brain template to define the regions to consider. However, this is not achieved in a trivial manner, as

the EEG channels do not simply relate to only one source. It requires solving the inverse problem, an ill-posed problem, as it does not provide a unique solution. Due to the imbalance between the small number of measurements and the large number of source voxels, infinite solutions exist (highly undetermined), being necessary to introduce *a priori* information about the neuronal electrical generators and other biophysical constraints characterizing the propagation of these signals in the brain [51].

Firstly, the scalp-recorded EEG signals and the electrodes' three-dimensional positions are needed to localize the brain sources and reconstruct their time courses. Also, the definition of a head model is necessary, reflecting the electrical and geometric characteristics of the different layers of the head, as well as a source model that contains information about the location and orientation of the dipole sources to be reconstructed [42]. These head models can be just simplistic spherical models with an uniform conductivity, or more realistic ones, differentiating layers (brain, skull and scalp) with different electrical conductivity, such as the boundary element method (BEM). Complementary, the anatomy of the source distribution can be defined using the structural MRI for each subject (segmented using Freesurfer software package) and the specific electrode positioning in an ideal situation, or, more frequently, using template anatomies, such as the ICBM152 head (a nonlinear average of MR images of 152 individuals heads), which will correspond to the source model [42, 47].

After establishing both the head and the source model, a regularization strategy must be chosen to find a solution for the inverse problem. Regularization is an approximation of an ill-posed problem, such as this one, by a family of well-posed problems, and the objective is to choose the one that yields to the best approximation solution, by minimizing the expected error or the sum of the absolute values of the solution components [52].

One of the most common and simple approaches is the Minimum Norm Estimates (MNE), where the solution with minimum power is searched for resorting to the L2-norm to regularize the problem [53]. This solution is appropriate to distributed source models, where the electrical activity will extend over neighbouring areas of the cortical surface [52]. However, this strategy tends to favor weak and surface sources, which can be compensated by introducing a weighting matrix. These additional weights adjust the properties of the solution, reducing the bias and noise sensitivity associated to MNE estimates [53]. One possibility is to use the Tikhonov regularization, where, in this case, the original problem is approximated by an unconstrained minimization of the combination of the residual error norm and the weighted L2-norm, choosing a regularization parameter λ [54].

It is important to mention that, in resting-state, the detection of deeper structures might be difficult since the amplitude of the signals measured by the EEG electrodes is smaller than in task-related trials. Also, an increase in the number of EEG channels allows a greater accuracy in source estimations by reducing the degrees of freedom, as it was demonstrated in [55].

2.1.4 Dynamic Functional Connectivity States

Besides localizing time-varying activity throughout the whole brain, the analysis of functional connectivity can be also used to understand the spatiotemporal organization by characterizing coactivation patterns, i.e., networks of brain regions whose activity is synchronized. Several networks of intrinsic connectivity

have been deeply studied, denoted as the resting state networks (RSNs), such as the default mode network (DMN) or the dorsal attention network (DAM). However, recently, it has been suggested and investigated a parcellation of these large scale networks into smaller parts, according to fluctuations in connectivity along time [2]. These fluctuations originate structured patterns of functional connectivity that emerge and dissolve in tens of seconds, reflecting a set of brain regions that diverges at least partly from these RSNs. These short-term stable patterns are known as dynamic functional connectivity (dFC) states and are, generally, consistent across subjects.

It is, therefore, important to describe the difference in connectivity to discriminate the dFC states, as well as examining their occurrence throughout time and the transitions between them. This can be achieved through matrix factorization techniques, such as k-means or principal component analysis (PCA) [5], or using a modularity approach to look for communities [9], that in this case correspond to patterns of connectivity. This is further explored in section 2.2.2.

The most commonly adopted approach is the k-means clustering, first applied in [2], which groups connectivity matrices, obtained for each time frame, to form non-overlapping clusters. Each cluster centroid will then reflect a dFC state that reoccurs over time, with the functional connectivity matrix of each time point being described by one of these patterns. In contrast, approaches like PCA allow temporal overlap between states, seen as building blocks of connectivity with different contributions over time [3, 5], where each connectivity matrix can be described as a linear combination of all the detected states with different weights over time [3].

Even if these states can be extracted and their transitions over time examined, it is desirable to bring the nature of dFC to the neural origin, i.e., their physiological underpinnings. This can be done by finding a link between the dynamic connectivity using fMRI data and concurrently collected EEG data, as mentioned before [56]. In a recent study, the fMRI and EEG-derived functional connectomes were analyzed to investigate their linked dynamics, by checking their mutual information, revealing a close relationship between the two, although with some differences regarding their spatial information [57]. Another study stepped even further, by investigating EEG microstates (transient, patterned and quasi-stable scalp topographies of electric potentials) as potential signatures of the fMRI-derived dFC states, assessing their ability to predict these states in a classification problem [3]. In addition, it has been proposed to capture the dFC patterns by combining EEG and fMRI information into a single connectivity matrix and extract those patterns with a modularity approach, this way, incorporating dynamic functional connectivity from both direct and indirect measures of brain activity [9]. Alternatively, a recent study performed a bimodal analysis by extracting the joint spatially independent components, suggesting that part of the synchronized activity is co-expressed in a similar way across fMRI and EEG [58].

2.2 Brain Complex Networks

The brain's functional systems can be modeled as complex networks through the measurement of pair-wise interactions between the different brain regions. Graph theory based analysis has emerged as a powerful new tool to analyze brain imaging data and capture the organization and dynamic of functional

(a) Node Degree (b) Clustering Coefficient (c) Average Path Length

Figure 2.2: Illustration of node degree, clustering coefficient and average path length properties in a small graph. Adapted from [63].

networks, since they provide physiological basis for information processing and mental representations and may be found altered in patients with brain disorders such as schizophrenia or Alzheimer's disease [4]. Graph theory provides a theoretical framework in which these networks' topology can be investigated, unraveling important information about local and global organization of functional brain networks, possibly exposing otherwise hidden phenomena given its schematically representation [1]. A network is composed by a set of nodes that represents the brain regions and by links connecting them, reflecting the functional synchronizations. The network's topological properties express how efficiently information is distributed between the nodes and provides information about the functional segregation and integration of the different components of the network [59], that result in complex dynamics.

A graph representation of a network is given by the tuple $G = (V, E)$, where V is the set of nodes or vertices and $E \subseteq V \times V$ the set of links or edges that compose the networks, and is often represented through an adjacency matrix, whose elements different than 0 indicate the presence of connections between each pair of nodes. Brain connectivity and functional networks can then be assessed constructing graph representations from the connectivity matrices obtained from the functional correlation between brain regions, as reviewed previously in Section 2.1.1.2 and 2.1.2.2. For the fMRI data, the nodes, representing these brain regions, are typically defined using predefined anatomical templates, such as the Automated Anatomical (AAL) parcellation [60] or the Desikan atlas [61], or using data-driven approaches to identify spatial brain components as functionally homogeneous nodes (ICA) [9]. For the EEG data, they can be defined as the EEG electrodes or as the reconstructed sources. It is important to note that the choice of parcellation schemes for node definition might affect network measures [62]. The edges, in turn, correspond to the functional connection established between each pair, whose weight will reflect the level of correlation. In order to retain significant interactions and exclude spurious connections and noise, the connectivity matrix is usually thresholded. This can be done, for instance, with a cutt-off threshold or using a proportional threshold, this way keeping the top T% connections, resulting in a binary matrix specifying only the presence or absence of a connection between brain regions [46]. Note that different thresholds will generate graphs of different sparsity or connection density.

Having defined this graphical model of a brain network, it is possible to assess network parameters of interest, such as node degree, clustering coefficient and average path length. The degree of a node corresponds to the number of connections linking it to the rest of the network [4], being possible to establish a degree distribution that can reveal the topology of the network. This said, most real-world networks approximate to a scale-free behaviour, for which the degree distribution is modeled by a power law as

described by Barabási and Albert [64], meaning that some nodes will have many more connections than others (typically known as hubs). These scale-free networks are known for their high level of resilience against random attacks (loss of a node or edge randomly), but quite vulnerable if there is an attack to a highly connected hub node, as it may be the case of brain connectivity diseases [1]. However, brain networks have been shown to have exponentially truncated power law degree distributions instead, i.e, having a lower probability of arising very high degree nodes, which may reveal limited physical capacity for the nodes (representing brain regions) to make connections [4]. Note, nevertheless, that some studies revealed that increasing the resolution of the node definition leads to a degree distribution closer to a pure power law [65].

The clustering coefficient provides information about the level of local neighbourhood clustering within the graph, i.e., how much the neighbours of a node tend to be connected between themselves, reflecting the tendency of a network to form topologically local circuits. It can be computed for each node individually and then averaged over the entire network, with the following equation:

$$Cl = \frac{1}{N}\sum_{i\in N} Cl(i) = \frac{1}{N}\sum_{i\in N}\frac{2t_i}{k_i(k_i-1)}, \tag{2.8}$$

where, $Cl(i)$ corresponds to the clustering coefficient for node i, t_i the number of closed triangles attached to i and k_i the degree of i. It takes values between 0 and 1, where zero suggests an absence of clustering in the network, while a value of one indicates a fully connected graph. Therefore, this is a metric of information segregation in networks and it can be regarded as a measure of local efficiency of information transfer [4].

The characteristic or average path length represents the global efficiency of a network, as it measures how close a node is, on average, to every other node of the network. This metric is given by the following expression:

$$L = \frac{1}{N}\sum_{i\in N} l_i = \frac{1}{N(N-1)}\sum_{i\neq j} l_{ij}, \tag{2.9}$$

where l_i is the average shortest path length from node i to all other nodes or, alternatively, l_{ij} is the shortest path length from node j to i, computed with Dijkstra's algorithm [4]. The smaller the number of steps between any pair of nodes, normally mediated by highly connected nodes (hubs), the higher is the level of connectivity of the network and more efficiently the information is integrated throughout the whole system [1]. Graph analysis of brain networks has revealed that they present a small-world topology [4]. This means that these networks are composed by several clusters or modules (leading to a high level of local clustering) but still with a short travel distance between any two nodes, this way, combining high level of local efficiency with a high level of global efficiency.

2.2.1 Null Model Definition and Spatial Constraints in Brain Networks

When analyzing networks and their topology, independently of the metrics being analyzed, it is important to guarantee that the results are representative. This can be achieved by comparing these metrics with

the ones extracted from a suitable null model. Such a null model must be a randomized version of the original network, defined in such a way that preserves some of its properties, except naturally the one to be tested. Consequently, if there is no significant difference between the null model's properties and the original network observations, i.e., if the network does not deviate from what would be expected by chance, then no meaningful conclusion can be drawn about the network's organization. However, if an observation is highly unlikely, it can be concluded that it results from a mechanism or characteristic inherent to the network, not taken into account by the null model [66].

Apart from the network properties described before, this can be applied to guarantee statistical significance of the subgraphs found in the network being studied, that is, to verify if these small patterns appear in a larger network with a higher or lower frequency than it would be expected (see section 2.2.3 for more). Moreover, null models have different applications beyond testing the significance of observations, such as in community detection (see section 2.2.2 for more in community analysis). For algorithms based on modularity maximization, the null model is integrated in the definition of this quality function to extract the communities with within module connectivity higher than expected by chance [66, 67].

Regarding the choice of the null model to be used, ideally, this model should possess all the properties of the empirical network, except for the ones to be tested. In practice, this corresponds to matching only the basic properties like the network size, density and degree distribution [66], which will necessarily impose some structure in the network. This is the case of the rewiring null model, which can be generated by the Maslov-Sneppen rewiring algorithm, being the most commonly used null model and the first choice when analyzing brain networks, since many properties in these networks are possibly driven by the degree distribution [68].

Nonetheless, when analyzing brain networks, other features can be contemplated in the random network to more accurately reproduce the topology observed in the brain. For instance, it is often overlooked that these networks are physically constrained by the anatomical space and also by the cost of maintaining connections between different brain regions, which gives primacy to local connectivity and results in fewer long-range connections [20]. To overcome this limitation, one can include the physical distances between brain regions, creating spatial constraints that will guarantee a more realistic null model [66]. That is desirable since this spatial embedding will naturally impact the network topology. Consequently, this raises the question of whether the features captured, such as modularity, can be explained solely by the spatial constraints determined by the brain's underlying structure, or if there is some functional coactivation beyond this proximity effect, responsible to some extent for the patterns found. In fact, in [19] it was shown that the brain's embedding strongly contributed to the structural connectome's topology, namely regarding its modularity, even though not entirely, by comparing this network's properties against three different randomized versions where the distance between regions was taken into account. If this is the case for structural brain networks, then some effect must be present in functional networks since brain regions can only be correlated if they are somehow connected physically, even if on an indirect way, as it was emphasized in [21].

In practice to test this spatial effect, it is necessary to generate random networks preserving some spatial characteristics of the brain network to test the statistical significance of a given property, i.e., if it

deviates from what would be expected based on the spatial constraints alone. There are several options already explored for the definition of such spatially informed null models, which necessarily give primacy to short distances and/or smaller wiring costs. For instance, one can extend the Maslov-Sneppen rewiring algorithm to include the wiring length, approximated by the Euclidean distance between nodes given by:

$$d_{ij} = \sqrt{(x_i - x_j)^2 + (y_i - y_j)^2 + (z_i - z_j)^2}, \tag{2.10}$$

where x_i, y_i and z_i correspond to the coordinates of brain region i in the three dimensional anatomical space. This was done in [20], excluding any rewiring step that changes the total wiring length of any region to surpass that of the network being studied. Another possible null model adequate to spatial embedded networks is the radiation model, designed for populations flows and ideal to characterize propagation across space. It considers each node's intrinsic strength and neighbourhood for the flow of information [69], which might be interesting with directed functional networks.

Considering that there is a clear tendency for functional networks to group nodes that are near one another, anatomically speaking [70], a gravity-based model seems an adequate choice in order to contemplate this geometrical proximity effect [71], meaning that the closer two brain regions are, the higher the probability with which they interact. Therefore, this model assumes that the probability of a connection between two regions is proportional to their intrinsic strength and decays with distance:

$$P_{ij} \sim n_i n_j f(d_{ij}), \tag{2.11}$$

where n_i is the intrinsic strength of node i, $f(d_{ij})$ corresponds to an estimated deterrence function that describes the effect of distance d_{ij}. Note that, whenever the deterrence function is constant, this model becomes identical to the configuration model. When that is not the case, the degree distribution of the observed network is not preserved. Since the intrinsic strength corresponds to the observed node degrees, the resulting randomized version will, therefore, have a different degree sequence affected by the spatial constrains.

To overcome this limitation and consequently use a null model that preserves both the spatial properties and degree distribution, a recent study [22] proposed a model for directed networks where the intrinsic strength of each node is estimated recursively, in parallel with the deterrence function, until the degrees obtained are close enough to the original network. The deterrence function is given by the following equation:

$$f(d) = \frac{\sum_{ij|d_{ij}=d} A_{ij}}{\sum_{ij|d_{ij}=d} n_i n_j}, \tag{2.12}$$

where A_{ij} is the weight associated to the edge connecting nodes i and j, d_{ij} is the distance between the two nodes and n_i is the intrinsic strength of node i, that in the case of directed networks is given by:

$$n^{in} = \frac{k_i^{in}}{\sum_i n^{out} f(d_{ij})}, n^{out} = \frac{k_i^{out}}{\sum_i n^{in} f(d_{ij})}, \tag{2.13}$$

where k_i^{in} and k_i^{out} correspond to in- and out-degree of node i, with starting values $n_i^{in} = k_i^{in}$ and $n_i^{out} = k_i^{out}$. In the case of an undirected network, the estimated intrinsic strength will be $n^{in} = n^{out}$. Additionally, this degree constrained spatial null model is of special interest because it has been integrated in the modularity definition, extending what is expected by chance into including the spatial constraints.

Statistical Testing with Null Model For a quantitative assessment of the features captured by the original network with respect to any null model, some statistical testing must be performed. To do so, it is assumed a normal distribution of the null model's properties being analyzed, to extract their mean and standard deviation value for statistical assessing. This distribution can be obtained from a high number of surrogates being generated according to the defined null model, as repeating the randomization many times ensures a more stable estimate of expectations under the null hypothesis placed.

One way of quantifying the deviation of a particular metric in the empirical network in comparison the null model is by means of the z-score, defined as:

$$z - score = \frac{\mu_{observed} - \bar{\mu_{nullmodel}}}{\sigma_{nullmodel}}, \tag{2.14}$$

with $\mu_{observed}$ the observed value, $\bar{\mu}_{nullmodel}$ the mean value and $\sigma_{nullmodel}$ the standard deviation according to the null model. Statistically speaking, the z-score reports how many standard deviations the observed metric is from the null model's mean value. Equivalently, the p-value can be estimated from the associated z-score and is defined as a binary criterion to know which observations are statistically significant (usually when $p < 0.05$) and which are not. As such, the p-value gives the probability of obtaining results as extreme as the observed ones in a statistical hypothesis test, assuming a null hypothesis. Thus, a smaller value means there is stronger evidence in favor of the alternative hypothesis, which in this case states that the parameter differs from the value expected with the null model [72]. Note that very high or very low (if negative) z-scores are associated with very small p-values, which can be estimated from these values by means of Gaussian cumulative distribution function. This depends on the type of test considered, either one- or two-tailed, testing in one or two directions in comparison to the null model's value, respectively.

2.2.2 Community Analysis

As mentioned before, functional connectivity can be analyzed to identify modules or patterns reflecting coherent activity between different brain regions. Therefore, besides the metrics presented in section 2.2, it is possible to further analyze the topology of these brain networks to unravel these structures, both on a macro- and meso-scale.

On a macro-scale, the presence of partitions in the network can be investigated, reflecting its global structure and organization into densely connected clusters with relatively few connections between them. This analysis can reveal groups or communities of brain regions with coordinated activity and is based on community finding algorithms. These algorithms are mainly based on the optimization of a quality function which typically corresponds to the modularity. This metric measures the quality of the partition of

network nodes into different communities, a value assessed by comparing to a null model. It then measures the difference between the network's real wiring (A_{ij}) and the expected number of links between each pair of nodes (i, j) if the network is randomly wired (p_{ij}) [73], usually according to a configuration model. The modularity, considering an undirected network, is then given by:

$$Q = \frac{1}{2E} \sum_{ij} (A_{ij} - p_{ij}) \delta(c_i, c_j), \tag{2.15}$$

where E corresponds to the number of edges, $\delta(c_i, c_j)$ equals to one if nodes i and j belong to the same partition (i.e., $c_i = c_j$) and zero otherwise and $p_{ij} = \frac{k_i k_j}{2E}$ with k_i and k_j being the degree of node i and j, respectively. Although maximizing modularity is a NP-hard problem, there are several community finding algorithms that solve this problem approximately, such as the Newman [67] or the Louvain algorithm [16].

Several studies have applied community analysis to investigate brain networks, namely in temporal perspective [11], for both fMRI and EEG data, revealing periods of high and low modularity for fMRI functional networks [12, 13, 74, 75], where the Louvain algorithm is the commonly used community finding method. It consists in a heuristic approach based on greedy modularity optimization, that runs in time $O(V \cdot log_2 V)$ where V is the number of nodes or vertices in the network. It also corresponds to a hierarchical method, as communities are constructed from local neighbourhoods to the entire network (for more check [16]).

However, since the brain networks are physically constrained by the anatomical space they are embedded in, a question arises if a spatially informed null model would be able to recreate the network's communities. And if that is the case, it would imply that the modular organization present is solely the result of the effects of space. Considering this, it is necessary an extension of modularity that regresses out the spatial constraints influence, so as to find if long-range functional connectivity contributes to these communities, in opposition to contemplating only the geometrical proximity between nodes [21]. To do this, Cazabet et al. [22] proposed a modification of the Louvain algorithm, including the degree constrained spatial null model, described in section 2.2.1, into the definition of modularity. This way, the modularity's modified version measures the difference between the network's real wiring (A_{ij}) and what is expected by chance considering the spatial constraints, being given by:

$$Q_{spatial} = \frac{1}{2E} \sum_{ij} (A_{ij} - P_{ij}^{null}) \delta(c_i, c_j) = \frac{1}{2E} \sum_{ij} (A_{ij} - [\frac{k_i k_j f(d)}{\sum_{ij} k_i k_j f(d)} * 2E]) \delta(c_i, c_j), \tag{2.16}$$

where P_{ij}^{null} corresponds to the probability that nodes with degree k_i and k_j link to each other, corrected to take into account the distance factor between then, expressed by the deterrence function $f(d)$. Note that removing the spatial factor, that is, making the deterrence function constant, the null model turns into the configuration model and the modularity expression returns to its original definition.

Even though such method has not been applied yet to brain functional networks, some studies have suggested that, despite the neural systems tendency to show an optimal spatial arrangement by minimizing the wiring and distance, this is not the only factor for the configuration observed [76]. Additionally,

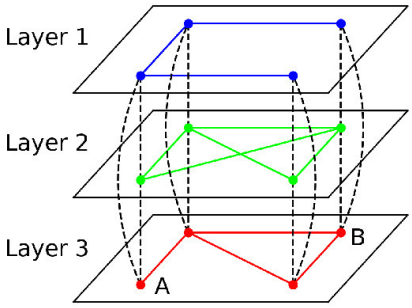

Figure 2.3: Representation of an undirected multilayer network with the same set of nodes between layers, also known as multiplex network. The coloured edges correspond to the link establish within each layer and the dashed lines reflect the inter-layer couplings between the same corresponding nodes. Adapted from [77].

a recent study has shown that, even when removing the short-distance connections, there is still a community structure present in the functional networks [21].

For a better characterization of the dynamic functional connectivity (dFC) changes, instead of analyzing the community structure at each time point, the analysis can be extended to take into account several interdependent time layers [78, 79]. This is possible using an extension of the Louvain algorithm to a multilayer context as proposed by Mucha et al. [17]. Briefly, a multilayer networks consists in generalization of the network construction, allowing for several layers to be grouped together, by establishing a coupling or a link between the nodes of the different layers [80]. As such, the community structure can be studied along the different layers, using the modularity definition proposed, given by:

$$Q_{multilayer} = \frac{1}{2E}\sum_{ijsr}[(A_{ijs} - \gamma_s p_{ijs})\delta_{sr} + \delta_{ij}C_{jsr}]\delta(c_{is}, c_{js}), \tag{2.17}$$

where s and r correspond to two adjacent layers, with an adjacency matrix A_{ijs} and resolution γ_s associated to each, C_{jsr} referencing the inter-layer couplings, that is, the probability of going from node j in layer r to node i in layer s, and $1delta_{sr}$ the restriction to only take into account common edges between the two layers in question.

As an alternative, this method can be applied to multimodal networks, where each layer corresponds to a type of interaction, information or even imaging technique. This type of approach has been applied, for instance, to combine structural and functional networks [81, 82] or to compare different subjects [83].

2.2.3 Motif Analysis

On the other hand, to identify patterns of synchronized activity or topological features on a meso-scale, the existence and count of overabundant small building blocks or subgraphs in the network can be explored. These reveal additional information about local structure and can be used as networks fingerprints or signatures [84]. These network motifs are small induced subgraphs that appear in a larger network at a higher or lower frequency than it would be expected, i.e., they are statistically significant when compared to an adequate null model. These motifs can be used to find differences in brain functionality between groups, equivalence between networks due to similar local structure or simply

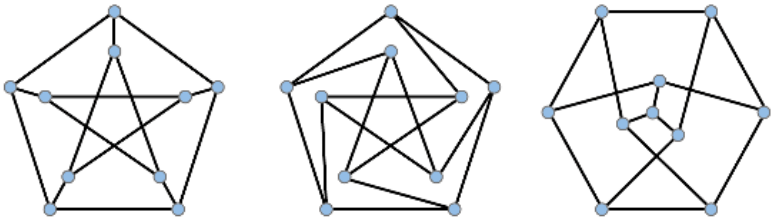

Figure 2.4: Three isomorphic graphs, with the same set of nodes and edges represented in different ways. Adapted from [84].

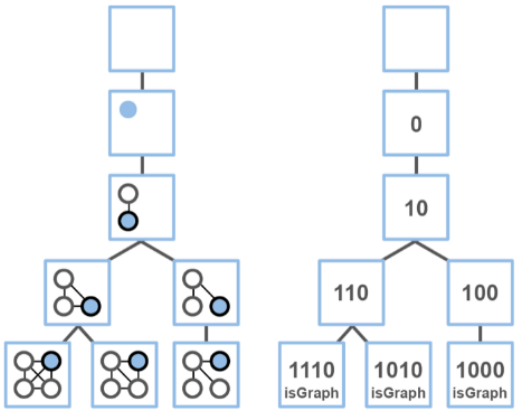

Figure 2.5: Representation of a g-trie storing a set of three undirected graphs. The root of the g-trie starts as empty and at each trie-node is added a new node from the graph (in blue) to the already existing subgraph in the previous trie-node. On the right, it is represented the corresponding boolean arrays that store the existing connections to the added graph-nodes. When more than one graph type emerges from the same common subgraph, there is a bifurcation in two trie-nodes. Adapted from [18].

to analyze functional connectivity coupling between a few brain regions with respect to some baseline [85, 86]. Therefore, they have the power to characterize and discriminate different networks.

All motifs of certain size can be enumerated in a network, determining the frequency of their occurrence, and classified into isomorphism classes, where two subgraphs are considered isomorphic if there is a mapping between their nodes, that is, if they are topologically equivalent (figure 2.4). However, both subgraph isomorphism and enumeration problems are known to computationally hard, being NP-complete, so this analysis is mainly focused on counting small subgraphs. One efficient way to store and enumerate them is to resort to g-tries data structure, proposed by Ribeiro and Silva [87], suited for enumerating many small graphs up until five nodes and with different shapes in large networks [18]. This is possible as this tree structure stores all common subtopologies between graphs in a compact and exact way, starting with the smaller common subgraph and expanding for the several extensions in each node of the data structure (represented in figure 2.5), avoiding redundancies and guaranteeing that each occurrence is only counted once. This then results in the fastest algorithm for general subgraph counting [84], with a time complexity of $O(V^2)$, where V corresponds to the number of nodes or vertices of the large network. Also, this algorithm implies a trade-off between the size of the subgraphs to be searched and the execution time, however, even having the subgraph discovery ratio (the number of subgraphs counted per second) degrading with size, it keeps the same magnitude [18].

This data structure has been already used in the characterization of brain networks with motif mining between auditory disease patients and healthy individuals [88]. In addition, several other studies have use motifs to characterize functional networks. In an early study, EEG functional networks were characterized over time by retrieving the directed motifs and analyzing the z-score value of each type over time [89]. Another study also investigated directed motifs but now on fMRI functional networks, reporting as well their topological distribution supporting the modular architecture and functional role of specific brain hubs [90]. Other studies have compared the distribution of motifs across the brain between different consciousness conditions and mental disorders [91]. A recent study went further by defining network fingerprints, that consist in the number of occurrences of each motif normalized by the total number of motifs in the network, and use them to characterize the fMRI functional networks in comparison with several possible null models [15].

2.2.4 Comparing Sets and Partitions

To make sense of the topological patterns or modules of coordinated activity extracted from the analysis of functional networks, these sets of brain regions can be compared across time, between different datasets or modalities, or can even be compared to randomized surrogates to assess the statistical significance of the results obtained. As such, the shared information or their similarity can be revealed with several possible metrics. For the community structure, one possibility is to use the Normalized Mutual Information (NMI), which allows the comparison between partitions with different size. This measure is given by:

$$NMI(X,Y) = \frac{-2\sum_{i=1}^{C_X}\sum_{j=1}^{C_Y} N_{ij}\log(\frac{N_{ij}N}{NiNj})}{\sum_{i=1}^{C_X} N_i\log(\frac{N_i}{N}) + \sum_{j=1}^{C_Y} N_j\log(\frac{N_j}{N})}, \tag{2.18}$$

where X and Y correspond to the community structure of two networks, C_X and C_Y are the community label in partitions X and Y, respectively, N is the total number of nodes, equal for both networks and N_i the number of nodes in community i, as defined in [92]. The NMI value range from 0 to 1, where 0 indicates that there is no common ground and information shared between the two partitions, and 1 when they correspond perfectly.

Another option is the Jaccard Index or similarity coefficient, which is defined as the size of the intersection of two sets or partitions divided by the size of the union of the two:

$$Jaccard \quad Index = \frac{|X \cap Y|}{|X \cup Y|}, \tag{2.19}$$

with its values varying between 0 and 1, from no intersection to complete match.

For the comparison of the motifs present in different functional networks, for instance when using the network fingerprints as defined in the previous section, these measures are not adequate since these fingerprints essentially correspond to ”vectors” characterizing a network. Consequently, these ”vectors” can be compared through the cosine of the angle between them, i.e., the inner product of the two normalized vectors. This can be done using the cosine similarity metric, given by:

$$cosine \quad similarity = \cos(\theta) = \frac{\mathbf{X} \cdot \mathbf{Y}}{\|\mathbf{X}\| \, \|\mathbf{Y}\|} = \frac{\sum_{i=1}^{n} X_i Y_i}{\sqrt{\sum_{i=1}^{n} X_i^2} \sqrt{\sum_{i=1}^{n} Y_i^2}}, \tag{2.20}$$

where $\mathbf{X}$ and $\mathbf{Y}$ correspond for instance to these network fingerprints, composed by n motif classes. This metric has already been applied for comparison of topographic distributions in brain networks [91], with values spanning from -1 to 1, meaning that the vectors are complete opposites or exactly the same, respectively, with 0 indicating orthogonality and therefore no correlation.

Chapter 3

Data Processing and Initial Analysis

This chapter includes the data acquisition and pre-processing steps, as well as the functional connectivity estimation for both fMRI and EEG data. It also contains the hemodynamic response delay estimation, for the alignment of the two modalities, and the threshold selection approach, to be applied to each functional network. Finally, it introduces this work's analysis with a connected components' study.

3.1 Methodology

3.1.1 Data Description

The dataset used in this work consists in simultaneous fMRI-EEG recordings acquired during rest in the scope of a previous project [93], having been made some changes regarding its pre-processing and brain segmentation, according to [94], as described below.

3.1.1.1 EEG-fMRI Data Acquisition

The concurrent data was acquired using a 7T MRI scanner along with a 64-channel EEG system, with the participation of 9 healthy subjects (with age range 22-26, 4 females) with no history of neurological or psychiatric illness. Each subject was scanned during a resting-state condition, with eyes-open for a period of 8 minutes, while focusing on a small red cross presented in a grey background. This was done so as to minimize head and eye movements.

The imaging was performed on an actively-shielded Magnetom 7T/68-cm head scanner (Siemens, Erlangen, Germany) using an 8-channel head RF coil (Rapid Biomedical, Germany), at the Centre for Biomedical Imaging (CIBM) at EPFL [93]. Whole-brain functional images were obtained using a 2D simultaneous multi-slice gradient-echo Echo-planar imaging (EPI) sequence, with repetition time (TR) of 1000 ms and 2.2 mm isotropic resolution, leading to a total of 480 volumes. Whole-brain, 1 mm isotropic resolution structural images were also acquired, in this case using a T_1-weighted 3D gradient-echo MP2RAGE sequence. Simultaneously, the EEG data were recorded using two 32-channel BrainAmp MR plus amplifiers (Brain Products, Munich, Germany) coupled with a 64-channel BrainCap MR model (EasyCap, Herrsching, Germany). This cap, containing 64 electrodes, was arranged according to the

10-20 system, including a reference electrode (FCz), one electrode placed in the back of the subject to record the Electrocardiogram (ECG) signal (for subsequent pulse artifact correction) and 4 modified EEG electrodes to be used as motion sensors. Thus, a total of 59 electrodes remained for the EEG recording. Scanner triggers marking the onset of each fMRI volume were also recorded.

All participants gave written informed consent and this study was approved by the Lausanne's Research Ethics Committee (CER-VD) [93].

3.1.1.2 fMRI Data Analysis

fMRI Pre-processing The pre-processing of the fMRI data was done previously in [94], consisting in the following steps described here. The first step consisted in a B_0-unwarping step applied with FSL-TOPUP (v6.0.2, [95]), using the reverse-phase encoding acquisition, so as to remove the more prominent image distortions present. Due to the short TR of 1 s, no slice timing correction was carried out, but a spatial realignment was performed using the Statistical Parametric Mapping (SPM12) toolbox (revision 7475, `http://www.fil.ion.ucl.ac.uk/spm/software/spm12`).

After, to achieve the segmentation of the data into several regions of interest, the Freesurfer toolbox (`http://surfer.nmr.mgh.harvard.edu/` v6.0.0) was used to process the T_1-weighted structural images for non-uniformity and intensity correction, skull stripping and grey/white matter segmentation. However, due to local signal drops near EEG lead convergence points in these images [96], it was not possible to run the individual segmentation for all subjects. Hence, so as not to lose any subject and keep data consistency, all the functional images were co-registered to the Montreal Neurological Institute (MNI) template and the Freesurfer was used to extract the surfaces of the MNI template. To take into account the subject specific variance, the atlas images were then dilated by 3 voxels (using `https://github.com/mattcieslak/easy_lausanne`). Using Advanced Normalization Tools (ANTS v2.2.0, [97]), white matter masks were obtained through segmentation, that were subsequently used for the transformation of the segmented MNI template to fMRI. This was achieved by co-registering the functional images with the respective structural ones using FSL's tool FMRIB's Linear Image Registration Tool (FLIRT v6.0.2) [98], with boundary-based registration, and later with the MNI template using FSL's tool FMRIBS's Nonlinear Image Registration Tool (FNIRT v6.0.2, [98, 99].

Parcellation was then performed by segmenting the resulting data into R = 68 non-overlapping regions of interest (ROIs), including only cortical areas, according to the Desikan(-Killiany) atlas [61]. This generalized labeling is based on the anatomical curvature information available on the 'inflated' images of the cortex. It incorporates a wide range of anatomic and atrophic variance by using 40 MRI scans of diverse controls, both healthy and with Alzheimer's disease. These regions of interest will then define the functional network's nodes.

Following this, to remove nuisance fluctuations, including physiological noise, no interest signals were regressed out of the BOLD time series [94], namely:

- the average signals of cerebrospinal fluid (CSF) and white matter (WM), which were extracted from manually defined ROIs (5 mm sphere, using Marsbar Toolbox 0.44 `http://marsbar.sourceforge.net`);

- the six rotation and translation motion parameters;
- the global gray matter signal;

Finally, the timeseries were bandpass-filtered at 0.009-0.08 Hz [100] and scrubbed using frame wise displacement (with threshold 0.5) as defined by Power et al. [101].

fMRI Dynamic Functional Connectivity The functional connectivity estimation from the BOLD time-series is limited by the acquisition time of each brain volume as well as by the duration of the hemodynamic response, which acts as a low-pass filter blurring the neural activity [6]. Therefore, to not lose even more temporal resolution and also to avoid the window size trade-off associated with sliding window approaches, it was chosen to use phase coherence (PC) as connectivity measure. This will produce an instantaneous connectivity value, without being smoothed by averaging over a window, based on phase synchronization. However, one must be careful as this metric comes at the expense of being more susceptible to noise than sliding window methods, as reported in [102].

As such, to estimate functional connectivity, the Hilbert transform was applied to the filtered BOLD time series of each brain region n, after regressing out the mean value, and the instantaneous phase of each time point, $\phi(n,t)$, was extracted. Then, according to 2.4, the PC was computed for each pair of regions, leading to a connectivity matrix representing the edges of the fMRI functional network for each time point. To process the BOLD data and obtain the PC, an adaptation of Cabral et al.'s implementation (`https://github.com/juanitacabral/LEiDA`) was used [35], consisting in the steps covered here.

Additionally, since some time points were excluded from the EEG data due to excessive motion, as it will be referenced in section 3.1.1.3, the connectivity matrices associated to these instances were removed. Which will result in the same number of connectivity matrices for both modalities, necessary for a correct comparison between the two.

Hemodynamic Response Delay Correction Even though the acquisition time points between the two modalities are aligned (check section 3.1.1.3 for EEG time-series segmentation according to fMRI TR), the BOLD time-series will have an intrinsic delay with respect to the EEG data, due to the different nature of the two signals, as mentioned before in section 2.1.1.1. This delay, due to the hemodynamic response following neuronal activity, has been reported typically being between 4 and 6 seconds [103]. Considering the existence of this temporal shift of the fMRI signal, a physiological alignment between the two types of functional networks seems to be necessary for a reliable spatiotemporal comparison between fMRI and EEG, so that, in theory, each time instance captures equivalent neuronal activity.

To achieve this temporal alignment between modalities, the hemodynamic response function (HRF) parameters - response height, time-to-peak and full width at half maximum (FWHM) - were estimated using a resting-state HRF deconvolution toolbox (rsHRF: a Toolbox for Resting State HRF Deconvolution and Connectivity Analysis by Wu et al., `https://github.com/compneuro-da/rsHRF`), with the time-to-peak interpreted as the delay of the hemodynamic response. The implemented method is usually known as blind deconvolution, since its typical use consists in estimating both the underlying neural time series and the HRF parameters directly from the observed fMRI data, with no additional external input taken

into account [104]. Specifically, it consists of fitting the hemodynamic response function (HRF) to the data and is based on the assumption that the HRF is equivalent across the several point process events detected in each region's time series. However, as the hemodynamic response has been shown to vary regarding its timing, amplitude and shape across different brain regions, even for resting-state conditions [105], the hemodynamic response parameters had to be estimated for each brain region:

- first, a pre-defined HRF was obtained with a linear combination of two gamma functions (canonical HRF from SPM toolbox, available in `https://www.fil.ion.ucl.ac.uk/spm/software/spm12/`), adding the temporal and dispersion derivatives to include some flexibility in the basic model. These two additional components, derived by a first-order multivariate Taylor expansion, allow the capture of the HRF's variability, relative to its response shift in time and activation extension, respectively [106, 107];
- afterwards, the neural events were detected in the resting BOLD time series, extracting signal fluctuations for which their amplitude surpassed a given threshold around a local maximum [104]. This resulted in a list of time points for which the BOLD signal's amplitude had a z-score of 1;
- the empirical HRF was then fitted by convolving the chosen canonical HRF and the selected BOLD events, testing for several delays and selecting the one for which the mean-squared error of the noise covariance was minimal;
- finally, the hemodynamic response function parameters characterizing the shape of the resulting HRF were obtained.

Furthermore, the distribution of time-to-peak values of the HRF for all regions was analyzed and the median value (rounded to seconds) was extracted for each subject, corresponding to the final hemodynamic response delay to be used for the functional networks' temporal alignment.

3.1.1.3 EEG Data Analysis

EEG Pre-processing The EEG data pre-processing steps were performed previously in [94], consisting in the following:

- gradient artifact correction slice-by-slice using average template subtraction (AAS) (as described in [108]);
- bad channel interpolation (1-4 channels per subject);
- temporal bandpass filtering (1-70 Hz);
- pulse-related artifact correction (using a k-means clustering-based approached verified in [93];
- downsampling to 500 Hz;
- motion artifact correction, consisting in an offline multi-channel recurse least-squares regression using the motion sensor signals (as described in [108]);

- manual ICA-based denoising for removal of gradient and pulse artifact residuals, as well as eye-blinks and muscle artifacts contributions.

Afterwards, the cleaned EEG data was analyzed with Brainstorm software [109](documented and freely available under the GNU general public license, `http://neuroimage.usc.edu/brainstorm` version 15th January 2019), which included bandpass filtering of the data at 0.3-70 Hz and segmenting it as a multiple of the TRs of the fMRI acquisition (with a sliding window of 4 s with 1 TR (1 s) steps). Subsequently, the EEG epochs with any motion exceeding the mean channel time course by 4 standard deviations were semi-automatically detected and removed. Also, through visual inspection, all motion segments in the whole time courses were also excluded.

Following this, a source reconstruction procedure was performed, also using the Brainstorm software, to have the electrical signal capture by the electrodes transformed into the underlying sources activity. These regions are defined using the same parcellation as for the fMRI, in order to have equivalent network nodes between the two signals to be analyzed. The source reconstruction process included the following steps:

- the electrode positions were first co-registered with T_1-weighted images by aligning manually the electrode positions with their artifacts visible in each image;
- a forward model of the skull was then computed based on the individual T_1-weighted image of each subject with the OpenMEEG BEM model [110, 111];
- the EEG signal was projected into the source space using the Tikhonov-regularized minimum norm [112] with the Tikhonov parameter set to 10% (with the Brainstorm 2018 implementation, assumed SNR ratio of 3.0, using current density maps, depth weighting 0.5/max amount 10 and flipping the constrained sources normal to cortex/signs into one direction);
- to finish, the source activity was averaged in each cortical region of the Desikan atlas, as defined for the fMRI data.

EEG Dynamic Functional Connectivity As mentioned previously in section 2.1.2.2, the interpretation of EEG data in terms of brain connectivity is not without obstacles, considering that the correlation between the signals of two channels may not reflect a true interaction between different brain regions. This because volume conduction allows the activity of a single source to be observed in multiple electrodes. Even though a source reconstruction procedure was applied to overcome this limitation, imaginary part of coherency was chosen as an adequate connectivity measure, since no inverse method is fully satisfactory and can still lead to misinterpretations of artifacts as brain interactions [41]. And this metric reflects the actual interaction between two signals, removing any zero-lag synchronizations associated to volume conduction.

However, in order to use coherency (and in particular, its imaginary part) as a measure of connectivity, it is necessary to guarantee that its values, namely the expected value of the cross-spectrum $\langle S_{xy} \rangle$ (see equation 2.6), are accurately estimated and correspond to a significant measure, in opposition to a

result of a random correlation. In theory, this would require averaging the cross-spectrum over a number of trials or subjects, but, since for this work only one session was performed in resting-state conditions, which will also correspond to different signals for each subject, it was not possible to apply this. As alternative, a different approach was employed, which relies on the Welch's weighted overlapped-segment averaging method, most used for spectral density estimation [113], but also for estimating coherence. For the particular case of this work, it consists in the following steps:

- for any pair of signals X and Y temporal windows of 4 seconds centered at each time point t (with step corresponding to 1 TR) were divided into $T = 14$ overlapping and equally spaced segments,
- these segments were later smoothed with a window that corresponds to the product between a Parzen and a Tukey window (that perform frequency smoothing equivalent to a convolution with a very shallow Gaussian window and last and first few samples removal to preserve smoothness and avoid jumps, respectively);
- the Fast Fourier transform was then applied to each segment, for both signals, and the resulting coefficients used to estimate the cross-spectrum for that same segment (equation 2.6);
- finally, the average of the cross-spectrum for all segments was computed, leading to the expected value of the cross-spectrum $\langle S_{xy} \rangle$, and thus the imaginary part of coherency for each t.

It is important to notice, however, that this method is based on the assumption of some temporal stability regarding the phase difference between the two signals, within the window interval considered. This might not be a reasonable assumption for resting-state data, especially for fast neurophysiological signals such as the ones captured by EEG, creating a downward bias in the coherency estimation [113]. Also, in addition to these steps, a parametric estimation of the significance level of the coherency was performed, taking into account the number of samples considered for each time point. With this procedure, all imaginary coherency values with $p - value$ below 0.05 were excluded, minimizing the spurious correlations.

The complete computation was done using the Brainstorm function *bst_cohn.m* (according to the Brainstorm 2018 implementation `http://neuroimage.usc.edu/brainstorm`, 'icohere' measure), between every pair of regions' source activity, for each time point (1 TR), using bins of 2Hz frequency resolution. Bins that were, subsequently, averaged for 5 canonical frequency bands: delta δ (1-4 Hz), theta θ (4-8 Hz), alpha (8-12 Hz), beta β (12-30 Hz), gamma γ (30-60 Hz) [94]. These pairwise estimates thus correspond to the connectivity matrix that represent the edges of the functional network, for each time point.

3.1.2 Data Representation

With the objective of the analysis of and comparison between the fMRI and EEG functional networks' topology on a meso- and macro-scale, a graph representation was used. The nodes were determined by the chosen brain parcellation, corresponding to the regions of interest defined by the Desikan(-Killiany) atlas [61], equivalent for both modalities, guaranteeing a spatial alignment between the two network

Table 3.1: Number of time points considered for each subject.

Subject	1	2	3	4	5	6	7	8	9
number of time points	400	448	405	342	282	420	407	365	424

types. The edges, on the other hand, were defined by the functional connectivity matrices obtained for each time point using PC and imaginary part of coherency, respectively. Furthermore, the functional networks were temporally aligned by taking into account the hemodynamic response delay, as mentioned in section 3.1.1.2. With these considerations, the graphical model of these functional networks corresponds to an untresholded weighted undirected graph, for each time instance. The number of functional networks considered for each subject, i.e., the number of time points to be examined, are described in table 3.1. These resulted from the removal of volumes and time segments, in the case fMRI and EEG respectively, where excessive motion was detected, as previously reported.

3.1.3 Threshold Estimation and Connected Components Analysis

This section is dedicated to the threshold estimation for both fMRI and EEG functional networks, followed by a brief connected component analysis for an initial preview of the potential correlation between fMRI and EEG regarding their topological structure as well as their individual organization over time. All the code was implemented using Python3.6 and is available in `https://github.com/franciscaabsr/Thesis_project/Code/graph_connected_components_analysis.ipynb`.

3.1.3.1 Threshold Selection

A common step in the definition of functional networks is to threshold the connectivity matrix by selecting a limited number of edges that reflect significant interactions. This way, it is possible reduce spurious connections by removing the weakest links, more susceptible to experimental noise, with the downside of potentially lose relevant information. Even though this can be done in several ways, as covered in section 2.2, it was chosen to use a proportional threshold to ensure equal network sparsity across time points and subjects and allow more reliable comparisons. Unfortunately, the choice of an adequate threshold value that optimizes the information-noise trade-off in these brain networks cannot be based on biological principles, but only be an 'educated guess'. With no current consensus in literature and considering that network properties are dependent on the structure retained [114], most studies explore these metrics across a range of threshold values and select *a posteriori* the most adequate.

Consequently, there are a few considerations to be taken into account for the selection of the threshold to be used in this work. First of all, one must be careful when selecting a percentage of edges to keep as it can lead to the inclusion of spurious connectivity whenever the overall functional connectivity values are lower [115]. Besides this, it is also desirable that thresholded graph keeps the giant component structure so as not to lose the network's main topological characteristics for further analysis. Recent studies have presented alternatives for threshold selection based on the percolation theory [92, 116], which is associated with the network's robustness, by assuming that the nodes or edges not included

in the giant component are somewhat more vulnerable [73]. Specifically, in [92], it was proposed a method that iteratively removes the weakest edges to find the critical point where the giant component starts to collapse. This will correspond to the percolation threshold at which the network's structure is still preserved, while removing the effects of noise. This allowed to find an optimal balance between the information gained by removing noise and lost by excluding potentially relevant connections, since it was found that this threshold led to the information maximization of the community structure.

Taking this as inspiration, in this work, the threshold selection was done by means of a connected components study based on a percolation approach, to guarantee the existence of the giant component in most time points' networks. This consisted in adding the edges by decreasing connectivity value until 90% of the network's nodes are connected (set as the necessary condition for the giant component existence), storing the median of the minimum value of connectivity for all time points of all 9 subjects. Then, after removing all edges with connectivity lower than this absolute value, the median sparsity value of these networks (concatenating all subjects) was set as the proportional threshold and slightly made stricter by subtracting its standard deviation. It is worth mentioning that it was chosen this indirect way of estimating the proportional threshold, since it was found that simply taking the median percentage of edges kept was too loose as a criterion, possibly leading to the inclusion of more spurious connections. It would also result in having fully connected networks for most time points, which is not desirable for a further connected component analysis and also not necessary for the capture of the network's structure.

Finally, the estimated threshold was applied to obtain undirected binary graph representations, for each time point, using Brain Connectivity Toolbox's *threshold_proportional* function. Since with this approach there is no equivalence between networks in terms of the connectivity level kept, the existence or not of certain edges cannot be the scope of the analysis and comparison between different time points or modalities. Instead, these networks topology can be studied in terms of their modular structure (reported in chapter 4) and recurrent patterns (explored in chapter 5, when compared to a random null model.

3.1.3.2 Connected Components Analysis

Comparison over time After applying the estimated threshold, each functional network will be organized into a set of connected components that can be analyzed over time, so as to slightly lift the curtain and obtain some initial information regarding these networks' topology.

With this objective, it was first obtained the distribution of the connected components' size over time, building a cumulative bar plot, where each bar corresponds to the number of nodes of the corresponding connected component, for all time points. In addition, a comparison between the giant component and the second biggest component was performed to analyze their size variation and, possibly, their relation over time. Following this, in order to find potential topological patterns over time, the connected components' set was compared between pairs of time points using the Normalized Mutual Information (NMI) metric, defined in section 2.2.4. It measures the common information between two random variables, that is, the amount of information that can be obtained about one variable by observing, establishing a level of mutual dependence between the two. Being normalized, it allows the comparison of values be-

tween different pairs of variables, that in this case correspond to all the pairs of connected components' sets. Using python-igraph's *compare_communities* function, a NMI matrix was obtained, with values between 0 and 1, from no similarity to full correspondence between the time points' component set. To potentially extract patterns of connected components over time and thus give a first insight into the networks' spatiotemporal organization, this similarity matrix was subject to a clustering procedure. This was achieved by grouping the time points, using both the Louvain algorithm and the Hierarchical Single Linkage algorithm, a bottom-up approach that merges the pair of clusters with shortest distance between them [117]. Finally, it was computed the Jaccard Index, as defined in 2.2.4, to establish a comparison between the set of nodes included in the giant component for every pair of time points. This was done to remove the undesirable influence of smaller components when there is a high number of them, as they might be responsible for a lower similarity value.

Comparison between modalities With hopes of getting some initial hints regarding the possible relationship between fMRI and EEG functional networks' topology as well, a component comparison analysis between the two modalities was performed. First, the connected components' set obtained for each type was compared for all time points, using again the NMI metric, reflecting the similarity between fMRI and EEG's connected components across time. Following this, a giant component comparison over time was performed using the Jaccard Index, in an equivalent way as described in section 3.1.3.2.

3.1.4 Null Model Definition

As previously covered in section 2.2.1, to reach meaningful conclusions regarding the functional networks' topology, one must choose an adequate null model that captures some of the networks properties to serve as a randomized benchmark. From the several possibilities present, the rewiring null model was deemed as a good first choice to capture the degree distribution's influence. Furthermore, since brain networks are constrained by the space they are embedded in, it is necessary to choose additionally a spatially informed null model to capture both fMRI and EEG functional networks' properties beyond these constraints. It was chosen the degree constrained spatial null model, defined in [22], because it includes both the spatial restrictions and the degree distribution of the original network. Also, it was considered that the assumption that the probability of an existing edge diminishes with the distance between the pair of nodes was adequate, since it was reported a tendency for modules in functional networks to be comprised of nodes closer to each other [70]. Moreover, this spatial null model has already been integrated into a modified version of the Louvain algorithm [22], extending the definition of modularity as described in section 2.2.2.

So as to obtain a rewiring null model, 100 random surrogates were generated according to the Maslov-Sneppen algorithm, for an unweighted and undirected graph. This was done using Brain Connectivity Toolbox's *randmio_und* function, setting the number of rewiring iterations per edge to 20 to ensure a thorough randomization [78].

Afterwards, it was generated a degree constrained spatial null model, according to [22], using an adaptation for undirected networks of the code implemented in (`https://github.com/Yquetzal/`

`spaceCorrectedLouvainDC`). First, using the three-dimensional coordinates obtained from the parcellation of the structural images for each brain regions, the distances between every pair of nodes were computed according to the Euclidean distance. It was chosen to use this distance definition instead of the great circle distance as suggested in [22], since the difference between the two is negligible for short distance, which is the case for brain networks. Following this, the intrinsic strength of each node and the deterrence function, given by equation 2.13 and 2.12 respectively, were estimated iteratively, using the distances computed before. From this, the spatial null model was estimated, resulting in a matrix of edge probabilities, defined by the equation 2.11. Finally, a random value between 0 and 1 was obtained for each pair of nodes and, whenever that value was below the probability defining the null model, the corresponding edge was added to the surrogate adjacency matrix. This was then repeated so as to generate 100 distinct surrogates of the spatial null model, with connection density slightly fluctuating between them, though still similar to the original network's.

It is important to mention that it was chosen to keep the 5 iterations suggested in [22] as stopping criteria for the estimation of the intrinsic strength and deterrence function, owning to the fact that the degree distribution was very similar to the original network's one. In figure A.1 of the appendix is represented the degree distribution and its cumulative version for a functional network and one of its randomized surrogates, for both fMRI and EEG alpha band. Additionally, a parameter named *minValsBin*, responsible for setting the number of times a distance value needs to appear for it to be relevant, was changed from 3 to 1, since, due to the low number of nodes in these networks, almost all distance values appear only once or twice. Finally, for the estimation of the intrinsic strength of each node, the code was adapted to consider an undirected graph not fully connected, or in other words, to take into account the possibility of having isolated nodes.

3.2 Results

3.2.1 Hemodynamic Response Delay Correction

The time delay associated to hemodynamic response was estimated for each brain regions' BOLD time-series, using a blind deconvolution method. The resulting distribution of time-to-peak (TTP) values for all brain regions of each subject is represented in the appendix in figure A.2 and the median values are summarized in table 3.2, as well as the resulting temporal shift (in TRs) that was applied to fMRI functional networks.

These results confirm once again the variability of the hemodynamic response estimates across different cortical regions and subjects. However, the delay obtained was lower than expected, usually reported around 5 seconds [118, 119]. One reason for this result might be due to the fact that resting-state signals have a faster associated hemodynamic response [120]. This because, these signals are characterized by fast and continuous oscillations, resulting in an accelerated signal rise and recovery. That in turn, translate into a faster response in blood flow, as reported in a study by Chen et al. [121]. As such, one would expect a lower time-to-peak value owing it to a faster hemodynamic response, in

Table 3.2: Median time-to-peak estimated values and final temporal delay to be imposed.

Subject	1	2	3	4	5	6	7	8	9
median TTP (s)	3.44	3.44	3.38	3.31	3.38	3.56	3.31	3.31	3.81
temporal delay (TR)	3	3	3	3	3	4	3	3	4

comparison to a task condition. On the other hand, deriving the hemodynamic response function from the data, parameterizing its shape across subjects and regions by means of the blind deconvolution procedure, might influence the results obtained. Finally, one must take into consideration that each dataset is unique in terms of its acquisition, pre-processing and conditions present, so different hemodynamic response delays are expected to be found.

3.2.2 Threshold Selection

The proportional threshold was estimated by means of bond percolation approach, looking for a percentage of edges to be kept that guarantees the giant component for most time points. The table 3.3 summarizes the values obtained for the fMRI and all the EEG frequency bands functional networks, concatenating all subjects, and table 3.4 the percentage of time points with giant component with more than 90% of the nodes.

From these results, it is possibly to conclude that the giant component was not present for all time points, at least according to its defining criteria. This was expected due to three reasons: the threshold chosen resulted from the median value of sparsity, which in theory would lead to approximately half of the time points without the giant component. Secondly, in practice, the giant component might be present, in comparison to smaller components in the network, but not be composed by 90% of the network's nodes. Finally, due to the signal fluctuations, whenever the signal is too weak, there will be no structure captured in the functional networks and therefore no giant component will be detected.

Table 3.3: Proportional threshold values corresponding to median sparsity value subtracting its standard deviation, for fMRI and all EEG frequency bands.

Data type	fMRI	EEG delta	EEG theta	EEG alpha	EEG beta	EEG gamma
threshold (%)	11.0	7.5	6.6	7.0	6.1	7.0

3.2.3 Connected Components Analysis

Comparison over time Regarding the size of the resulting connected components after thresholding the functional networks, it was obtained their size's distribution over time by building a cumulative bar plot as well as a comparison between the giant and second biggest component number of nodes, for all time points of each subject. Additionally, it was plotted this variation for both fMRI and EEG data to establish a parallel between the two regarding the giant component's size characteristics. The resulting plots for the fMRI and all EEG frequency bands are presented in the appendix, in figures A.3 and A.4, respectively, for an arbitrary subject.

Table 3.4: Percentage of time points with a giant component with more than 90% of the network's nodes, for all subjects and types of data.

Subject	1	2	3	4	5	6	7	8	9
fMRI (%)	43.8	39.1	39.8	51.8	44.3	46.7	36.2	40.8	42.2
EEG delta (%)	44.0	63.4	45.7	42.7	43.9	55.0	48.6	38.4	43.2
EEG theta (%)	42.8	51.8	52.6	52.0	36.9	53.6	40.0	37.3	36.8
EEG alpha (%)	49.5	40.6	34.6	53.8	40.8	33.6	46.4	43.3	52.7
EEG beta (%)	54.5	54.0	34.6	21.1	23.4	45.0	39.3	42.7	39.4
EEG gamma (%)	63.8	74.8	27.9	36.0	33.3	52.1	11.5	61.9	43.6

First, considering the distribution of the connected components size for both data types, it is possible to observe that the EEG functional networks have a higher number of connected components than the fMRI ones, independently of the frequency band being analyzed. Additionally, the giant component is substantially larger than all the other components, as they are essentially either isolated nodes or very small (with a maximum of 4/5 nodes), in the case of EEG. For the fMRI, a different panorama occurs as two larger components can be visualized in comparison to all others. This is also contemplated in figure A.4, where for the fMRI there is a distinct second biggest component, not observed in the EEG networks. Also, from this plot one notices that, for most time points where the giant component decreases size, the second biggest component increases its size, in the case of fMRI. This effect was not expected since, according to the percolation theory and emergence of the giant component studies [73], when the giant component collapses, it is usually disintegrated into several smaller disconnected components, resulting in a loss of structure of the whole network. One possible reason for both these observations is that the fMRI functional networks are probably more clustered than the EEG ones. That is, they might be divided into strongly connected groups of brain regions linked by weaker connections, that probably might be removed by the sparsification procedure. While, for the EEG frequency bands, the higher connectivity edges kept sustain a larger giant component, with only a few isolated nodes. This hypothesis regarding the clustered nature of these functional networks will be further tested in the community analysis in chapter 4. Moreover, relatively to the decrease of size of the giant component followed by an increase of the second biggest one, these results might suggest a relevant state of connectivity repeating from time to time. However, considering that the fMRI data was bandpass filtered into a frequency of 0.01 - 0.1 Hz, it is only possible to identify significant and stable variations corresponding to at least 10 time frames. This means that no conclusion can be reached from these results, which can either reflect a possible interesting network state or just a consequence of noise presence in the data.

To study the potential existence of topological patterns over time, the connected components were compared for every pair of time points using the NMI metric. Identically, the giant component's similarity over time was computed using the Jaccard Index. These measures' matrices are represented in A.5 and in A.6, respectively, with values between 0 and 1 associated to a colour scale.

Relatively to the NMI matrices, there is a clear repetition over time, for the fMRI, which is not observed in the case of EEG. However, it is only because it corresponds to the time points where the fMRI functional networks are fully connected (with only one component) and will naturally have maximal

similarity. Besides these, it was found a relative similarity (NMI = 0.3-0.6, depending on the frequency band in question) for some time points in both fMRI and EEG networks, while having other time points completely uncorrelated (NMI = 0). When clustering these time points into groups using the Louvain algorithm and the Hierarchical Single Linkage algorithm, no interesting patterns of components where extracted. For the fMRI only two clusters were found with both methods, separating the time points where the network is fully connected and the ones that had more than one component, with a very low modularity for the first algorithm. In the case of EEG, despite having been able to extract about 5 to 8 groups of time points (depending on the frequency band) by the Louvain algorithm, the corresponding modularity was again very low. Also, when using the Hierarchical Single Linkage algorithm in such a way that avoid merging very distinct groups of time points, more than 200 clusters where found. From these results, it is only possible to conclude that, at least from a connected component analysis, no distinct topological patterns can be reported.

Finally, regarding the Jaccard Index matrices, the similarity between time points increased greatly in comparison to the NMI ones, which is in accordance with the hypothesis that there was an undesirable influence of the smaller components. It was also found that most time points' networks have a similar giant component and that these time points are interspersed with some time points where this similarity decreases greatly, corresponding to lower signal instances for which there will not exist a giant component.

Since no interesting results were found, in terms of temporal comparison, no additional analysis was pursued and the topological analysis over time was continued with a community detection and motif enumeration study, in chapters 4 and 5, respectively.

Comparison between modalities With hopes of getting some initial clues of a possible correlation between fMRI and EEG functional networks' topology, the connected components obtained for each were compared with the NMI metric as well as the giant component for each time instance, in this case with the Jaccard Index. It is important to mention that an additional step was added to the NMI value computation: a correction to this value was performed whenever the NMI value was precisely 1, that is, when in rare occasions both fMRI and EEG networks are fully connected and therefore have only one component including all nodes. In these cases, this value was changed for the second highest score found for all time points, to avoid stretching the colour scale and thus making the interpretation more difficult. The resulting values are represented in colored arrays in figures A.7 and A.8, respectively, for an arbitrary subject and all frequency bands. In table 3.5, it is summarized the average of the highest NMI value over all subjects as well as the average interval of similarity, for each frequency band. In the second case, it was considered only the time points with some similarity but not the highest.

From the colored arrays and table 3.5, it is possible to observe that the NMI values obtained were not particularly high. Specifically, there were some time points with very low similarity while others had a low-moderate value mainly around 0.2-0.3. Interesting enough, even with small fluctuations in the similarity values, no significant difference was found between subjects or between frequency bands. This suggests an equivalence between subjects relatively to the threshold applied and also in the main

Table 3.5: Highest NMI value and interval of NMI values (excluding lower and higher values) obtained for comparison of fMRI and each frequency band connected components - average over all subjects.

Data type	fMRI-EEG delta	fMRI-EEG theta	fMRI-EEG alpha	fMRI-EEG beta	fMRI-EEG gamma
highest NMI	0.33	0.33	0.33	0.32	0.32
NMI interval	0.17-0.28	0.18-0.29	0.18-0.29	0.17-0.28	0.17-0.28

Table 3.6: Highest Jaccard Index value and interval of Jaccard Index values (excluding lower and higher values) obtained for comparison of fMRI and each frequency band connected components - average over all subjects.

Data type	fMRI-EEG delta	fMRI-EEG theta	fMRI-EEG alpha	fMRI-EEG beta	fMRI-EEG gamma
highest Jaccard Index	0.99	0.99	0.99	0.98	0.98
Jaccard Index interval	0.81-0.95	0.80-0.95	0.80-0.94	0.80-0.94	0.81-0.94

structure of the resulting networks for the two modalities comparison, which is desirable for an adequate analysis. In addition, despite applying different thresholds to distinct frequency bands, all seem to capture a structure partially similar to the fMRI networks, at least to the same extent. In spite of the low similarity found between fMRI and EEG connected components, these values are in line with the similarity results obtained in [94], using the same dataset. In this study, the correlation between fMRI and EEG static connectomes was analyzed for each frequency band, resulting in the following Pearson correlation coefficient values: $r_{delta} = 0.31$, $r_{theta} = 0.32$, $r_{alpha} = 0.32$, $r_{beta} = 0.34$ and $r_{gamma} = 0.32$. Therefore, the similarity obtained between fMRI and EEG connected components is enough to suggest some common features between the two modalities' topology.

Moreover, when analysing the Jaccard Index results (table 3.6), a high similarity between fMRI and EEG connected components is found for most time points. This implies that each data type will capture a fairly similar giant component, meaning that the edges with higher connectivity kept after thresholding connect essentially the same group of brain regions. This supports the hypothesis of a relationship between fMRI and EEG functional networks' topology.

Having set some ground for the potential topological similarity between these two modalities, the next step is to explore it further with community detection (macro-scale network analysis explored in chapter 4) as well as with a motif enumeration study (meso-scale network analysis reported in chapter 5).

Chapter 4

Community Structure Analysis

This chapter contains a community structure analysis performed to characterize both fMRI and EEG functional networks on a macro-scale, to explore their potential correlation over time and also to investigate the possible influence of the proximity constraints, imposed by the spatial embedding, in the modular structure captured for the two modalities. All the code was implemented using Python3.6 and is available in `https://github.com/franciscaabsr/Thesis_project/Code/`.

4.1 Methodology

4.1.1 Null Model Comparison Analysis

The analysis of time-varying functional connectivity is based on the fact that resting-state data is characterized by relatively fast fluctuations that arise spontaneously. Naturally, the signal captured will fluctuate in amplitude, resulting in some time instances with overall lower functional connectivity, when the signal is not as strong. This might then translate into a higher degree of randomness in the inferred network, especially considering lower connectivity values are more prone to be polluted by noise. Noise that might not be eliminated by the threshold chosen, as mentioned in section 3.1.3.1, since a percentage of edges must be kept, possibly including more random connections when the connectivity values are low. When this is the case, the network as a whole and consequently its topology will be more comparable to a random null model. On the other hand, when the signal is stronger, it will deviate from the random case and be organized into clusters of nodes more densely connected among them than with the rest of the network [92]. Therefore, to study the community structure present in these networks, it is necessary to select the time points for which the functional networks' topology deviates from the random case, i.e., when they are significantly more clustered than a randomized version, in order to obtain meaningful modules.

To account for the clustering present in each functional network, three different metrics were chosen: the clustering coefficient, the average path length and modularity, defined in section 2.2. All of these metrics are expected to be higher when the network shows a more clustered topology, since nodes will have a larger tendency to form densely connected groups linked by few edges, reflected in both the clus-

tering coefficient and modularity, which will translate into longer average distance between any pair of nodes. Owing to the presence of hubs in brain networks, one could anticipate low average path length. However, when the network has higher clustering and modular structure, this value will increase, deviating more from the random case where all nodes are at a small distance from each other. In addition, it is important to take into consideration that the functional networks are composed by several disconnected components for most time points, due to the threshold used. This will ultimately result in an infinite average path length, according to equation 2.9. To avoid this, the metric was computed by taking the weighted average for all components, using NetworkX's *average_shortest_path_length* function for each and accounting for their size as well. The clustering coefficient was computed with NetworkX's *average_clustering* function while modularity with functions *best_partition* and *modularity* from NetworkX's community package, using Louvain algorithm.

4.1.1.1 Rewiring Null Model

For the quantitative comparison of these metrics between the original functional networks and the rewiring null model, and consequent selection of the time points that deviate from this random configuration, the z-score can be computed (equation 2.14) considering a one-tailed test. That is, it is only being inspected if the observed values are significantly higher than for the null model.

But first, it was assessed if the distribution of these metrics, according to the rewiring null model, approximates to a Gaussian. This was done by selecting a few time points arbitrarily, generating 100 surrogates for each corresponding network, as described in section 3.1.4, and computing the distribution of the clustering coefficient, average path length and modularity. Afterwards, for each time point corresponding functional network, an ensemble of surrogates was generated and the mean and standard deviation value of each one of the three metrics were obtained. From this, the z-score was computed and translated into a p-value for every single time point, using SciPy's *ndtr* function (a Gaussian cumulative distribution function that integrates the area under the curve of the normal distribution) and selecting the time instances for which the computed probability was under 0.05. It was chosen this criterion, as it was deemed to be enough for the assumption of a clustered topology for the functional network, for each time point. This was followed by an intersection of the selected time instances for the three metrics, for each modality. Lastly, since the ultimate goal is to compare the community structure between fMRI and EEG and check if they capture, at least partly, the same topology, a unique set of time points was obtained by choosing only the common ones, for each frequency band independently. This because it only makes sense to compare the two modalities for time points where both functional networks deviate from the null model.

Apart from the selection of time points, the variation over time of the clustering coefficient, average path length and modularity for the functional network was obtained and plotted in comparison to the rewiring null model's metric values, for both fMRI and EEG frequency bands separately. Additionally, the selected time points, common to both modalities, were compared between all frequency bands using the Jaccard Index.

4.1.1.2 Degree Constrained Spatial Null Model

Since this clustered topology may be due to spatial constraints imposing a segregated structure, it was selected a second set of time points for which the functional networks deviate from a random configuration that takes into account this intrinsic influence of space. For this, an identical approach as the one described above was performed, now with the degree constrained spatial null model. Also, as done for the rewiring null model, it was obtained a plot for the temporal variation of each of the three chosen properties, in comparison to this spatial null model's values, for both modalities. In addition, the similarity between selected time points for all frequency bands was computed, using the Jaccard Index. Finally, the time points selected for both null models were compared by finding their intersection, so as to check the amount of time points for which the network deviates significantly beyond the influence of the spatial constraints, in comparison to the typical random case.

4.1.2 Community Analysis over Static Connectome

Before proceeding to the community analysis with the selected time points according to each null model, the functional networks for both modalities were averaged in order to reach their static connectome representation. This was done with the objective of establishing a baseline, regarding the functional networks topology and correlation between modalities, to be compared with the results from the temporal community analysis. As such, the Louvain algorithm was then used to extract the communities, by means of the NetworkX community package's *best_partition* function, and the corresponding modularity was computed with function *modularity*. The resulting partitions for both modalities were afterwards subjected to comparison using the NMI and Jaccard Index metrics. In parallel, the median modularity was computed for the communities obtained using the rewiring and degree constrains spatial null model, in order to statistically test the values obtained for the static connectomes. Additionally, the modified version of the Louvain algorithm, as defined in section 2.2.2, was applied using *spaceCorrectedLouvainDC* toolbox, in order to verify if the static connectomes present a community structure beyond the spatial embedding nature of these networks. The NMI and Jaccard index values were computed as well from the partitions obtained when regressing out the spatial influence.

4.1.3 Community Analysis with Louvain Algorithm

As mentioned in section 2, these functional networks have the potential of revealing the spatiotemporal organization of the brain's complex activity. In fact, several studies have reported patterns of functional connectivity, clustering different brain regions, known as dynamic functional connectivity (dFC) states, and others even found a correlation between these patterns found for fMRI data and the underlying neuronal activity captured by the EEG data [3].

Hence, with the objective of identifying modules reflecting synchronized activity of different brain regions, possibly repeating over time and potentially similar between modalities, the community structure of these functional networks was analyzed. This was done for each one of the selected time points obtained according to previous section 4.1.1.1, whose functional networks deviated from the random

configuration defined by the rewiring null model, using the Louvain algorithm, as defined in section 2.2.2. To obtain the partitions for each time point, the NetworkX community package's *best_partition* function was used, and the corresponding modularity was computed with *modularity* function from the same package. Following this, the median number of communities and median modularity, considering all selected time points, was estimated for both fMRI and each EEG frequency band. Additionally, in order to establish a baseline for the portion of modularity imposed by the spatial constraints, the median modularity value was also obtained for the degree constrained spatial null model as well.

Comparison between time points In order to evaluate the possibility of existing a pattern over time regarding the community structure of these functional networks, the resulting partitions were compared between all pairs of time points using the NMI, in a similar fashion as performed for the connected component analysis. In order to guarantee that the results are statistically significant, a shuffling of the functional networks was performed so as to compare partitions obtained for one time point with the ones obtained with a completely random time point. To achieved this, for each time point t, 100 shuffled time points were selected and their communities estimated. Following this, the NMI value was computed between each pair of partitions, consisting of the communities for time point t and the ones from each of the shuffled time points, resulting in 100 different values. The average and standard deviation were then extracted from this distribution and compared with the original NMI value, in order to compute the z-score and thus the corresponding p-value, as defined in section 2.2.1. As such, the percentage of values deemed significant, i.e., with a p-value lower than 0.05, was obtained as the level of confidence over the results found. This temporal comparison with statistical significance testing was performed in a similar way using the Jaccard Index as well, as a second measure of similarity. Since this metric is defined for set comparison, it was performed the comparison between all pairs of communities for each two time points in consideration, resulting in a matrix of Jaccard Index values. Following this, the maximum of each row was extracted, so as to associate the similar communities, and the average maximum was obtained, corresponding to the similarity value between the two partitions.

Modalities comparison Furthermore, to study the potential correlation between the two modalities, namely regarding to the modular structure captured by both functional networks, the communities extracted were compared for all selected time points, again using the NMI and Jaccard Index metrics. This way, reflecting the similarity between fMRI and EEG's community structure across time already suggested by the connected component analysis. Identically as it was done for the communities comparison over time, the statistical significance of the similarity values was tested, by comparing the communities found for the fMRI for one time point with the set of partitions for the EEG corresponding to randomly selected time points. This was achieved, again, for each time point t, computing the NMI and Jaccard Index value between the fMRI communities of that time point and the EEG partitions from 100 different shuffled time points. Subsequently, in a similar fashion as described above, the average and standard deviation values were compared to the original similarity values, estimating the p-value. With this, the percentage of significant values (with $p<0.05$) was obtained corresponding to the level of confidence over the similarity found between the two modalities' communities over time.

4.1.4 Community Analysis with modified Louvain Algorithm

Taking into account the influence of the spatial constraints in the functional networks topology explored in sections 4.1.1.2 and 4.1.3, it was desirable to check if some modular configuration present in these functional networks emerges from functional necessity and not just as a consequence of space. That is, if it was possible to identify modules of synchronized activity involving long-distance connections instead of detecting communities consisting only of nodes in proximity of each other.

With this objective, the community structure of these functional networks beyond these spatial constraints was investigated. This was done for each one of the selected time points obtained according to section 4.1.1.2, whose functional networks deviated significantly from the degree constrained spatial null model, using a modified version of the Louvain algorithm defined in section 2.2.2, that maximizes a modularity function which regresses out these restrictions. To obtain the partitions for each time point, the *spaceCorrectedLouvainDC* toolbox's *computeCommunityDetectionUsingRefNullModel* function was used and the corresponding modularity was computed with the *modularity* function from this toolbox's *louvainModified* package. Identically as done according to the previous section, the median number of communities and modularity value was estimated, for both fMRI and each EEG frequency band. Additionally, the communities extracted with and without the spatial influence considered in the modularity maximization were compared using the NMI metric, to investigate their difference. This was done solely for the selected time points according to section 4.1.1.2.

Comparison between time points Equivalent to the previous analysis with Louvain algorithm, it was studied the possibility of existing a pattern over time regarding this community structure beyond spatial constraints. This analysis was done by comparing the resulting partitions between all pairs of time points, using the NMI and Jaccard Index metrics.

Modalities comparison Regarding the potential correlation between the two modalities, the communities extracted while regressing out the influence of space were compared for all time points, again using the NMI and Jaccard Index metrics. This was done with the objective of distinguishing and quantifying the influence of the spatial constraints into correlating the two modalities and verify if there is a correlation beyond that, reflecting the underlying synchronous activity captured by the two.

4.1.5 Community Analysis with multilayer Louvain Algorithm

Considering that the two modalities under study capture neural activity through two different processes, resulting in complementary temporal and spatial resolution, one might ask the question whether combining the two types of data can lead to new and improved results in terms of the functional networks spatiotemporal organization.

To explore this, a multilayer version of the Louvain algorithm, defined in section 2.2.2, was used to extract communities common to both modalities' functional networks, one corresponding to each layer, for all time points selected according to section 4.1.1.1. This algorithm can be used as a multiplex case, since all layers share the same node set, considering that the same parcellation was used for

both modalities. Therefore, the common partitions were obtained for each time instance using i-graph's louvain package *find_partition* function, based on Mucha et al community detection algorithm (described in section 2.2.2), which also returns the improved modularity. This quality value consists in the sum of the individual qualities for the various partitions, over all layers, weighting each layer equally in this case. This way, the optimization is equivalent to the standard algorithm, with the overall modularity difference of moving a node to another community being the sum of the individual differences for each layer. Following this, the median number of communities and median improved modularity, considering all selected time points, were estimated for both fMRI and each EEG frequency band. In parallel, the median modularity associated to these communities when isolating the two layers was obtained in order to check if different partitions were obtained for each modality in comparison to the previous optimized ones, obtained according to section 4.1.3.

Furthermore, it is important to mention that this is the first time, at least according to the reported literature, that a multilayer analysis combining these two modalities has been done. With this in mind, there are no benchmarks or any expectations for comparison with this analysis.

Comparison with spatial null model Additionally, in order to establish a baseline for the portion of the common community structure imposed by the spatial constraints, the median improved modularity value was also obtained using the degree constrained spatial null model applied to both modalities. Again, the median modularity value associated to these communities when isolating the two layers was investigated. Finally, using the improved modularity for the spatial null model, the statistical significance of the value obtained for the multiplex functional networks was estimated, so as to determine the amount of time points with a combined topology deviating from the spatial null model.

4.2 Results

4.2.1 Null model comparison analysis

4.2.1.1 Rewiring null model

The distributions of three chosen properties (clustering coefficient, average path length and modularity) to inspect the functional network's structure are represented in the appendix's figure B.1, for an arbitrarily chosen time point, subject and frequency band, verifying the assumption of a normal distribution, for either fMRI or EEG functional networks.

Regarding the temporal variation of each metric, the values for the functional networks, for both fMRI and EEG frequency bands, were plotted while comparing with the rewiring null model's mean value (more and less the standard deviation), extracted from the distributions discussed above. These plots are represented in the appendix, in figures B.3, B.4 and B.5, respectively for each metric, for all frequency bands and arbitrary subject, while here, in title of example, these results are summarized in figure 4.1 for subject 7, with fMRI and EEG gamma band.

From these results, it is possible to notice a variation over time for all three metrics, independently

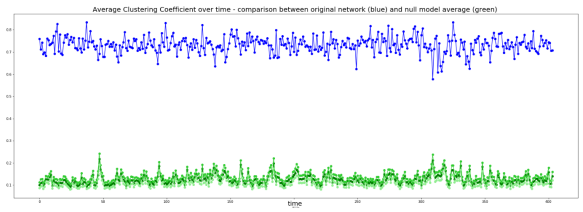

(a) Clustering coefficient - fMRI

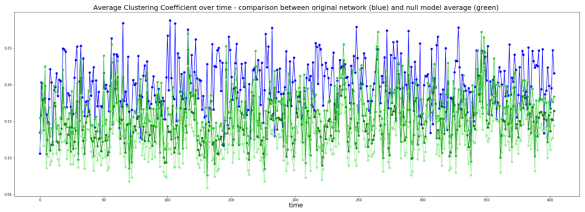

(b) Clustering coefficient - EEG gamma

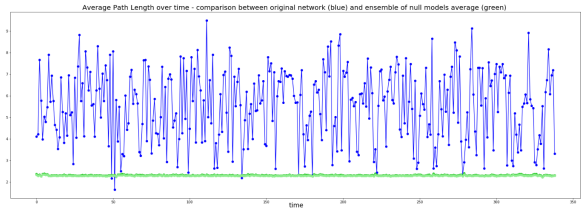

(c) Average path length - fMRI

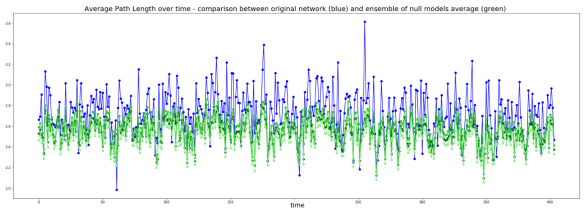

(d) Average path length - EEG gamma

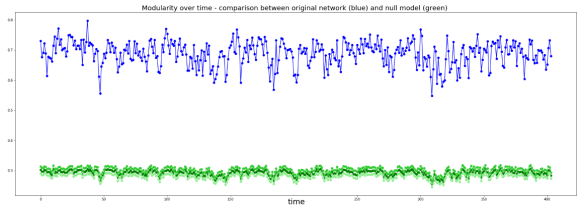

(e) Modularity - fMRI

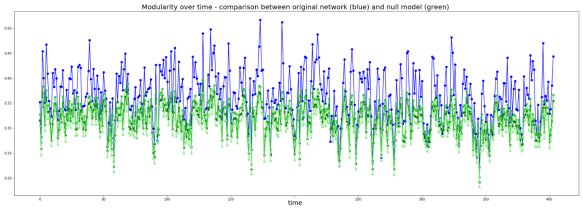

(f) Modularity - EEG gamma

Figure 4.1: Variation over time of clustering coefficient (top), average path length (middle) and modularity (bottom, all in blue), for fMRI (left) and EEG gamma band (right) of subject 7, in comparison to a rewiring null model (in green).

of the imaging technique, which is not surprising considering that brain functional connectivity tends to oscillate between segregated and integrated states [12, 74]. Besides this, one can also immediately see a big difference between the fMRI and EEG functional networks, as the first one appears to possess a much more clustered structure than the second one. Moreover, the fMRI networks appeared to be too clustered as there are almost no time points or even none, for all three properties, that do not deviate from the null model. One could hypothesize that the fMRI might be more affected by the spatial constraints that impose this clustered structure, in comparison to the EEG. This hypothesis is further explored with the results obtained using the spatial null model, in section 4.2.1.2.

We can then conclude that, on opposition to fMRI, not all time points of EEG work for the community analysis, as there is no evident clustered structure. As such, the resulting time points obtained from the intersection between the two modalities' selection were almost entirely the same as the EEG ones. Even considering the potential lack of clustered structure in the EEG networks, these are the time points for which makes more sense to investigate the potential correlation between modalities regarding the community structure captured. The percentage of selected time points for each fMRI-EEG frequency band combination are summarized in table 4.1, with respect to the total number of time instances.

Despite the variation between subjects, around half of the time points were selected as corresponding to functional network deviating significantly from the random configuration, for both modalities. Also, no frequency band was found to be evidently capturing more clustered topology than others, with the exception of possibly the gamma band, for which a slightly higher number of time points was selected.

Table 4.1: Percentage of time points for which both modalities functional networks reflect a clustered structure in comparison to a rewiring null model - for each frequency band.

Subject	EEG delta (%)	EEG theta (%)	EEG alpha (%)	EEG beta (%)	EEG gamma (%)
1	58.9	56.3	63.5	68.0	81.3
2	73.3	60.7	56.5	73.2	78.8
3	60.0	62.5	58.0	55.6	51.6
4	56.4	58.5	65.8	47.3	60.8
5	59.9	48.2	47.5	54.6	62.1
6	67.4	56.4	57.9	61.2	69.5
7	62.4	63.1	63.9	58.2	46.4
8	48.5	47.7	56.4	59.7	76.2
9	58.3	58.0	62.7	57.5	60.8
average	60.6 ± 6.5	56.8 ± 5.3	59.1 ± 5.3	59.5 ± 7.1	65.3 ± 11.4

Table 4.2: Jaccard Index computed between all set of time points selected, considering all EEG frequency bands.

Subject	1	2	3	4	5	6	7	8	9	average
Jaccard Index	0.21	0.26	0.14	0.13	0.13	0.16	0.15	0.18	0.14	0.17 ± 0.04

Finally, these selected time points were compared between all frequency bands by computing the Jaccard Index and the results are summarized in table 4.2. Since each frequency band is associated to different aspects of brain activity and functionality at different time scales [7], it is not surprising not having a higher Jaccard Index value. Moreover, one would even expect that each frequency band detects different temporal variations regarding the functional networks' topology [122, 123]. However, some equivalence between time points with clustered structure exists, suggesting that this structure emerged from synchronizations detected in two or more frequency bands, for some time points at least. This is in accordance with some studies that have shown that each resting-state network, contributing to the brain network's topology, is characterized by a combination of brain rhythms associated to these frequency bands [124].

4.2.1.2 Degree Constrained Spatial null model

The distributions of the clustering coefficient, average path length and modularity values, with respect to the degree constrained spatial null model, are represented in figure B.2 of the appendix, for an arbitrarily chosen time point, subject and frequency band, approximating to a normal distribution for either fMRI or EEG functional networks.

Identically as it was done for the rewiring null model and with hopes of exploring the effect of the spatial constraints, the temporal variation of each one of these properties was obtained for both modalities and analyzed against this spatial null model's mean value (more and less the standard deviation), according to the distributions discussed above. These plots are represented in the appendix in figures B.6, B.7 and B.8, respectively for each metric, for all frequency bands, selecting arbitrarily a subject. Here, these results are summarized for subject 7 and EEG gamma band, in figure 4.2.

As it was expected, the degree constrained spatial null model presents a somewhat clustered topol-

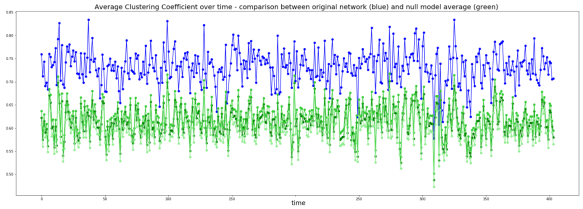

(a) Clustering coefficient - fMRI

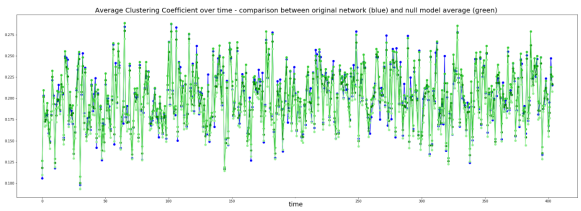

(b) Clustering coefficient - EEG gamma

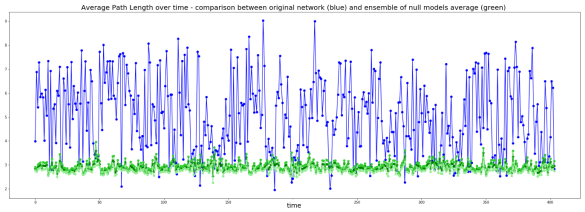

(c) Average path length - fMRI

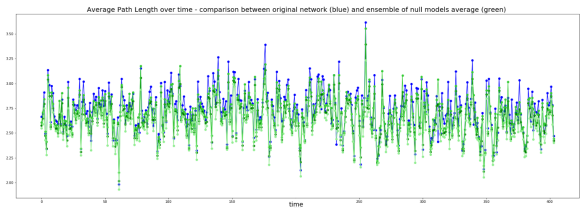

(d) Average path length - EEG gamma

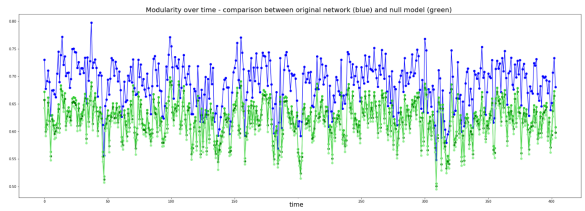

(e) Modularity - fMRI

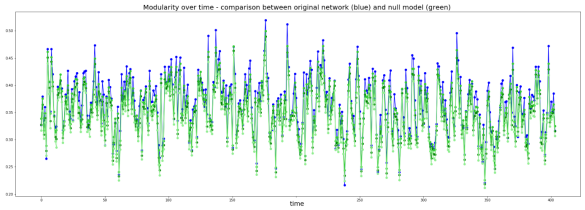

(f) Modularity - EEG gamma

Figure 4.2: Variation over time of clustering coefficient (top), average path length (middle) and modularity (bottom, all in blue), for fMRI (left) and EEG gamma band (right) of subject 7, in comparison to a degree constrained spatial null model (in green).

Table 4.3: Percentage of time points for which fMRI functional networks reflect a clustered structure in comparison to a degree constrained spatial null model - for each frequency band.

Subject	1	2	3	4	5	6	7	8	9	average
fMRI (%)	89.0	83.9	86.7	89.5	89.4	89.0	84.8	86.3	88.0	87.4 ± 2.0

ogy, resulting in higher mean values of clustering coefficient, average path length and modularity, for both modalities of networks. However, the increase of these values in comparison to the ones obtained with the rewiring null model, was much more substantial for the fMRI than for the EEG, independently of the frequency band analyzed. As such, one might speculate that these spatial constraints have little effect on the EEG networks, for which the degree distribution appears to have a bigger influence. On the other hand, these values suggest that spatial embedding has a large contribution for the clustered topology of the fMRI functional networks, supporting the hypothesis placed in the previous section. In other words, since these networks appeared to be too clustered when analyzed against the rewiring null model, it was hoped that, with the spatial null model to remove the intrinsic spatial influence, only a portion of the time points would still reflect a meaningful topology. However, this was not the case, as they still significantly deviate from the spatial null model structure for most time points, as it can be seen in figure 4.2, with the percentage of time points selected exclusively for the fMRI represented in table 4.3.

From figure 4.2, it is also possible to verify that the EEG functional networks' structure is almost

Table 4.4: Percentage of time points for which both modalities functional networks reflect a clustered structure in comparison to a degree constrained spatial null model - for each frequency band.

Subject	EEG delta (%)	EEG theta (%)	EEG alpha (%)	EEG beta (%)	EEG gamma (%)
1	8.3	7.0	8.3	8.3	13.3
2	18.9	7.4	7.6	10.3	15.6
3	11.9	8.9	8.1	5.2	4.4
4	9.1	6.4	8.2	5.8	9.1
5	12.8	2.8	9.9	3.9	10.6
6	17.9	7.1	9.8	8.9	10.0
7	15.0	8.6	11.5	6.9	2.7
8	9.9	4.7	8.2	9.0	14.0
9	12.0	9.7	9.9	7.3	9.2
average	12.9 ± 3.5	7.0 ± 2.0	9.1 ± 1.2	7.2 ± 1.9	9.9 ± 4.0

identical to the spatial null model's, especially with respect to the clustering coefficient. This suggests that the little topology detected, deviating from the random configuration of the rewiring null model, might be a result of the spatial constraints imposed in these functional networks, thus pointing for the possibility that the EEG networks' topology is mainly that of a random configuration for most time points.

Even though the two modalities showed different results with respect to the degree constrained spatial null model, the common time points significantly deviating from this random configuration were selected, being mostly dependent on the EEG networks' structure naturally. The resulting time points for each fMRI-EEG frequency band combination are essentially a subset of the ones selected with the rewiring null model and their percentage with respect to the total number of instances are illustrated in table 4.4.

Despite some variations between subjects, around 9% of the time points were selected for both modalities, corresponding to functional networks deviating significantly from the random configuration including the spatial impositions. Again, it is possible to observe that the gamma band (if excluding outliers) shows an overall higher percentage of time points selected, but now it is accompanied as well by the delta band, showing an even higher percentage. From these results, one can notice an overall decrease in the percentage of time points selected, in comparison to the values obtained for the rewiring null model (around 60%, see table 4.1 for more), showing that in fact the spatial constraints explain a relevant portion of the EEG functional networks' structure. Moreover, it is important to notice that this decrease was more substantial when considering the two data types, than just for the fMRI isolated. That suggests that this proximity effect has a large impact for the EEG networks, even though at first not much difference was found between the rewiring and spatial null models. However, from these percentages, one can see that there is still some meaningful structure captured in some time points' functional networks of potential relevance beyond these spatial restrictions. Therefore, further analysis is necessary, to explore if this modality is able to capture any interesting modular structure beyond the anatomical proximity, considering this set of time points.

Finally, the selected time points were compared between frequency bands by computing the Jaccard Index of all time point sets, resulting in a zero value for all subjects. This is coherent with the fact that

each frequency band is associated with different aspects of brain activity and thus will capture distinct topology at different time scales, as referred in the previous section. As such, all frequency bands are deemed interesting for investigating the potential correlation between the communities extracted in the two modalities' functional networks when regressing out the spatial influence (see section 4.2.4 for more).

4.2.2 Community Analysis over Static Connectome

With the objective of setting a baseline for the correlation between the community structure investigated with the two modalities, the static functional connectomes were computed by averaging the connectivity values over time. The modularity values associated to the communities extracted using the Louvain algorithm are summarized in table 4.5, while the corresponding values for the rewiring null model and degree constrained spatial null model are represented in the appendix in tables B.1 and B.2. Relatively to these last two tables, the values were marked with * when they were not significantly lower when compared statistically with the static connectome ones.

Table 4.5: Modularity values associated to the communities extracted from fMRI and EEG frequency bands static connectomes using the Louvain algorithm, for each subject and the resulting average and standard deviation for all subjects.

Subject	fMRI	EEG delta	EEG theta	EEG alpha	EEG beta	EEG gamma
1	0.401	0.427	0.464	0.487	0.506	0.539
2	0.428	0.407	0.379	0.511	0.552	0.509
3	0.355	0.540	0.551	0.498	0.536	0.514
4	0.393	0.398	0.513	0.390	0.580	0.466
5	0.392	0.439	0.426	0.296	0.481	0.471
6	0.471	0.452	0.522	0.306	0.566	0.548
7	0.359	0.487	0.503	0.481	0.546	0.340
8	0.429	0.376	0.352	0.478	0.495	0.539
9	0.432	0.538	0.610	0.538	0.597	0.461
average	0.407 ± 0.035	0.452 ± 0.056	0.480 ± 0.078	0.443 ± 0.085	0.540 ± 0.037	0.487 ± 0.061

From these results, one can notice that the modularity values are statistically significant against the rewiring null model, for both fMRI and EEG frequency bands. However, this is not the case when comparing with the spatial null model for the EEG data, where for some subjects, these values were either similar or even higher to the ones obtained for the static connectomes, varying between frequency bands. One can speculate that the spatial influence might now have a larger impact in the EEG networks when averaging all connections over time, as these links will then approximate to the anatomical wiring, which is not the case on a dynamic point of view (section 4.2.1.2). Still, it appears that there is no structure deviating consistently from this random configuration for the EEG, which is in accordance to the results obtained so far. This is not the case for the fMRI data, which is in line with the previous results as well, suggesting a clear clustered structure for the fMRI, that arises beyond the spatial constraints.

Looking for the correlation between the communities extracted for both modalities static connectomes, the NMI and Jaccard Index values were computed and are illustrated in table 4.6. Since a

Table 4.6: NMI and Jaccard Index values obtained from the comparison of fMRI and EEG frequency bands static connectomes' communities obtained using the Louvain algorithm, for each subject and the resulting average and standard deviation (std) for all subjects.

Data type	fMRI-EEG delta	fMRI-EEG theta	fMRI-EEG alpha	fMRI-EEG beta	fMRI-EEG gamma
NMI					
1	0.412	0.430	0.358	0.324	0.311
2	0.320	0.427	0.329	0.362	0.363
3	0.212	0.332	0.302	0.294	0.348
4	0.401	0.377	0.432	0.307	0.314
5	0.257	0.400	0.432	0.376	0.397
6	0.404	0.347	0.533	0.374	0.388
7	0.365	0.365	0.432	0.382	0.393
8	0.370	0.406	0.294	0.301	0.275
9	0.363	0.273	0.390	0.288	0.343
$average$	0.345	0.373	0.389	0.334	0.348
std	$\pm$ 0.065	$\pm$ 0.048	$\pm$ 0.073	$\pm$ 0.037	$\pm$ 0.040
$Jaccard\quad Index$					
1	0.209	0.200	0.194	0.159	0.178
2	0.327	0.410	0.345	0.298	0.188
3	0.143	0.237	0.199	0.208	0.232
4	0.287	0.301	0.409	0.268	0.284
5	0.192	0.177	0.266	0.256	0.210
6	0.185	0.183	0.281	0.214	0.220
7	0.142	0.138	0.183	0.191	0.237
8	0.149	0.195	0.150	0.182	0.176
9	0.188	0.152	0.200	0.184	0.175
$average$	0.202	0.221	0.247	0.218	0.211
std	$\pm$ 0.061	$\pm$ 0.081	$\pm$ 0.080	$\pm$ 0.044	$\pm$ 0.034

moderate similarity was found between fMRI and EEG partitions, one can now expect some correlation arising as well from the dynamic community analysis, that will be further explored in the following sections.

The modularity associated to the partitions obtained with the modified Louvain algorithm for both modalities and the resulting similarity values computed again with NMI and Jaccard Index metrics are represented in tables 4.7 and 4.8, respectively. Relatively to the resulting modularity values, it is possible to observe that there is still a community structure arising beyond the spatial constraints, especially for the fMRI static connectome, as it was expected. Existing for the EEG as well is surprising, even if at a lower degree than for the fMRI, considering that the modularity values were not always significant against the spatial null model for the EEG static connectome, when using the Louvain algorithm definition. This observed topology will be further explored over time for both modalities in section 4.2.4.

From the results regarding the partitions' comparison between modalities, both similarity values were lower than the ones reported in table 4.6, except for the EEG alpha band, which showed an increased Jaccard Index value. Despite this variation, these results translate in a decrease of the correlation between the two modalities, when excluding the spatial influence, at least for the static connectomes. One can then hypothesize that the spatial embedding might be behind of part of the correlation and

Table 4.7: Modularity values associated to the communities extracted from fMRI and EEG frequency bands from their static connectomes using the modified Louvain algorithm, for each subject and the resulting average and standard deviation for all subjects.

Subject	fMRI	EEG delta	EEG theta	EEG alpha	EEG beta	EEG gamma
1	0.034	0.005	0.011	0.022	0.014	0.017
2	0.062	0.028	0.009	0.026	0.018	0.031
3	0.039	0.027	0.025	0.041	0.027	0.033
4	0.055	0.008	0.021	0.011	0.023	0.020
5	0.052	0.036	0.019	0.012	0.023	0.021
6	0.052	0.020	0.019	0.014	0.036	0.025
7	0.031	0.031	0.030	0.024	0.016	0.027
8	0.041	0.009	0.005	0.015	0.016	0.017
9	0.036	0.025	0.029	0.019	0.035	0.026
average	0.045 ± 0.010	0.021 ± 0.011	0.019 ± 0.008	0.020 ± 0.009	0.023 ± 0.008	0.024 ± 0.005

common structure observed between fMRI and EEG functional networks. Again, this will be further investigated considering the modular structure over time in the following sections.

4.2.3 Community Analysis with Louvain Algorithm

In order to analyze the spatiotemporal organization of the brain's functional networks on a macro-scale, the community structure was analyzed over time, for the selected time points obtained considering the rewiring null model for both modalities. The resulting median modularity values associated to the communities extracted using the Louvain algorithm, for each pair of fMRI and EEG frequency band, are represented in table 4.9, while the median number of communities obtained are summarized in the appendix B.3. Additionally, the median modularity for the corresponding spatial null model was computed, being illustrated in table 4.10.

First of all, relatively to the community structure of the fMRI functional network, independently of the set of selected time points, it was obtained a high modularity value around 0.7, suggesting an overall segregated topology. This is in line with the previous observations pointing for a highly clustered structure for the fMRI functional networks. Besides this, it is relevant to mention that this value is slightly higher than the ones reported in literature, usually between 0.45 and 0.6 [12, 13].

Furthermore, it is also possible to notice that the modularity associated to the fMRI networks is higher than any of the EEG frequency bands'. This was expected, considering the difference in topology already observed in section 4.2.1.1, reinforcing the hypothesis that the EEG data tends to capture a less modular configuration. In fact, it has been reported in previous study [58] a more moderate modularity for the EEG networks in comparison to the high value found for the fMRI case, when compared to an ensemble of random networks. However, considering that the modularity found in this analysis was still statistically significant compared to the rewiring null model, this implies that there is still a modular topology captured. Indeed, it has been previously detected a community structure for these EEG functional networks, namely with a modularity value around 0.5 for networks with a density of 10% [125, 126], which is fairly similar to the values obtained in this analysis. Additionally, from these results, one can see

Table 4.8: NMI and Jaccard Index values obtained from the comparison of fMRI and EEG frequency bands static connectomes' communities obtained using the modified Louvain algorithm, for each subject and the resulting average and standard deviation (std) for all subjects.

Data type	fMRI-EEG delta	fMRI-EEG theta	fMRI-EEG alpha	fMRI-EEG beta	fMRI-EEG gamma
NMI					
1	0.309	0.251	0.235	0.237	0.168
2	0.261	0.331	0.317	0.252	0.253
3	0.150	0.245	0.265	0.247	0.301
4	0.328	0.303	0.283	0.228	0.289
5	0.161	0.223	0.278	0.306	0.270
6	0.237	0.266	0.400	0.265	0.194
7	0.307	0.205	0.371	0.251	0.313
8	0.284	0.386	0.278	0.333	0.229
9	0.271	0.219	0.254	0.204	0.287
$average$	0.256	0.270	0.298	0.258	0.256
std	$\pm$ 0.060	$\pm$ 0.056	$\pm$ 0.052	$\pm$ 0.037	$\pm$ 0.047
$Jaccard \quad Index$					
1	0.162	0.158	0.156	0.173	0.167
2	0.290	0.397	0.411	0.271	0.154
3	0.107	0.210	0.193	0.164	0.207
4	0.355	0.338	0.548	0.366	0.349
5	0.139	0.121	0.255	0.284	0.210
6	0.126	0.126	0.258	0.131	0.123
7	0.135	0.063	0.205	0.124	0.226
8	0.131	0.246	0.162	0.244	0.140
9	0.149	0.116	0.161	0.122	0.143
$average$	0.177	0.197	0.261	0.209	0.191
std	$\pm$ 0.080	$\pm$ 0.105	$\pm$ 0.134	$\pm$ 0.081	$\pm$ 0.065

that no frequency band showed a particularly higher modularity than other, although the gamma band networks had a slightly lower value with more variability between subjects. Moreover, a much higher number of communities was detected for the EEG data, with about 10-14 in comparison to the 6-7 communities found on average for the fMRI networks. However, part of these many partitions correspond to isolated nodes, already reported during the connected components' analysis.

Finally, comparing the modularity obtained for these functional networks and for the corresponding spatial null model, it is possible to notice an important contribution of the anatomical embedding for the modular structure observed. This is true in particular for the fMRI case, as it is possible to observe a high modularity value associated to the spatial null model, considering that a small modularity was found for the rewiring null model in section 4.2.1.1. Moreover, as shown before in section 4.2.1.2, only a small portion of the EEG functional networks deviate significantly from the degree constrained spatial null model, and the small difference between the two can be observed with more detail here. However, existing still a difference between the two, for both modalities, a further analysis is required, removing the spatial influence, as it will be reported in the following section 4.2.4.

Table 4.9: Median modularity values associated to the communities extracted from fMRI and EEG frequency bands over time using the Louvain algorithm, for each subject and the resulting average and standard deviation (std) for all subjects. These modularity values were computed considering each set of selected time points, using the rewiring null model, for every pair fMRI-EEG frequency band.

Subject	fMRI — EEG delta	fMRI — EGG theta	fMRI — EEG alpha	fMRI — EEG beta	fMRI — EEG gamma
1	0.699 — 0.450	0.701 — 0.464	0.698 — 0.446	0.696 — 0.478	0.700 — 0.442
2	0.697 — 0.459	0.697 — 0.465	0.694 — 0.447	0.697 — 0.477	0.699 — 0.445
3	0.694 — 0.457	0.691 — 0.467	0.687 — 0.442	0.692 — 0.463	0.690 — 0.404
4	0.704 — 0.455	0.705 — 0.462	0.702 — 0.445	0.702 — 0.452	0.702 — 0.424
5	0.705 — 0.450	0.704 — 0.466	0.698 — 0.446	0.698 — 0.448	0.702 — 0.426
6	0.703 — 0.460	0.704 — 0.468	0.703 — 0.452	0.705 — 0.467	0.700 — 0.431
7	0.693 — 0.459	0.692 — 0.469	0.693 — 0.453	0.695 — 0.459	0.693 — 0.402
8	0.700 — 0.453	0.704 — 0.463	0.699 — 0.445	0.702 — 0.474	0.702 — 0.444
9	0.701 — 0.456	0.702 — 0.466	0.703 — 0.445	0.701 — 0.471	0.702 — 0.432
average	0.700 — 0.455	0.700 — 0.466	0.697 — 0.447	0.699 — 0.465	0.699 — 0.428
std	$\pm$ 0.004 — $\pm$ 0.004	$\pm$ 0.005 — $\pm$ 0.002	$\pm$ 0.005 — $\pm$ 0.003	$\pm$ 0.004 — $\pm$ 0.010	$\pm$ 0.004 — $\pm$ 0.015

Table 4.10: Median modularity values associated to the degree constrained spatial null model over time using the Louvain algorithm, for each subject and the resulting average and standard deviation (std) for all subjects. These modularity values were computed considering each set of selected time points, for every pair fMRI-EEG frequency band.

Subject	fMRI — EEG delta	fMRI — EGG theta	fMRI — EEG alpha	fMRI — EEG beta	fMRI — EEG gamma
1	0.623 — 0.424	0.624 — 0.435	0.623 — 0.424	0.622 — 0.452	0.623 — 0.422
2	0.623 — 0.432	0.625 — 0.438	0.619 — 0.425	0.623 — 0.452	0.624 — 0.423
3	0.621 — 0.430	0.618 — 0.442	0.616 — 0.415	0.619 — 0.439	0.619 — 0.381
4	0.628 — 0.428	0.627 — 0.438	0.627 — 0.420	0.630 — 0.433	0.627 — 0.407
5	0.628 — 0.423	0.631 — 0.440	0.625 — 0.418	0.625 — 0.429	0.627 — 0.404
6	0.628 — 0.429	0.630 — 0.439	0.626 — 0.427	0.631 — 0.446	0.626 — 0.410
7	0.618 — 0.432	0.618 — 0.442	0.618 — 0.428	0.622 — 0.438	0.618 — 0.381
8	0.624 — 0.424	0.628 — 0.440	0.624 — 0.422	0.624 — 0.449	0.624 — 0.418
9	0.627 — 0.429	0.626 — 0.442	0.627 — 0.424	0.628 — 0.448	0.628 — 0.406
average	0.624 — 0.428	0.626 — 0.440	0.623 — 0.423	0.625 — 0.443	0.624 — 0.408
std	$\pm$ 0.003 — $\pm$ 0.004	$\pm$ 0.004 — $\pm$ 0.002	$\pm$ 0.004 — $\pm$ 0.004	$\pm$ 0.004 — $\pm$ 0.008	$\pm$ 0.003 — $\pm$ 0.018

4.2.3.1 Comparison between time points

To study the potential existence of topological patterns over time, the partitions resulting from the community analysis were compared for all pairs of selected time points, using the NMI and Jaccard Index metrics. These matrices are represented in the appendix in figures B.9 and B.10, respectively, with values between 0 and their maximum value associated to a colour scale, and the corresponding percentage of statistically significant ($p < 0.05$) values is summarized in table B.4.

From these matrices obtained, it is possible to notice a partial similarity between the partitions found for the various time points, seemingly alternating between moderate and lower values. However, no complete correlation can be seen between any pair of time points nor clear patterns can be observed over time. Furthermore, this variation of similarity over time does not appear to match between the EEG frequency bands and the BOLD counterpart. Curiously, for the fMRI networks, the most similar set of communities are the ones in the neighbouring time points, which is not the case for the EEG frequency bands. These results suggest that there are no distinct topological patterns repeating over time, as

previously concluded regarding the connected component analysis. This was not expected considering that several studies report the presence of somewhat stable functional connectivity configurations [2, 35]. Instead, the communities found over time are most likely a combination of partitions or connectivity states [3, 5], with slight variations of similarity over time, this way reflecting a changing synchronization between different groups of brain regions and a continuous reorganization of these networks.

Additionally, only about 5% and 7% of the NMI and Jaccard Index values, respectively, were deemed significant when comparing each set of communities with 100 shuffled time points' partitions. This suggests that only a portion of time points have a significant similarity between them, possibly corresponding to these expected stable states. However, this further points out for the possibility of each time point's topology correspond to a combination of connectivity states [127], since an overall moderate similarity was found between most time points community structure. It is also important to mention that most studies consider a sliding window for the connectivity estimation, this way averaging over time the signal fluctuations and leading to more stable connectivity structures, while in this study a quasi-instantaneous measure was used.

4.2.3.2 Modalities comparison

With the objective of studying the potential correlation in the topology captured by the two imaging techniques, the communities obtained over time were compared using again the NMI and Jaccard Index metrics. The coloured arrays representing these values can be found in figure B.11 and B.12, respectively, in the appendix, and the resulting average values and associated standard deviation are summarized in table 4.11, for all subjects. Moreover, the percentage of the selected time points for which the similarity was statistically significant ($p<0.05$) is represented also in the appendix in table B.5.

As previewed with the connected component analysis and previously observed with the analysis of the community structure of the static connectomes, there is indeed a moderate correlation between the topology captured by the two modalities, in line with the results obtained in [94]. This was expected considering that dynamic functional connectivity fluctuations are constrained by the static functional connectivity observed [12]. However, a lower similarity value was observed, which might be because, when averaging over time, the structure of these networks emerges as more stable and thus resulting in a more consistent correlation between the two modalities. Additionally, one can notice that the beta band showed a higher correlation for the NMI metric, although not for the Jaccard Index, for which all values were more or less equivalent.

From the colored arrays obtained, it is possible to observe an variation in similarity over time, specific to each frequency band. Which is not surprising considering that the modular structure oscillates over time [74, 128], as observed in section 4.2.1.1, but also because each frequency band led to a different set of time points. However, only about 6% to 8% of the similarity values were found to be statistically significant, for NMI and Jaccard Index respectively. First, this is in line with the temporal comparison of the community structure, so one could hypothesize that there is an overall correlation between modalities independently of the time points, due to the partial similarity of the partitions found over time. On the other hand, this might suggest that some time instances, presenting significantly higher correlation between

Table 4.11: Average NMI and Jaccard Index values and corresponding standard deviation obtained from the comparison of fMRI and EEG frequency bands communities obtained using the Louvain algorithm, for each subject and the resulting average and standard deviation for all subjects.

Data type	fMRI-EEG delta	fMRI-EEG theta	fMRI-EEG alpha	fMRI-EEG beta	fMRI-EEG gamma
NMI					
1	0.250 ± 0.044	0.266 ± 0.042	0.261 ± 0.046	0.279 ± 0.043	0.263 ± 0.042
2	0.250 ± 0.048	0.263 ± 0.045	0.264 ± 0.047	0.288 ± 0.041	0.260 ± 0.042
3	0.243 ± 0.045	0.262 ± 0.042	0.270 ± 0.052	0.283 ± 0.045	0.281 ± 0.046
4	0.244 ± 0.043	0.259 ± 0.046	0.258 ± 0.051	0.289 ± 0.043	0.274 ± 0.044
5	0.246 ± 0.047	0.264 ± 0.048	0.258 ± 0.049	0.297 ± 0.047	0.281 ± 0.044
6	0.241 ± 0.044	0.263 ± 0.044	0.267 ± 0.050	0.282 ± 0.043	0.273 ± 0.042
7	0.249 ± 0.043	0.270 ± 0.045	0.267 ± 0.044	0.290 ± 0.045	0.292 ± 0.045
8	0.249 ± 0.045	0.271 ± 0.044	0.265 ± 0.048	0.284 ± 0.042	0.267 ± 0.044
9	0.250 ± 0.044	0.267 ± 0.046	0.256 ± 0.046	0.287 ± 0.043	0.268 ± 0.040
$average$	0.247 ± 0.048	0.265 ± 0.048	0.262 ± 0.053	0.287 ± 0.049	0.273 ± 0.053
$Jaccard\ \ Index$					
1	0.183 ± 0.026	0.186 ± 0.025	0.185 ± 0.025	0.183 ± 0.023	0.184 ± 0.023
2	0.186 ± 0.027	0.183 ± 0.027	0.183 ± 0.027	0.189 ± 0.028	0.184 ± 0.027
3	0.181 ± 0.026	0.185 ± 0.028	0.186 ± 0.028	0.183 ± 0.025	0.185 ± 0.029
4	0.184 ± 0.021	0.184 ± 0.025	0.185 ± 0.026	0.187 ± 0.025	0.186 ± 0.023
5	0.182 ± 0.022	0.186 ± 0.025	0.184 ± 0.025	0.186 ± 0.025	0.187 ± 0.026
6	0.183 ± 0.022	0.186 ± 0.023	0.181 ± 0.025	0.188 ± 0.027	0.187 ± 0.024
7	0.183 ± 0.030	0.183 ± 0.030	0.183 ± 0.029	0.183 ± 0.023	0.188 ± 0.033
8	0.182 ± 0.021	0.186 ± 0.024	0.186 ± 0.025	0.184 ± 0.021	0.186 ± 0.026
9	0.185 ± 0.024	0.187 ± 0.027	0.185 ± 0.023	0.186 ± 0.026	0.186 ± 0.025
$average$	0.183 ± 0.026	0.185 ± 0.027	0.184 ± 0.027	0.185 ± 0.027	0.186 ± 0.028

fMRI and EEG networks, reflect a closer structure captured, while others will translate into a dissonance between the features detected by the two modalities. Even so, these results are in accordance to reports in literature regarding the dynamic connectivity captured by fMRI and EEG [10, 57, 94, 122], implying that the relationship found may be indeed meaningful.

4.2.4 Community Analysis with modified Louvain Algorithm

To examine the influence of the spatial embedding in the correlation found until now between the two modalities and to further analyze the spatiotemporal organization of these functional networks beyond these spatial constraints, the community structure was analyzed for the selected time points obtained considering the degree constrained spatial null model for both modalities. The resulting median modularity values associated to the communities extracted using the modified Louvain algorithm, for each pair of fMRI and EEG frequency band, are represented in table 4.12, while the median number of communities obtained are summarized in the appendix in table B.6.

From these results, similar to what was found for the static connectomes, it is possible to observe that there is still a community structure arising beyond the spatial constraints, even though the resulting modularity values are quite low. This is because they are associated to functional networks deviating from a random configuration that includes both degree distribution and spatial proximity's influence,

Table 4.12: Median modularity values associated to the communities extracted from fMRI and EEG frequency bands over time using the modified Louvain algorithm, for each subject and the resulting average and standard deviation (std) for all subjects. These modularity values were computed considering each set of selected time points, using the degree constrained spatial null model, for every pair fMRI-EEG frequency band.

Subject	fMRI — EEG delta	fMRI — EGG theta	fMRI — EEG alpha	fMRI — EEG beta	fMRI — EEG gamma
1	0.073 — 0.031	0.072 — 0.033	0.072 — 0.032	0.074 — 0.033	0.074 — 0.035
2	0.073 — 0.034	0.070 — 0.031	0.075 — 0.034	0.078 — 0.031	0.075 — 0.033
3	0.074 — 0.037	0.071 — 0.033	0.071 — 0.034	0.069 — 0.030	0.071 — 0.033
4	0.073 — 0.032	0.071 — 0.033	0.080 — 0.034	0.079 — 0.029	0.076 — 0.029
5	0.071 — 0.038	0.082 — 0.035	0.073 — 0.034	0.074 — 0.034	0.069 — 0.031
6	0.069 — 0.040	0.065 — 0.035	0.068 — 0.037	0.072 — 0.032	0.069 — 0.030
7	0.069 — 0.036	0.064 — 0.032	0.074 — 0.033	0.066 — 0.033	0.066 — 0.033
8	0.068 — 0.037	0.069 — 0.038	0.076 — 0.035	0.072 — 0.036	0.071 — 0.034
9	0.075 — 0.037	0.074 — 0.034	0.071 — 0.033	0.068 — 0.031	0.070 — 0.035
average	0.072 — 0.036	0.071 — 0.034	0.073 — 0.034	0.072 — 0.032	0.071 — 0.033
std	$\pm$ 0.002 — $\pm$ 0.003	$\pm$ 0.005 — $\pm$ 0.002	$\pm$ 0.003 — $\pm$ 0.001	$\pm$ 0.004 — $\pm$ 0.002	$\pm$ 0.003 — $\pm$ 0.002

making the communities retrieved statistically significant. Furthermore, this modular topology was found to be more prominent for the fMRI functional networks, whereas for the EEG frequency bands only a very small portion of the topology seems to arise from long-distance connections, when removing what is expected by chance. This is in accordance to all the results seen so far, that point for a less modular structure of the EEG functional networks. It is also noticeable that these median modularity values are higher than the ones found for the static connectomes. This might suggest that averaging over time leads to a structure more bounded to the spatial embedding, which is not strange considering that the dynamic functional connectivity arises from fluctuations in brain activity set on the anatomical space [20, 70]. However, it is important to take into consideration that this analysis is done only for the time points deviating from the spatial null model (around 9%), while the static connectome was constructed by averaging over all time points.

Additionally, to investigate the difference in the community structure when excluding the influence of the spatial constraints, the communities obtained with the regular and modified version of the Louvain algorithm were compared using the NMI metric. The corresponding coloured arrays are illustrated in figure B.13 of the appendix. From these values, it is possible to notice that there is an overall high similarity between the different communities extracted over time, but not a complete match. On one hand, this, combined with the modularity results, implies the existence of relevant spatial patterns that arise out of functional necessity and not just as a consequence of space, even if not at a major extent. On the other hand, this shows the importance of analyzing the community structure giving preference to long distance connections during the modularity maximization, since it led to different communities, as previously reported in [21]. Also, it is important to note that the similarity values are lower for the EEG frequency bands, in comparison to the fMRI. Which means that, even though there is not as distinct modular structure as for the fMRI, the spatial effects show a higher influence relatively to the communities captured for the EEG frequency bands, as reported in section 4.2.1.2.

4.2.4.1 Comparison between time points

Even though it was not found a clear spatiotemporal pattern regarding the community structure for these functional networks, it was still investigated the possibility of existing a repetition over time for the communities obtained when removing the spatial influence. This was done again using the NMI and Jaccard Index metrics and the resulting matrices are represented in the appendix in figures B.14 and B.15, respectively. Even though some partial similarity was found over time, there is not much difference in comparison to the results obtained for the communities in section 4.2.3. Nevertheless, some variations in the similarity values can be observed again, especially for the EEG case when using the NMI metric, however, not in a clear and distinct way.

Also, because of the lack of variability in the observed similarity between the community structure for all time points considered as well as the low number of selected time points according to the spatial null model analysis, it was not considered relevant to test the statistical significance of these values by shuffling the time points. This would lead to a very low percentage of values deviating from the overall similarity, since it appears to always exist a partially shared structure between all pairs of time points.

4.2.4.2 Modalities comparison

In order to assess the correlation between the two modalities excluding the spatial influence, it was performed the comparison across time of the communities extracted with the modified Louvain algorithm, using the again the NMI and Jaccard Index metrics. The coloured arrays representing these values can be found in the appendix in figures B.16 and B.17, respectively, and the resulting average values and associated standard deviation are summarized in table 4.13, for all subjects.

Comparing to the results obtained in section 4.2.3, the NMI values are lower for the communities obtained regressing out the spatial proximity influence, but the Jaccard Index values are essentially the same, on average for all subjects. This might be due to a bias associated to the computation of this metric, that optimizes the similarity by averaging over the maximum values associated to the best pairs of communities, while the NMI consists in a weighted metric, taking into account all contributions through the comparison of all clusters pairs between the partitions of the two modalities. Nevertheless, these results point out the possibility of having part of the correlation found guaranteed by the underlying spatial embedding, as hypothesized in the previous section 4.2.3. Even so, some moderate similarity relatively to the global topology of the fMRI and EEG functional networks can be reported, pointing for a common structure capture by the two modalities. In fact, when observing the similarity arrays in the appendix, it is possible to notice that almost all time points show a moderate correlation between the two data types, especially for the beta and gamma frequency band, with some fluctuations naturally. However, it is important to notice that this correlation was only obtained considering the time points deviating from the spatial null model for both modalities, that were only about 9% of the total time points considered.

Furthermore, it was again considered that it would not be appropriate neither would lead to interesting results the assessment of the statistical significance of these values by shuffling the time points,

Table 4.13: Average NMI and Jaccard Index values and corresponding standard deviation obtained from the comparison of fMRI and EEG frequency bands communities obtained using the modified Louvain algorithm, for each subject and the resulting average and standard deviation for all subjects.

Data type	fMRI-EEG delta	fMRI-EEG theta	fMRI-EEG alpha	fMRI-EEG beta	fMRI-EEG gamma
NMI					
1	0.186 ± 0.035	0.202 ± 0.043	0.189 ± 0.040	0.198 ± 0.049	0.186 ± 0.048
2	0.186 ± 0.045	0.198 ± 0.033	0.188 ± 0.047	0.210 ± 0.047	0.195 ± 0.047
3	0.184 ± 0.040	0.190 ± 0.039	0.208 ± 0.055	0.208 ± 0.041	0.226 ± 0.042
4	0.183 ± 0.041	0.198 ± 0.045	0.172 ± 0.050	0.210 ± 0.043	0.222 ± 0.046
5	0.174 ± 0.046	0.188 ± 0.043	0.203 ± 0.055	0.244 ± 0.059	0.206 ± 0.051
6	0.172 ± 0.044	0.201 ± 0.043	0.195 ± 0.050	0.202 ± 0.054	0.204 ± 0.046
7	0.192 ± 0.051	0.205 ± 0.039	0.203 ± 0.046	0.205 ± 0.041	0.228 ± 0.052
8	0.186 ± 0.051	0.195 ± 0.051	0.184 ± 0.042	0.206 ± 0.039	0.193 ± 0.046
9	0.187 ± 0.055	0.216 ± 0.058	0.193 ± 0.038	0.217 ± 0.049	0.200 ± 0.038
$average$	0.182 ± 0.052	0.199 ± 0.052	0.193 ± 0.057	0.211 ± 0.060	0.207 ± 0.061
$Jaccard\ \ Index$					
1	0.194 ± 0.035	0.196 ± 0.034	0.181 ± 0.031	0.175 ± 0.029	0.180 ± 0.025
2	0.182 ± 0.032	0.178 ± 0.029	0.173 ± 0.027	0.176 ± 0.031	0.179 ± 0.035
3	0.185 ± 0.042	0.186 ± 0.026	0.186 ± 0.036	0.197 ± 0.039	0.193 ± 0.048
4	0.199 ± 0.043	0.192 ± 0.035	0.181 ± 0.029	0.191 ± 0.033	0.184 ± 0.027
5	0.182 ± 0.026	0.182 ± 0.020	0.189 ± 0.032	0.180 ± 0.034	0.196 ± 0.042
6	0.186 ± 0.031	0.181 ± 0.027	0.186 ± 0.030	0.187 ± 0.034	0.180 ± 0.030
7	0.187 ± 0.041	0.194 ± 0.056	0.181 ± 0.030	0.200 ± 0.045	0.190 ± 0.026
8	0.185 ± 0.028	0.179 ± 0.044	0.181 ± 0.029	0.186 ± 0.033	0.186 ± 0.040
9	0.187 ± 0.033	0.192 ± 0.034	0.183 ± 0.030	0.180 ± 0.026	0.186 ± 0.037
$average$	0.187 ± 0.040	0.187 ± 0.040	0.182 ± 0.035	0.186 ± 0.042	0.186 ± 0.040

considering this similarity over time as well as the low number of selected time points. Otherwise, this would lead to a very low percentage or even just resulting in one or two time points being considered significant. Which is problematic for concluding with confidence that there is a correlation between the fMRI and EEG dynamic connectomes. However, as mentioned in the previous section 4.2.3, these results are in line with the ones reported in [94], and other studies showing a link between these two imaging techniques regarding the neural activity detected [10, 57, 122], supporting the limited correlation found in this analysis.

4.2.5 Community Analysis with multilayer Louvain Algorithm

Since it was not retrieved a total match between the topology captured by two modalities on a global scale, even though some correlation was found, one can speculate that these complementary imaging techniques capture different information regarding the underlying neuronal activity and its functional organization. With the objective of investigating whether the combination of the two modalities leads to new information and improved results relatively to the community structure of the functional connectome, a multilayer analysis was performed. In general, the maximization of the modularity allows partitioning the network into the most optimal (approximately) community structure. However, in this case, the partitions will not be optimal individually but grouped together, by measuring the sum of modularity of

Table 4.14: Median modularity values associated to the common communities extracted from both fMRI and EEG frequency bands over time using the multiplex Louvain algorithm, for each subject and the resulting average and standard deviation (std) for all subjects. These modularity values were computed considering each set of selected time points, using the rewiring null model, for every pair fMRI-EEG frequency band.

Data type	fMRI-EEG delta	fMRI-EEG theta	fMRI-EEG alpha	fMRI-EEG beta	fMRI-EEG gamma
Multilayer					
1	0.747	0.751	0.747	0.752	0.749
2	0.751	0.750	0.745	0.763	0.756
3	0.739	0.747	0.738	0.753	0.742
4	0.749	0.753	0.747	0.759	0.758
5	0.750	0.757	0.753	0.747	0.751
6	0.746	0.755	0.751	0.762	0.754
7	0.746	0.747	0.747	0.752	0.744
8	0.752	0.757	0.755	0.760	0.754
9	0.744	0.754	0.752	0.750	0.754
average	0.747	0.752	0.748	0.755	0.751
std	$\pm$ 0.004	$\pm$ 0.004	$\pm$ 0.005	$\pm$ 0.005	$\pm$ 0.005
Isolated					
1	0.616 — 0.098	0.596 — 0.119	0.600 — 0.105	0.567 — 0.154	0.609 — 0.105
2	0.615 — 0.096	0.590 — 0.118	0.600 — 0.112	0.571 — 0.164	0.611 — 0.133
3	0.608 — 0.090	0.582 — 0.129	0.588 — 0.108	0.570 — 0.148	0.611 — 0.090
4	0.639 — 0.071	0.609 — 0.107	0.618 — 0.096	0.587 — 0.136	0.631 — 0.088
5	0.625 — 0.083	0.586 — 0.130	0.605 — 0.100	0.587 — 0.128	0.623 — 0.102
6	0.623 — 0.091	0.593 — 0.118	0.613 — 0.100	0.583 — 0.139	0.610 — 0.106
7	0.600 — 0.105	0.577 — 0.135	0.598 — 0.110	0.560 — 0.157	0.613 — 0.086
8	0.625 — 0.091	0.603 — 0.121	0.614 — 0.104	0.565 — 0.156	0.608 — 0.114
9	0.617 — 0.096	0.579 — 0.134	0.607 — 0.106	0.561 — 0.152	0.621 — 0.096
average	0.619 — 0.091	0.591 — 0.123	0.603 — 0.105	0.571 — 0.148	0.615 — 0.102
std	$\pm$ 0.011 — $\pm$ 0.009	$\pm$ 0.010 — $\pm$ 0.009	$\pm$ 0.009 — $\pm$ 0.005	$\pm$ 0.009 — $\pm$ 0.011	$\pm$ 0.007 — $\pm$ 0.014

the two layers and maximizing this value instead. As such, the median improved modularity values obtained as well as the individual values obtained for each of the two modalities are summarized in table 4.14, while the median number of communities, common to fMRI and EEG functional networks, is represented in the appendix's table B.7.

First, one can immediately notice that the independent values obtained are lower than the single-layer ones reported before in section 4.2.3. This means that the multilayer approach finds clusters common to both modalities that were not found previously, since these partitions possessed too low modularity to be selected in the community detection procedure. Furthermore, the resulting number of communities was found to be lower when combining the two modalities. These two observations are a result of the maximization method employed by the multiplex approach, which allows an information exchange between the two types of functional networks to find the highest modularity common partitions. Therefore, from these results, one can hypothesize that using the two modalities together leads to interesting communities that would not be found if looking at each functional network individually.

4.2.5.1 Comparison with spatial null model

To explore the spatial influence contribution for the common community structure found when combining the two modalities functional networks, the degree constrained spatial null model was analyzed using the multilayer approach as well. The resulting median improved modularity and the independent values for this spatial null model are represented in table 4.15, while the percentage of time points whose multilayer community structure deviates from the expected by chance considering the spatial constraints is summarized in table 4.16.

Table 4.15: Median modularity values associated to the common communities extracted from both fMRI and EEG frequency bands degree constrained spatial null model over time using the multiplex Louvain algorithm, for each subject and the resulting average and standard deviation (std) for all subjects. These modularity values were computed considering each set of selected time points, using the rewiring null model, for every pair fMRI-EEG frequency band.

Data type	fMRI-EEG delta	fMRI-EEG theta	fMRI-EEG alpha	fMRI-EEG beta	fMRI-EEG gamma
Multilayer					
1	0.677	0.676	0.677	0.681	0.678
2	0.675	0.684	0.678	0.690	0.684
3	0.672	0.676	0.670	0.679	0.673
4	0.674	0.682	0.674	0.686	0.680
5	0.679	0.685	0.682	0.686	0.684
6	0.672	0.680	0.678	0.690	0.679
7	0.676	0.679	0.679	0.685	0.676
8	0.679	0.684	0.684	0.688	0.681
9	0.675	0.683	0.682	0.687	0.682
average	0.675	0.681	0.678	0.686	0.680
std	$\pm$ 0.002	$\pm$ 0.003	$\pm$ 0.004	$\pm$ 0.004	$\pm$ 0.003
Isolated					
1	0.518 — 0.116	0.490 — 0.152	0.500 — 0.133	0.459 — 0.187	0.501 — 0.141
2	0.514 — 0.122	0.587 — 0.156	0.500 — 0.137	0.456 — 0.197	0.513 — 0.136
3	0.520 — 0.114	0.480 — 0.163	0.500 — 0.128	0.458 — 0.180	0.523 — 0.109
4	0.537 — 0.101	0.496 — 0.144	0.513 — 0.124	0.483 — 0.164	0.521 — 0.118
5	0.531 — 0.110	0.496 — 0.153	0.523 — 0.124	0.467 — 0.167	0.528 — 0.125
6	0.516 — 0.119	0.492 — 0.151	0.512 — 0.123	0.481 — 0.175	0.519 — 0.124
7	0.513 — 0.125	0.484 — 0.161	0.506 — 0.136	0.465 — 0.179	0.528 — 0.105
8	0.529 — 0.108	0.504 — 0.153	0.517 — 0.134	0.456 — 0.185	0.505 — 0.134
9	0.522 — 0.115	0.485 — 0.162	0.513 — 0.131	0.463 — 0.183	0.519 — 0.124
average	0.522 — 0.114	0.502 — 0.155	0.509 — 0.130	0.465 — 0.180	0.517 — 0.124
std	$\pm$ 0.008 — $\pm$ 0.007	$\pm$ 0.031 — $\pm$ 0.006	$\pm$ 0.008 — $\pm$ 0.005	$\pm$ 0.009 — $\pm$ 0.010	$\pm$ 0.007 — $\pm$ 0.011

From these results, it is possible to notice a higher percentage of time points deviating from the spatial null model by combining the two modalities, when comparing to the percentage obtained by intersecting the time points for both functional networks in section 4.2.1.2. However, as the EEG captures a closer topology to the one present in the null model, this multiplex analysis results in a lower percentage of time points than when considering the fMRI individually (see section 4.2.1.2). Additionally, observing the independent modularity values of each modality for the degree constrained spatial null model, it can be noticed a lower contribution of the fMRI and a higher contribution of the EEG counterpart in comparison to what was found for the functional networks. All this suggests that for the functional networks, the communities are mainly induced by the BOLD signal's structure, as expected. However, these results

Table 4.16: Percentage of time points for which the multilayer functional networks modular organization deviates significantly from a degree constrained spatial null model - for each frequency band.

Subject	fMRI-EEG delta (%)	fMRI-EEG theta (%)	fMRI-EEG alpha (%)	fMRI-EEG beta (%)	fMRI-EEG gamma (%)
1	57.4	53.9	62.5	65.7	78.1
2	70.1	58.9	54.6	69.7	77.3
3	58.2	59.7	57.0	53.5	53.2
4	55.8	56.6	64.3	46.3	60.2
5	58.4	48.0	46.2	53.0	59.1
6	67.5	55.8	56.7	59.9	68.3
7	60.1	62.1	63.4	56.2	45.3
8	48.9	46.4	55.8	57.5	74.3
9	56.4	57.4	61.2	55.0	60.2
average	59.2 ± 6.0	55.4 ± 4.9	58.0 ± 5.3	57.4 ± 6.6	64.0 ± 10.6

also imply that the fMRI, while compromising its optimal community distribution, forces clusters on the EEG networks that are not optimal, and even further, clusters that are against what is expected by the spatial null model.

Therefore, these results show that the joint analysis of these two functional networks allows to incorporate the information from both modalities, leading to significant and interesting results. They also show that it is not just the spatial embedding that leads to the common partitions selected. Moreover, this also points out for the relevance of further analysis of the community structure of the brain networks, by combining different imaging techniques, to maximize the information captured and possibly contribute to the understanding of the neuronal activity and hemodynamic response coupling.

4.3 Discussion

The study of functional networks can provide features for the description of the brain's behaviour and functional interaction, that might be key to identify abnormalities or distinguish connectivity patterns arising in a given condition. Therefore, it was performed a community analysis to extract macro-scale patterns of synchronized activity for both fMRI and EEG functional networks and also with hopes of uncovering the relationship between the whole-brain connectivity captured by the electrophysiological and hemodynamic signals.

This analysis revealed a clear modular organization for the fMRI functional networks, deviating significantly from a rewiring and a degree constrained spatial null model. However, some variations were found over time, which are thought to reflect an alternation between whole-brain connectivity states associated to a more segregated or a more integrated topology. In other words, corresponding to alternating periods of local, specialized information processing that result in a more clustered topology and periods of communication between different modules for complex cognitive processing and information transfer, decreasing the modular structure, as reported previously in [12, 46, 74, 128]. These findings were in accordance with previous studies that also reported a community structure for the fMRI networks with similar modularity values, although using different parcellations, connectivity metrics and/or approaches [13, 79, 129], establishing that indeed there is a modular structure for these networks. Besides this, it was surprising to find a high percentage of, if not all, time points for which the fMRI networks deviated

from the random case, appearing to be too clustered, since it was speculated the existence of time points for which the activity captured would be lower and/or result in a higher degree of randomness [115]. However, even having a variety of dynamic functional connectivity states, ones more connected than others, there is never truly a random topology in brain networks [2, 35, 56] and thus this high percentage of time points translates again into the ability of the BOLD signal to capture the segregated connectivity arising from the underlying neuronal activity within groups of brain regions.

In opposition, the EEG functional networks, independently of the frequency band analyzed, showed a less clustered topology, closer to the null models evaluated, with lower modularity values than for the fMRI case, as previously reported in [58]. This is thought to be due to a worse quality of the data collected, being more affected by noise, to a lack of sensibility of the imaging technique to capture the topology of the underlying functional networks, or even to a combination of both. On one hand, there is a lack of reliability regarding these electrical signals due to their high intrinsic variability and their low signal-to-noise ratio (SNR) [130], meaning that more noise is incorporated in these signals, which result in a less defined community structure [131]. In fact, as covered in section 2.1.3, some artifacts will be introduced in both signals owing to the electromagnetic perturbations originated by the two acquisition systems and their interaction [49]. Additionally, it has been reported that the effects of the EEG hardware are substantially lower for the fMRI signal, than the other way around [48]. However, these artifacts are expected to have been corrected, at least partially, by using the artifact acquisition approach proposed in [108] which records 4 electrodes isolated from the scalp to improve data quality (see section 3.1.1.3 for more). On the other hand, since the EEG connectivity comes from highly correlated signals due to mixing at the electrode level, even when performing source reconstruction, it will result in a low sensitivity to differentiate co-activation at a spatial level [44, 132]. Moreover, it is hard to perform an accurate source reconstruction with resting-state data as the signal capture is generally of low amplitude [133] and no method is fully satisfactory. This means that the source mixing cannot be totally excluded, even using methods such the imaginary part of coherency, which will necessarily affect the topology of these networks. Even so, it was still possible to detect some modular structure in the EEG functional networks, as reported in past studies [125, 126]. This difference in modularity was not found in the static connectome analysis, which might be due to averaging the connections over time, leading to a more stable structure and thus a higher modularity for the EEG functional networks.

From the community structure detected, it was possible to find some similarity between the two modalities using the Normalized Mutual Information (NMI) and the Jaccard Index (Jacc) metrics to compare the partitions (averaging over time: $NMI_\delta = 0.247$, $NMI_\theta = 0.265$, $NMI_\alpha = 0.262$, $NMI_\beta = 0.287$ and $NMI_\gamma = 0.273$; $Jacc_\delta = 0.183$, $Jacc_\theta = 0.185$, $Jacc_\alpha = 0.184$, $Jacc_\beta = 0.186$ and $Jacc_\gamma = 0.186$), as previously shown for the connected component analysis. This moderate correlation is in line with past reports comparing the fMRI and EEG static connectomes with a different dataset [57, 134] and also using the same one [94], as well as with what was observed for the static connectomes analyzed in this work. Moreover, it is also in accordance to a study examining the dynamic functional connectivity detected by the two imaging techniques [57]. Furthermore, other studies have reported a link between fMRI and EEG connectivity patterns not only in a resting-state context [122, 127], but also in a task-specific

conditions [10], thus corroborating the similarity obtained through this new approach.

However, the community structure in both functional networks is not identical over time and, as such, their correlation, even though present, is not particularly high. This might be because of the lack of modular topology in the case of EEG, possibly due to noise and limitations in the methodology associated to this imaging technique, as mentioned before. It might also be that this modality captures different interactions, associated to the inter-connectivity between groups of synchronized activity, therefore resulting in a more integrated topology instead of segregated one, as found for the fMRI networks. In fact, it has been shown in [135] that EEG functional connectivity clusters into groups of brain regions in a different way as the fMRI functional connectivity, and that these clusters appear to be extended in space, with lower connectivity within modules than between them. Moreover, in another study [58], where a joint analysis of fMRI-EEG connectivity is performed, besides detecting a co-occurring functional component linked to intrinsic connectivity networks for both modalities, it was also captured an additional component exposing spatially divergent components, correlating intra-connectivity in fMRI with inter-connectivity for the EEG. Therefore, taking this into consideration, one might suggest that the difference between the topology detected by the two modalities, resulting only in moderate similarity, might be due to the fMRI and EEG capturing different aspects of the neuronal activity and its coordination over the whole-brain, besides all the limitations associated to the EEG connectivity data.

Additionally, it is important to mention that the different frequencies bands capture different topology across time, as shown by selecting different time points, corresponding to networks deviating from the random configuration. Besides this, it was found that the similarity between fMRI and EEG's community structure oscillates over time in a specific way for each frequency band. This is not surprising considering that each frequency band has been speculated to be associated to different functional roles and origins [7, 122, 123], and has in fact been reported to translate in different connectivity within and between different modules [74], as well as different spatial distribution over the whole-brain in terms of the communities detected [123]. Also, past studies have reported a different contribution of each EEG frequency band to the BOLD connectivity dynamics [9, 122, 124], in particular, varying across space [134] with a more local topology captured for higher frequency bands such as the gamma band and a more global connectivity for lower ones, like the delta band [39, 57, 58, 123], but still capturing some common topology as well. Relatively to the overall relationship between the two modalities, there is no clear consensus in literature to which frequency band resembles best to the connectivity captured by the BOLD signal, although it has been shown that the gamma frequency range of EEG signals correlate the most with BOLD fMRI signal [122, 136]. However, it cannot be excluded the influence of distinct signal-to-noise ratio (SNR) across frequencies in the differences found for the correlation between fMRI and EEG networks' topology. Even so, for this study it was found a higher value for the beta and gamma bands, particularly when using the NMI metric. Identifying the beta band as the most correlated with the fMRI is in accordance to what has been previously reported for the same dataset in [94], while for that study, the gamma band was found to have a weaker but still meaningful correlation. Despite this, it is important to mention that the scalp EEG gamma band is more susceptible to noise and artifacts, which might influence the reliability of the results obtained [94, 135].

Finally, it is worth noting that even though some variations in the results were found, particularly between subjects, this is to be expected as there is no common cognitive activity to be performed during resting-state acquisition. Since rest is a condition that may include varying levels of attention and mind-wandering [74], different fluctuations can be detected, depending on subject variability as well as noise associated with specific acquisition artifacts.

Spatial Influence in the Community Structure Throughout this study, a question has been raised regarding the constraints that the spatial embedding imposes on the community structure obtained, as well as its contribution for the relationship between the two modalities. Naturally, the dynamic functional connectivity (dFC), reflecting the continuous communication and synchronization between spatially distributed brain regions, is bounded by the underlying anatomical structure [137]. Therefore, the resulting topology will be physically constrained by space, giving preference to closer connections [19, 20] and thus influencing the modular structure of these networks. Also, fMRI and EEG functional dynamics arise from the same underlying structural connectomes and so one can speculate that this might contribute for a certain similarity of the dynamic topology observed. In order to evaluate this effect, it was performed a similar community analysis but removing this spatial influence, using a modified version of the Louvain algorithm.

First, from the comparison with a degree constrained spatial null model, proposed by Cazabet et al. [22], it was found that there is indeed a spatial influence over the topology recovered for both modalities functional networks. That is not surprising since it has been reported that there is a general tendency for the clusters in functional networks to be composed by regions that are near one another in the physical space [70]. However, it was revealed that the EEG seems to be more susceptible to these proximity constraints than the fMRI, since it was shown that this influence explains a higher portion of these networks' topology. This might be due to the lower spatial resolution intrinsic to this imaging technique, as well as to volume conduction and source mixing which will bias the connectivity captured by increasing the synchronization of nearby regions. In fact, in an attempt to reduce this effect, it was chosen the imaginary part of coherency as the connectivity metric, so as to discard instantaneous synchronizations that might arise from these limitations. However, it is not possible to guarantee that this effect is completely removed. Additionally, one must take into consideration that these two imaging techniques' signals detect distinct aspects associated to neuronal activity which might result in a difference in structure between the two [135].

Despite this spatial influence, it was still retrieved a significant community structure, for both modalities, in about 7-13% of the time points, varying between frequency bands and with the delta band having the highest percentage. This might be due to the fact that this frequency band captures synchronized oscillations between brain regions at a longer distance than higher frequencies [39, 122]. Even so, these findings suggest that there is truly some connectivity captured arising out of functional necessity and integrating long-distance synchronizations, even though most of the topology is explained by the expected nearby connections. Indeed, when comparing the communities obtained with and without this spatial influence, a high similarity was found but not a complete match between the two sets, for both modalities.

As previously suggested in [137], it is possible to conclude then that the long-distance connections are of particular importance to describe the topology resulting from the brain regions interaction and coupling beyond the spatial proximity. Furthermore, it was found that removing the spatial constraints had a bigger impact in the resulting communities for the EEG functional networks, as expected due to the results discussed before. However, lower modularity values were obtained in comparison with the fMRI, which might be because of the limitations associated to the quality of the EEG data or simply by capturing a different topology, less segregated. Even so, these results show the importance of removing the spatial influence of the modularity maximization in order to detect new and meaningful communities, enabled by the synchronization of anatomically separate brain regions. In fact, a recent study has even pointed out for the possibility of existing distinct contribution of long-distance and short-range connections regarding the community structure of functional networks, by studying their topology when removing the short-distance connections [21].

Regarding the relationship between the two modalities, it was found a lower similarity between the topology captured by the fMRI and EEG dynamic functional networks, when considering the community structure supported by long-distance connections beyond the proximity effects of space. Furthermore, when analyzing the two modalities static connectomes, it was found a higher similarity than the one obtained when analyzing the dynamic functional connectivity. This might result from the fact that averaging the connectivity matrices will necessary create a more stable version of these networks [137] and approximate these connections to the anatomical wiring [19]. Thus implying that the higher similarity between the two modalities found for the static connectomes is supported by the spatial embedding constraining the topology observed. Which, in turn, leads to the hypothesis that the proximity constraints also make the fMRI and EEG modalities dynamic connectomes more similar, resulting in a lower correlation when removing this influence. Even so, it was still possible to retrieve some correlation beyond the spatial constraints, which further supports the link between the fMRI and EEG dynamic functional connectivity and hence the relationship between the hemodynamic response and the underlying neuronal activity. However, it is important to not forget that this correlation is only found for the time points whose networks deviate from the spatial null model. This means that only about 9% of the time points will be moderately correlated between the two modalities beyond the spatial embedding.

Multiplex Community Structure and Complementary Contributions As mentioned before, it was found a similarity between fMRI and EEG functional networks, but only to some extent, meaning that the two modalities might still capture different information relative to the underlying neuronal activity and its functional organization. Therefore, to test if combining the two modalities leads to improved and new results, a multilayer approach was used to study the community structure. This constitutes, to our knowledge, a novel analysis for investigating the functional networks topology through the combination of these two modalities. Moreover, this was possible since it was guaranteed a temporal equivalence between the two types of functional as well as resorting to a source reconstruction procedure to have an identical set of nodes and, this way, obtain a set of multiplex networks, one for each time point.

With this approach, it was indeed retrieved a different community structure with a high modularity,

corresponding to clusters common to both fMRI and EEG that would not been found otherwise, if looking at each modality individually. This is because these partitions corresponded to lower values of modularity that would not be preferred by the community detection algorithm, which proves that combining the two data types leads to new results. These findings are in line with two previous studies that performed a joint-analysis of these modalities, by means of a hybrid independent component analysis [58] and by building a multimodal graph, joining the fMRI and EEG nodes into a single network [9], to identify new connectivity structure. Additionally, it was also noticeable that the contribution of the fMRI is much larger than the one from the EEG frequency bands, which might be due to the noise and sensibility limitations associated to this imaging technique, as well as for reflecting an overall less modular configuration. Moreover, it can be hypothesized that, combining all the frequency bands into several layers, the EEG contribution might become equivalent to the fMRI, since each one captures a different topology correlated to the BOLD counterpart, as mentioned before. Indeed, it has been shown in [58] that a joint fMRI-EEG component had a strong contribution from all frequency bands.

Afterwards, when comparing with a multiplex degree constrained spatial null model, built by combining the surrogates obtained for each of the two modalities, more than half of the time points' multiplex functional networks were found to be deviating significantly from this random configuration. Which means that these common communities, combining the functional information with high spatial and temporal resolution, are relevant and significant and do not arise strictly from the shared underlying anatomical architecture. Despite this, it is important to mention that a high modularity was still obtained for the multiplex spatial null model, with a larger contribution of the EEG layer than it was found for the functional networks, suggesting that the spatial embedding is still responsible for most of the multiplex community structure obtained. In fact, it has been reported in [134], that combining both fMRI and EEG functional dynamics leads to a better prediction of the structural connectivity, again pointing out that the community structure detected with both modalities is very much associated to the anatomical proximity constraints. However, since it was captured a modular configuration statistically significant in comparison to this null model, it would be interesting to explore the multiplex community structure beyond this spatial influence. Unfortunately, this analysis leaves open the comparison of the multilayer communities obtained with and without the spatial constraints, for which the modified Louvain algorithm would need to be extended to accommodate multiple layers.

Nevertheless, it is possible to conclude that, despite the somewhat correlated community structure found for fMRI and EEG functional connectivity, mostly due to their spatial embedding, these two modalities can be combined in order to retrieve new information relative to the functional organization arising from the brain's complex activity.

Chapter 5

Motif Analysis

This chapter contains a motif counting analysis performed to characterize both fMRI and EEG functional networks on a meso-scale, to explore their potential correlation over time and also to investigate the influence of the proximity constraints, imposed by the spatial embedding in the local structure captured for the two modalities. All the code was implemented using Python3.6 and is available in `https://github.com/franciscaabsr/Thesis_project/Code/motif_analysis.ipynb`.

5.1 Methodology

As covered before in the Background chapter, the spatiotemporal organization of the brain's functional connectivity can be analyzed also on a meso-scale, by means of motif enumeration. Since subgraphs consist in building blocks that can be used to characterize and discriminate different networks in a finer and powerful way, it is possible to use them to describe the topology arising from the time-varying functional synchronization between different brain regions. Also, this type of analysis can be applied to investigate a potential relationship between fMRI and EEG functional networks, now based on their local structure. Therefore, this analysis essentially consisted in identifying subgraphs that are over- or under-represented, tested against a null model, with the objective of describing these two modalities networks using these motifs as features and then establishing a topological comparison between the two by means of these network fingerprints. Again, it was used both the rewiring and degree constrained spatial null models for the statistical testing and thus selection of the motifs, as it will be described below.

5.1.1 Motif Analysis using the Rewiring Null Model

Motif counting and statistical testing With the objective of obtaining the significant motifs of both fMRI and EGG functional networks over time, it was used the g-tries algorithm proposed by Ribeiro et al. (available in `https://www.dcc.fc.up.pt/gtries/#manual`) [18], already described in section 2.2.3. This algorithm takes each network and the desired subgraph size and returns the number of occurrences of each subgraph and the associated z-score value, with respect to a rewiring null model. This was performed for both modalities' functional networks, for all time points, considering undirected subgraphs

with 3, 4 and 5 nodes, which correspond to 2, 6 and 21 different motif classes (defined by the subgraph code returned), respectively. It was considered that these subgraphs were enough to characterize and distinguish the different functional networks, since these networks have an overall low number of nodes and using 5 nodes subgraphs seemed to lead to a finer enough analysis. Also, using larger sizes would produce too many subgraphs, with some of them, mainly the most dense and sparse ones, being unlikely to occur for both functional networks and their randomized version, leading to uninteresting and biased results [138]. The different subgraphs analyzed are represented in figure 5.1.

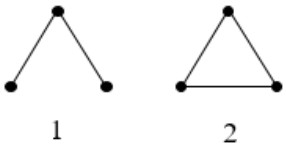

(a) The 2 possible motifs of size 3

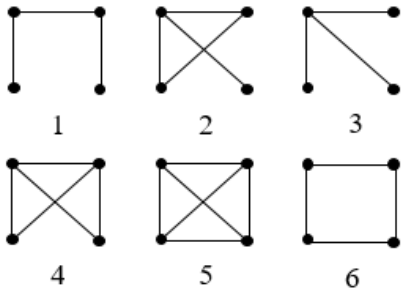

(b) The 6 possible motifs of size 4

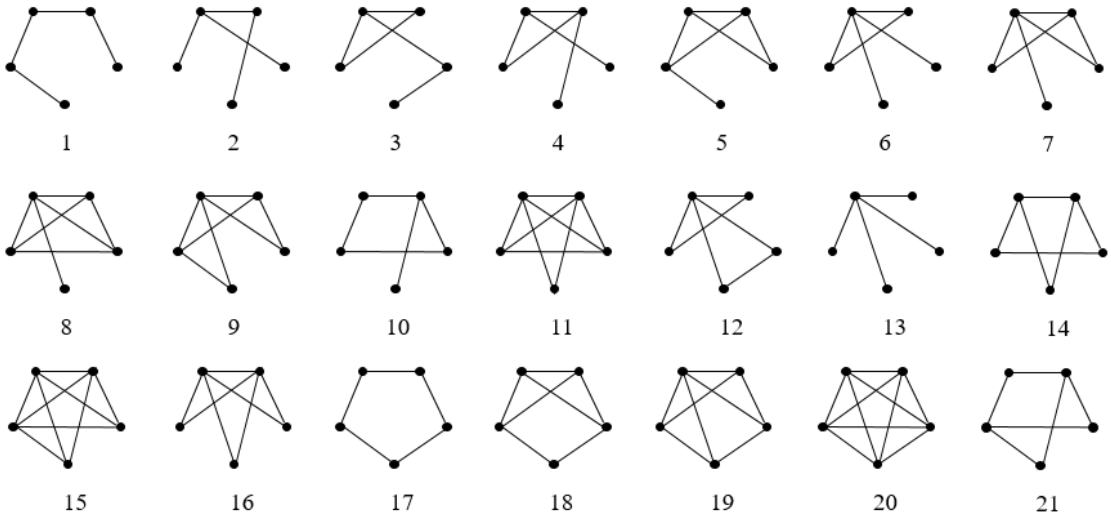

(c) The 21 possible motifs of size 5

Figure 5.1: All possible 3-node, 4-node and 5-node undirected subgraphs.

5.1.1.1 Comparison of motifs extracted over time

As reported for the community analysis, the functional networks' topology varies over time, grouping different brain regions and oscillating between more or less segregated states. So, from these findings, it was considered to be relevant to also study the variation of the observed motifs over time, to investigate if the motifs characterizing these functional networks were persistent or oscillated over time, resulting in a variation of the local structure that would translate into a different overall topology across time.

Selection of most recurring motif classes With the objective of discriminating the most significant subgraphs in the functional networks, occurring recurrently over time either at a higher or lower frequency than expected by chance, the percentage of time points for which each motif class appeared on the significance top was computed, that is, considering all the time points where that specific motif was one of the most over- or under-represented. As such, the top 1, 2 and 5 motif classes were selected for the 3, 4 and 5 nodes' subgraphs, respectively, for each time point, guaranteeing that the associated z-score was either higher than 2 or lower than -2, respectively. This additional step was performed to make sure that only the motifs deviating significantly from what was expected by chance were taken into account. Following this, the motifs that appeared most often over time in each position of the chosen top were obtained for each subject and the percentage of appearance over time of each motif was computed, for both fMRI and EEG functional networks independently. This allows a comparison of the most significantly over- and under-represented motifs between the two modalities. Also, with the intention of assessing the consistency between subjects, the most recurring motifs on each position of the significance top were compared.

Comparison of motif classes distribution over time As mentioned previously, the networks and their topology can be described by the motifs that constitute them, meaning that one can establish a network fingerprint that encompasses these features to define and distinguish a given network. These fingerprints can then represent the frequency of occurrence of the different motifs in the whole network, constituting a characteristic motif profile [14]. So, in order to explore the temporal organization of these networks with a motif-based outlook, first, it was computed this network fingerprint for each time point by obtaining the number of occurrences of each motif class, normalized by the total number of occurrences of all motifs, considering only the subgraphs that were statistically significant in comparison to the rewiring null model. That is, the motifs for which the associated z-score was either higher than 2 for the over-represented or lower than -2 for the under-represented ones. Subsequently, these network fingerprints were compared between each pair of time points using the cosine similarity metric, defined in section 2.2.4, using SciPy's distance package's *cosine* function. Additionally, to analyze the motif diversity across time, the total number of motif classes retrieved was obtained for each time point and the resulting variation plotted, for either over- or under-represented motifs, using the same z-score criteria as before. This was performed for both fMRI and EEG frequency bands separately, considering all subgraph sizes (3, 4 and 5 nodes).

5.1.1.2 Comparison of motifs extracted between modalities

Furthermore, to study the correlation between the two modalities regarding the motifs extracted and thus between the local functional organization captured by each imaging technique, the network fingerprints, defining the motif profile of each these functional networks, were computed and compared for all time points, using again the cosine distance metric. Additionally, since fMRI and EEG are expected to capture different information regarding the whole-brain's functional connectivity, it was investigated if these two networks show a different level of diversity regarding the types of motifs that are found. For this, the

total average number of motif classes encountered as well as the corresponding standard deviation, considering all time points and combining all subjects, were computed and compared for fMRI and EEG frequency bands, considering the over- and under-represented motifs independently.

5.1.2 Motif Analysis using the Degree Constrained Null Model

Motif counting and statistical testing Since it was found during the community analysis that the spatial constraints influence the functional networks, by giving prevalence to nearby connections, the subgraphs obtained using the g-tries algorithm were tested against the ones retrieved from the degree constrained spatial null model. This was done to verify the impact of the spatial influence in the motifs present in both functional networks and to analyze the ones that still occur beyond these constraints. To do this, 100 surrogates of this null model were generated for each time point, and the g-tries algorithm was then applied to obtain the subgraphs' codes and their respective frequency for each one of the surrogates. From these values, the average and standard deviation values were obtained to compute the z-score for each motif and thus establishing its statistical significance according to the spatial null model. Again, this was performed for both modalities' functional networks, for all time points, considering undirected subgraphs with 3, 4 and 5 nodes, which correspond to 2, 6 and 21 different motif classes (defined by the subgraph code returned), respectively. The different subgraphs analyzed are represented in figure 5.1, in the previous section.

5.1.2.1 Comparison of motifs extracted over time

Equivalent to the previous motif analysis with respect to the rewiring null model, it was investigated the temporal variation and persistence of the motifs obtained, that were either over- or under-represented in comparison to the spatial null model.

Selection of most recurring motif classes To search for the most significantly over- and under-represented motifs in the functional networks, that recurrently occur over time beyond the spatial influence, the percentage of time points for which each motif class was found to be one of the most significant ones was computed. As such, the significant top 1, 2 and 5 motif classes were selected for the 3, 4 and 5 nodes' subgraphs, respectively, for each time point, guaranteeing that the associated z-score was either higher than 2 or lower than -2. Following this, the motifs that appeared the most often over time in each position of the chosen top were obtained for each subject and the percentage of appearance over time of each motif was computed, for both fMRI and EEG functional networks independently. This was done also with the purpose of comparing the two modalities functional networks through the motifs that still arise beyond the proximity constraints. Besides this, with the intention of assessing the consistency between subjects, the most recurring motifs on each position of the significance top were obtained.

Comparison of motif classes distribution over time In an identical way as done in the section 5.1.1.1, to explore the possibility of having motif profiles repeating over time, the network fingerprints, defined by the number of occurrences of each significant motif class, normalized by the total number of

occurrences of all motifs, were obtained and compared between time points using the cosine similarity. Additionally the motif diversity over time was analyzed. For this, the variation of the total number of classes was plotted, considering again only the ones with higher and lower frequency than expected by chance. Again, this analysis was performed for both fMRI and EEG frequency bands separately, considering all subgraph sizes (3, 4 and 5 nodes).

5.1.2.2 Comparison of motifs extracted between modalities

To investigate if a relationship between fMRI and EEG functional networks, regarding the motifs extracted and thus the local functional organization captured by each imaging technique, can be still be found beyond the spatial embedding influence, the network fingerprints were computed and compared for all time points, using again the cosine similarity metric. In similar way, to examine the level of motif diversity found between the two modalities, the total average number of motif classes and corresponding standard deviation was obtained for both fMRI and EEG networks, considering all time points and combining all subjects. This was performed for both the motifs over- and under-represented with respect to the spatial null model.

5.2 Results

5.2.1 Motif Analysis using the Rewiring Null Model

5.2.1.1 Selection of most recurring motif classes

In order to select the most significant subgraphs recurring over time, in both fMRI and EEG functional network, the motifs that appeared most often as the top most over- and under-represented ones were obtained and the associated percentage of time points computed. These percentage values are summarized in tables C.1, C.2 and C.3/C.5, for subgraphs of size 3, 4 and 5, respectively, with the results obtained for the over- and under-represented motifs with 5 nodes divided in these two last tables. Furthermore, to evaluate the consistency between subjects regarding the most recurring motifs, the motif that appeared in each top position for most time points was selected for each subject, for both modalities. These results are represented in tables 5.1 and 5.2, for each of the last two cases, since there was full consistency between subjects and frequency bands with subgraphs of size 3.

First of all, regarding the motifs of size 3, it is possible to notice an overall consistency of the most significant subgraphs over time, due to the high percentage of time points selecting the same motif class as the most over- or under-represented one, which is then followed by a total consistency between subjects. Moreover, the most commonly over-represented motif is the motif 2, that corresponds to a *triangle* or K_3, according to the nomenclature defined in (`https://www.graphclasses.org/smallgraphs.html`), while the corresponding under-represented one is motif 1, that represents a *path* P_3. These results are not surprising, since the functional brain networks display a clustered topology for most time points, or even all of them as it was found for the fMRI networks in chapter 4. And, from the definition of the clustering coefficient, one understands that this structure is then guaranteed by the presence of many triangles,

allowing a more efficient information transfer for these networks locally. Furthermore, one can observe an increasing percentage of time points selecting these two motifs with frequency, with the gamma band being the closest one to the percentages obtained for the fMRI. In parallel, this is accompanied with a decreasing percentage of time points for which no motif was select, that is, no subgraph occurred in a higher or lower frequency than expected by the rewiring null model. This implies that for higher frequency bands, the topology of these networks will deviate further from the random configuration and closer to a clustered one, on a meso-scale level. Despite this, it is important to take into consideration that, with 3 nodes, only two types of undirected subgraphs are possible, so this does not result in a very interesting and fine analysis.

Moving to the motifs of size 4, one can immediately notice in table 5.1 some differences between the most recurrent motif classes for the fMRI and for the EEG frequency bands. On one hand, the over-represented motif with highest z-score for most time points corresponds to a *clique* or K_4 (motif 5) for the fMRI, while for the EEG it varies with frequency band, from a *cycle* (motif 6), to a clique minus an edge (motif 4), also known as *diamond*, to finally a *clique* (motif 5) as for the fMRI. This variation goes in hand with an increase in frequency, pointing out the beta and specially the gamma bands as the closest ones to fMRI regarding the most recurring over-represented motifs. Interestingly, this is in line with the results obtained in chapter 4 for the comparison with the rewiring null model, where the gamma band showed a higher percentage of time points deviating from the null model, in comparison to the other frequency bands. However, it is curious that the delta band, in particular, selects a *cycle* as the most significant subgraph for a large percentage of time points, a subgraph that does not favor clustering, even though it showed a similar percentage of selected time points as the beta band, for the referred community analysis. Besides this, a higher variability over time as well as between subjects can be found for the EEG case, while for the fMRI all time points and subjects select the same over-represented motifs. On the other hand, relative to the least occurring motifs, the ones with lowest (negative) z-score are identical for fMRI and EEG, corresponding to a *path* (motif 1), although the second most significant ones are not. In fact, it is possible to observe that for the fMRI there is no second least represented motif for most time points (65.7 %), being selected motif 2 or *paw* for the rest, while for the EEG frequency bands the motif 3 is selected, corresponding to a *star* or a *claw*. Both *path* (motif 1) and *star* (motif 3) motifs do not allow an efficient and fast communication between several brain regions, which might be why they appear less in these functional networks. Also, due to the high clustering of the fMRI functional networks and preference for fully connected motifs (motif 5), there is a high tendency for the node belonging to loose edge of motif 2 (see figure 5.1) to connect and originate *diamond* motifs (motif 4), resulting then in a low number of occurrences in the networks analyzed. Besides this, it is possible to observe that there is a high consistency between time points as well as subjects, for both fMRI and EEG, regarding the under-represented motifs.

Regarding the 5 node motifs, a large difference can be found between the two modalities' most recurrent motif classes, either for the over- or the under-represented ones. First, from the results associated to the subgraphs positively deviating from the rewiring null model, one can notice that the motifs with highest z-score correspond to a *clique* or K_5 (motif 20) and a clique minus an edge or $K_5 - e$ (motif 15)

Table 5.1: The most and second most common over- (+) and under-represented (-) motif classes for each subject, considering subgraphs with 4 nodes, for fMRI and EEG frequency bands functional networks. The symbol — is used when no motif class is present, meaning that for most time points no significant subgraph was selected. If there is only a little different in percentage for two motif classes, the second one is represented inside parentheses, as $(\cdot)$.

Subject	1	2	3	4	5	6	7	8	9
$fMRI$									
Top-1 (+)	5	5	5	5	5	5	5	5	5
Top-2 (+)	4	4	4	4	4	4	4	4	4
Top-1 (-)	1	1	1	1	1	1	1	1	1
Top-2 (-)	—	—	—	—	—	—	—	—	—
$EEG \quad delta$									
Top-1 (+)	6	4	6	6	6 (4)	6 (4)	6 (4)	6	6
Top-2 (+)	4	4	4	4	4	4	4	4	4
Top-1 (-)	1	1	1	1	1	1	1	1	1
Top-2 (-)	3	3	3	3	3	3	3	3	3
$EEG \quad theta$									
Top-1 (+)	4 (6)	6	4	6 (4)	6	6 (4)	4 (6)	6	6
Top-2 (+)	4	4	4	4	4	4	4	4	4
Top-1 (-)	1	1	1	1	1	1	1	1	1
Top-2 (-)	3	3	3	3	3	3	3	3	3
$EEG \quad alpha$									
Top-1 (+)	4	4	4	4	6	4 (5)	4	4 (6)	4 (5)
Top-2 (+)	4	4	4	4	4	4	4	4	4
Top-1 (-)	1	1	1	1	1	1	1	1	1
Top-2 (-)	3	3	3	3	3	3	3	3	3
$EEG \quad beta$									
Top-1 (+)	5 (4)	5	4 (5)	5 (4)	5	4 (5)	5 (4)	5 (4)	5
Top-2 (+)	4	4	4	4	4	4	4	4	4
Top-1 (-)	1	1	1	1	1	1	1	1	1
Top-2 (-)	3	3	3	3	3	3	3	3	3
$EEG \quad gamma$									
Top-1 (+)	5	5	5	5	5	5	5	5	5
Top-2 (+)	4	4	4	4	4	4	4	4	4
Top-1 (-)	1	1	1	1	1	1	1	1	1
Top-2 (-)	3	3	3	3	3	3	3	3	3

for the fMRI, being followed by decreasingly but still densely connected subgraphs - motifs 11, 8 and 9. For the EEG, in a similar fashion to what was observed for the size 4 motifs, the selected most significant subgraphs recurring over time vary with frequency: shifting from motif 21, known as $K_{2,3}$, $P_3 \cup P_2$ (motif 18) and *wheel* W_5 (motif 19) motifs, followed by a *wheel* W_4 (motif 16) and $P_3 \cup 2K_1$, (motif 11), to the same clustered ones selected for fMRI, a *clique* (motif 20) and $K_5 - e$ (motif 15). Again, this

Table 5.2: The top-5 most common over- (+) and under-represented (-) motif classes for each subject, considering subgraphs with 5 nodes, for fMRI and EEG frequency bands functional networks. The symbol — is used when no motif class is present, meaning that for most time points no significant subgraph was selected. If there is only a little different in percentage for two motif classes, the following ones are represented inside parentheses, as (·).

Subject	1	2	3	4	5	6	7	8	9
$fMRI$									
Top-1 (+)	20	20	20	20	20	20	20	20	20
Top-2 (+)	15	15	15	15	15	15	15	15	15
Top-3 (+)	11	11	11	11	11	11	11	11	11
Top-4 (+)	8	8	8	8	8	8	8	8	8
Top-5 (+)	9	9	9	9	9	9	9	9	9
Top-1 (-)	1	1	1	1	1	1	1	1	1
Top-2 (-)	4	4	4	4	4	4	4	4	4
Top-3 (-)	3	3	3	3	3	3	3	3	3
Top-4 (-)	—	—	—	—	—	—	—	—	—
Top-5 (-)	—	—	—	—	—	—	—	—	—
$EEG \quad delta$									
Top-1 (+)	21 (19)	19	21	21 (19)	19 (21)	19 (21)	21 (19)	21	21
Top-2 (+)	18	18	18	18	18	18	18	18	18
Top-3 (+)	18 (19)	19 (18)	18 (19)	18 (19)	16 (19)	18 (19)	18 (19)	18 (19)	18
Top-4 (+)	16	16	16	16	16 (18)	16	16	16	16
Top-5 (+)	11 (16)	16	11 (16)	16 (15)	16 (11)	16	16 (11)	16	16
Top-1 (-)	1	1	1	1	1	1	1	1	1
Top-2 (-)	2	2	2	2	2	2	2	2	2
Top-3 (-)	17	17	17	17	17	17	17	17	17
Top-4 (-)	13 (4)	13	13 (4)	13 (4)	13	13	13	13 (4)	13 (4)
Top-5 (-)	6	—	— (6)	— (6)	6	6	—	6 (17)	6
$EEG \quad theta$									
Top-1 (+)	21 (19)	19 (21)	19	21 (19)	21	21	19 (21)	21	21 (19)
Top-2 (+)	18	18	18	18	18	18	18	18	18
Top-3 (+)	19 (16)	19 (16)	16 (19)	18 (19)	18 (19)	18 (19)	16 (19)	18 (19)	19 (16)
Top-4 (+)	16	16	16	16 (19)	16	16	16	16	16
Top-5 (+)	11 (9)	16 (11)	16 (11)	16 (11)	11 (16)	11 (16)	11 (16)	11 (16)	11 (9)
Top-1 (-)	1	1	1	1	1	1	1	1	1
Top-2 (-)	2	2	2	2	2	2	2	2	2
Top-3 (-)	17	17	17	17	17	17	17	17	17
Top-4 (-)	13	13	13	13	13	13	13	13 (4)	4 (13)
Top-5 (-)	—	—	—	—	—	—	—	—	—

variation goes in hand with an increase in frequency, making beta and specially the gamma bands the closest ones to the fMRI regarding their local structure, pointing for their increased clustered topology in comparison to the other frequency bands.

Looking into these results with more detail, relative to top-1 corresponding to the highest z-score, the motifs most recurrent over time in this position are indeed the most clustered ones, however, especially

Table 5.3: Continuation of table 5.2.

Subject	1	2	3	4	5	6	7	8	9
$EEG \quad alpha$									
Top-1 (+)	19	19 (21)	19 (21)	15 (19)	21	19	19	19 (21)	19
Top-2 (+)	18	18	19 (18)	18 (19)	18	18	15		4
Top-3 (+)	19 (16)	19 (16)	16 (18)	16 (18)	19 (18)	19 (16)	18 (19)	16 (19)	16 (19)
Top-4 (+)	16	16	16	16 (11)	16	16	16	16	16 (11)
Top-5 (+)	11 (16)	11 (16)	11 (16)	16 (11)	— (11)	11 (15)	11	11	11 (16)
Top-1 (-)	1	1	1	1	1	1	1	1	1
Top-2 (-)	2	2	2	2	2	2	2	2	2
Top-3 (-)	17	17	17	17	17	17	17	17	17
Top-4 (-)	13	13	13	—3	4 (13)	13	13	13	13
Top-5 (-)	—	—	—	—	—	—	—	—	—
$EEG \quad beta$									
Top-1 (+)	15	15	15 (19)	15 (19)	20 (15)	15 (19)	15	15	15
Top-2 (+)	15	15 (18)	15 (18)	18	15	18	18 (19)	15 (18)	15 (18)
Top-3 (+)	11	11	19 (11)	11 (19)	11	11	11	11	11
Top-4 (+)	16 (19)	16 (11)	16 (19)	16 (11)	16 (11)	11 (18)	11 (16)	16 (11)	16 (19)
Top-5 (+)	9 (16)	9 (16)	9	— (9)	— (8)	5 (16)	— (9)	9 (16)	— (16)
Top-1 (-)	1	1	1	1	1	1	1	1	1
Top-2 (-)	2	2	2	2	2	2	2	2	2
Top-3 (-)	17	17	17	17	17	17	17	17	17
Top-4 (-)	13	13 (17)	13	— (13)	13	13	13	13 (17)	13
Top-5 (-)	—	—	—	—	—	—	—	—	—
$EEG \quad gamma$									
Top-1 (+)	20 (15)	15 (20)	15 (20)	20 (15)	20	20 (15)	20	20	20 (15)
Top-2 (+)	15	15	15 (18)	15	15	15	15	15	15
Top-3 (+)	11	11	11	11	11	11	11	11	11
Top-4 (+)	8	8	11 (16)	19 (16)	8 (16)	8 (19)	16 (11)	8 (11)	16 (11)
Top-5 (+)	16 (9)	9 (16)	—	9 (11)	8 (19)	8 (9)	19 (16)	16 (8)	8 (19)
Top-1 (-)	1	1	1	1	1	1	1	1	1
Top-2 (-)	2	2	2	2	2	2	2	2	2
Top-3 (-)	17	17	17	17	17	17	17	17	17
Top-4 (-)	13 (17)	13 (17)	13	13	13	13	13 (17)	13	13
Top-5 (-)	10	10	—	—	—	—	—	—	—

for the delta and theta bands, around 30% of the time points present a less densely connected motif (motif 21). This is not entirely surprising considering that this motif is composed by two 4-node cycle and, in the previous results for motifs of size 4, the most over-represent one for these frequency bands was indeed K_4 (motif 6). As such, the same question arises regarding the clustered topology captured by the delta band, as these findings do not appear to be accordingly to what was reported for the null model comparison, in chapter 4. Despite this, it is noticeable that there is a larger percentage of time points selecting motifs 20, 15 and even 19 for the delta band, in comparison to theta band, which might

then translate into a difference in their global topology, as observed previously in the community analysis. Even so, this corresponds to an odd result, since this frequency band seems to be still connected but less locally clustered than expected. For top-2 and top-3, there is an overall preference for motifs 19 and 18, which are also not as densely connected as hoped. Furthermore, these motifs decrease their presence with frequency from around 50% to 25% of the time points and are substituted by denser motifs 15 and 11, as mentioned before. For top-4 and top-5, the less densely connected motifs emerge and, even though different motifs can be found between the two modalities, they roughly correspond to the same level of edge density. Curiously, for the alpha and theta band, around 15% and 13% of the time points, respectively, present motif 11 for top-5, even though it corresponds to a more densely connected subgraph than a wheel W_4 motif in top-4 or even than motifs 8 or 9 obtained for the fMRI. This suggests that, for these frequency bands, the denser subgraphs are not as preferred and over-represented resulting in a sparser topology than for beta and gamma, for which these motifs appear in higher z-score positions. Once again, these results are in accordance with the ones reported in chapter 4, where the alpha and, explicitly theta, showed an overall less clustered structure, in comparison to the rewiring null model. Additionally, for top-5 in particular, it is possible to observe a percentage of time points with no motifs for both modalities, but with higher values for the EEG. Which translates into a local structure slightly closer to the random configuration for this imaging technique. Besides this, it was found a high fluctuation over time and across subjects for the EEG frequency bands, while almost no variation can be observed for the fMRI.

Subsequently, for the under-represented motifs, even though some similarity can be seen from table 5.2, the two modalities result in different least occurring motifs, independently of the frequency band, again reflecting distinct local organizations. The motif with lowest z-score corresponds to a *path* or P_5 (motif 1) for both fMRI and EEG, which is not surprising considering that it constitutes the less efficient way for five different brain regions to communicate and coordinate their activity. Moreover, for the fMRI case, this motif is followed by a *bull* (motif 4) and a path including a triangle or $\bar{P}$ (motif 3). In turn, for the EEG, the following least occurring motifs are the *chair* (motif 2), a *cycle* C_5 or *hole* (motif 17), a *star* (motif 13), for all frequency bands. From this selection of motifs, one can notice that, for the EEG, these subgraphs are sparser ones than for the fMRI, corresponding to holes in the network (motif 17) or stars joining several brain regions (motif 13), that will naturally be less favored by the brain networks. In opposition, for the fMRI, the under-represented motifs include in their configuration more triangles, which might be due to the overall high clustering coefficient associated to the BOLD signal, as observed in chapter 4, resulting in even the least occurring motifs reflecting this clustered characteristic. This is also in line with the results obtained for the subgraphs with 3 nodes, where, for the fMRI, all time points select a *triangle* as the most over-represented one, while not being always the case for the EEG.

Taking a closer look into these results, namely regarding their percentages for each position of the z-score top in table C.5, it is possible to observe an increase in the percentage of time points selecting a *path* (motif 1) as the least occurring motif with an increase of frequency as well, which goes in hand with the results observed for the over-represented motifs. Relative to top-2, this same tendency was found for motif 2, with an increase from 50% to 70%. That was also accompanied, in parallel, by a decrease in

the percentage of time points where *cycle* C_5 (motif 17) is selected, except, curiously, for the delta band for which a similar percentage as for the gamma band can be observed. Furthermore, both motifs 17 and 13 are retrieved as being recurrently top-3 and top-4 least significant subgraphs, again decreasing the percentage of *cycle* (motif 17) motifs, but now with motif 13 increasing with frequency. Interestingly, for top-4, the *bull* (motif 4) motif, previously selected for the fMRI, is retrieved for around 20% of the time points, for both delta and theta band, with a lower percentage for alpha and residually for the two highest frequency bands. Finally, for most time points no motif was identified in top-5, being selected in the rest a *cricket* (motif 6), in particular for the delta band, while a *banner* (motif 10) motif is retrieved for the beta and especially the gamma band. One can notice that this last motif is constituted in part by a *cycle* C_4, that was highly detected for the lower frequency bands, which might be why this motif was not selected as a least occurring one for these frequency bands.

Even though all these under-represented motifs are sparse and reflect inefficiency in information distribution between brain regions, these results reveal that each frequency band captures a different structure, on a meso-scale. Additionally, it is important to mention that the lack of motifs identified in top-4 and top-5, for the fMRI functional networks, implies that only 3 motifs are under-represented for this modality, with the rest either being over-represented, identical to what is expected by chance or even not occurring at all in these networks, as it is suspected for motif 10 and 17. Besides this, identically to what was found for the over-represented motifs, a high variability over time can be observed for the EEG, that decreases with frequency, while almost no fluctuation was obtained for the fMRI. However, there is an overall high consistency for the under-represented motifs across subjects, for both modalities.

5.2.1.2 Comparison of motif classes distribution over time

To explore further the temporal organization of both functional networks relative to the over- and under-represented motifs present, a network fingerprint, representing each time point's motif profile, was obtained and compared across time, with the cosine similarity measure. Also, to also analyze the local structure diversity over time, the total number of motifs retrieve was obtained and the resulting temporal variation plotted. These results are represented in figure C.3, with the colour associated to the level of similarity between pairs of time points, and C.1, respectively, for the significant subgraphs of size 3,4 and 5, for both fMRI and EEG frequency bands of an arbitrary subject. Here, as an example, the variation of total number of motifs is illustrated for fMRI and EEG beta band, for subject 3, in figure 5.2.

From both these results, first, it is possible to observe that, for the fMRI, all time points present over- and under-represented motifs, with respect to the rewiring null model. This, combined with the motifs selected with highest z-score in previous section, suggests that these functional networks are locally optimized for efficient communication at all times, with no time points capturing a configuration closer to random. Which is again in accordance with the results obtained for the community analysis. On the other hand, for the EEG, there are indeed some time points for which the networks describe a local organization similar to this null model, as it can be clearly seen in figure 5.2 for subgraphs with 3 nodes, as well as by the presence of zero similarity values in the cosine similarity matrices, due to the absence of over- and under-represented motifs. However, the number of these time points decreases as it is

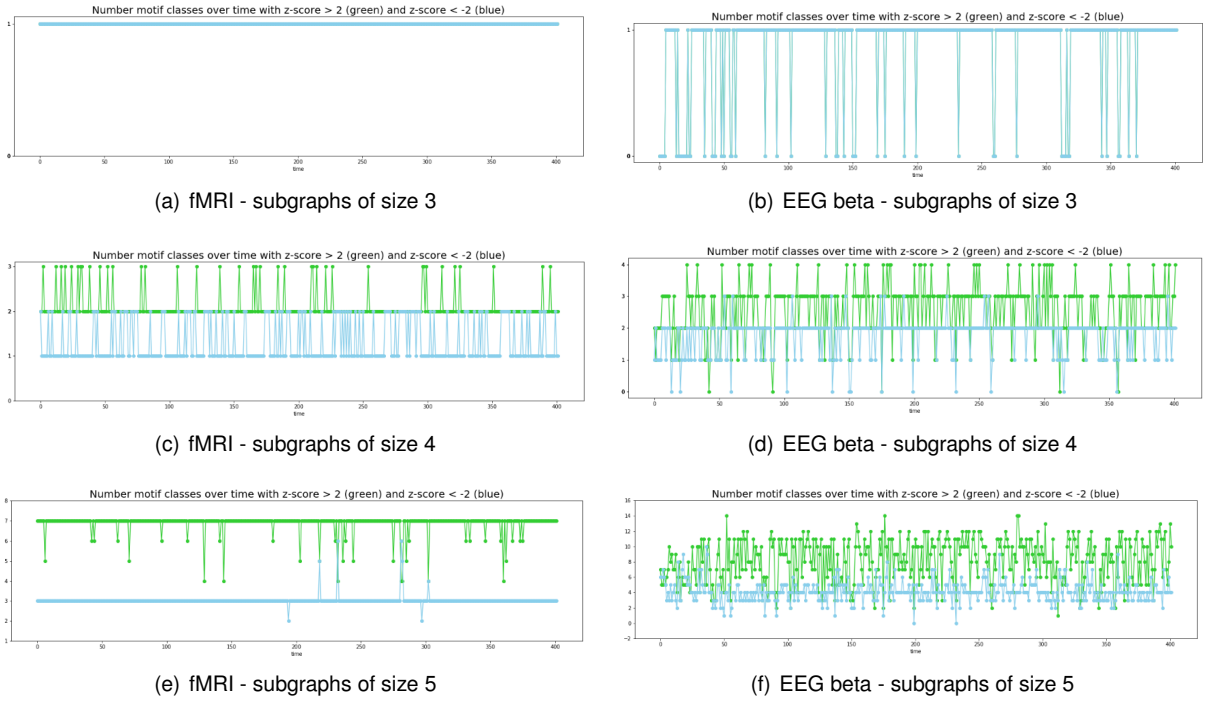

(a) fMRI - subgraphs of size 3

(b) EEG beta - subgraphs of size 3

(c) fMRI - subgraphs of size 4

(d) EEG beta - subgraphs of size 4

(e) fMRI - subgraphs of size 5

(f) EEG beta - subgraphs of size 5

Figure 5.2: Variation of number of motif classes over- (in green) and under-represented (in blue), for subgraphs with 3, 4 and 5 nodes, for fMRI and EEG beta, for subject 3.

moved on to a finer analysis, with increasing size of the subgraphs. Even so, a high temporal variability can be observed, as reported for the previous section, suggesting a local structure alternating between time points either closer or further way from the random case.

Relatively to the network fingerprints comparison over time, a high similarity was found for most time points, with values between 0.8 and 1, for both modalities. Particularly for the subgraphs of size 3, there is only complete similarity or total absence of it, which is not surprising considering that there are only two types of motifs. In turn, with subgraphs of size 4 and 5 a finer analysis can be done, resulting in a more clear oscillation of similarity over time. Even so, there is still an equivalent distribution of motifs for almost all time points, for both modalities. Moreover, for the EEG, these time instances are alternated by moments of slightly lower similarity and sometimes none at all, as mentioned, corresponding to time points for which the networks do not deviate from the random local structure. From these results, it can also be noticed the consistency between time points for the fMRI, and clearly for the gamma band as well, in comparison to other frequency bands. Curiously, though, there is a higher oscillation for the fMRI with 4 nodes' motifs than with 5.

Furthermore, from the temporal variation of motif diversity specifically, one can notice that the number of motif classes over-represented is overall higher than the under-represented ones, translating into a high diversity of motifs characterizing the local structure of both modalities' functional networks. Therefore, this suggests that there is a rich topology for these networks, most likely to increase efficient cognitive processing between different brain regions, but also to allow multiple and distinct interactions in a higher frequency than it would be expected for a random network. In fact, as reported in the previous sections, the least recurring motifs are subgraphs that would not allow this efficiency and, as such,

they are essentially excluded from these networks, for both modalities. Additionally, it is possible to see that, particularly for the EEG, the variation of the total number of motif classes oscillates in a similar fashion for both over- and under-represented ones, pointing out again for a varying local structure for this modality, approximating for some time points to the random configuration described by the rewiring null model.

5.2.1.3 Comparison of motifs extracted between modalities

Finally, to quantify the relative similarity between the two modalities, regarding their local structure characterized by the over- and under-represented motifs, the network fingerprints were compared using the cosine distance metric again. The coloured arrays illustrating this similarity values are represented in the appendix in figure C.5 for an arbitrary subject, considering the subgraphs with 3, 4 and 5 nodes. The resulting average similarity values are, in turn, represented in table 5.4.

From these results, it is possible to notice that there is a higher similarity between the two modalities for motifs of size 3 and 4, than with motifs of 5 nodes. This was expected from the most recurrent motifs analysis in section 5.2.1.1, for which an equivalence was found for fMRI and EEG functional networks, especially for the smaller motifs. Naturally, with larger subgraphs, a finer and more precise analysis is possible, resulting in lower similarity values but still interesting to be reported. However, even though for all the three cases the similarity values do not seem to vary substantially over time, from the coloured arrays one can observes some time points with zero similarity, particularly for the first two sizes, resulting in higher standard deviation values. This absence of similarity is observed for time points with no significant subgraphs selected in the case of the EEG functional networks, as mentioned before. Finally, it is worth mentioning that higher level of correlation between the two modalities was found for the higher frequency bands, as expected, irrespectively of the size of the subgraphs analyzed.

Following this, considering that the two modalities capture different information as shown in section 5.2.1.1, it was analyzed the overall difference between the average number of motif classes retrieved for the fMRI and EEG networks. This diversity comparison is summarized in figure 5.3, for all frequency bands and combining all subjects. From these results it is possible to verify what was observed previously, that indeed the EEG functional networks seem to capture a richer local structure than the fMRI, either regarding the over- or under-represented motifs.

5.2.2 Motif Analysis using the Degree Constrained Spatial Null Model

5.2.2.1 Selection of most recurring motif classes

With the objective of discriminating the spatial influence in the local structure of the functional networks, the most significant subgraphs with respect to a degree constrained spatial null model were selected and their percentage over time computed, for both modalities. The percentages associated to the motifs that appeared most often on the top as the most over- or under-represented are summarized in tables C.7, C.8 and C.9/C.11, for subgraphs of size 3, 4 and 5, respectively. Furthermore, to evaluate the consistency between subjects, the motif that appeared in each top position for most time points, if any

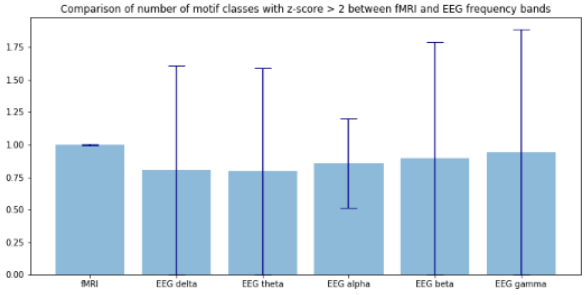

(a) over-represented motifs of size 3

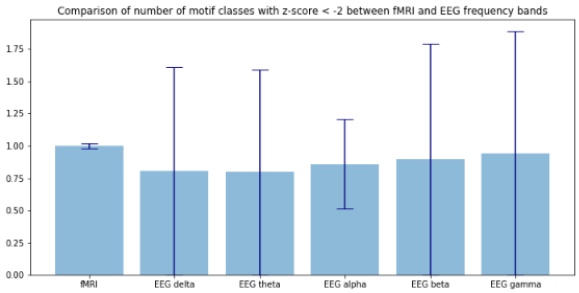

(b) under-represented motifs of size 3

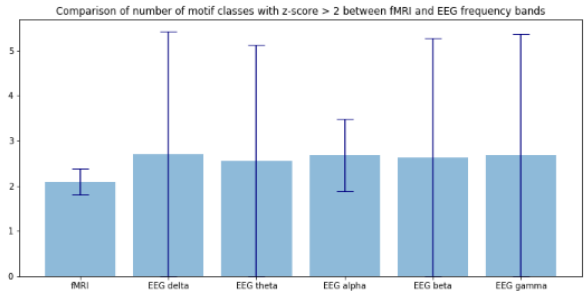

(c) over-represented motifs of size 4

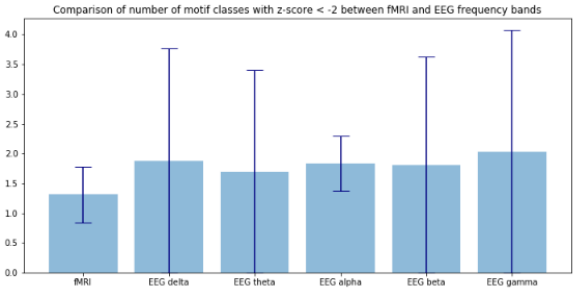

(d) under-represented motifs of size 4

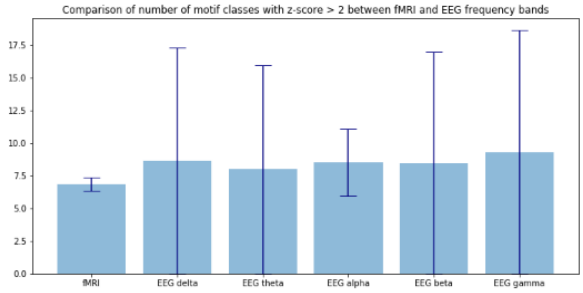

(e) over-represented motifs of size 5

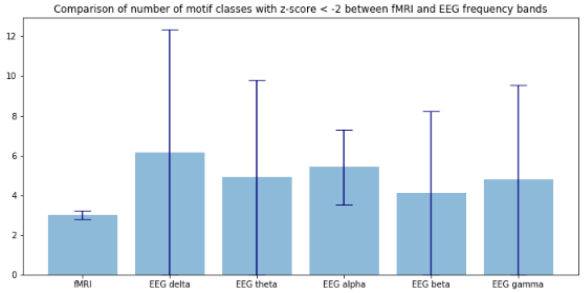

(f) under-represented motifs of size 5

Figure 5.3: Number of motif classes over- and under-represented, average for all time points and combining all subjects, for subgraphs with 3, 4 and 5 nodes, for fMRI and EEG frequency bands.

Table 5.4: Cosine similarity average values and corresponding standard deviation, obtained from the comparison of network fingerprints between fMRI and EEG frequency bands for all time points, for significant subgraphs with 3, 4 and 5 nodes, for all subjects.

Data type	fMRI-EEG delta	fMRI-EEG theta	fMRI-EEG alpha	fMRI-EEG beta	fMRI-EEG gamma
$size$ 3					
1	0.618 ± 0.319	0.609 ± 0.314	0.680 ± 0.261	0.707 ± 0.215	0.770 ± 0.101
2	0.671 ± 0.267	0.613 ± 0.304	0.650 ± 0.283	0.733 ± 0.151	0.766 ± 0.073
3	0.637 ± 0.308	0.645 ± 0.287	0.663 ± 0.287	0.667 ± 0.267	0.681 ± 0.261
4	0.606 ± 0.326	0.631 ± 0.296	0.672 ± 0.270	0.632 ± 0.300	0.716 ± 0.216
5	0.609 ± 0.325	0.549 ± 0.350	0.621 ± 0.314	0.684 ± 0.259	0.758 ± 0.161
6	0.649 ± 0.296	0.614 ± 0.308	0.699 ± 0.252	0.710 ± 0.208	0.747 ± 0.158
7	0.647 ± 0.297	0.626 ± 0.305	0.706 ± 0.236	0.683 ± 0.244	0.711 ± 0.244
8	0.579 ± 0.339	0.579 ± 0.332	0.628 ± 0.306	0.684 ± 0.240	0.751 ± 0.137
9	0.620 ± 0.318	0.630 ± 0.302	0.697 ± 0.240	0.688 ± 0.240	0.709 ± 0.226
$average$	0.626 ± 0.337	0.611 ± 0.339	0.668 ± 0.301	0.687 ± 0.263	0.734 ± 0.204
$size$ 4					
1	0.694 ± 0.165	0.699 ± 0.155	0.707 ± 0.143	0.709 ± 0.149	0.735 ± 0.108
2	0.710 ± 0.127	0.696 ± 0.152	0.699 ± 0.150	0.710 ± 0.121	0.731 ± 0.089
3	0.699 ± 0.167	0.704 ± 0.153	0.707 ± 0.154	0.695 ± 0.176	0.695 ± 0.186
4	0.680 ± 0.182	0.705 ± 0.144	0.716 ± 0.135	0.673 ± 0.204	0.715 ± 0.145
5	0.701 ± 0.177	0.698 ± 0.172	0.678 ± 0.195	0.700 ± 0.177	0.715 ± 0.148
6	0.713 ± 0.144	0.711 ± 0.146	0.716 ± 0.137	0.704 ± 0.159	0.724 ± 0.122
7	0.705 ± 0.165	0.715 ± 0.135	0.715 ± 0.122	0.700 ± 0.165	0.701 ± 0.170
8	0.651 ± 0.221	0.684 ± 0.180	0.710 ± 0.146	0.700 ± 0.166	0.724 ± 0.120
9	0.681 ± 0.176	0.702 ± 0.161	0.711 ± 0.124	0.709 ± 0.151	0.692 ± 0.180
$average$	0.693 ± 0.188	0.702 ± 0.163	0.707 ± 0.157	0.700 ± 0.173	0.715 ± 0.156
$size$ 5					
1	0.369 ± 0.087	0.348 ± 0.086	0.372 ± 0.082	0.400 ± 0.103	0.450 ± 0.082
2	0.386 ± 0.103	0.343 ± 0.091	0.356 ± 0.091	0.397 ± 0.102	0.443 ± 0.079
3	0.376 ± 0.095	0.358 ± 0.087	0.374 ± 0.095	0.371 ± 0.105	0.379 ± 0.117
4	0.366 ± 0.095	0.362 ± 0.083	0.386 ± 0.088	0.364 ± 0.117	0.404 ± 0.105
5	0.377 ± 0.095	0.344 ± 0.097	0.330 ± 0.097	0.367 ± 0.117	0.433 ± 0.094
6	0.393 ± 0.106	0.359 ± 0.094	0.386 ± 0.091	0.376 ± 0.105	0.421 ± 0.099
7	0.392 ± 0.092	0.366 ± 0.081	0.384 ± 0.084	0.385 ± 0.104	0.384 ± 0.100
8	0.349 ± 0.116	0.336 ± 0.091	0.366 ± 0.086	0.381 ± 0.102	0.415 ± 0.09
9	0.367 ± 0.100	0.353 ± 0.088	0.376 ± 0.083	0.378 ± 0.099	0.402 ± 0.108
$average$	0.375 ± 0.112	0.352 ± 0.098	0.370 ± 0.106	0.380 ± 0.117	0.415 ± 0.121

appeared at all, was selected for each subject. These results are represented in tables 5.5 and 5.6, for each of the last two cases for both modalities, since there was full consistency between subjects with subgraphs of size 3.

From these results, one can immediately notice a clear distinction between the fMRI and EEG functional networks retrieved motifs, independently of their size. On one hand, for the fMRI, no over-represented motif was obtained for the majority of time points, while for the EEG, some time points' networks presented a local structure deviating from this null model, with subgraphs appearing at a higher frequency than expected, particularly relative to subgraphs of size 4 and 5. On the other hand, relatively

Table 5.5: The most and second most common over- (+) and under-represented (-) motif classes for each subject, considering subgraphs with 4 nodes, for fMRI and EEG delta functional networks. The symbol — is used when no motif class is present, meaning that for most time points no significant subgraph was selected. The rest of the frequency bands are not contemplated here, since no subgraph was statistically significant for an enough number of time points for any subject.

Subject	1	2	3	4	5	6	7	8	9
$fMRI$									
Top-1 (+)	—	—	—	—	—	—	—	—	—
Top-2 (+)	—	—	—	—	—	—	—	—	—
Top-1 (-)	2	2	2	2	2	2	2	2	2
Top-2 (-)	1	1	1	1	1	1	1	1	1
$EEG \quad delta$									
Top-1 (+)	—	—	—	—	—	—	—	6	—
Top-2 (+)	—	—	—	—	—	—	—	—	—
Top-1 (-)	—	—	—	—	—	—	—	—	—
Top-2 (-)	—	—	—	—	—	—	—	—	—

to the under-represented motifs, the fMRI reflects a local structure arising beyond the spatial constraints, more clustered than it would occur only by the spatial influence. This is because it contemplates sparse subgraphs, mainly at a significantly lower frequency than this null model, consistently for all subjects. In opposition, for the EEG almost no motif was obtained for all time points, except curiously for the alpha band when examining 5 node subgraphs.

Taking a closer look into these results, regarding the motifs of size 3 in specific, no over-represented motif was retrieved for most time points for both fMRI and EEG functional networks, with the exception of delta and especially alpha band, for which 2% and 8% of the time points, respectively, retrieved a *triangle* motif (motif 2). Suggesting for these frequency bands a clustered structure beyond what would be expected from spatial proximity in some time points, guaranteed by the presence of these triangles. In turn, motif 1 or *path* $P3$ did not appear under-represented for any of the EEG frequency bands. However, this motif is avoided significantly for the fMRI networks for all time points, despite the spatial impositions that clearly explain much of the local clustered structure, in comparison to the rewiring null model. Also, it is possible to observe a high consistency of fMRI most under-represented motif over time, across subjects, which is in line to what was observed in the analysis with respect to the rewiring null model.

Moving to the 4 node motifs, again no over-represented motif was found for most time points of the fMRI functional networks but, as mentioned before, the EEG frequency bands showed a slightly different panorama. Despite the low percentages for the theta and beta bands, all frequency bands retrieved *clique* motifs (motif 5) as the most significant one for a relevant portion of time points, meaning that there is a highly dense local structure for some time instances, pointing for a more clustered topology that expected by the corresponding spatial null model. Curiously, for the delta band, around 30% of the time points retrieved a *cycle* C_4 (motif 6) associated with the highest z-score, similarly to what was reported with respect to the rewiring null model, while for the theta and alpha bands this motif occurred in

top-1 in 10% of the time points. These findings further prove that there is a specific and interesting local configuration captured by the lower frequency bands and, even more, a structure that is not explained by the spatial constraints. Therefore, from these results, and considering that more than 50% of the time points present over-represented motifs, the delta band seems to be one of the frequency bands that deviates more from the spatial embedding, on a local perspective. Identically to what was observed for the 3 node subgraphs analysis, no under-represented motif was found for most, if not all, time points for the EEG frequency bands. But again, the fMRI networks reflect a local structure distinct from the spatial null model by avoiding certain motifs. Indeed, these networks possess *path* P_4 motifs (motif 1) with a lower frequency than expected by chance, although the motif with lowest z-score was not this, but a *paw* (motif 2) instead. This goes hand in hand to what was hypothesized in the previous section: that this modality captures such a local clustered structure that the node on the loose edge (see figure 5.1) will very easily be connected to another brain region, resulting in a lower occurrence for this subgraph. Furthermore, appearing here as the most significant under-represented motif suggests that the spatial null model contemplates this configuration with a higher frequency than the rewiring null model, which is not surprising considering this spatial null model has been shown to result in a more clustered topology in chapter 4. Additionally, it is possible to notice a high consistency between subjects regarding the most under-represented motifs present in the fMRI functional networks, as expected by the previous results. This is not observed for the delta band, relatively to its over-represented motifs, due to an oscillation over time regarding the occurrence of motif 6, for which subject 8 might an exception deviating positively.

Relatively to the subgraphs of size 5, once again, for almost all time points of the fMRI functional networks, no motif was retrieved as being over-represented. In opposition and in particular, for the EEG delta, theta and gamma bands, at least half of the time points' networks possess subgraphs at a higher frequency than expected by the spatial null model. The delta band, as hypothesized before, clearly deviates from these proximity impositions on a local perspective, since only 23% of the time points did not select any significant subgraph. Furthermore, it is interesting to notice that around 30% of the time points retrieved motif 21 as the one with highest z-score, revealing once again the preference for this local configuration from the delta frequency band. This motif is also selected for the theta band for 20% of the time points, meaning that there is truly a specific and unexpected local configuration captured by the lower frequency bands. Moreover, even though motif 21 corresponds to a less densely connected pattern, the delta band detects a *clique* (motif 20) as the most significant subgraph for 10% of the time points, further pointing out for a clustered topology deviating from the spatial null model, which is in line with what was reported for the community analysis' null model comparison. For the higher frequency bands no interesting results were found, except that both beta and especially gamma band selected a *clique* as the most over-represented motif for 10% and 20% time points, respectively. Also, for the gamma band, around 10% of the time points select $K_5 - e$ (motif 15) as the second most significant motif. This is in accordance with the previous results, suggesting a more densely connected structure on a local level for the gamma band, in this case emerging beyond what was expected by the influence of space. Even so, it was surprising to find these motifs for this frequency band and not for the fMRI functional networks, since it was hypothesized that the gamma band captured a local structure closer

Table 5.6: The top-5 most common over- (+) and under-represented (-) motif classes for each subject, considering subgraphs with 5 nodes, for fMRI and EEG delta and alpha bands functional networks. The symbol — is used when no motif class is present, meaning that for most time points no significant subgraph was selected. If there is only a little different in percentage for two motif classes, the following ones are represented inside parentheses, as (·). The rest of the frequency bands are not contemplated here, since no subgraph was statistically significant for an enough number of time points of any subject, with respect to a degree constrained spatial null model.

Subject	1	2	3	4	5	6	7	8	9
$fMRI$									
Top-1 (-)	3	3	3	3	3	3	3	3	3
Top-2 (-)	8	8	8	8	8	8	8	8	8
Top-3 (-)	4	4	4	4	4	4	4	4	4
Top-4 (-)	1	1	1	1	1	1	1	1	1
Top-5 (-)	5	5	5	5	5	5	5	5	5
$EEG \quad delta$									
Top-1 (+)	21	—	21	21	21	—	21	21	21
Top-2 (+)	—	—	—	—	—	—	—	—	—
Top-3 (+)	—	—	—	—	—	—	—	—	—
Top-4 (+)	—	—	—	—	—	—	—	—	—
Top-5 (+)	—	—	—	—	—	—	—	—	—
$EEG \quad alpha$									
Top-1 (-)	1	—	3 (1)	—	—	—	—	—	—
Top-2 (-)	3 (1)	—	3 (1)	—	—	—	—	—	—
Top-3 (-)	3	—	3	—	—	—	—	—	—
Top-4 (-)	4 (2)	—	4	—	—	—	—	—	—
Top-5 (-)	5 (2)	—	4	—	—	—	—	—	—

to the fMRI. Moreover, it is worth mentioning that, unexpectedly, the gamma band selects a *cycle* C_5 (motif 17) as the motif with second highest z-score for 9% of the time points, even though this motif was previously classified as under-represented with respect to the rewiring null model. Naturally, this motif is not expected by chance considering the spatial constraints that connected nearby nodes with higher probability, implying that this motif, also known as a *hole* in the network, constitutes a specific pattern captured by this frequency band. Besides this, it was found a high fluctuation over time and across subjects for the EEG frequency bands, even though a large portion of time points did not select any over-represented motif. For the fMRI, on contrary and as before, no variation can be observed.

For the under-represented motifs, the opposite situation occurs, identically to what was reported for subgraphs of size 3 and 4. In this case, the fMRI selects for most time points motif 3, also known as $\bar{P}$, as the one with lowest z-score, being followed by a *claw* (motif 8), *bull* (motif 4), *path* P_5 (motif 1) and even for some time points motif 5 or *kite*. It is possible to notice that three of these motifs were also found to be under-represented with respect to the rewiring null model, even though in a different position of the significance top. This change might be due to an overall lower probability for the spatial null model to include a *path* configuration, because of the proximity constraints, resulting in a lower difference between

the fMRI functional networks and the corresponding null model. Despite this, it was interesting to find motif 8, a densely connected subgraph, as being significantly under-represented, considering it was selected as one of most significantly over-expressed patterns against the rewiring null model. Similarly to what was hypothesized for the equivalent 4-node motif (motif 2), since the spatial null model has a more clustered topology than the previous null model, these motifs will appear with a higher frequency for this random configuration, resulting in these findings. Furthermore, one might speculate that this type of motifs is responsible for bridging two densely connected clusters, due to having an isolated edge connected to a *clique*. And so, with motif 8 appearing in fMRI functional networks with less frequency than expected, it might suggest that there is a preference for a higher superposition of cliques forming densely connected clusters, instead of loosely connected ones. On the other hand, for the EEG, almost none of frequency bands seems to retrieve under-represented motifs of 5 nodes for the majority of time points, with the exception of the alpha band. Curiously, this frequency band selects sparse subgraphs, mainly motif 1 and 3, as the ones with lowest z-score for around 50% of the time points. These results imply that the alpha band captures a local structure arising from neuronal activity that avoids these inefficient connectivity patterns even more than the spatial embedding would suggest. Finally, once again, a high consistency between time points and across subjects can be found for the fMRI, while this is not the case for the EEG.

5.2.2.2 Comparison of motif classes distribution over time

Despite the lack of over- and under-represented motifs, for fMRI and EEG functional networks, respectively, it was still considered to be relevant to study the local structure's temporal organization that deviates from the spatial null model. As such, the network fingerprints were obtained for all time points presenting subgraphs at a higher or lower frequency than expected by this null model, for each modality functional networks. The cosine similarity coloured matrices, resulting from the comparison of these network fingerprints between all these pairs of time points, are illustrated in the appendix in figure C.9, for an arbitrary subject and all subgraph sizes. Furthermore, to analyze the diversity of this local structure over time, the total number of motifs retrieved was obtained for all time points. This temporal representation is summarized in figure C.7, for the significant subgraphs of size 3,4 and 5, for both modalities. Here, in title of example, the variation of total number of motifs is illustrated for fMRI and EEG alpha band, for subject 3, in figure 5.2.

These results further clarify the findings reported in the previous section, that is, the distinct way the two modalities deviate from what would be expected from the corresponding spatial influence. On one hand, the fMRI functional networks report under-represented motifs for all time points, with very little oscillations over time, relatively to both the number of motif classes extracted and their similarity. On the other hand, only a portion of the time points deviates from the spatial null model for the EEG, mainly due to over-represented motifs, with the percentage of time points varying with frequency band. This is in accordance to the results obtained from a global point-view, in chapter 4. However, in opposition to what is reported for the fMRI, a clear oscillation across time can be observed regarding the motif classes diversity, but also relatively to their similarity over time, with some similar motif profiles recurring

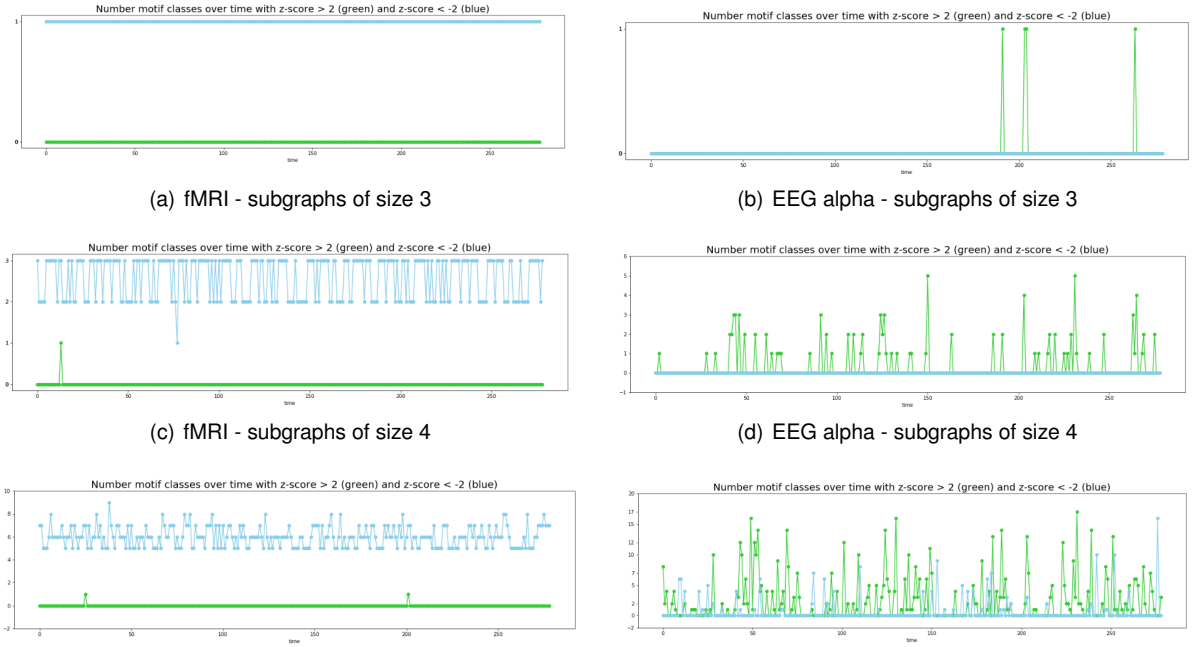

(a) fMRI - subgraphs of size 3

(b) EEG alpha - subgraphs of size 3

(c) fMRI - subgraphs of size 4

(d) EEG alpha - subgraphs of size 4

(e) fMRI - subgraphs of size 5

(f) EEG alpha - subgraphs of size 5

Figure 5.4: Variation of number of motif classes over- (in green) and under-represented (in blue) with respect to the degree constrained spatial null model, for subgraphs with 3, 4 and 5 nodes, for fMRI and EEG alpha, for subject 5.

for different time points.

5.2.2.3 Comparison of motifs extracted between modalities

Subsequently, it was investigated the reduced correlation between the two modalities relatively to their local structure characterized by the over- and under-represented motifs arising beyond the spatial embedding. The coloured arrays corresponding to the cosine similarity computed between the network fingerprints characterizing both fMRI and EEG networks for all time points are illustrated in the appendix in figure C.11. The resulting average similarity, excluding all time points with no significant subgraph extracted for either modality, is represented in table 5.7.

First, from the similarity coloured arrays, it is possible to notice that some time points have zero similarity, which partly correspond to the points where the EEG functional networks do not retrieve any over- or under-represented motif or, in other words, the time points for which the local structure does not deviate from the degree constrained spatial null model. Furthermore, as suggested before, the delta, alpha and gamma bands seem the most interesting for analyzing the relationship between fMRI and EEG, since these frequency bands capture interesting local structure deviating from the spatial null model, with some similarity with the fMRI one. However, this correlation is quite low and not consistent over time, except possibly for the alpha band, as it can be observed from the standard deviation values, in table 5.7.

Therefore, the two modalities capture different local information beyond the spatial influence, with the fMRI discarding sparser subgraphs and the EEG detecting denser ones, more than it would be expected. So, naturally, these modalities will have a higher diversity of under- and over-represented motifs,

Table 5.7: Cosine similarity average values and corresponding standard deviation, obtained from the comparison of network fingerprints between fMRI and EEG frequency bands for the time points with significant subgraphs with 4 and 5 nodes, with respect to the degree constrained spatial null model, for all subjects. It was not included the similarity values for the 3-node motifs, since almost no time points (or even none) retrieved a significant subgraph expressed at a higher or lower frequency than expected by chance.

Data type	fMRI-EEG delta	fMRI-EEG theta	fMRI-EEG alpha	fMRI-EEG beta	fMRI-EEG gamma
$size$ 4					
1	0.216 ± 0.262	0.111 ± 0.199	0.147 ± 0.233	0.025 ± 0.082	0.088 ± 0.220
2	0.248 ± 0.279	0.078 ± 0.188	0.135 ± 0.216	0.063 ± 0.140	0.091 ± 0.201
3	0.197 ± 0.259	0.058 ± 0.155	0.130 ± 0.198	0.022 ± 0.082	0.212 ± 0.285
4	0.222 ± 0.266	0.091 ± 0.203	0.100 ± 0.191	0.120 ± 0.226	0.170 ± 0.282
5	0.234 ± 0.273	0.087 ± 0.163	0.064 ± 0.137	0.074 ± 0.183	0.235 ± 0.318
6	0.199 ± 0.254	0.119 ± 0.210	0.452 ± 0.346	0.055 ± 0.115	0.150 ± 0.261
7	0.229 ± 0.278	0.079 ± 0.198	0.651 ± 0.279	0.125 ± 0.238	0.289 ± 0.300
8	0.209 ± 0.263	0.067 ± 0.143	0.593 ± 0.305	0.081 ± 0.164	0.067 ± 0.190
9	0.128 ± 0.226	0.029 ± 0.114	0.421 ± 0.372	0.007 ± 0.047	0.054 ± 0.163
$average$	0.209 ± 0.260	0.080 ± 0.117	0.299 ± 0.434	0.063 ± 0.094	0.150 ± 0.223
$size$ 5					
1	0.120 ± 0.177	0.055 ± 0.137	0.460 ± 0.095	0.174 ± 0.221	0.164 ± 0.184
2	0.147 ± 0.207	0.050 ± 0.131	0.166 ± 0.210	0.215 ± 0.230	0.159 ± 0.194
3	0.131 ± 0.183	0.052 ± 0.129	0.461 ± 0.103	0.190 ± 0.227	0.153 ± 0.190
4	0.130 ± 0.181	0.047 ± 0.114	0.192 ± 0.211	0.112 ± 0.175	0.148 ± 0.190
5	0.127 ± 0.180	0.023 ± 0.066	0.104 ± 0.193	0.101 ± 0.147	0.212 ± 0.206
6	0.125 ± 0.190	0.089 ± 0.176	0.132 ± 0.193	0.188 ± 0.233	0.146 ± 0.197
7	0.069 ± 0.158	0.045 ± 0.144	0.046 ± 0.130	0.042 ± 0.136	0.071 ± 0.149
8	0.051 ± 0.116	0.023 ± 0.066	0.117 ± 0.218	0.023 ± 0.090	0.020 ± 0.117
9	0.109 ± 0.168	0.056 ± 0.132	0.448 ± 0.111	0.170 ± 0.218	0.110 ± 0.161
$average$	0.112 ± 0.180	0.049 ± 0.104	0.236 ± 0.296	0.135 ± 0.184	0.131 ± 0.188

respectively, as it can be observed in figure 5.5, with the exception of the alpha band for subgraphs of size 5, as expected from the previous results, in section 5.2.2.1.

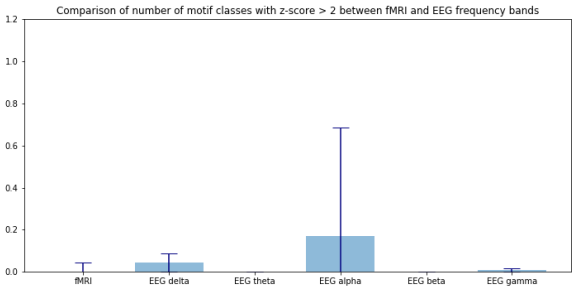

(a) over-represented motifs of size 3

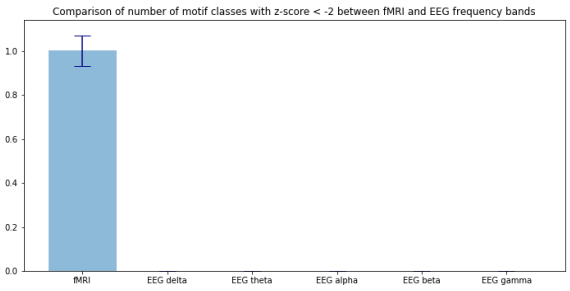

(b) under-represented motifs of size 3

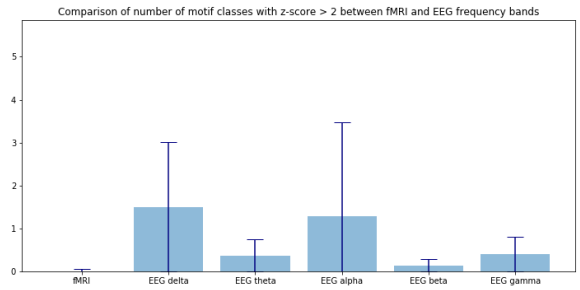

(c) over-represented motifs of size 4

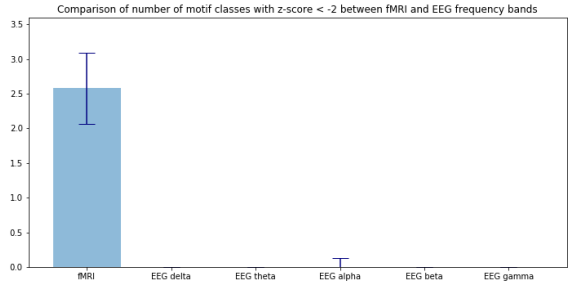

(d) under-represented motifs of size 4

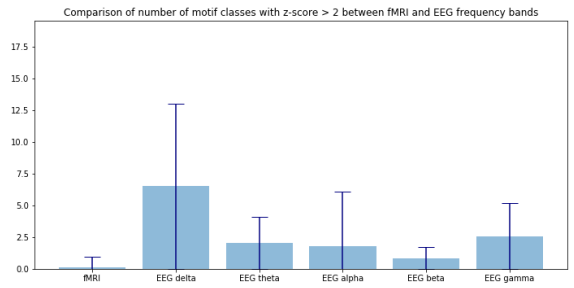

(e) over-represented motifs of size 5

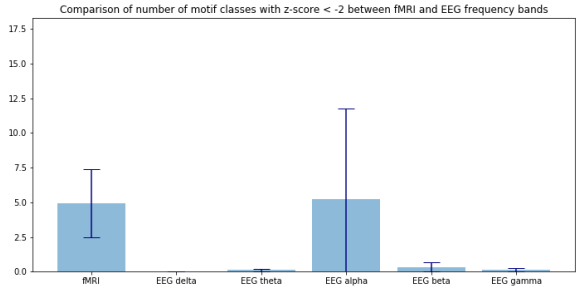

(f) under-represented motifs of size 5

Figure 5.5: Number of motif classes over- and under-represented with respect to the degree constrained spatial null model, average for all time points and combining all subjects, for subgraphs with 3, 4 and 5 nodes, for fMRI and EEG frequency bands.

5.3 Discussion

The brain's functional connectivity and its spatiotemporal organization can be also studied on a local perspective, by retrieving patterns of synchronized activity between small sets of brain regions. These patterns, when occurring significantly more (or less) compared to a null model, can then characterize the structure of these functional networks and can even be used to discriminate them. Therefore, it was performed a motif analysis to extract these patterns and reveal how these building blocks contribute for the topology captured in both fMRI and EEG functional networks.

This analysis revealed a densely connected structure for the fMRI in comparison to the rewiring null model, characterized by the presence of many cliques and other dense configurations that promote highly efficient coordination between brain regions and thus intense local connectivity [139], combined with an absence of sparser motifs such as *path*, *star* and *cycle* motifs, associated to extended pathways of information transfer [139]. These findings are in accordance with a previous study by Morgan et al. [15] with 4 node subgraphs, reporting motif 4 and 5 (see figure 5.1) as being over-represented against degree preserving randomized networks, while lower proportions were found for motifs 1, 3 and 6. In addition, this study suggests that using 5 node subgraphs led to similar results, further supporting the results obtained in this analysis. Moreover, these motif profiles were found to be quite consistent over time, with only some slight oscillations for motifs with 4 and 5 nodes. This was surprising considering that previous studies reported a temporal variation of functional motifs [14, 140], oscillating between different synchronization states, more segregated or more integrated. However, that was not the case for fMRI's local structure in this work, for which a highly clustered structure was observed, constraining the motif possibilities much more than it would be expected. This is in fact according to what was previously observed on a global point of view, where the clustering coefficient reportedly did not oscillate substantially, always maintaining high value throughout time.

In opposition, the EEG functional networks are mainly described by less densely connected motifs, particularly when considering subgraphs of size 5, which suggests that the topology captured by this imaging technique is sparser and therefore less clustered than for the fMRI. Even so, it presented densely connected patterns and sparser motifs as being over- and under-represented, respectively. This is not in accordance to a study performing a motif analysis using 3-node directed subgraphs [89], where *path* motifs were found to be over-represented, instead of *triangle* ones that were retrieved in the present study. However, in opposition to this work, these reports refer to effective connectivity patterns compared with randomized networks that do not preserve the degree distribution, thus it is possible that these different methodology approaches lead to distinct results. Nonetheless, it was found that for higher frequency bands the local structure was closer to its BOLD counterpart, by selecting cliques as the most over-represented motifs. These findings are in line with previous reports that place the gamma band signals as the ones correlating the most with the BOLD signal [136] and, more specifically, on a local level [57]. In general, oscillations at higher frequencies tend to be more localized over cortical brain regions, which might result in the gamma band capturing a higher percentage of cliques than other frequency bands [39], since cliques are associated to highly interconnected local synchronizations between brain

regions [139]. Furthermore, these results are in accordance with the null model's comparison performed previously for the community analysis, for which the gamma band clearly revealed a higher percentage of time points exhibiting a more clustered topology. Besides this, some unique and unexpected features were found for the EEG lower frequency bands. Both theta and especially delta band report the presence of C_4 *cycles* occurring at a higher level than expected by chance, resulting in motif 6 (for 4 nodes) and motif 21 (for 5 nodes) - corresponding to a combination of two C_4 *cycles* - being over-represented for a significant portion of time points, more than densely connected configurations. This implies that these frequency bands, particularly the delta band, capture a specific local organization described by cycles, that might correspond to pathways allowing the integration of information from different local processing centers [139]. However, a further analysis is necessary to investigate the placement of these motifs in the whole-brain's topology and hence reveal their functionality. Despite the differences between frequency bands, which are expected considering each brain rhythm captures distinct topology and is associated to different origins [7, 122], all frequency bands showed a high variability over time, relatively to the motifs most and least present in the functional networks. This fluctuation across time might arise from EEG's higher temporal resolution, in comparison to the fMRI, but might also be due to this imaging technique's increased susceptibility to noise. In fact, the EEG showed a higher percentage of time points with no over-represented motifs, which translates into a local structure closer to the random configuration for these time instances.

From this, it is possible to conclude that the two modalities capture functional connectivity with different levels of local clustering, equivalently to what was observed on a global level. In other words, the fMRI captures a more densely connected topology while the EEG appears to be less clustered, even having some time points approximating to the rewiring null model' local structure, specially for smaller sized subgraphs. Nevertheless, a question remains open whether the time points clearly deviating from this random configuration are equivalent between the macro- and meso-scale analysis, for which further analysis is needed. Despite this, it is important to mention that, even though both modalities reported a rich motif repertoire, necessary to enable flexible and varying functional interaction [14, 15], the EEG functional networks showed an overall richer set of motifs arising across time. These motifs, despite having equivalent density levels, show a different distribution of the number of connections involved, reflecting a more flexibility in the functional connectivity captured by the EEG. Additionally, it is worth noting that some motifs seem to be exclusive to each modality. For instance, considering the over-represented 5 node motifs, motif 21 or 18 were only obtained for the EEG, while motif 12, also known as a *friendship* subgraph or *hourglass*, or even motif 8, appear for the BOLD counterpart. Relatively to the under-represented motifs, all were different between the two modalities, except motif 1 as it would be expected, since it represents the least efficient way of communication between 5 different brain regions. These findings point out for a difference between these modalities regarding their functional networks structure on a meso-scale, which might eventually result in a difference on a larger scale, namely in the community structure [140].

Despite these differences in local structure for fMRI and EEG, some similar over- and under-represented motifs were captured for the two modalities, independently of the frequency band in question, as both

modalities capture patterns that favor efficient information transfer locally and show a reduced presence of sparser ones. As such, it was still possible to find a similarity between the two by comparing the network fingerprints characterizing their topology, for all subgraph sizes. However, considering motifs with 5 nodes, which allows a finer analysis, a lower similarity was obtained considering the results reported, but even so, it was relevant and consistent over time. For this case, the cosine similarity values corresponded to $r_\delta = 0.375$, $r_\theta = 0.352$, $r_\alpha = 0.370$, $r_\beta = 0.380$ and $r_\gamma = 0.415$, when comparing each EEG frequency band with the fMRI, revealing once again a higher similarity for the gamma band as expected. Therefore, this suggests that, despite the differences between the two modalities local structure, there is still some correlation between the two.

Finally, it is worth noting again that even though some differences in the results were found between subjects, this is expected as there is no common cognitive activity to be performed during resting-state acquisition. Since rest is a condition that may include varying levels of attention and mind-wandering [74], different fluctuations can be detected, due to intrinsic subject variability and specific noise artifacts from each individual acquisition.

Spatial Influence in the Local Structure The brain has a tendency to minimize the distance between interacting brain regions, resulting in a higher probability for nearby nodes to interact with each other, which is responsible for the segregated structure typically observed in the brain [19, 20]. Moreover, since this influence of space was found to have a significant impact on the community structure for both modalities and to explain most of the results, such as the correlation between fMRI and EEG global topology, it was even more relevant to explore this effect on a local scale. This way, the motif analysis was performed considering the degree constrained spatial null model, in order to identify the motifs that still arise beyond these constraints.

This analysis revealed distinct effects for fMRI and EEG local structure. On one hand, for the fMRI, no subgraph was found to occur at a higher frequency than expected by this null model, independently of the number of nodes considered. Which implies that the densely connected local structure observed previously is guaranteed and therefore explained by the spatial constraints. This might be due to the fact that these functional networks are so dense that not much is allowed beyond the degree distribution and the spatial proximity. Nevertheless, it was possible to retrieve under-represented motifs, meaning that the sparsity of these networks is substantially lower than expected by the spatial embedding. Even though the spatial null model includes the existence of sparser motifs, most likely responsible for linking two clusters, the lack of these configurations translate to a preference of the fMRI networks for having superposition between the densely connected clusters, composed by cliques. Meaning that, possibly, the modules of synchronized activity observed might be formed by the overlap of highly dense patterns, such as cliques, instead of having loosely connected groups of brain regions. In fact, several studies have indicated that the brain networks can also be overlapping, that is to some extent brain regions may belong to several modules [141–143]. To verify this, a further analysis would be necessary, for instance by applying a clique percolation method to extract these potentially overlapping communities for the fMRI functional networks and compare with the communities obtained in this work. Interestingly,

a recent study by Sizemore et al. [139] has characterized the structural connectome as being composed by large cliques, over-represented with respect to a wiring-minimization null model, that are organized so as to form cycles or holes that allow for distribution or integration of information throughout the whole brain. This suggests that this highly dense structure might be present as well for functional networks, still allowing for high-dimensional holes to guarantee the global efficiency of these networks [144]. Again, further work needs to be done to explore all these possibilities, but also to investigate the distribution of the motifs retrieved in this analysis over the brain space.

On the other hand for the EEG, the local structure seems to deviate positively from the spatial embedding, appearing slightly more densely connected for some time points and even presenting unexpected motifs for the lower frequency bands. Also, these findings were found to be more prevalent for higher size subgraphs. One of the most relevant frequency bands deviating from this spatial null model is the delta band, for which motif 21 appears over-represented, more than any other pattern. This further points out for the relevance of this motif in the topology captured by this frequency band. Apart from this, the delta band has the highest percentage of time points deviating from this null model, for both 4- and 5-node subgraph analysis. This is in accordance with the assumption that lower frequency bands reflect synchronized oscillations between long-distance regions, thus capturing connections that are not expected by the spatial null model by definition [39]. Moreover, the alpha band captured an interesting structure as it includes both over- and under-represented motif, for a substantial portion of time points, unlike any other frequency band. Additionally, the gamma band also shows a high percentage of time points with over-representing motifs, which is in line with the assumption that this frequency band captures a more clustered structure and closer to the fMRI. Furthermore, these findings are in line with the null model's comparison performed in the community analysis chapter, for which these same three frequency bands showed a higher percentage of time points whose functional networks global topology deviated from the spatial null model, particularly the delta band, as found here. Besides this, it is important to mention that, contrary to what was found with respect to the rewiring null model, this densely connected structure does not increase with frequency. Instead, it is observed a high heterogeneity between frequency bands, each capturing a different topology deviating from the spatial constraints.

Summarizing, on a local point of view, the fMRI functional networks show a more densely connected structure by avoiding many subgraphs allowed by the spatial null model (with a negative z-score) and, in opposition, the EEG captures a more clustered topology by giving a higher preference to denser patterns than expected by chance (with a positive z-score). Nevertheless, it is important to notice that EEG leads to sparser networks than the fMRI, as reported in the global topology analysis in chapter 4. As such, the spatial null model will be different between the two functional networks, since it combines both the proximity constraints and the degree distribution, and therefore should not be seen as a common baseline for the two modalities. Besides this, the EEG functional networks show a rich repertoire of over-represented motifs, while for the fMRI there is a low variety of under-represented ones. That makes sense since a large set of motifs is desired to facilitate the efficiency of brain communication and processing [14]. Due to the clear differences between the two modalities, even further evidenced with this analysis, the correlation between their local structure deviating from the spatial null model was

reduced, with only a few time points revealing some level of similarity. With the exception of the alpha band, that still showed a relevant similarity with the fMRI motif profile for subgraphs of size 5, consistently over time. Interestingly, these findings are in opposed to the ones reported for the community analysis, the beta and gamma bands showed a higher similarity with fMRI's global topology

Therefore, from this motif analysis, it is possible to conclude that each modality captures a different information regarding the dynamic functional connectivity on a local perspective, with most of this structure being explained by the spatial constraints, especially for the fMRI network. However, some additional topology and similarity between the two modalities can still be found beyond the influence of space, particularly for the delta and alpha band.

Chapter 6

Conclusions

To our knowledge, this work consists in the first study to perform a comparative network analysis with fMRI and EEG functional connectivity data, both on a macro- and meso-scale, by means of a community and a motif analysis, respectively. For that, several established approaches were used, such as the Louvain algorithm for the extraction of large groups of coordinated activity, as well as its multiplex version here applied to find partitions combining both modalities for the first time. Also the g-tries data structure was used to efficiently count occurrences of subgraphs in these functional networks, while determining if they are statistically significant. Furthermore, with hopes of exploring the influence of space in the global and local topology, it was also investigated the functional networks structure beyond these spatial constraints. With this objective, new approaches were applied, such as a modified version of the Louvain algorithm, that includes a degree constrained spatial null model in the modularity definition, but also a motif analysis where the subgraphs are statistically tested against this spatial null model as well.

Consequently, from the results obtained it was possible to draw several conclusions. First of all, the fMRI and EEG functional connectivity seem to capture different information on both global and local levels. On one hand, the fMRI networks appeared to have a more modular configuration, consistent over time, also being characterized by densely connected motifs, with the presence of many cliques and absence of sparser motifs. On the other hand, the EEG captures a less clustered topology, both on a macro- and meso-scale, with lower modularity and less densely connected subgraphs, with each frequency band capturing a slightly different structure oscillating across time. Moreover, when combining the two modalities, interesting and relevant communities were extracted, that would not be possible with each network individually.

Secondly, both functional networks' organization is mostly explained by the spatial influence, giving preference to close connections and densely connected local modules and also resulting in very low modularity values when regressing out this effect. However, the spatial constraints showed a different impact for each modality and it was still possible to retrieve some structure deviating from these expectations. For the fMRI, there was still a significant community structure for most time points, despite the low modularity value, and even though the densely connected local patterns were explained by the spatial null model, its local structure was found to be even more dense by avoiding loosely connected config-

urations, otherwise allowed by the spatial embedding. For the EEG it was different case, since only a small portion of time points retrieved a global and local topology deviating from the spatial null model. Nevertheless, interesting communities and densely connected patterns were still obtained beyond the proximity constraints, for the delta, alpha and gamma bands. Curiously, the delta band was the one selecting a higher percentage of time points deviating from this spatial null model, for either macro- or meso-scale analysis, which might be due to this signal capturing more long-distance synchronizations than the others. In addition, it is worth mentioning that this frequency band also showed an unexpected pattern, composed by cycles being over-expressed in comparison to other denser configurations, a pattern that is usually associated to information integration, suggesting that this band might capture more global interactions and less localized ones.

Finally, despite the differences between the fMRI and EEG functional networks, there is a correlation between the two modalities over time, which is mostly explained by the spatial embedding. Nonetheless, when investigating these networks structure beyond the influence of space, a small correlation was still retrieved for a small portion of time points. Interestingly, this correlation was not equivalent between the two perspectives: while the beta and gamma band were found to capture a more similar global topology to the fMRI, these findings being in accordance with previous studies comparing fMRI and EEG dynamic connectomes, the alpha band seems to be the most correlated with the fMRI relatively to their local organization, especially when considering 5-node subgraphs.

From this work, it is possible to conclude then that, even though fMRI and EEG functional connectomes are slightly linked, the two modalities essentially capture different information, on a topological level. Therefore, combining the two modalities seems to be desirable to characterize the brain's complex activity and to distinguish different states and conditions, as those due to mental disorders. Furthermore, this work reinforces the importance of analyzing these functional networks choosing a null model that better mimics the brain networks organization, to retrieve the truly meaningful features arising from functional connectivity.

6.1 Limitations and Possible Solutions

The analysis performed in this work and the methodology employed entailed several limitations. First, relatively to the fMRI connectivity metric, even though the phase coherence allows for a higher temporal resolution in comparison to sliding window approaches, it has the downside of being more susceptible to noise fluctuations [35]. This is because synchronization might arise from random oscillations with small phase difference between them [145], leading to spurious connections that would otherwise be averaged out if considering the adjacent time points. Notably, this might occur even considering that the Hilbert transform already integrates the signal over time to estimate its phase at each time point. As such, these spurious synchronizations will most likely not be removed with thresholding due to their high connectivity value. Consequently, in order to improve this metric and to allow for more reliable quasi-instantaneous connectivity values, a statistical testing can be performed by generating a phase coherence null model, producing phase randomized BOLD time series surrogates that preserve the signal's amplitude [146].

Another limitation of this work lies on the source reconstruction of the underlying signals detected by the EEG channels. As mentioned before, there is no inverse method that is fully satisfactory, so there is an inherent spatial resolution limitation associated to the EEG functional networks that might affect the results obtained from both community and motif analysis. The difficulty in estimating the EEG sources is enhanced in resting-state data, in which no large amplitude changes occur, hence leading to reduced SNR. Moreover, even though it was used a metric designed to be relatively insensitive to volume conduction effects, these may still be contaminating the EEG functional connectivity measures. Unfortunately, there is no approach to overcome this limitation completely. Nonetheless, there is evidence that supports the possibility of using denser EEG systems to recover more information and improve the reconstruction of the underlying sources [132]. Indeed for this work it was used a 64-channel system, but there are even denser systems available with 128 or even 256 electrodes. However, it is important to mention that if the problem associated to the EEG functional networks' results is the noise associated with the acquisition of these signals, the use of more electrodes will not increase the spatial resolution significantly [147].

For simplicity, it was chosen to use an atlas parcellation based on the brain structure for both fMRI and EEG data. Nevertheless, this type of approach comes with some disadvantages as it does not necessarily respect the functional boundaries when defining the nodes of these networks [65], which might compromise the analysis. As an alternative, data-driven approaches, such as independent component analysis (ICA), could be used to define functionally homogeneous nodes. However, this would lead to different sets of nodes between the fMRI and EEG functional networks, no longer having an equivalent spatial mapping between the two modalities. Another option would be to test several different parcellations with higher number of nodes, to verify the results obtained and take more advantage of the significant spatial resolution that the fMRI can offer.

An additional limitation regarding the definition of the functional networks is the threshold used. Even though it consists in a desirable step to remove weaker links more susceptible to noise, it might also result in the loss of relevant synchronization. Besides this, the binarization of these networks also means that the strength of the connectivity obtained between the different brain regions is no longer taken into account, which will naturally limit the analysis. Furthermore, it is important to mention that, although the same criterion was used to select the threshold for both fMRI and EEG networks, a different proportion of the edges to be kept was obtained for each case. This resulted in sparser networks for the EEG, possibly influencing the comparison between the two modalities, namely regarding the network fingerprint comparison in the motif analysis for which an equivalent edge density is desirable [15]. In addition, this comparison could also be compromised by the estimation of the hemodynamic response delay, necessary for a correct temporal alignment between the two modalities. In order to overcome this, it would be necessary to perform a deconvolution of the fMRI signal, which is also potentially fallible.

Regarding the community detection, in this work it was only performed one iteration for the extraction of the communities of each functional network. However, there is generally a large number of alternative partitions possible with modularity values that only differ slightly from the selected one [66]. In fact, the Louvain algorithm consists in a greedy optimization method, for which there is no clear maximum

modularity. As such, to increase the reliability of the communities found, a consensus partition could be obtained in order to identify communities that are robust to the intrinsic degeneracy of this algorithm.

Besides this, considering that the fMRI functional networks appeared to be highly clustered, being composed with densely connected local patterns and avoiding motifs that would allow for a bridge between different modules, it was suggested that these networks' topology was composed by a superposition of cliques. That brings the question whether it is adequate to assume non-overlapping communities and to use modularity maximization methods that look for groups of coordinated activity with few edges connecting each other, in particular for the fMRI functional networks. In fact, some studies have proposed that brain functional networks are indeed highly overlapping, due to a continuous shift in internal states and cognitive processing [148], having applied different methods to retrieve these patterns of correlated activity [143, 149, 150]. Therefore, it would be prudent to search the global structure of these networks for overlapping communities, possibly even using a clique percolation method, considering the high presence of cliques in these functional networks, mostly for the fMRI.

Finally, for both macro- and meso-scale analysis, there is a lack of functional meaning associated with the patterns extracted, which would be necessary to make sense out of the characterization of functional connectivity with the complex networks approach done in this work. To fill the gap between these topological results and the underlying physiological meaning, it would be necessary to analyse which concrete brain regions are involved in each community and possibly if these communities can be compared with the resting-state networks already reported in the literature. Also, an enumeration of the motifs found for these functional networks could be performed, in order to observe their distribution in the brain space. Moreover, a motif fingerprint could be obtained for each brain region to find which motifs are associated the most with each region and possibly understand their function in the whole network [14].

6.2 Future Work

The present work introduces several new approaches for the analysis and comparison between fMRI and EEG functional networks. Being so, before any future development, it is essential to verify these findings with different datasets, community detection algorithms or even with distinct spatial null models. Even so, there are several possible approaches to explore even further the dynamic functional connectivity (dFC) captured with the two modalities.

Community Analysis Combining both fMRI and EEG functional networks led to different and relevant partitions and the spatial embedding was shown to have a strong effect in these networks topology. Therefore, it would be interesting to extend the modified Louvain algorithm to a multilayer approach, in order to analyze the common communities captured beyond the proximity expectations. Also, to avoid a static perspective of each time point and to better track the dFC transitions between different states throughout time, a temporal analysis could be done for this dataset, using a multilayer network for each modality independently [79, 151]. In fact, the present work speculated about the possibility of

having a flexible change of the communities present over time, which could be further investigated with such an approach. Moreover, this temporal outlook could even be extended to combine fMRI and EEG information over time as well, by adding an additional dimension to the currently available multilayer algorithms [152]. Besides this, since each frequency band was shown to correlate differently with the fMRI, possibly reflecting different aspects of neuronal activity, it could be worth exploring the global topology captured when combining them all in a multilayer network.

Motif Analysis Equivalently to the community analysis, the motifs present in these functional networks could also be analysed using a temporal multilayer network [85]. With this type of approach, it would be possible to obtain a time-series for each motif class and thus have a clearer picture of its temporal evolution. Another alternative to further explore motifs and their transitions over time in these networks would be by means of temporal and topological network fingerprints, known as graphlet-orbit transitions recently proposed approach in [153]. These network fingerprints provide information about how these graphlets (small, induced subgraphs, without comparison with null model) vary but also about how the role of the nodes included in those subgraphs changes with time (orbit transitions), which could lead to new findings regarding dFC's local organization. Besides this, it could be interesting to investigate motifs that occur for both fMRI and EEG functional networks, taking advantage of their different information regarding the local structure, similarly to what was performed in [154] with respect to structural and functional information.

Finally, the work done in this thesis allows for the identification of features characterizing the functional networks, that could eventually be used in the classification of networks into different families [86] and, thus, in the prediction of distinct brain states. This could be done, for instance, through the comparison of resting-state activity between healthy individuals and mental disorders patients, using both the community structure [155] and the motif profiles [91] extracted from the functional networks, to distinguish their topology and, in the future, possibly, to train a model for early-diagnosis.

Bibliography

[1] M. P. van den Heuvel and H. E. Hulshoff Pol. Exploring the brain network: A review on resting-state fMRI functional connectivity. *European Neuropsychopharmacology*, 20(8):519–534, 2010. ISSN 0924977X. doi: 10.1016/j.euroneuro.2010.03.008. URL http://dx.doi.org/10.1016/j.euroneuro.2010.03.008.

[2] E. A. Allen, E. Damaraju, S. M. Plis, E. B. Erhardt, T. Eichele, and V. D. Calhoun. Tracking whole-brain connectivity dynamics in the resting state. *Cerebral Cortex*, 24(3):663–676, 2014. ISSN 10473211. doi: 10.1093/cercor/bhs352.

[3] R. Abreu, A. Leal, and P. Figueiredo. Identification of epileptic brain states by dynamic functional connectivity analysis of simultaneous EEG-fMRI: a dictionary learning approach. *Scientific Reports*, 9(1):1–18, 2019. ISSN 20452322. doi: 10.1038/s41598-018-36976-y.

[4] E. Bullmore and O. Sporns. Complex brain networks: Graph theoretical analysis of structural and functional systems. *Nature Reviews Neuroscience*, 10(3):186–198, 2009. ISSN 1471003X. doi: 10.1038/nrn2575.

[5] M. G. Preti, T. A. Bolton, and D. Van De Ville. The dynamic functional connectome: State-of-the-art and perspectives. *NeuroImage*, 160(December 2016):41–54, 2017. ISSN 10959572. doi: 10.1016/j.neuroimage.2016.12.061.

[6] R. B. Buxton. *Introduction to Functional Magnetic Resonance Imaging: Principles and Techniques*. Cambridge University Press, 2 edition, 2009. doi: 10.1017/CBO9780511605505.

[7] F. Lopes da Silva. *EEG: Origin and measurement*, pages 19–38. 01 2010. ISBN 978-3-540-87918-3. doi: 10.1007/978-3-540-87919-0_2.

[8] G. Mele, C. Cavaliere, V. Alfano, M. Orsini, M. Salvatore, and M. Aiello. Simultaneous EEG-fMRI for functional neurological assessment. *Frontiers in Neurology*, 10(JUL), 2019. ISSN 16642295. doi: 10.3389/fneur.2019.00848.

[9] Q. Yu, L. Wu, D. A. Bridwell, E. B. Erhardt, Y. Du, H. He, J. Chen, P. Liu, J. Sui, G. Pearlson, and V. D. Calhoun. Building an EEG-fMRI multi-modal brain graph: A concurrent EEG-fMRI study. *Frontiers in Human Neuroscience*, 10(SEP2016):1–17, 2016. ISSN 16625161. doi: 10.3389/fnhum.2016.00476.

[10] L. Bréchet, D. Brunet, G. Birot, R. Gruetter, C. M. Michel, and J. Jorge. Capturing the spatiotemporal dynamics of self-generated, task-initiated thoughts with EEG and fMRI. *NeuroImage*, 2019. ISSN 10959572. doi: 10.1016/j.neuroimage.2019.03.029.

[11] D. T. Jones, P. Vemuri, M. C. Murphy, J. L. Gunter, M. L. Senjem, M. M. Machulda, S. A. Przybelski, B. E. Gregg, K. Kantarci, D. S. Knopman, B. F. Boeve, R. C. Petersen, and C. R. Jack. Non-stationarity in the ”resting brain’s” modular architecture. *PLoS ONE*, 2012. ISSN 19326203. doi: 10.1371/journal.pone.0039731.

[12] R. F. Betzel, M. Fukushima, Y. He, X. N. Zuo, and O. Sporns. Dynamic fluctuations coincide with periods of high and low modularity in resting-state functional brain networks. *NeuroImage*, 2016. ISSN 10959572. doi: 10.1016/j.neuroimage.2015.12.001.

[13] M. Fukushima and O. Sporns. Comparison of fluctuations in global network topology of modeled and empirical brain functional connectivity. *PLoS Computational Biology*, 2018. ISSN 15537358. doi: 10.1371/journal.pcbi.1006497.

[14] O. Sporns and R. Kötter. Motifs in Brain Networks. *PLoS Biology*, 2004. ISSN 15449173. doi: 10.1371/journal.pbio.0020369.

[15] S. E. Morgan, S. Achard, M. Termenon, E. T. Bullmore, and P. E. Vértes. Low-dimensional morphospace of topological motifs in human fMRI brain networks. *Network Neuroscience*, 2018. ISSN 24721751. doi: 10.1162/netn_a_00038.

[16] V. D. Blondel, J. L. Guillaume, R. Lambiotte, and E. Lefebvre. Fast unfolding of communities in large networks. *Journal of Statistical Mechanics: Theory and Experiment*, 2008. ISSN 17425468. doi: 10.1088/1742-5468/2008/10/P10008.

[17] P. J. Mucha, T. Richardson, K. Macon, M. A. Porter, and J. P. Onnela. Community structure in time-dependent, multiscale, and multiplex networks. *Science*, 2010. ISSN 00368075. doi: 10.1126/science.1184819.

[18] P. Ribeiro. *Efficient and scalable algorithms for network motifs discovery*. PhD thesis, Faculdade Ciências da Universidade do Porto, Porto, Portugal, 2011.

[19] J. A. Roberts, A. Perry, A. R. Lord, G. Roberts, P. B. Mitchell, R. E. Smith, F. Calamante, and M. Breakspear. The contribution of geometry to the human connectome. *NeuroImage*, 2016. ISSN 10959572. doi: 10.1016/j.neuroimage.2015.09.009.

[20] D. Samu, A. K. Seth, and T. Nowotny. Influence of Wiring Cost on the Large-Scale Architecture of Human Cortical Connectivity. *PLoS Computational Biology*, 2014. ISSN 15537358. doi: 10.1371/journal.pcbi.1003557.

[21] F. Zamani Esfahlani, M. A. Bertolero, D. S. Bassett, and R. F. Betzel. Space-independent community and hub structure of functional brain networks. *NeuroImage*, 2020. ISSN 10959572. doi: 10.1016/j.neuroimage.2020.116612.

[22] R. Cazabet, P. Borgnat, and P. Jensen. Enhancing space-aware community detection using degree constrained spatial null model. In *Springer Proceedings in Complexity*. 2017. doi: 10.1007/978-3-319-54241-6_4.

[23] J. S. Lewin. Functional MRI: An introduction to methods. *Journal of Magnetic Resonance Imaging*, 17(3):383–383, 2003. ISSN 1053-1807. doi: 10.1002/jmri.10284.

[24] . John R.Giudicessi, BA.Michael J.Ackerman. Assessing Functional Connectivity in the Human Brain by FMRI. *Bone*, 23(1):1–7, 2008. ISSN 15378276. doi: 10.1038/jid.2014.371. URL `https://www.ncbi.nlm.nih.gov/pmc/articles/PMC3624763/pdf/nihms412728.pdf`.

[25] a. S. Huettel, A. W. Song, G. McCarthy, S. A. Huettel, A. W. Song, G. McCarthy, a. S. Huettel, A. W. Song, G. McCarthy, S. A. Huettel, A. W. Song, and G. McCarthy. *Functional Magnetic Resonance Imaging, Second Edition*. 2004.

[26] N. K. Logothetis and B. A. Wandell. Interpreting the BOLD Signal. *Annual Review of Physiology*, 66(1):735–769, 2004. ISSN 0066-4278. doi: 10.1146/annurev.physiol.66.082602.092845.

[27] R. A. Poldrack, T. Nichols, and J. Mumford. *Handbook of Functional MRI Data Analysis*. 2011. ISBN 9780521517669. doi: 10.1017/cbo9780511895029.

[28] D. Rangaprakash, R. Tadayonnejad, G. Deshpande, J. O'Neill, and J. D. Feusner. FMRI hemodynamic response function (HRF) as a novel marker of brain function: applications for understanding obsessive-compulsive disorder pathology and treatment response. *Brain Imaging and Behavior*, 2020. ISSN 19317565. doi: 10.1007/s11682-020-00358-8.

[29] J. M. Soares, R. Magalhães, P. S. Moreira, A. Sousa, E. Ganz, A. Sampaio, V. Alves, P. Marques, and N. Sousa. A Hitchhiker's guide to functional magnetic resonance imaging. *Frontiers in Neuroscience*, 10(November):1–35, 2016. ISSN 1662453X. doi: 10.3389/fnins.2016.00515.

[30] G. H. Glover and C. Chang. Time–frequency dynamics of resting-state brain connectivity measured with fMRI, 2010. URL `https://www.sciencedirect.com/science/article/pii/S1053811909012981{%}0Ahttp://www.sciencedirect.com/science/article/pii/S1053811909012981`.

[31] V. Kiviniemi, T. Vire, J. Remes, A. A. Elseoud, T. Starck, O. Tervonen, and J. Nikkinen. A Sliding Time-Window ICA Reveals Spatial Variability of the Default Mode Network in Time. *Brain Connectivity*, 1(4):339–347, 2011. ISSN 21580022. doi: 10.1089/brain.2011.0036.

[32] E. Glerean, J. Salmi, J. M. Lahnakoski, I. P. Jääskeläinen, and M. Sams. Functional Magnetic Resonance Imaging Phase Synchronization as a Measure of Dynamic Functional Connectivity. *Brain Connectivity*, 2(2):91–101, 2012. ISSN 21580022. doi: 10.1089/brain.2011.0068.

[33] A. Laird, J. Carew, and M. E. Meyerand. Analysis of the instantaneous phase signal of a FMRI time series via the Hilbert transform, 2001. ISSN 10586393.

[34] E. Bedrosian. A product theorem for Hilbert transforms, 1962. ISSN 00189219. URL http://ieeexplore.ieee.org/lpdocs/epic03/wrapper.htm?arnumber=1457763.

[35] J. Cabral, D. Vidaurre, P. Marques, R. Magalhães, P. Silva Moreira, J. Miguel Soares, G. Deco, N. Sousa, and M. L. Kringelbach. Cognitive performance in healthy older adults relates to spontaneous switching between states of functional connectivity during rest. *Scientific Reports*, 7(1), 2017. ISSN 20452322. doi: 10.1038/s41598-017-05425-7.

[36] G. XUE, C. CHEN, Z.-L. LU, and Q. DONG. Brain Imaging Techniques and Their Applications in Decision-Making Research. *Acta Psychologica Sinica*, 42(1):120–137, 2010. ISSN 0439-755X. doi: 10.3724/sp.j.1041.2010.00120.

[37] P. Olejniczak. Neurophysiologic Basis of EEG EEG DEFINITION What is EEG? *J Clin Neurophysiol*, 23(3):186–189, 2006. URL http://norwalk.braincoretherapy.com/wp-content/uploads/2014/01/Neurophysiologic-Basis-of-EEG.pdf.

[38] M. Teplan. Fundamentals of EEG measurement. *Measurement science review*, 2(2):1–11, 2002.

[39] F. Lopes da Silva. EEG and MEG: Relevance to neuroscience, 2013. ISSN 08966273.

[40] A. M. Bastos and J. M. Schoffelen. A tutorial review of functional connectivity analysis methods and their interpretational pitfalls. *Frontiers in Systems Neuroscience*, 9(JAN2016):1–23, 2016. ISSN 16625137. doi: 10.3389/fnsys.2015.00175.

[41] G. Nolte, O. Bai, L. Wheaton, Z. Mari, S. Vorbach, and M. Hallett. Identifying true brain interaction from EEG data using the imaginary part of coherency. *Clinical Neurophysiology*, 115(10):2292–2307, 2004. ISSN 13882457. doi: 10.1016/j.clinph.2004.04.029.

[42] M. Hassan and F. Wendling. Electroencephalography Source Connectivity: Aiming for High Resolution of Brain Networks in Time and Space. *IEEE Signal Processing Magazine*, 35(3):81–96, 2018. ISSN 10535888. doi: 10.1109/MSP.2017.2777518.

[43] J. P. Lachaux, A. Lutz, D. Rudrauf, D. Cosmelli, M. Le Van Quyen, J. Martinerie, and F. Varela. Estimating the time-course of coherence between single-trial brain signals: An introduction to wavelet coherence, 2002. ISSN 09877053.

[44] K. Mahjoory, V. V. Nikulin, L. Botrel, K. Linkenkaer-Hansen, M. M. Fato, and S. Haufe. Consistency of EEG source localization and connectivity estimates. *NeuroImage*, 152(March):590–601, 2017. ISSN 10959572. doi: 10.1016/j.neuroimage.2017.02.076. URL http://dx.doi.org/10.1016/j.neuroimage.2017.02.076.

[45] R. Plonsey and D. B. Heppner. Considerations of quasi-stationarity in electrophysiological systems, 1967. ISSN 00074985.

[46] A. Kabbara, W. El Falou, M. Khalil, F. Wendling, and M. Hassan. The dynamic functional core network of the human brain at rest. *Scientific reports*, 7(1):2936, 2017. ISSN 20452322. doi: 10.1038/s41598-017-03420-6.

[47] M. Lai, M. Demuru, A. Hillebrand, and M. Fraschini. A comparison between scalp- and source-reconstructed EEG networks. *Scientific Reports*, 8(1):1–8, 2018. ISSN 20452322. doi: 10.1038/s41598-018-30869-w. URL http://dx.doi.org/10.1038/s41598-018-30869-w.

[48] R. Abreu, A. Leal, and P. Figueiredo. EEG-informed fMRI: A review of data analysis methods. *Frontiers in Human Neuroscience*, 12(February):1–23, 2018. ISSN 16625161. doi: 10.3389/fnhum.2018.00029.

[49] J. Jorge, W. Van der Zwaag, and P. Figueiredo. EEG-fMRI integration for the study of human brain function. *NeuroImage*, 102(P1):24–34, 2014. ISSN 10959572. doi: 10.1016/j.neuroimage.2013.05.114.

[50] M. J. Rosa, J. Daunizeau, and K. J. Friston. EEG-fMRI integration: A critical review of biophysical modeling and data analysis approaches. *Journal of Integrative Neuroscience*, 9(4):453–476, 2010. ISSN 02196352. doi: 10.1142/S0219635210002512.

[51] R. Grave De Peralta Menendez, M. M. Murray, C. M. Michel, R. Martuzzi, and S. L. Gonzalez Andino. Electrical neuroimaging based on biophysical constraints. *NeuroImage*, 21(2):527–539, 2004. ISSN 10538119. doi: 10.1016/j.neuroimage.2003.09.051.

[52] R. Grech, T. Cassar, J. Muscat, K. P. Camilleri, S. G. Fabri, M. Zervakis, P. Xanthopoulos, V. Sakkalis, and B. Vanrumste. Review on solving the inverse problem in EEG source analysis. *Journal of NeuroEngineering and Rehabilitation*, 5:1–33, 2008. ISSN 17430003. doi: 10.1186/1743-0003-5-25.

[53] M. Hassan, O. Dufor, I. Merlet, C. Berrou, and F. Wendling. EEG source connectivity analysis: From dense array recordings to brain networks. *PLoS ONE*, 9(8), 2014. ISSN 19326203. doi: 10.1371/journal.pone.0105041.

[54] R. M. Leahy, J. C. Mosher, and J. W. Phillips. A Comparative Study of Minimum Norm Inverse Methods for MEG Imaging. In *Biomag 96*. 2000. doi: 10.1007/978-1-4612-1260-7_66.

[55] M. Seeber, L. M. Cantonas, M. Hoevels, T. Sesia, V. Visser-Vandewalle, and C. M. Michel. Subcortical electrophysiological activity is detectable with high-density EEG source imaging. *Nature Communications*, 10(1):1–7, 2019. ISSN 20411723. doi: 10.1038/s41467-019-08725-w. URL http://dx.doi.org/10.1038/s41467-019-08725-w.

[56] E. A. Allen, E. Damaraju, T. Eichele, L. Wu, and V. D. Calhoun. EEG Signatures of Dynamic Functional Network Connectivity States. *Brain Topography*, 2018. ISSN 15736792. doi: 10.1007/s10548-017-0546-2.

[57] J. Wirsich, A. L. Giraud, and S. Sadaghiani. Concurrent EEG- and fMRI-derived functional connectomes exhibit linked dynamics, 2018.

[58] J. Wirsich, E. Amico, A. L. Giraud, J. Goñi, and S. Sadaghiani. Multi-timescale hybrid components of the functional brain connectome: A bimodal EEG-fMRI decomposition, 2019. ISSN 2472-1751.

[59] G. Fraga González, D. J. Smit, M. J. van der Molen, J. Tijms, C. J. Stam, E. J. de Geus, and M. W. van der Molen. EEG Resting State Functional Connectivity in Adult Dyslexics Using Phase Lag Index and Graph Analysis. *Frontiers in Human Neuroscience*, 12(August):1–12, 2018. ISSN 16625161. doi: 10.3389/fnhum.2018.00341.

[60] N. Tzourio-Mazoyer, B. Landeau, D. Papathanassiou, F. Crivello, O. Etard, N. Delcroix, B. Mazoyer, and M. Joliot. Automated anatomical labeling of activations in SPM using a macroscopic anatomical parcellation of the MNI MRI single-subject brain. *NeuroImage*, 15(1):273–289, 2002. ISSN 10538119. doi: 10.1006/nimg.2001.0978.

[61] R. S. Desikan, F. Ségonne, B. Fischl, B. T. Quinn, B. C. Dickerson, D. Blacker, R. L. Buckner, A. M. Dale, R. P. Maguire, B. T. Hyman, M. S. Albert, and R. J. Killiany. An automated labeling system for subdividing the human cerebral cortex on MRI scans into gyral based regions of interest. *NeuroImage*, 2006. ISSN 10538119. doi: 10.1016/j.neuroimage.2006.01.021.

[62] S. Hayasaka and P. J. Laurienti. Comparison of characteristics between region-and voxel-based network analyses in resting-state fMRI data. *NeuroImage*, 2010. ISSN 10538119. doi: 10.1016/j.neuroimage.2009.12.051.

[63] S. Micheloyannis. Graph-based network analysis in schizophrenia. *World Journal of Psychiatry*, 2012. ISSN 2220-3206. doi: 10.5498/wjp.v2.i1.1.

[64] A. L. Barabási and R. Albert. Emergence of scaling in random networks, 2011.

[65] Q. Yu, Y. Du, J. Chen, J. Sui, T. Adali, G. D. Pearlson, and V. D. Calhoun. Application of Graph Theory to Assess Static and Dynamic Brain Connectivity: Approaches for Building Brain Graphs. *Proceedings of the IEEE*, 106(5):886–906, 2018. ISSN 00189219. doi: 10.1109/JPROC.2018.2825200.

[66] E. T. Bullmore. *Fundamentals of Brain Network Analysis Andrew Zalesky*. 2016. ISBN 9780124079083.

[67] M. E. Newman. Modularity and community structure in networks. *Proceedings of the National Academy of Sciences of the United States of America*, 2006. ISSN 00278424. doi: 10.1073/pnas.0601602103.

[68] S. Maslov and K. Sneppen. Specificity and stability in topology of protein networks. *Science*, 2002. ISSN 00368075. doi: 10.1126/science.1065103.

[69] M. Sarzynska, E. A. Leicht, G. Chowell, and M. A. Porter. Null models for community detection in spatially embedded, temporal networks. *Journal of Complex Networks*, 2016. ISSN 20511329. doi: 10.1093/comnet/cnv027.

[70] D. S. Bassett and J. Stiso. Spatial brain networks. *Comptes Rendus Physique*, 19(4):253–264, May 2018. doi: 10.1016/j.crhy.2018.09.006.

[71] P. Expert, T. S. Evans, V. D. Blondel, and R. Lambiotte. Uncovering space-independent communities in spatial networks. *Proceedings of the National Academy of Sciences of the United States of America*, 2011. ISSN 00278424. doi: 10.1073/pnas.1018962108.

[72] C. Andrade. The P value and statistical significance: Misunderstandings, explanations, challenges, and alternatives, 2019. ISSN 09751564.

[73] A.-L. Barabási et al. *Network science*. Cambridge university press, 2016.

[74] S. Dimitriadis, N. Laskaris, V. Tsirka, M. Vourkas, and M. Sifis. An EEG Study of Brain Connectivity Dynamics at the Resting State. *Nonlinear dynamics, psychology, and life sciences*, 16:5–22, 01 2012.

[75] R. Liégeois, E. Ziegler, C. Phillips, P. Geurts, F. Gómez, M. A. Bahri, B. T. Yeo, A. Soddu, A. Vanhaudenhuyse, S. Laureys, and R. Sepulchre. Cerebral functional connectivity periodically (de)synchronizes with anatomical constraints. *Brain Structure and Function*, 2016. ISSN 18632661. doi: 10.1007/s00429-015-1083-y.

[76] M. Kaiser and C. C. Hilgetag. Nonoptimal component placement, but short processing paths, due to long-distance projections in neural systems. *PLoS Computational Biology*, 2006. ISSN 1553734X. doi: 10.1371/journal.pcbi.0020095.

[77] R. Matsuno and T. Murata. MELL: Effective Embedding Method for Multiplex Networks. In *The Web Conference 2018 - Companion of the World Wide Web Conference, WWW 2018*, 2018. ISBN 9781450356404. doi: 10.1145/3184558.3191565.

[78] D. S. Bassett, N. F. Wymbs, M. A. Porter, P. J. Mucha, J. M. Carlson, and S. T. Grafton. Dynamic reconfiguration of human brain networks during learning. *Proceedings of the National Academy of Sciences of the United States of America*, 108(18):7641–7646, 2011. ISSN 00278424. doi: 10.1073/pnas.1018985108.

[79] M. Pedersen, A. Zalesky, A. Omidvarnia, and G. D. Jackson. Multilayer network switching rate predicts brain performance. *Proceedings of the National Academy of Sciences of the United States of America*, 115(52):13376–13381, 2018. ISSN 10916490. doi: 10.1073/pnas.1814785115.

[80] M. Kivelä, A. Arenas, M. Barthelemy, J. P. Gleeson, Y. Moreno, and M. A. Porter. Multilayer networks. *Journal of Complex Networks*, 2(3):203–271, 2014. ISSN 20511329. doi: 10.1093/comnet/cnu016.

[81] J. J. Crofts, M. Forrester, and R. D. O'Dea. Structure-function clustering in multiplex brain networks. *EPL*, 2016. ISSN 12864854. doi: 10.1209/0295-5075/116/18003.

[82] S. Lim, F. Radicchi, M. P. van den Heuvel, and O. Sporns. Discordant attributes of structural and functional brain connectivity in a two-layer multiplex network. *Scientific Reports*, 2019. ISSN 20452322. doi: 10.1038/s41598-019-39243-w.

[83] R. F. Betzel, M. A. Bertolero, E. M. Gordon, C. Gratton, N. U. Dosenbach, and D. S. Bassett. The community structure of functional brain networks exhibits scale-specific patterns of inter- and intra-subject variability. *NeuroImage*, 2019. ISSN 10959572. doi: 10.1016/j.neuroimage.2019.07.003.

[84] A. C. Meira. Subgraph patterns in multiplex networks. Master's thesis, Faculdade Ciências da Universidade do Porto, Porto, Portugal, 2019.

[85] T. Nurmi et al. Construction and multilayer motif analysis of temporal fmri brain networks. Master's thesis, Aalto University, Aalto, Finland, 2019.

[86] D. O. Aparício. *Network Comparison and Node Ranking in Complex Networks*. PhD thesis, Faculdade Ciências da Universidade do Porto, Porto, Portugal, 2019.

[87] P. Ribeiro and F. Silva. G-Tries: A data structure for storing and finding subgraphs. *Data Mining and Knowledge Discovery*, 28(2):337–377, 2014. ISSN 13845810. doi: 10.1007/s10618-013-0303-4.

[88] P.-Z. Li, Y.-X. Cai, C.-D. Wang, M.-J. Liang, and Y.-Q. Zheng. Higher-order brain network analysis for auditory disease. *Neural Processing Letters*, 49:1–19, 06 2019. doi: 10.1007/s11063-018-9815-7.

[89] F. De Vico Fallani, L. Astolfi, F. Cincotti, D. Mattia, A. Tocci, S. Salinari, M. G. Marciani, H. Witte, A. Colosimo, and F. Babiloni. Brain network analysis from high-resolution EEG recordings by the application of theoretical graph indexes. *IEEE Transactions on Neural Systems and Rehabilitation Engineering*, 2008. ISSN 15344320. doi: 10.1109/TNSRE.2008.2006196.

[90] Y. Wei, X. Liao, C. Yan, Y. He, and M. Xia. Identifying topological motif patterns of human brain functional networks. *Human Brain Mapping*, 2017. ISSN 10970193. doi: 10.1002/hbm.23557.

[91] D. Nadin, C. Duclos, Y. Mahdid, A. Rokos, M. Badawy, J. Létourneau, C. Arbour, G. Plourde, and S. Blain-Moraes. Brain network motif topography may predict emergence from disorders of consciousness: a case series. *Neuroscience of Consciousness*, 2020. ISSN 2057-2107. doi: 10.1093/nc/niaa017.

[92] C. Bordier, C. Nicolini, and A. Bifone. Graph analysis and modularity of brain functional connectivity networks: Searching for the optimal threshold. *Frontiers in Neuroscience*, 2017. ISSN 1662453X. doi: 10.3389/fnins.2017.00441.

[93] J. Jorge, C. Bouloc, L. Bréchet, C. M. Michel, and R. Gruetter. Investigating the variability of cardiac pulse artifacts across heartbeats in simultaneous EEG-fMRI recordings: A 7T study. *NeuroImage*, 191(February):21–35, 2019. ISSN 10959572. doi: 10.1016/j.neuroimage.2019.02.021. URL `https://doi.org/10.1016/j.neuroimage.2019.02.021`.

[94] J. Wirsich, J. Jorge, G. R. Iannotti, E. A. Shamshiri, F. Grouiller, R. Abreu, F. Lazeyras, A.-L. Giraud, R. Gruetter, S. Sadaghiani, and S. Vulliémoz. EEG and fMRI connectomes are reliably related: a simultaneous EEG-fMRI study from 1.5T to 7T. *bioRxiv*, 2020. doi: 10.1101/2020.06.16.154625. URL `https://www.biorxiv.org/content/early/2020/06/17/2020.06.16.154625`.

[95] J. L. Andersson, S. Skare, and J. Ashburner. How to correct susceptibility distortions in spin-echo echo-planar images: Application to diffusion tensor imaging. *NeuroImage*, 2003. ISSN 10538119. doi: 10.1016/S1053-8119(03)00336-7.

[96] J. Jorge, F. Grouiller, Ö. Ipek, R. Stoermer, C. M. Michel, P. Figueiredo, W. Van Der Zwaag, and R. Gruetter. Simultaneous EEG-fMRI at ultra-high field: Artifact prevention and safety assessment, 2015. ISSN 10959572.

[97] B. B. Avants, N. J. Tustison, J. Wu, P. A. Cook, and J. C. Gee. An open source multivariate framework for N-tissue segmentation with evaluation on public data. *Neuroinformatics*, 9(4):381–400, 2011. ISSN 15392791. doi: 10.1007/s12021-011-9109-y.

[98] M. Jenkinson, P. Bannister, M. Brady, and S. Smith. Improved Optimization for the Robust and Accurate Linear Registration and Motion Correction of Brain Images. *NeuroImage*, 17(2):825–841, 2002. ISSN 10538119. doi: 10.1006/nimg.2002.1132.

[99] M. Jenkinson and S. Smith. A global optimisation method for robust affine registration of brain images. *Medical Image Analysis*, 5(2):143–156, 2001. ISSN 13618415. doi: 10.1016/S1361-8415(01)00036-6.

[100] J. D. Power, A. Mitra, T. O. Laumann, A. Z. Snyder, B. L. Schlaggar, and S. E. Petersen. Methods to detect, characterize, and remove motion artifact in resting state fMRI. *NeuroImage*, 2014. ISSN 10538119. doi: 10.1016/j.neuroimage.2013.08.048.

[101] J. D. Power, K. A. Barnes, A. Z. Snyder, B. L. Schlaggar, and S. E. Petersen. Spurious but systematic correlations in functional connectivity MRI networks arise from subject motion. *NeuroImage*, 2012. ISSN 10538119. doi: 10.1016/j.neuroimage.2011.10.018.

[102] T. S. Zarghami, G. A. Hossein-Zadeh, and F. Bahrami. Deep Temporal Organization of fMRI Phase Synchrony Modes Promotes Large-Scale Disconnection in Schizophrenia. *Frontiers in Neuroscience*, 2020. ISSN 1662453X. doi: 10.3389/fnins.2020.00214.

[103] M. Voss. *The Chronic Exercise–Cognition Interaction*, pages 187–209. 12 2016. ISBN 9780128007785. doi: 10.1016/B978-0-12-800778-5.00009-8.

[104] G. R. Wu, W. Liao, S. Stramaglia, J. R. Ding, H. Chen, and D. Marinazzo. A blind deconvolution approach to recover effective connectivity brain networks from resting state fMRI data. *Medical Image Analysis*, 2013. ISSN 13618415. doi: 10.1016/j.media.2013.01.003.

[105] G.-R. Wu and D. Marinazzo. Retrieving the Hemodynamic Response Function in resting state fMRI: methodology and applications. 2015. ISSN 2167-9843. doi: 10.7287/peerj.preprints.1317.

[106] M. A. Lindquist, J. Meng Loh, L. Y. Atlas, and T. D. Wager. Modeling the hemodynamic response function in fMRI: Efficiency, bias and mis-modeling. *NeuroImage*, 45(1, Supplement 1):S187 – S198, 2009. ISSN 1053-8119. doi: https://doi.org/10.1016/j.neuroimage.2008.10.065. URL `http://www.sciencedirect.com/science/article/pii/S1053811908012056`.

[107] R. N. Henson, C. J. Price, M. D. Rugg, R. Turner, and K. J. Friston. Detecting latency differences in event-related BOLD responses: Application to words versus nonwords and initial versus repeated face presentations. *NeuroImage*, 2002. ISSN 10538119. doi: 10.1006/nimg.2001.0940.

[108] J. Jorge, F. Grouiller, R. Gruetter, W. van der Zwaag, and P. Figueiredo. Towards high-quality simultaneous EEG-fMRI at 7 T: Detection and reduction of EEG artifacts due to head motion, 2015. ISSN 10959572.

[109] F. Tadel, S. Baillet, J. Mosher, D. Pantazis, and R. Leahy. Brainstorm: A user-friendly application for meg/eeg analysis. *Computational intelligence and neuroscience*, 2011:879716, 04 2011. doi: 10.1155/2011/879716.

[110] A. Gramfort, T. Papadopoulo, E. Olivi, and M. Clerc. OpenMEEG: Opensource software for quasistatic bioelectromagnetics. *BioMedical Engineering Online*, 2010. ISSN 1475925X. doi: 10.1186/1475-925X-9-45.

[111] J. Kybic, M. Clerc, T. Abboud, O. Faugeras, R. Keriven, and T. Papadopoulo. A common formalism for the integral formulations of the forward EEG problem. *IEEE Transactions on Medical Imaging*, 2005. ISSN 02780062. doi: 10.1109/TMI.2004.837363.

[112] S. Baillet, J. C. Mosher, and R. M. Leahy. Electromagnetic brain mapping. *IEEE Signal Processing Magazine*, 2001. ISSN 10535888. doi: 10.1109/79.962275.

[113] G. C. Carter. Coherence and time delay estimation. *Proceedings of the IEEE*, 1987. ISSN 15582256. doi: 10.1109/PROC.1987.13723.

[114] K. A. Garrison, D. Scheinost, E. S. Finn, X. Shen, and R. T. Constable. The (in)stability of functional brain network measures across thresholds. *NeuroImage*, 2015. ISSN 10959572. doi: 10.1016/j.neuroimage.2015.05.046.

[115] M. P. van den Heuvel, S. C. de Lange, A. Zalesky, C. Seguin, B. T. Yeo, and R. Schmidt. Proportional thresholding in resting-state fMRI functional connectivity networks and consequences for patient-control connectome studies: Issues and recommendations. *NeuroImage*, 2017. ISSN 10959572. doi: 10.1016/j.neuroimage.2017.02.005.

[116] G. Del Ferraro, A. Moreno, B. Min, F. Morone, Ú. Pérez-Ramírez, L. Pérez-Cervera, L. C. Parra, A. Holodny, S. Canals, and H. A. Makse. Finding influential nodes for integration in brain networks using optimal percolation theory. *Nature Communications*, 2018. ISSN 20411723. doi: 10.1038/s41467-018-04718-3.

[117] D. S. B. Everitt, S. Landau, M. Leese. *Cluster Analysis, 5th Edition*. 2011. ISBN 9780470749913.

[118] S. Ganger, A. Hahn, M. Küblböck, G. S. Kranz, M. Spies, T. Vanicek, R. Seiger, R. Sladky, C. Windischberger, S. Kasper, and R. Lanzenberger. Comparison of continuously acquired resting state and extracted analogues from active tasks. *Human Brain Mapping*, 2015. ISSN 10970193. doi: 10.1002/hbm.22897.

[119] F. Cignetti, E. Salvia, J. L. Anton, M. H. Grosbras, and C. Assaiante. Pros and cons of using the informed basis set to account for hemodynamic response variability with developmental data. *Frontiers in Neuroscience*, 2016. ISSN 1662453X. doi: 10.3389/fnins.2016.00322.

[120] L. D. Lewis, K. Setsompop, B. R. Rosen, and J. R. Polimeni. Fast fMRI can detect Oscillatory neural activity in humans. *Proceedings of the National Academy of Sciences of the United States of America*, 2016. ISSN 10916490. doi: 10.1073/pnas.1608117113.

[121] J. E. Chen and G. H. Glover. BOLD fractional contribution to resting-state functional connectivity above 0.1Hz. *NeuroImage*, 2015. ISSN 10959572. doi: 10.1016/j.neuroimage.2014.12.012.

[122] F. Deligianni, M. Centeno, D. W. Carmichael, and J. D. Clayden. Relating resting-state fMRI and EEG whole-brain connectomes across frequency bands. *Frontiers in Neuroscience*, 2014. ISSN 1662453X. doi: 10.3389/fnins.2014.00258.

[123] J. O. Garcia, A. Ashourvan, S. M. Thurman, R. Srinivasan, D. S. Bassett, and J. M. Vettel. Reconfigurations within resonating communities of brain regions following tms reveal different scales of processing. *Network Neuroscience*, 2020. ISSN 24721751. doi: 10.1162/netn_a_00139.

[124] A. Kurgansky. Functional organization of the human brain in the resting state. *Neuroscience and Behavioral Physiology*, 49, 11 2019. doi: 10.1007/s11055-019-00850-9.

[125] A. Kabbara, M. Khalil, G. O'neill, K. Dujardin, Y. El Traboulsi, F. Wendling, and M. Hassan. Detecting modular brain states in rest and task. *Network Neuroscience*, 2019. ISSN 24721751. doi: 10.1162/netn_a_00090.

[126] A. Joudaki, N. Salehi, M. Jalili, and M. G. Knyazeva. EEG-based functional brain networks: does the network size matter? *PloS one*, 2012. ISSN 19326203. doi: 10.1371/journal.pone.0035673.

[127] R. Abreu, J. Jorge, A. Leal, T. Koenig, and P. Figueiredo. EEG Microstates Predict Concurrent fMRI Dynamic Functional Connectivity States. *Brain Topography*, 2020. ISSN 15736792. doi: 10.1007/s10548-020-00805-1.

[128] R. F. Betzel, L. Byrge, F. Z. Esfahlani, and D. P. Kennedy. Temporal fluctuations in the brain's modular architecture during movie-watching. *NeuroImage*, 2020. ISSN 10959572. doi: 10.1016/j.neuroimage.2020.116687.

[129] A. Ashourvan, Q. K. Telesford, T. Verstynen, J. M. Vettel, and D. S. Bassett. Multi-scale detection of hierarchical community architecture in structural and functional brain networks. *PLoS ONE*, 2019. ISSN 19326203. doi: 10.1371/journal.pone.0215520.

[130] M. Petti, J. Toppi, F. Babiloni, F. Cincotti, D. Mattia, and L. Astolfi. EEG Resting-State Brain Topological Reorganization as a Function of Age. *Computational Intelligence and Neuroscience*, 2016. ISSN 16875273. doi: 10.1155/2016/6243694.

[131] M. G. Puxeddu, M. Petti, F. Pichiorri, F. Cincotti, D. Mattia, and L. Astolfi. Community detection: Comparison among clustering algorithms and application to EEG-based brain networks. In *Proceedings of the Annual International Conference of the IEEE Engineering in Medicine and Biology Society, EMBS*, 2017. ISBN 9781509028092. doi: 10.1109/EMBC.2017.8037724.

[132] A. K. Robinson, P. Venkatesh, M. J. Boring, M. J. Tarr, P. Grover, and M. Behrmann. Very high density EEG elucidates spatiotemporal aspects of early visual processing. *Scientific Reports*, 2017. ISSN 20452322. doi: 10.1038/s41598-017-16377-3.

[133] A. Custo, D. Van De Ville, W. M. Wells, M. I. Tomescu, D. Brunet, and C. M. Michel. Electroencephalographic Resting-State Networks: Source Localization of Microstates. *Brain Connectivity*, 2017. ISSN 21580022. doi: 10.1089/brain.2016.0476.

[134] J. Wirsich, B. Ridley, P. Besson, V. Jirsa, C. Bénar, J. P. Ranjeva, and M. Guye. Complementary contributions of concurrent EEG and fMRI connectivity for predicting structural connectivity. *NeuroImage*, 2017. ISSN 10959572. doi: 10.1016/j.neuroimage.2017.08.055.

[135] M. Nentwich, L. Ai, J. Madsen, Q. K. Telesford, S. Haufe, M. P. Milham, and L. C. Parra. Functional connectivity of EEG is subject-specific, associated with phenotype, and different from fMRI. *NeuroImage*, 2020. ISSN 10959572. doi: 10.1016/j.neuroimage.2020.117001.

[136] R. Scheeringa, P. Fries, K. M. Petersson, R. Oostenveld, I. Grothe, D. G. Norris, P. Hagoort, and M. C. Bastiaansen. Neuronal Dynamics Underlying High- and Low-Frequency EEG Oscillations Contribute Independently to the Human BOLD Signal. *Neuron*, 2011. ISSN 10974199. doi: 10.1016/j.neuron.2010.11.044.

[137] J. Cabral, M. L. Kringelbach, and G. Deco. Exploring the network dynamics underlying brain activity during rest, 2014. ISSN 18735118.

[138] P. Ribeiro, P. Paredes, M. E. Silva, D. Aparício, and F. Silva. A survey on subgraph counting: Concepts, algorithms and applications to network motifs and graphlets, 2019.

[139] A. E. Sizemore, C. Giusti, A. Kahn, J. M. Vettel, R. F. Betzel, and D. S. Bassett. Cliques and cavities in the human connectome. *Journal of Computational Neuroscience*, 2018. ISSN 15736873. doi: 10.1007/s10827-017-0672-6.

[140] L. L. Gollo and M. Breakspear. The frustrated brain: From dynamics on motifs to communities and networks. *Philosophical Transactions of the Royal Society B: Biological Sciences*, 2014. ISSN 14712970. doi: 10.1098/rstb.2013.0532.

[141] L. Pessoa. Understanding brain networks and brain organization, 2014. ISSN 15710645.

[142] B. T. Yeo, F. M. Krienen, M. W. Chee, and R. L. Buckner. Estimates of segregation and overlap of functional connectivity networks in the human cerebral cortex. *NeuroImage*, 2014. ISSN 10538119. doi: 10.1016/j.neuroimage.2013.10.046.

[143] M. Najafi, B. W. McMenamin, J. Z. Simon, and L. Pessoa. Overlapping communities reveal rich structure in large-scale brain networks during rest and task conditions. *NeuroImage*, 2016. ISSN 10959572. doi: 10.1016/j.neuroimage.2016.04.054.

[144] M. W. Reimann, M. Nolte, M. Scolamiero, K. Turner, R. Perin, G. Chindemi, P. Dłotko, R. Levi, K. Hess, and H. Markram. Cliques of neurons bound into cavities provide a missing link between structure and function. *Frontiers in Computational Neuroscience*, 2017. ISSN 16625188. doi: 10.3389/fncom.2017.00048.

[145] R. M. Hutchison, T. Womelsdorf, E. A. Allen, P. A. Bandettini, V. D. Calhoun, M. Corbetta, S. Della Penna, J. H. Duyn, G. H. Glover, J. Gonzalez-Castillo, D. A. Handwerker, S. Keilholz, V. Kiviniemi, D. A. Leopold, F. de Pasquale, O. Sporns, M. Walter, and C. Chang. Dynamic functional connectivity: Promise, issues, and interpretations. *NeuroImage*, 2013. ISSN 10538119. doi: 10.1016/j.neuroimage.2013.05.079.

[146] A. Ponce-Alvarez, G. Deco, P. Hagmann, G. L. Romani, D. Mantini, and M. Corbetta. Resting-State Temporal Synchronization Networks Emerge from Connectivity Topology and Heterogeneity. *PLoS Computational Biology*, 2015. ISSN 15537358. doi: 10.1371/journal.pcbi.1004100.

[147] O. R. Ryynänen, J. A. Hyttinen, P. H. Laarne, and J. A. Malmivuo. Effect of electrode density and measurement noise on the spatial resolution of cortical potential distribution. *IEEE Transactions on Biomedical Engineering*, 2004. ISSN 00189294. doi: 10.1109/TBME.2004.828036.

[148] M. L. Anderson, J. Kinnison, and L. Pessoa. Describing functional diversity of brain regions and brain networks. *NeuroImage*, 2013. ISSN 10538119. doi: 10.1016/j.neuroimage.2013.01.071.

[149] L. Pessoa. Beyond disjoint brain networks: Overlapping networks for cognition and emotion. *Behavioral and Brain Sciences*, 2016. ISSN 14691825. doi: 10.1017/S0140525X15001636.

[150] S. Mirzaei and H. Soltanian-Zadeh. Overlapping brain Community detection using Bayesian tensor decomposition. *Journal of Neuroscience Methods*, 2019. ISSN 1872678X. doi: 10.1016/j.jneumeth.2019.02.014.

[151] M. Vaiana and S. F. Muldoon. Multilayer Brain Networks. *Journal of Nonlinear Science*, pages 1–23, 2018. ISSN 14321467. doi: 10.1007/s00332-017-9436-8.

[152] S. F. Muldoon and D. S. Bassett. Network and multilayer network approaches to understanding human brain dynamics, 2016. ISSN 00318248.

[153] D. Aparício, P. Ribeiro, and F. Silva. Graphlet-orbit transitions (got): A fingerprint for temporal network comparison. *PLOS ONE*, 13:e0205497, 10 2018. doi: 10.1371/journal.pone.0205497.

[154] F. Battiston, V. Nicosia, M. Chavez, and V. Latora. Multilayer motif analysis of brain networks. *Chaos*, 2017. ISSN 10541500. doi: 10.1063/1.4979282.

[155] Y. Song, T. M. Epalle, and H. Lu. Characterizing and predicting autism spectrum disorder by performing resting-state functional network community pattern analysis. *Frontiers in Human Neuroscience*, 2019. ISSN 16625161. doi: 10.3389/fnhum.2019.00203.

Appendix A

Data Processing and Initial Analysis Results

The following figures summarize the results regarding the surrogate generation of the degree constrained spatial null model, the hemodynamic response delay values and the results for the connected components analysis.

A.1 Degree Constrained Spatial Null Model Definition

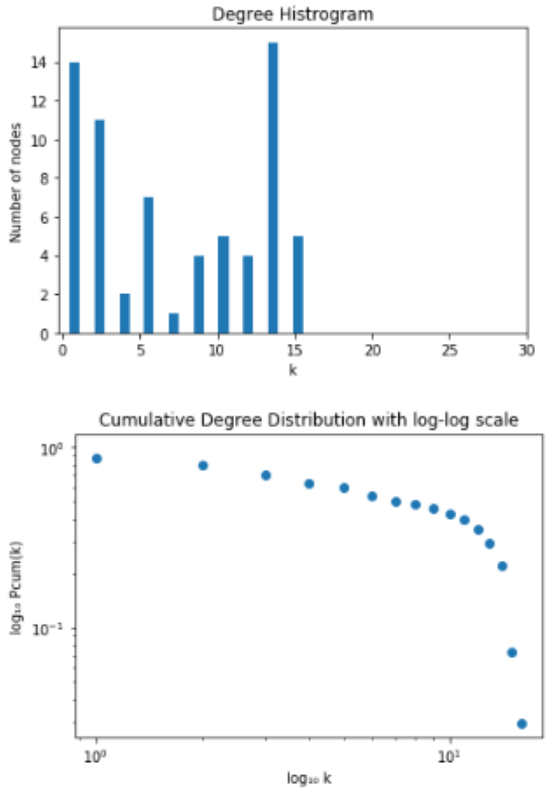

(a) fMRI functional network

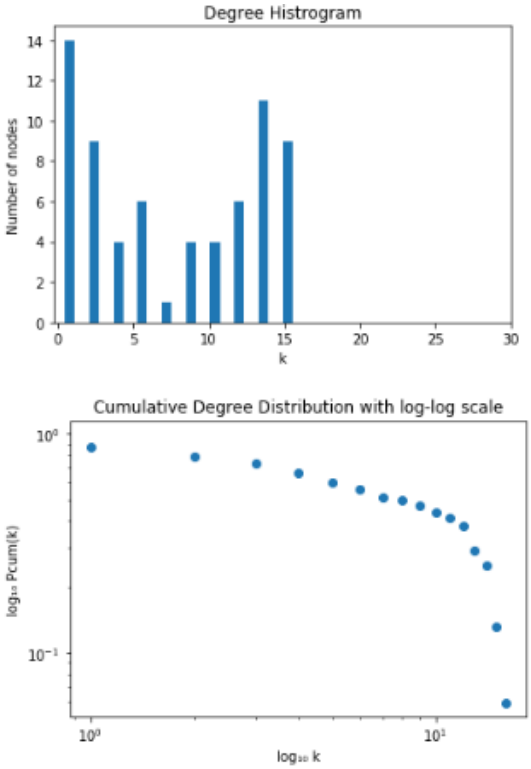

(b) fMRI spatial null model surrogate

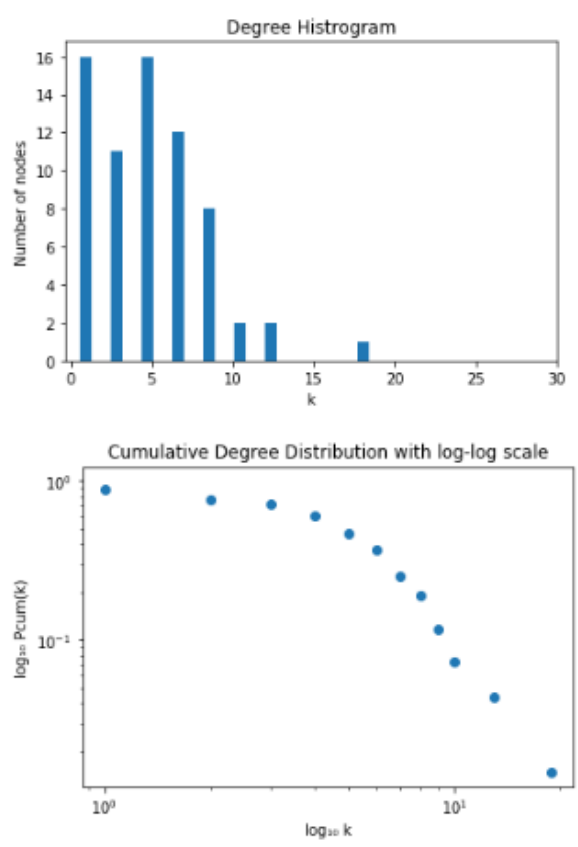

(c) EEG alpha band functional network

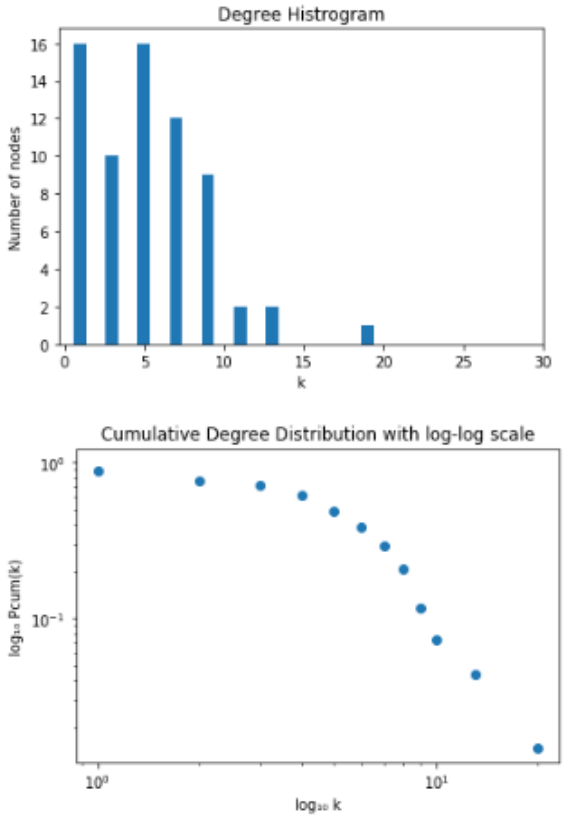

(d) EEG alpha band spatial null model surrogate

Figure A.1: Degree distribution and cumulative degree distribution for functional networks and one of its randomized spatial surrogates, for subject 1.

A.2 Hemodynamic Response Function (HRF) Time-to-peak Estimations

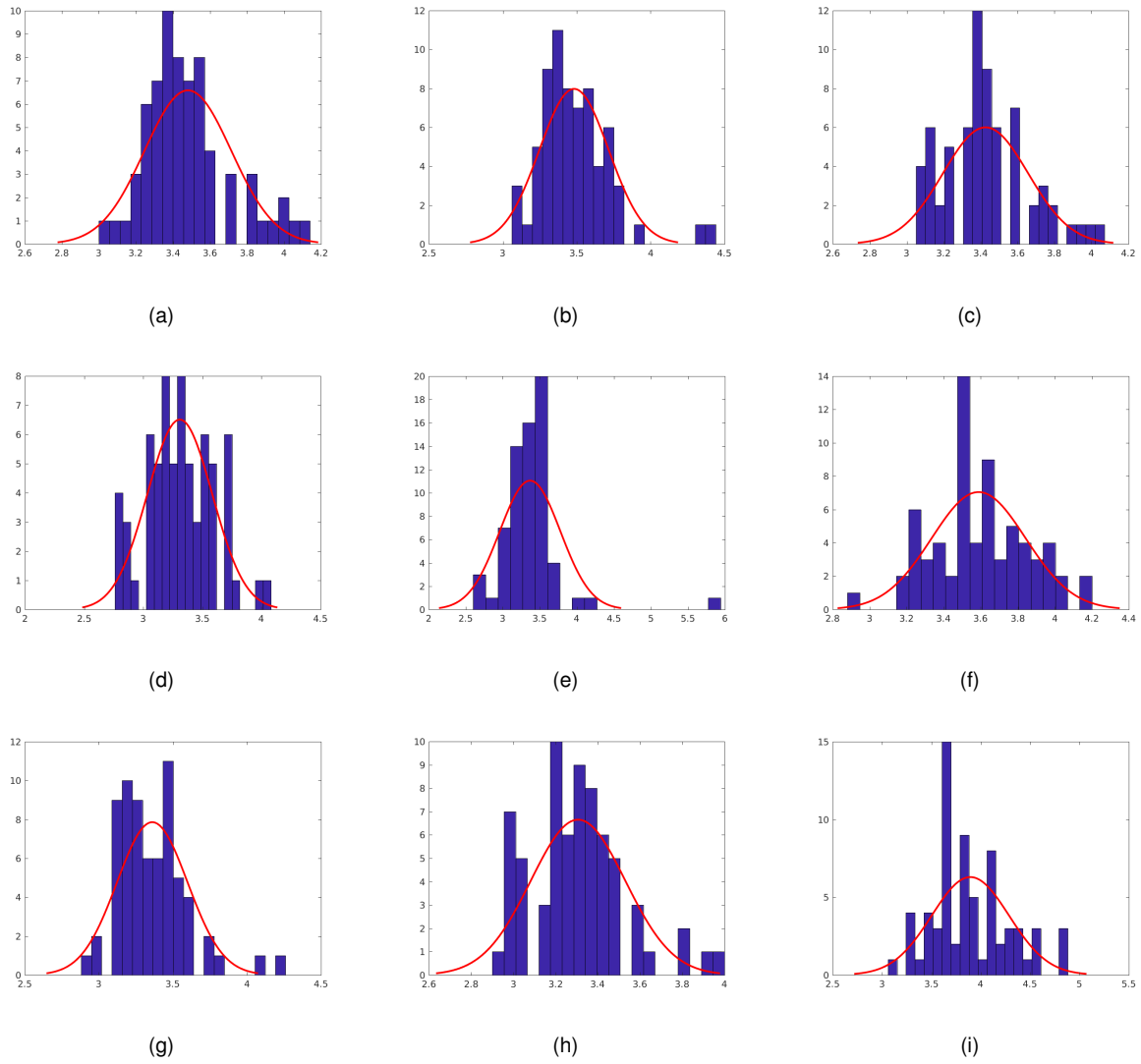

Figure A.2: Distribution of time-to-peak values over all brain regions, for all 9 subjects (a-i, for subject 1-9, respectively).

A.3 Connected Components Analysis

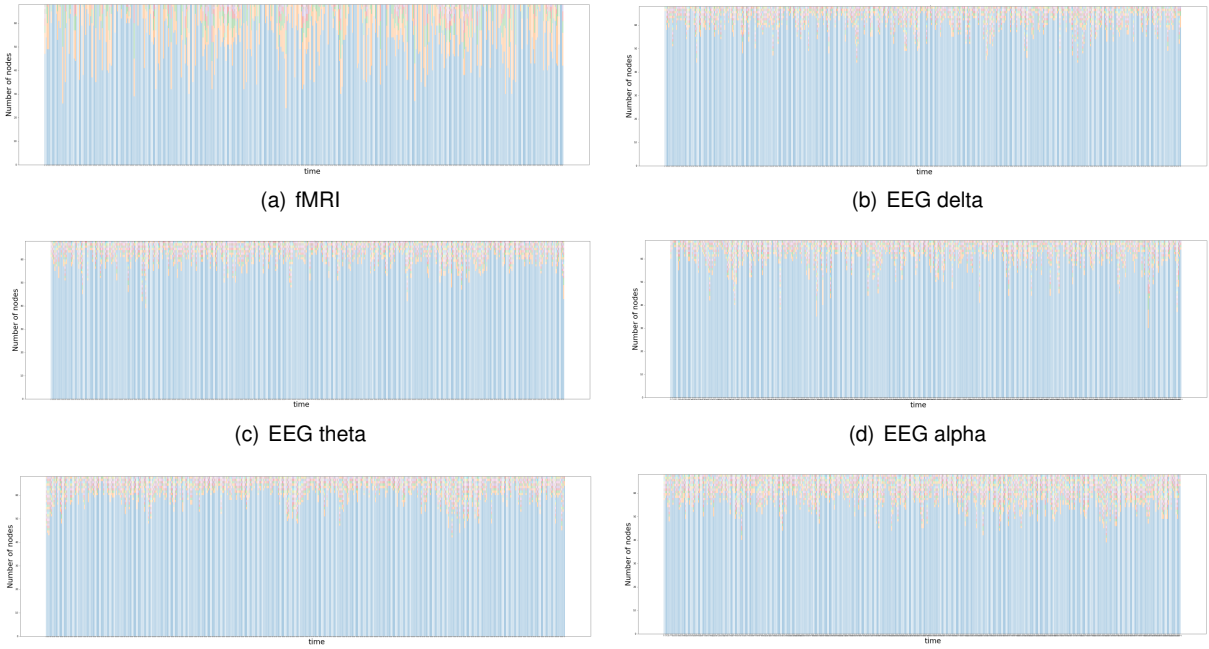

(a) fMRI (b) EEG delta

(c) EEG theta (d) EEG alpha

(e) EEG beta (f) EEG gamma

Figure A.3: Distribution of connected components' size over time, for fMRI and EEG frequency bands functional networks, for subject 7.

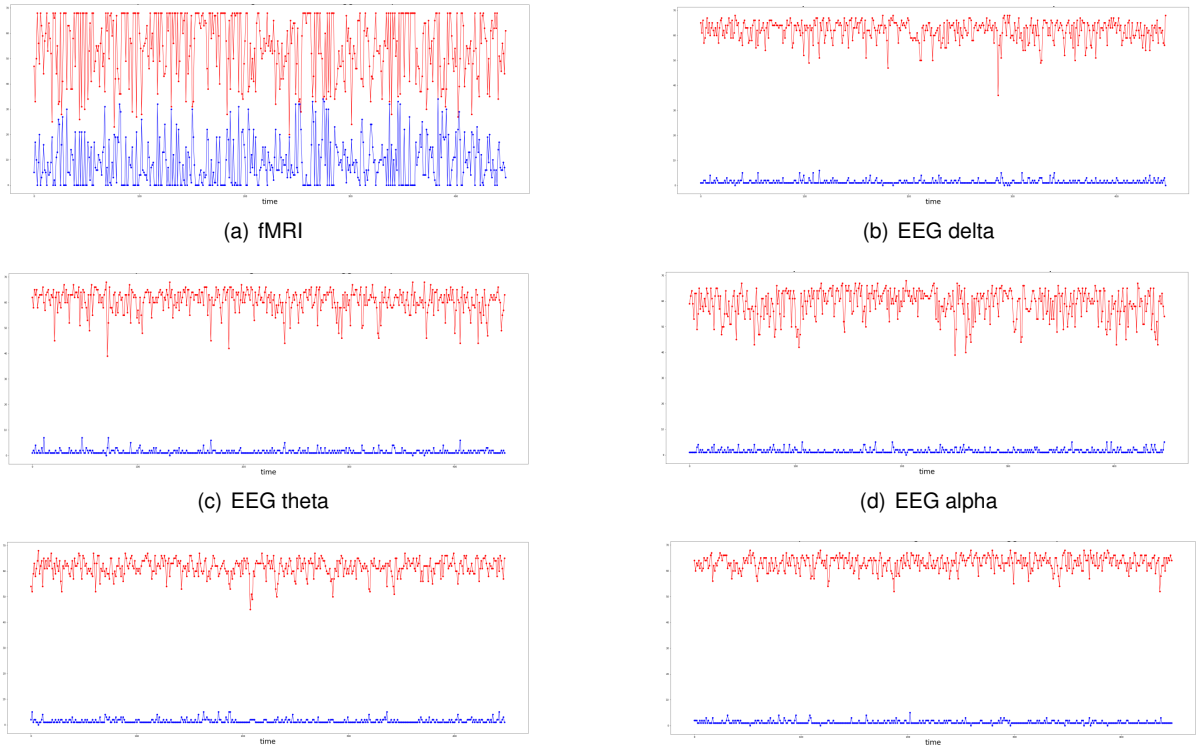

(a) fMRI (b) EEG delta

(c) EEG theta (d) EEG alpha

(e) EEG beta (f) EEG gamma

Figure A.4: Comparison between giant and second biggest component regarding their size over time, for fMRI and EEG frequency bands functional networks, for subject 2.

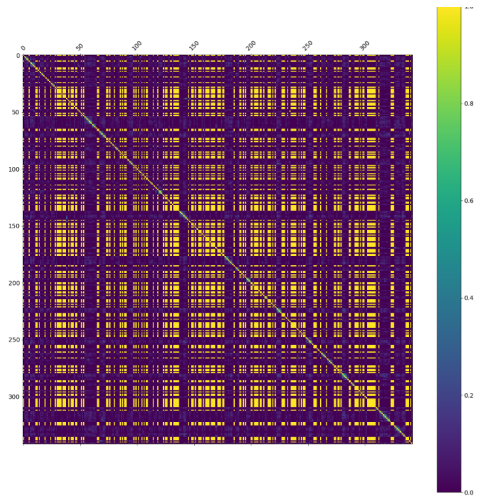

(a) fMRI

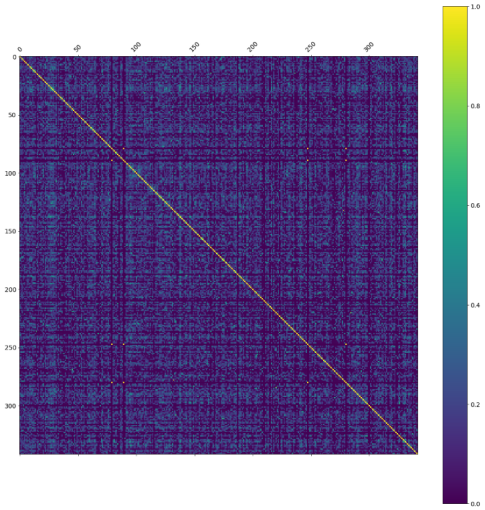

(b) EEG delta

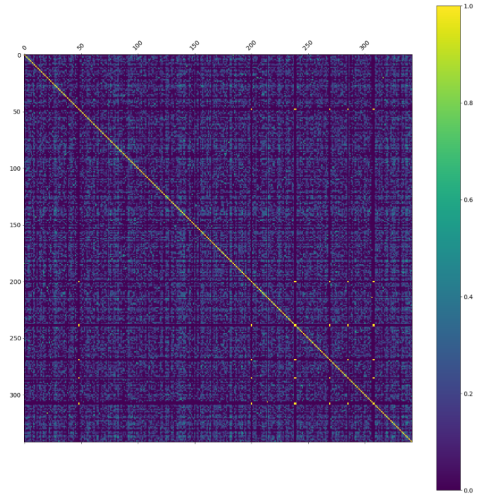

(c) EEG theta

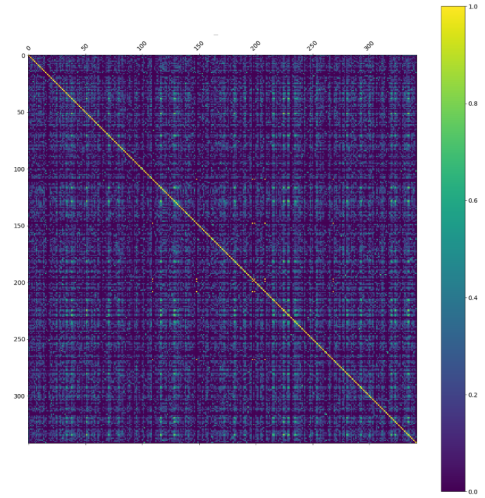

(d) EEG alpha

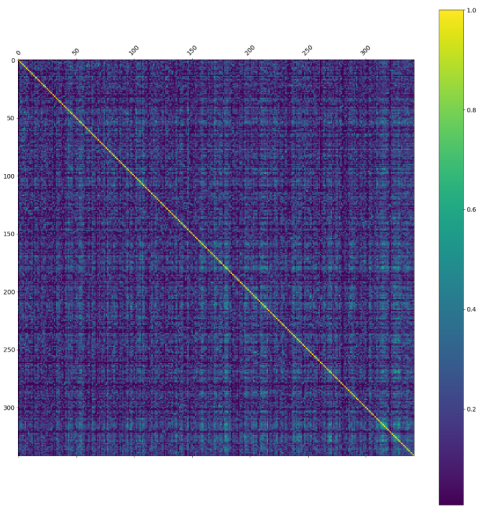

(e) EEG beta

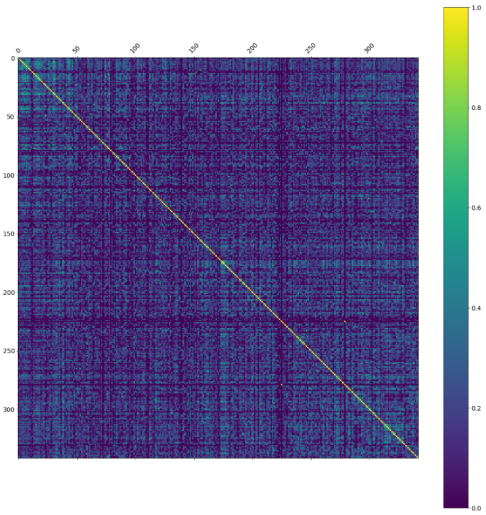

(f) EEG gamma

Figure A.5: Normalized Mutual Information (NMI) matrices regarding the temporal comparison of the connected components present in the functional networks after thresholding, for fMRI and EEG frequency bands, for subject 4.

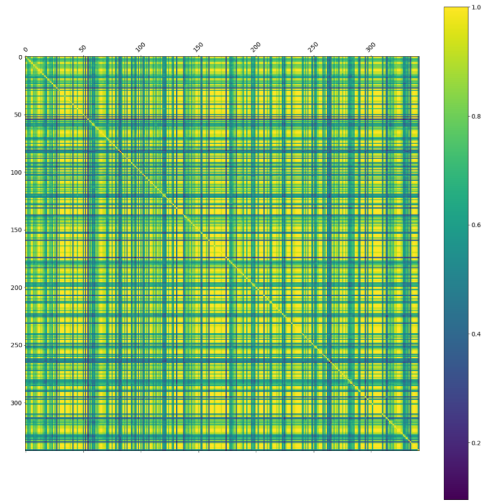

(a) fMRI

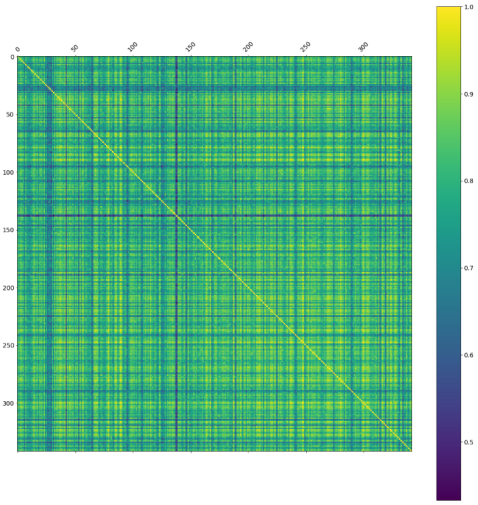

(b) EEG delta

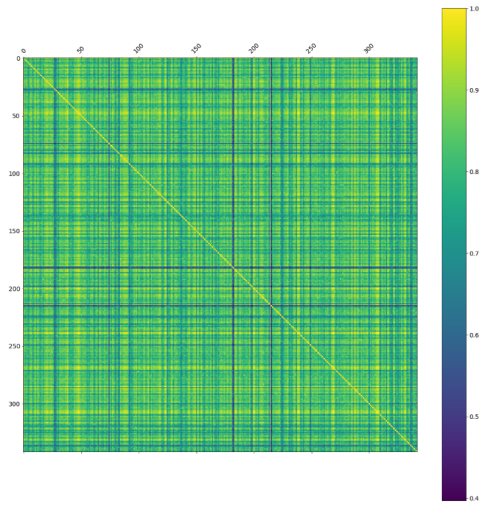

(c) EEG theta

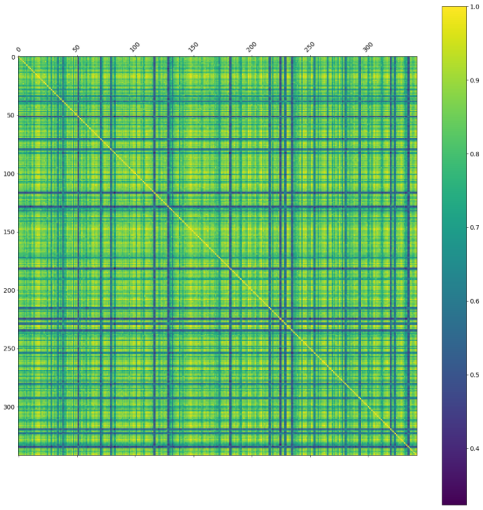

(d) EEG alpha

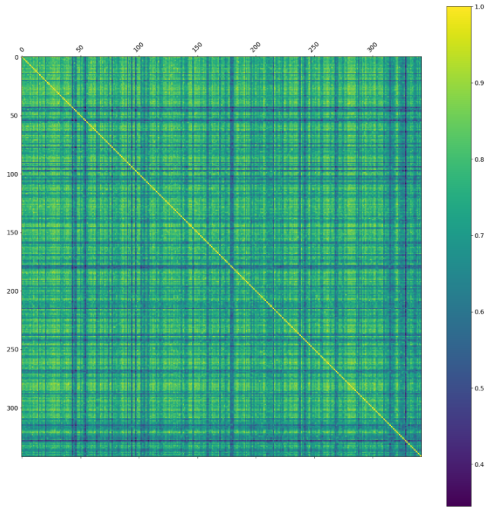

(e) EEG beta

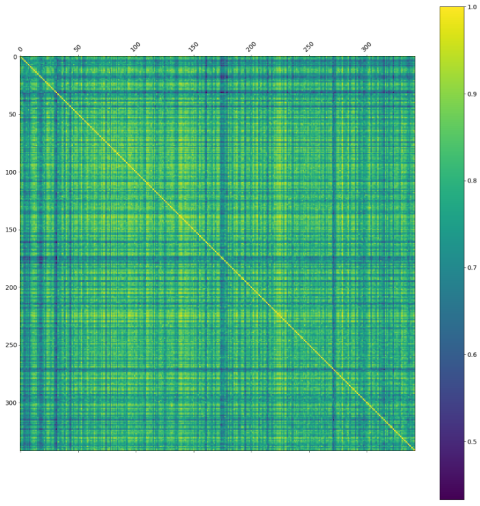

(f) EEG gamma

Figure A.6: Jaccard Index matrices regarding the temporal comparison of the giant component present in the functional networks after thresholding, for fMRI and EEG frequency bands, for subject 4.

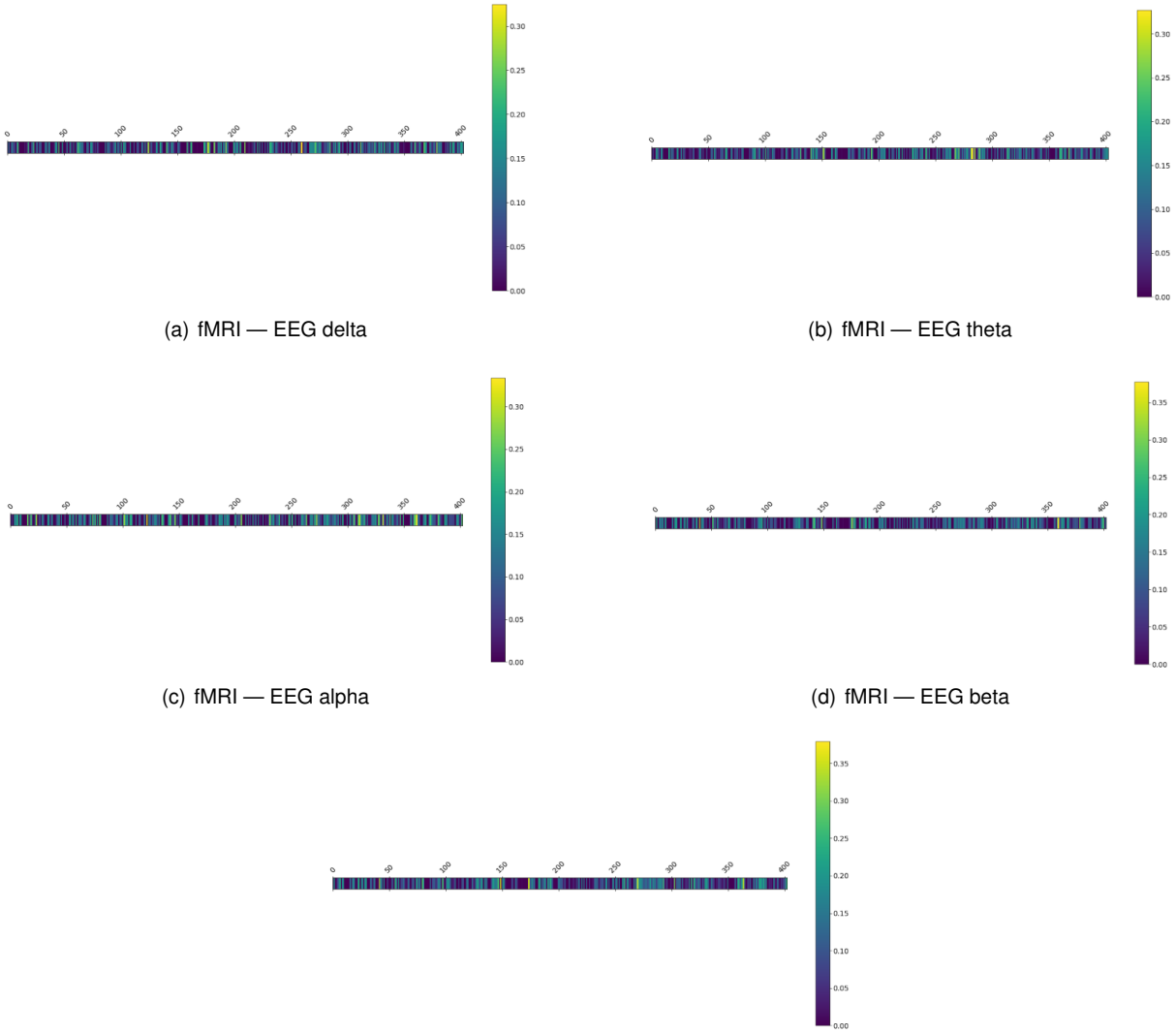

(a) fMRI — EEG delta

(b) fMRI — EEG theta

(c) fMRI — EEG alpha

(d) fMRI — EEG beta

(e) fMRI — EEG gamma

Figure A.7: NMI coloured arrays regarding the comparison of the connected components present in the functional networks after thresholding, between fMRI and EEG frequency bands, for subject 3.

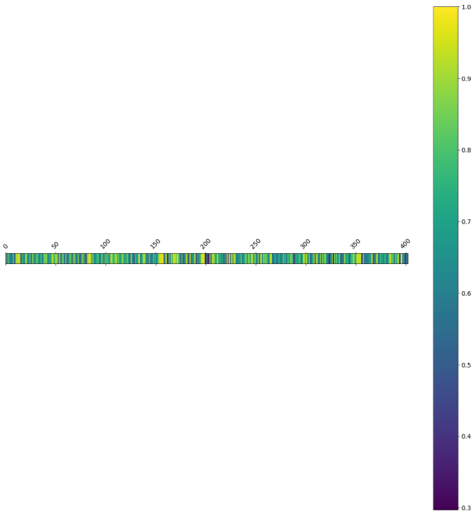

(a) fMRI — EEG delta

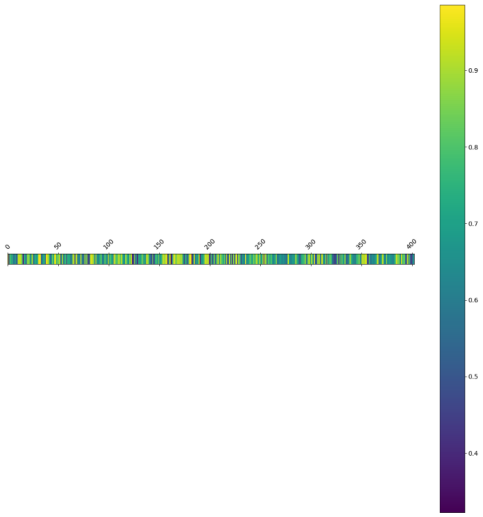

(b) fMRI — EEG theta

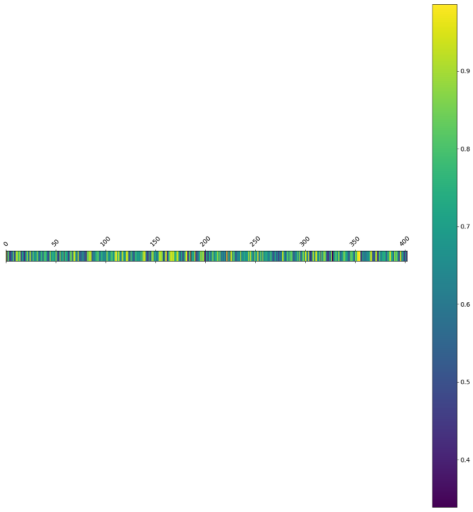

(c) fMRI — EEG alpha

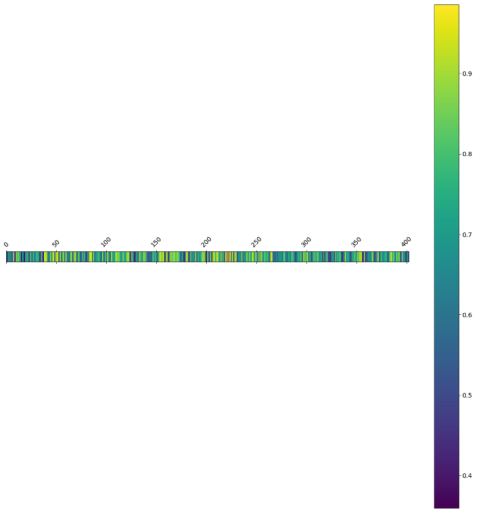

(d) fMRI — EEG beta

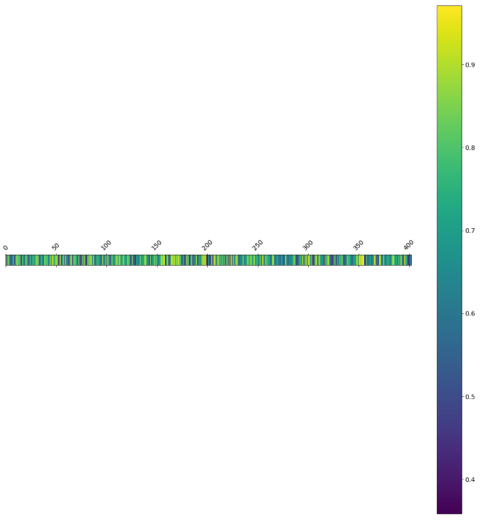

(e) fMRI — EEG gamma

Figure A.8: Jaccard Index coloured arrays regarding the comparison of the connected components present in the functional networks after thresholding, between fMRI and EEG frequency bands, for subject 3.

Appendix B

Community Analysis Results

The following figures and tables summarize the results regarding the community analysis, contemplating the comparison with the two null models, the similarity over time and between the two modalities.

B.1 Distribution of Metrics according to both Null Models

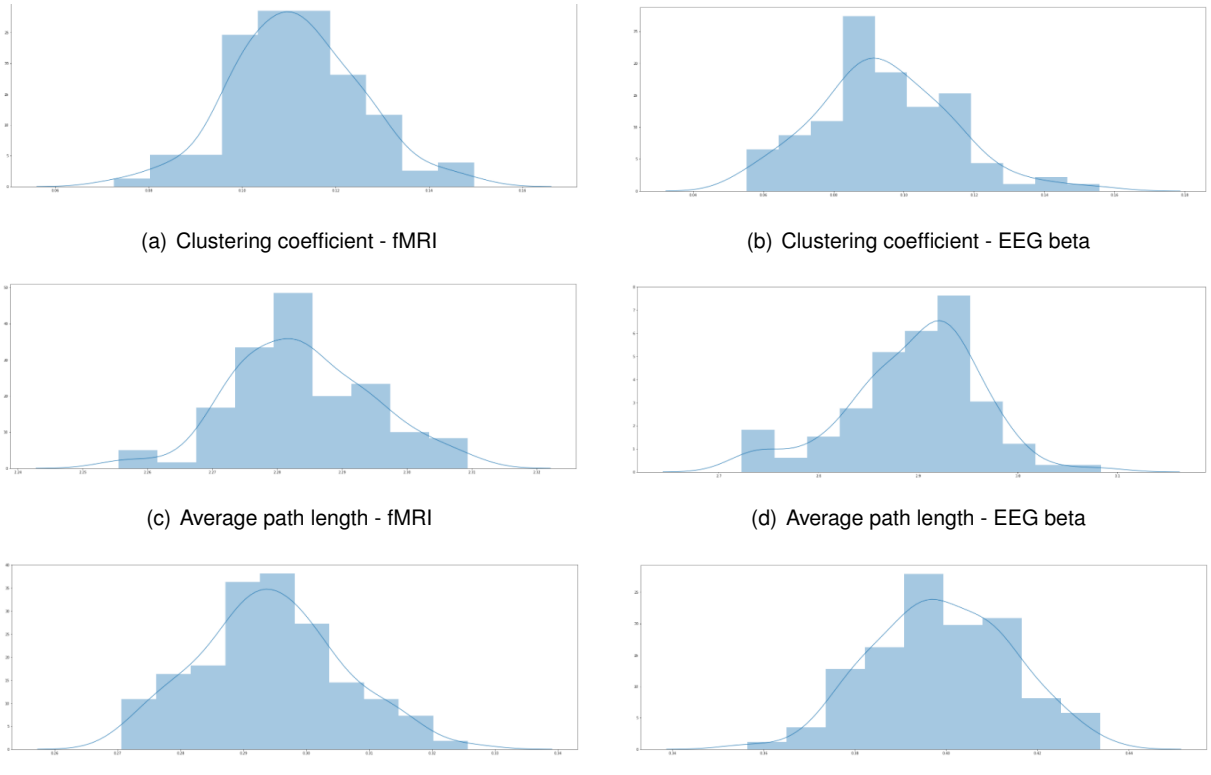

(a) Clustering coefficient - fMRI

(b) Clustering coefficient - EEG beta

(c) Average path length - fMRI

(d) Average path length - EEG beta

(e) Modularity - fMRI

(f) Modularity - EEG beta

Figure B.1: Distribution of clustering coefficient, average path length and modularity according to rewiring null model - fMRI and EEG beta band, for subject 1.

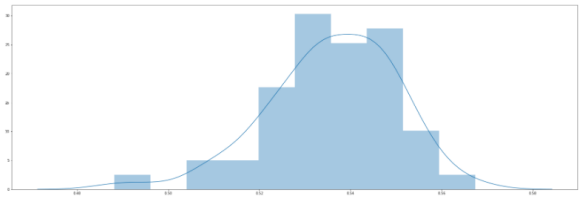

(a) Clustering coefficient - fMRI

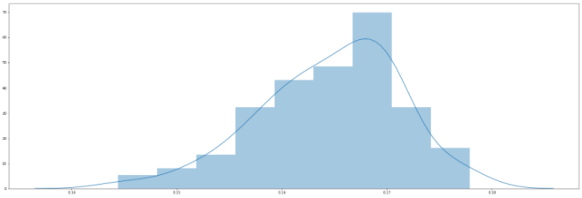

(b) Clustering coefficient - EEG theta

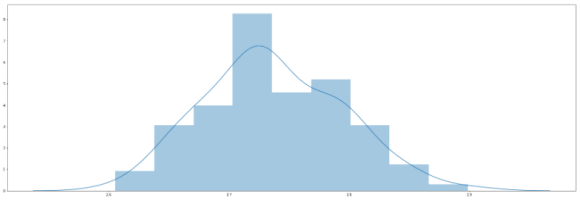

(c) Average path length - fMRI

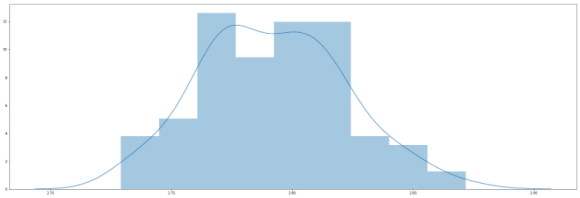

(d) Average path length - EEG theta

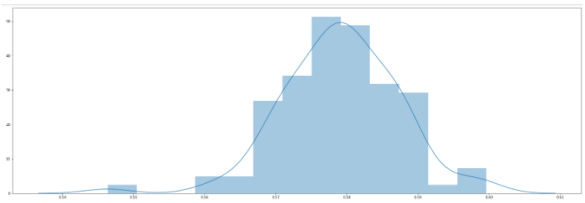

(e) Modularity - fMRI

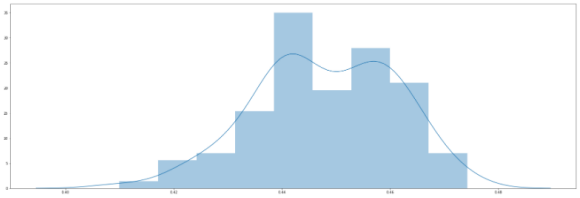

(f) Modularity - EEG theta

Figure B.2: Distribution of clustering coefficient, average path length and modularity according to degree constrained spatial null model - fMRI and EEG theta band, for subject 2.

B.2 Comparison of Metrics between Functional Networks and Null Models

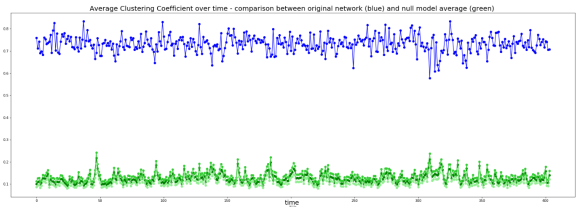

(a) Clustering coefficient - fMRI

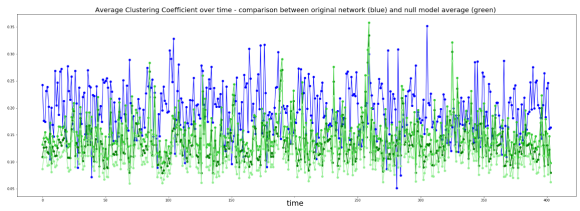

(b) Clustering coefficient - EEG delta

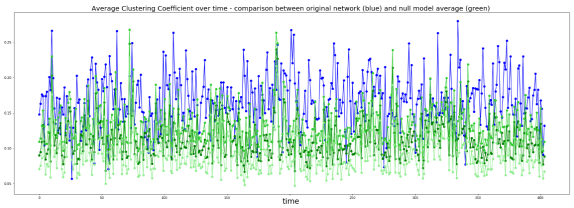

(c) Clustering coefficient - EEG theta

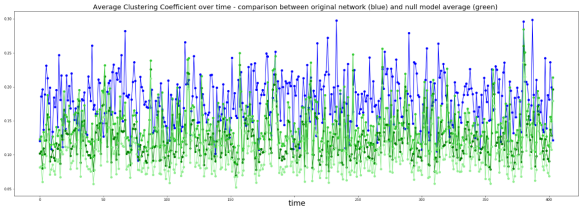

(d) Clustering coefficient - EEG alpha

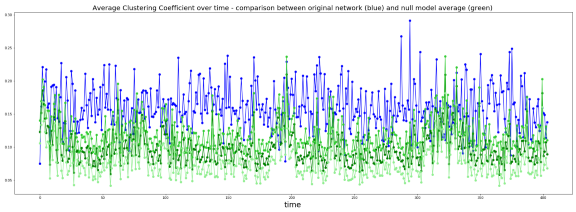

(e) Clustering coefficient - EEG beta

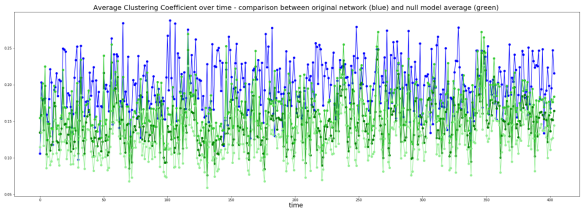

(f) Clustering coefficient - EEG gamma

Figure B.3: Variation over time of clustering coefficient for fMRI and EEG frequency bands, and corresponding rewiring null model, for subject 7.

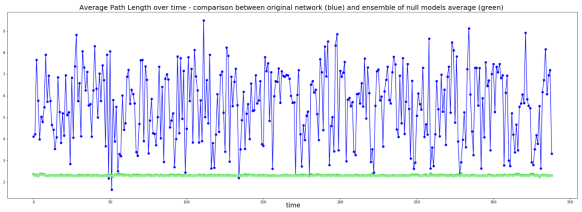

(a) Average path length - fMRI

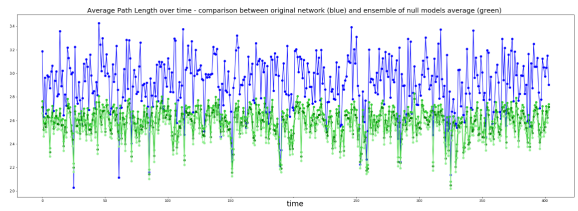

(b) Average path length - EEG delta

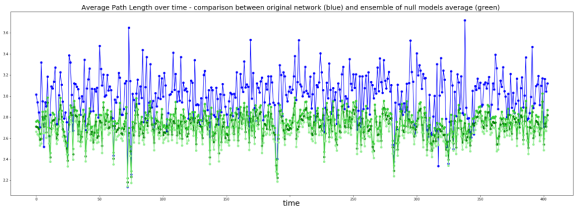

(c) Average path length - EEG theta

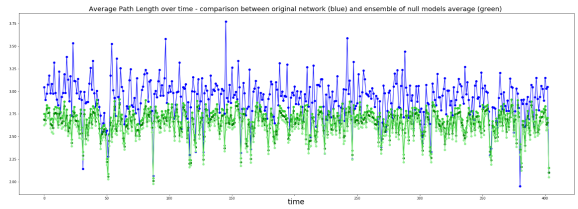

(d) Average path length - EEG alpha

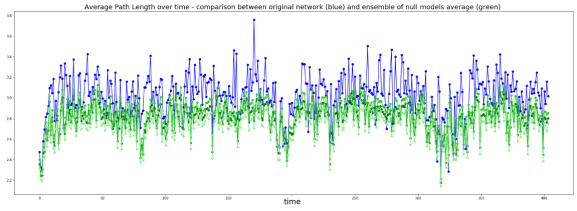

(e) Average path length - EEG beta

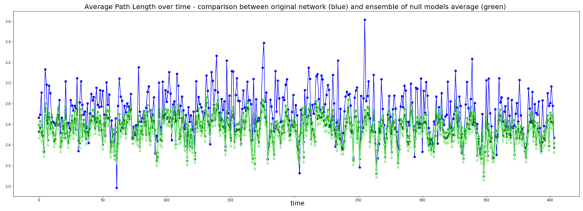

(f) Average path length - EEG gamma

Figure B.4: Variation over time of average path length for fMRI and EEG frequency bands, and corresponding rewiring null model, for subject 7.

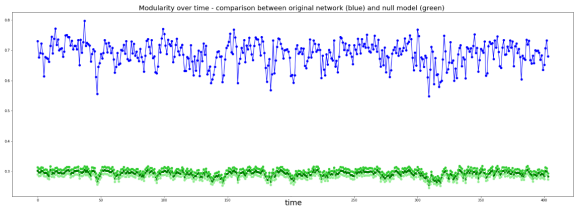

(a) Modularity - fMRI

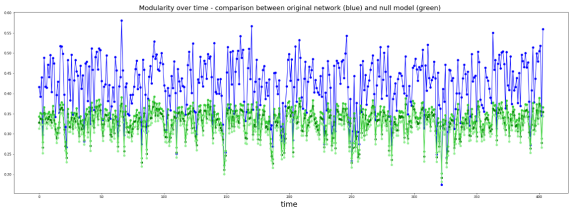

(b) Modularity - EEG delta

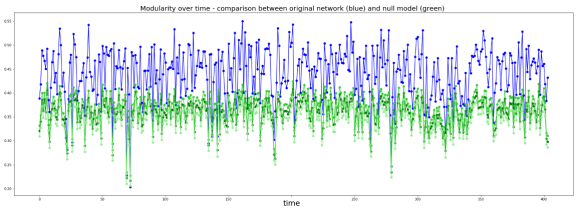

(c) Modularity - EEG theta

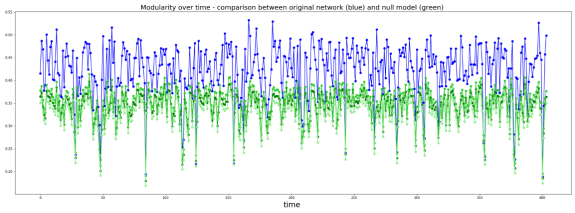

(d) Modularity - EEG alpha

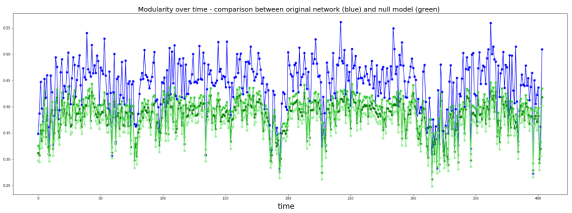

(e) Modularity - EEG beta

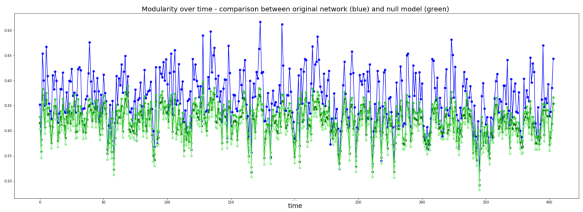

(f) Modularity - EEG gamma

Figure B.5: Variation over time of modularity for fMRI and EEG frequency bands, and corresponding rewiring null model, for subject 7.

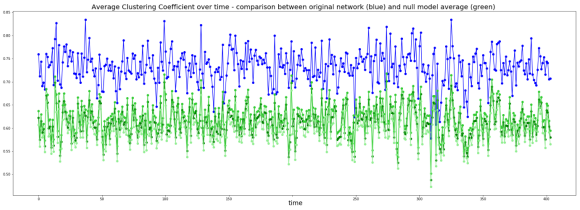

(a) Clustering coefficient - fMRI

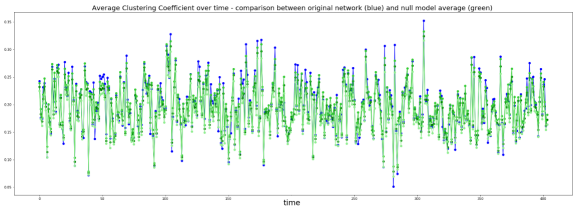

(b) Clustering coefficient - EEG delta

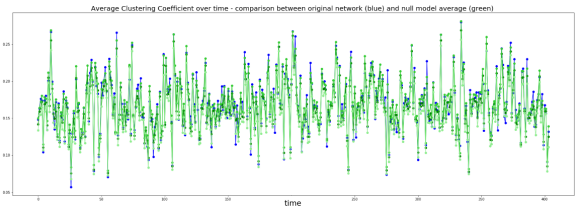

(c) Clustering coefficient - EEG theta

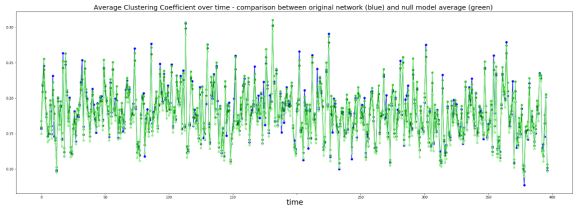

(d) Clustering coefficient - EEG alpha

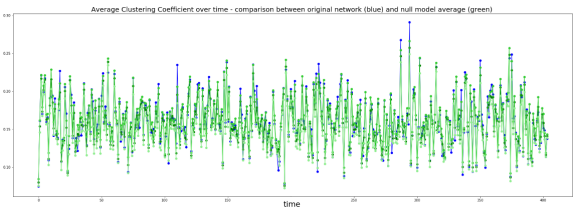

(e) Clustering coefficient - EEG beta

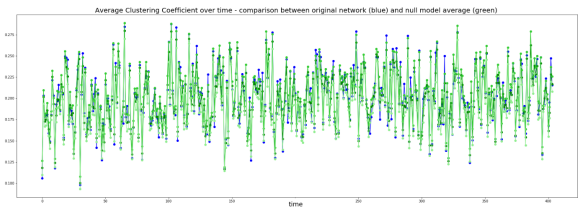

(f) Clustering coefficient - EEG gamma

Figure B.6: Variation over time of clustering coefficient for fMRI and EEG frequency bands, and corresponding degree constrained spatial null model, for subject 7.

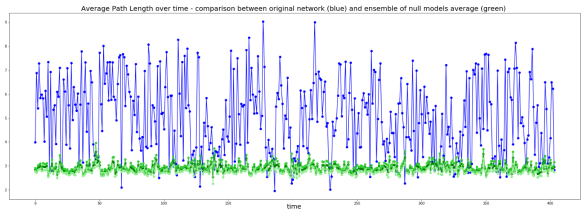

(a) Average path length - fMRI

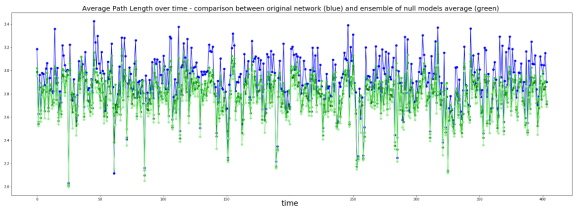

(b) Average path length - EEG delta

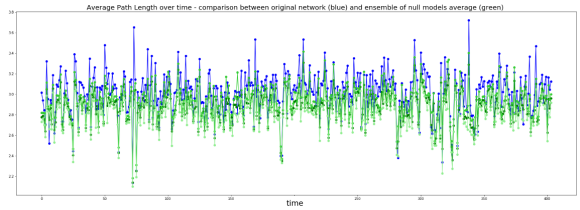

(c) Average path length - EEG theta

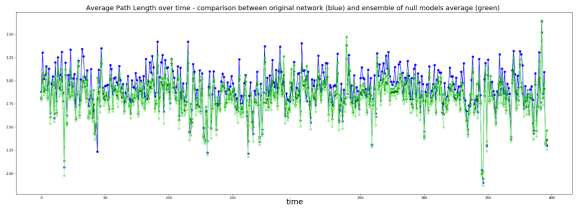

(d) Average path length - EEG alpha

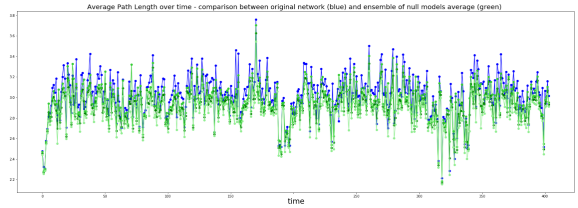

(e) Average path length - EEG beta

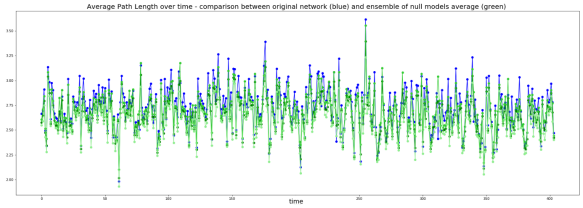

(f) Average path length - EEG gamma

Figure B.7: Variation over time of average path length for fMRI and EEG frequency bands, and corresponding degree constrained spatial null model, for subject 7.

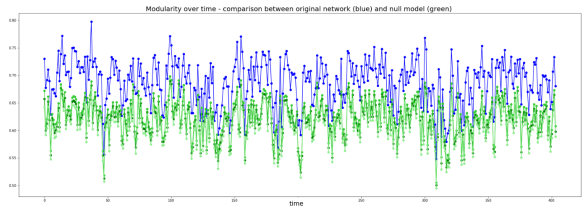

(a) Modularity - fMRI

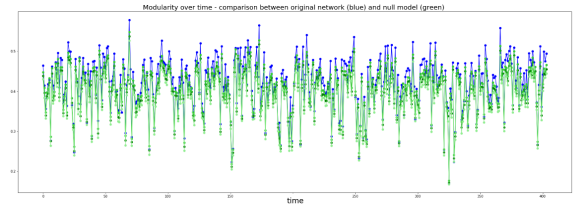

(b) Modularity - EEG delta

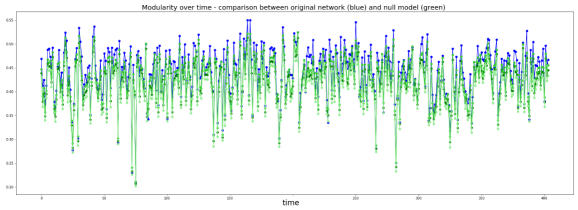

(c) Modularity - EEG theta

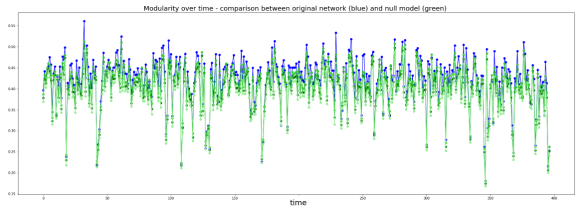

(d) Modularity - EEG alpha

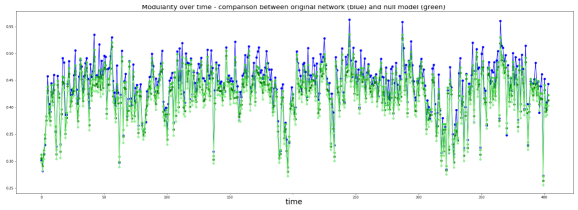

(e) Modularity - EEG beta

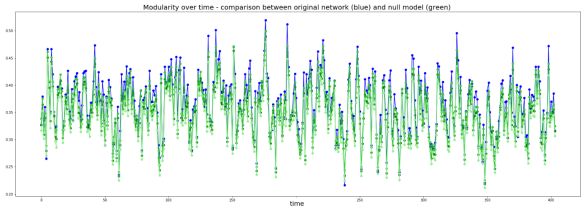

(f) Modularity - EEG gamma

Figure B.8: Variation over time of modularity for fMRI and EEG frequency bands, and corresponding degree constrained spatial null model, for subject 7.

B.3 Community Analysis with Louvain Algorithm for the static connectome

Table B.1: Modularity values associated to the communities obtained using the Louvain algorithm with the rewiring null model, averaging over all 100 surrogates generated from fMRI and EEG frequency bands static connectomes, for all subjects.

Subject	fMRI	EEG delta	EEG theta	EEG alpha	EEG beta	EEG gamma
1	0.266	0.273	0.316	0.328	0.381	0.362
2	0.257	0.301	0.278	0.301	0.353	0.351
3	0.230	0.355	0.358	0.338	0.389	0.334
4	0.268	0.284	0.342	0.268	0.398	0.347
5	0.266	0.342	0.313	0.246	0.362	0.342
6	0.270	0.328	0.357	0.240	0.383	0.375
7	0.216	0.345	0.358	0.326	0.408	0.266
8	0.279	0.268	0.279	0.316	0.357	0.355
9	0.254	0.317	0.368	0.347	0.413	0.324
average	0.252 ± 0.021	0.313 ± 0.031	0.330 ± 0.033	0.301 ± 0.038	0.383 ± 0.021	0.340 ± 0.030

Table B.2: Modularity values associated to the communities obtained using the Louvain algorithm with the degree constrained spatial null model, averaging over all 100 surrogates generated from fMRI and EEG frequency bands static connectomes, for all subjects. The values with * correspond to modularity values that were not significantly lower ($p>0.05$) in comparison to the static connectomes ones.

Subject	fMRI	EEG delta	EEG theta	EEG alpha	EEG beta	EEG gamma
1	0.370	0.424*	0.462*	0.463	0.517*	0.516
2	0.372	0.408*	0.377*	0.485	0.528	0.491*
3	0.330	0.508	0.529	0.466	0.538*	0.474
4	0.360	0.396*	0.496	0.363*	0.576	0.461
5	0.363	0.424*	0.414*	0.299*	0.455	0.456*
6	0.431	0.433*	0.513	0.299*	0.538*	0.536*
7	0.338	0.456	0.477	0.456	0.533*	0.343*
8	0.392	0.377*	0.349*	0.467	0.492*	0.525*
9	0.374	0.507	0.583	0.517*	0.575	0.449
average	0.407 ± 0.035	0.437 ± 0.043	0.467 ± 0.071	0.424 ± 0.077	0.528 ± 0.036	0.472 ± 0.055

B.4 Community Analysis with Louvain Algorithm

Table B.3: Median number of communities communities extracted from fMRI and EEG frequency bands over time using the Louvain algorithm, for all subjects.

Subject	fMRI	EEG delta	EGG theta	EEG alpha	EEG beta	EEG gamma
1	6	10	11	11	12	11
2	7	10	11	11	12	10
3	7	10	11	12	12	13
4	6	10	11	11	13	12
5	6	10	12	11	14	12
6	6	10	11	12	12	11
7	7	10	12	11	13	14
8	7	11	11	11	12	11
9	6	10	11	11	12	12

Table B.4: Percentage of NMI and Jaccard Index values statistically significant for comparison between time points' partitions, using a time shuffled null model.

Subject	fMRI (%) — EEG delta (%)	fMRI (%) —EEG theta (%)	fMRI (%) — EEG alpha (%)	fMRI (%) — EEG beta (%)	fMRI (%) — EEG gamma (%)
NMI					
1	4.59 — 6.13	4.45 — 6.26	4.65 — 5.83	4.86 — 5.13	4.45 — 4.75
2	4.59 —5.51	4.91 — 5.65	5.14 — 6.86	4.84 — 5.99	5.07 — 5.40
3	4.90 — 5.15	5.27 — 5.69	4.81 — 6.38	5.50 — 5.23	5.41 — 5.17
4	4.56 — 6.04	4.68 — 5.79	4.59 — 6.00	4.64 — 4.88	4.98 — 5.96
5	4.55 — 6.02	4.16 — 5.52	4.24 — 5.88	4.60 — 6.02	4.55 — 5.85
6	4.73 — 6.35	4.69 — 6.20	4.63 — 5.97	4.68 — 6.28	4.59 — 5.78
7	5.23 — 5.75	5.51 — 5.60	5.00 — 5.64	5.19 — 6.29	4.96 — 4.99
8	4.61 — 5.24	4.26 — 6.05	4.58 — 5.72	4.78 — 5.76	4.67 — 5.99
9	4.61 — 5.82	4.64 — 6.23	4.34 — 5.96	4.56 — 5.41	4.33 — 5.04
$average$	4.71 — 5.78	4.73 — 5.89	4.66 — 6.03	4.85 — 5.67	4.78 — 5.39
std	± 0.21 — ± 0.39	± 0.42 — ± 0.28	± 0.27 — ± 0.35	± 0.29 — ± 0.49	± 0.33 — ± 0.45
$Jaccard\ \ Index$					
1	6.54 — 12.30	6.02 — 12.33	6.68 — 12.00	6.78 — 11.73	6.45 — 12.09
2	7.14 — 12.66	6.87 — 12.32	6.93 — 12.35	7.10 — 11.36	7.08 — 12.17
3	6.56 — 12.41	6.75 — 12.69	6.80 — 12.45	6.66 — 12.06	6.50 — 11.01
4	6.18 — 12.23	6.40 — 12.03	6.59 — 12.40	6.16 — 11.84	6.31 — 12.54
5	6.05 — 12.69	5.32 — 11.96	6.02 — 13.26	5.71 — 11.45	6.18 — 12.00
6	6.95 — 13.18	6.93 — 12.52	6.66 — 12.19	6.61 — 11.76	6.92 — 12.13
7	7.11 — 12.64	7.16 — 12.17	7.11 — 12.68	7.19 — 11.80	6.77 — 11.34
8	6.51 — 12.67	6.36 — 12.25	6.55 — 12.51	6.42 — 11.76	6.73 — 12.10
9	6.57 — 12.37	6.66 — 12.15	6.38 — 12.61	6.29 — 11.51	6.32 — 11.93
$average$	6.62 — 12.57	6.50 — 12.27	6.64 — 12.49	6.55 — 11.70	6.58 — 11.92
std	± 0.36 — ± 0.27	± 0.53 — ± 0.22	± 0.30 — ± 0.33	± 0.44 — ± 0.21	± 0.29 —± 0.44

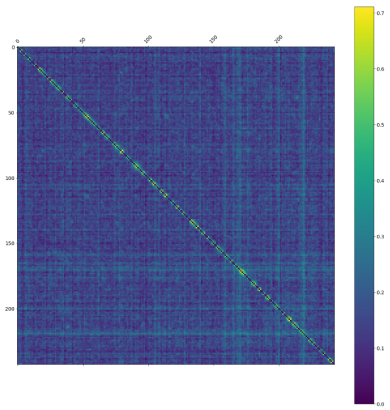

(a) fMRI (for time points obtained with EEG delta)

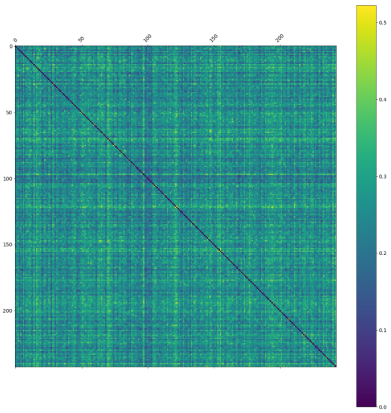

(b) EEG delta

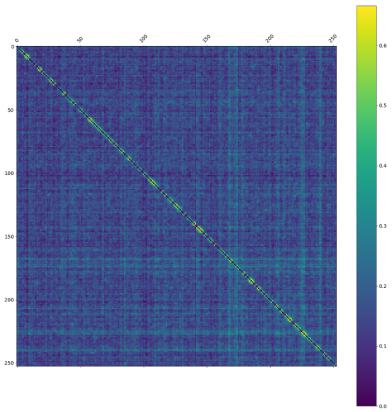

(c) fMRI (for time points obtained with EEG theta)

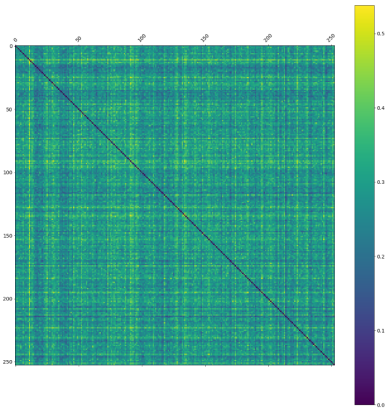

(d) EEG theta

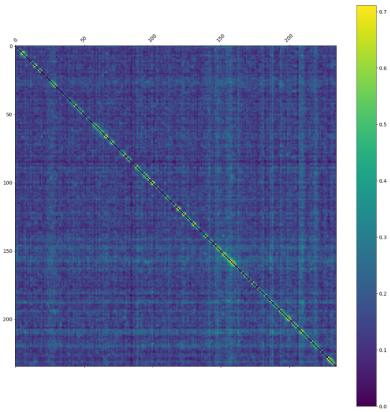

(e) fMRI (for time points obtained with EEG alpha)

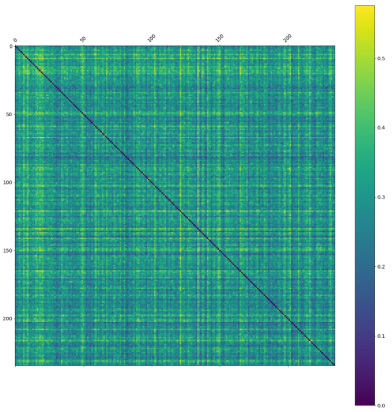

(f) EEG alpha

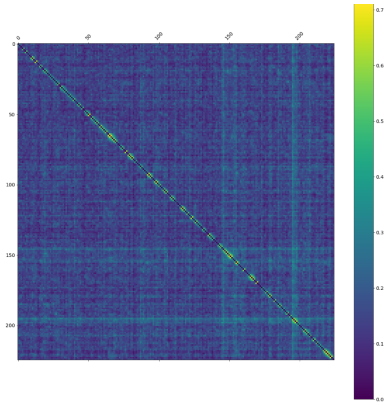

(g) fMRI (for time points obtained with EEG beta)

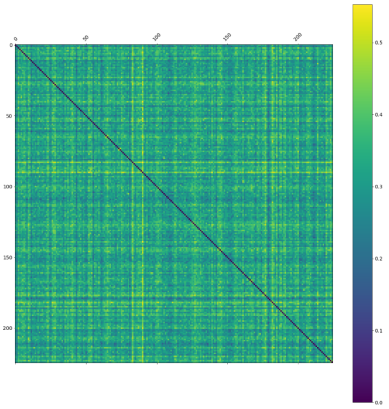

(h) EEG beta

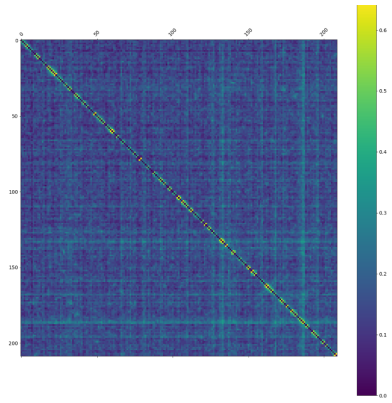

(i) fMRI (for time points obtained with EEG gamma)

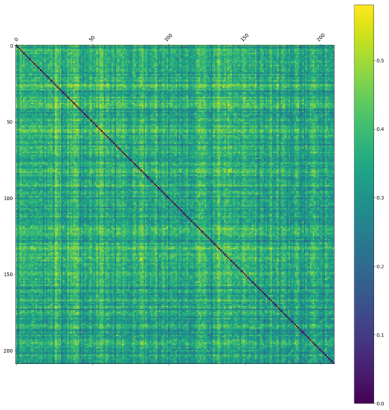

(j) EEG gamma

Figure B.9: Normalized Mutual Information (NMI) matrices regarding the temporal comparison of the communities obtained with the Louvain algorithm, for fMRI and EEG frequency bands, for subject 3.

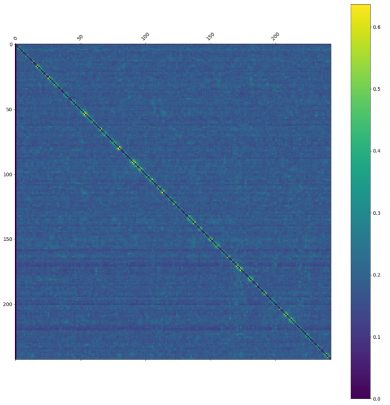

(a) fMRI (for time points obtained with EEG delta)

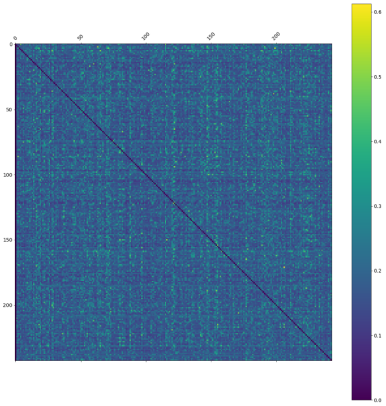

(b) EEG delta

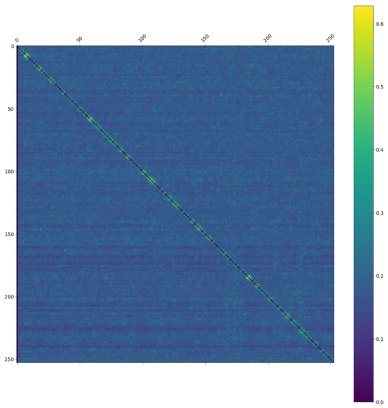

(c) fMRI (for time points obtained with EEG theta)

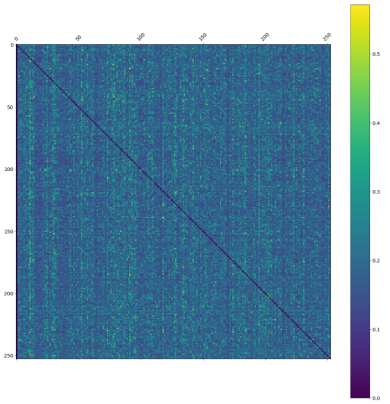

(d) EEG theta

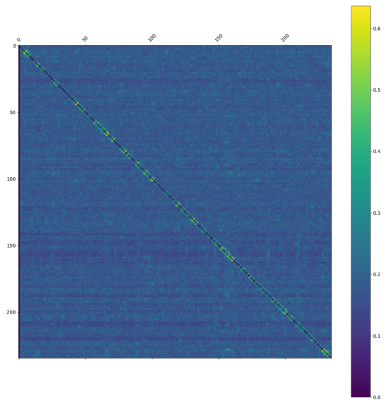

(e) fMRI (for time points obtained with EEG alpha)

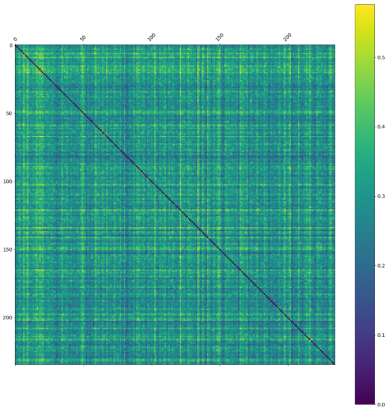

(f) EEG alpha

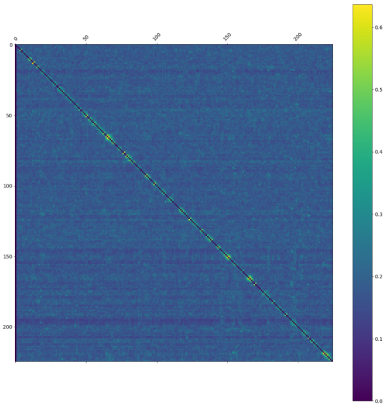

(g) fMRI (for time points obtained with EEG beta)

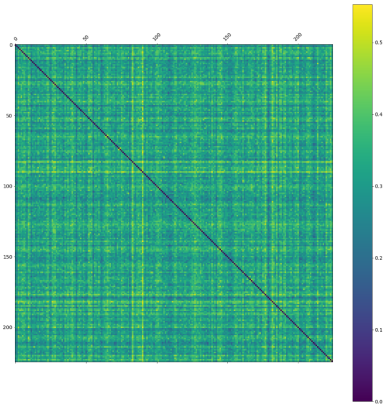

(h) EEG beta

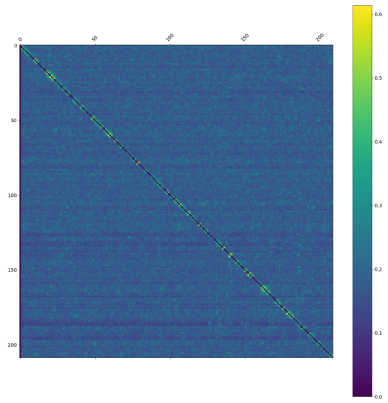

(i) fMRI (for time points obtained with EEG gamma)

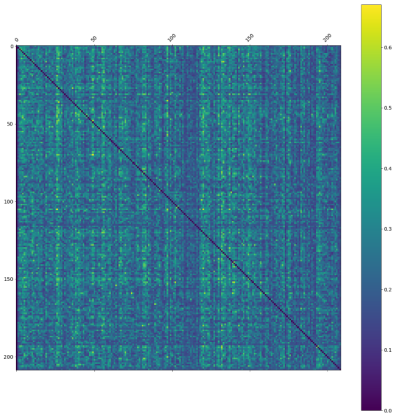

(j) EEG gamma

Figure B.10: Jaccard Index matrices regarding the temporal comparison of the communities obtained with the Louvain algorithm, for fMRI and EEG frequency bands, for subject 3.

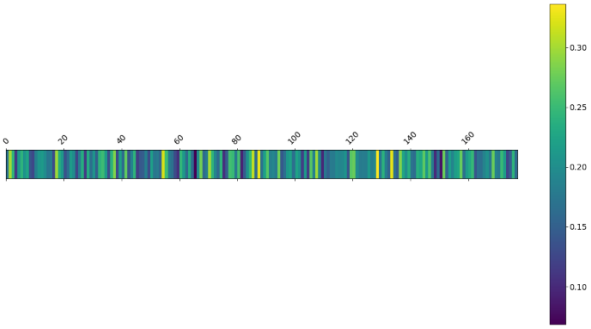

(a) fMRI-EEG delta

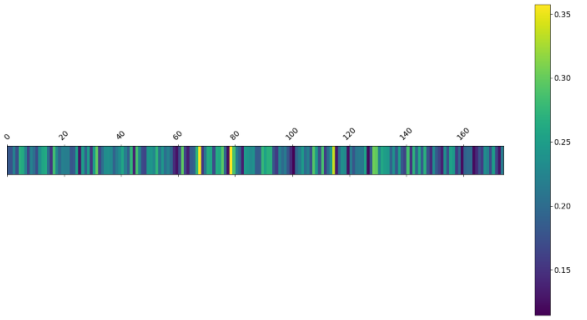

(b) fMRI-EEG theta

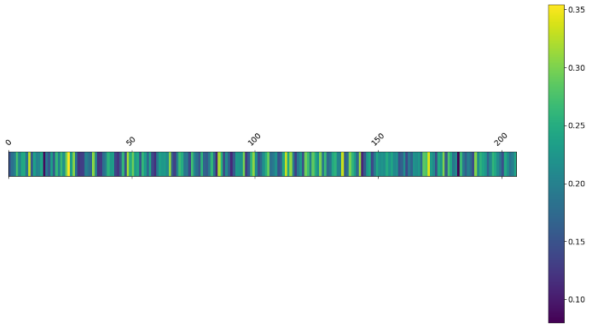

(c) fMRI-EEG alpha

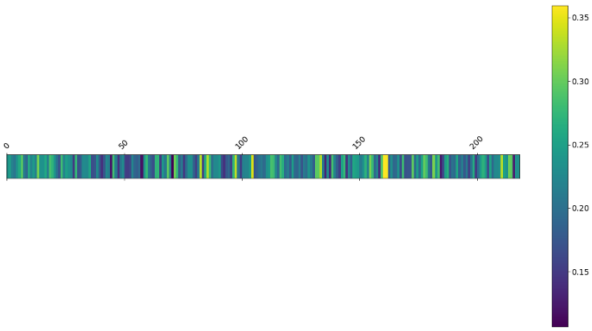

(d) fMRI-EEG beta

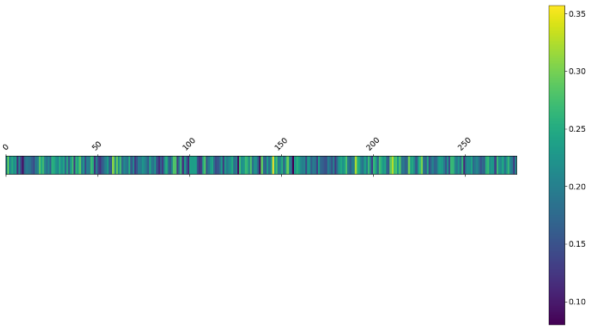

(e) fMRI-EEG gamma

Figure B.11: NMI coloured arrays regarding the comparison of the communities obtained over time with the Louvain algorithm, between fMRI and EEG frequency bands, for subject 8.

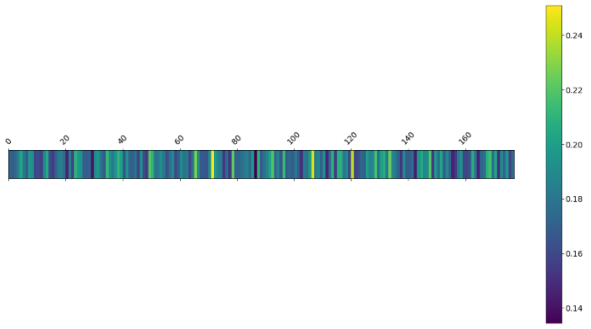

(a) fMRI-EEG delta

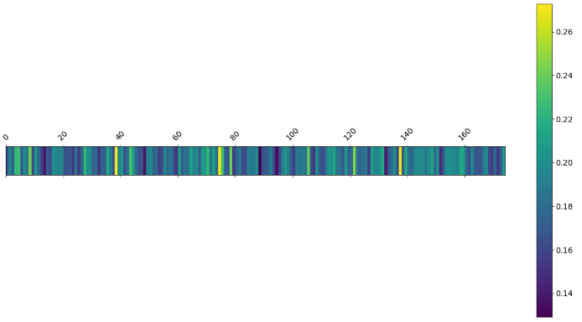

(b) fMRI-EEG theta

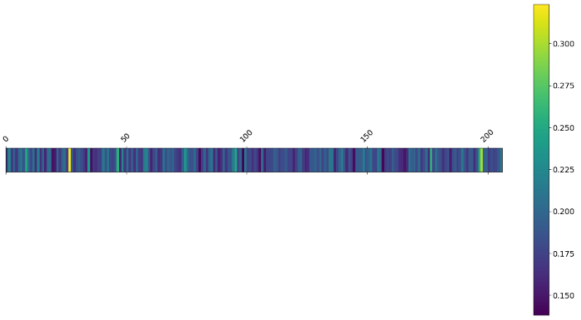

(c) fMRI-EEG alpha

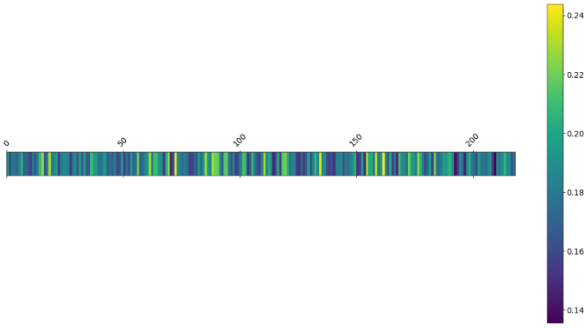

(d) fMRI-EEG beta

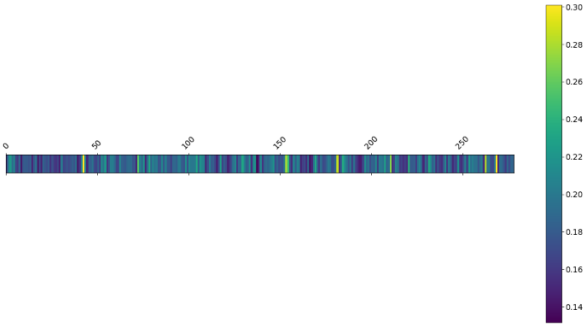

(e) fMRI-EEG gamma

Figure B.12: Jaccard Index coloured arrays regarding the comparison of the communities obtained over time with the Louvain algorithm, between fMRI and EEG frequency bands, for subject 8.

Table B.5: Percentage of NMI and Jaccard Index values statistically significant for comparison between the two modalities' partitions, using a time shuffled null model.

Subject	fMRI-EEG delta (%)	fMRI-EEG theta (%)	fMRI-EEG alpha (%)	fMRI-EEG beta (%)	fMRI-EEG gamma (%)
NMI					
1	6.41	5.33	5.51	6.62	7.38
2	6.71	3.68	6.32	5.18	4.25
3	6.17	6.72	7.24	4.44	6.22
4	5.70	5.00	8.00	5.56	6.73
5	5.92	5.89	8.96	6.29	5.71
6	5.30	5.07	6.58	5.84	6.51
7	6.69	4.38	3.85	7.18	5.30
8	5.65	5.74	6.80	5.05	5.75
9	6.88	7.32	7.90	5.74	6.59
$average$	6.16	5.46	6.80	5.77	6.05
$std \pm 0.52$	$\pm$ 1.06	$\pm$ 1.42	$\pm$ 0.79	$\pm$ 0.87	..
$Jaccard \quad Index$					
1	6.41	9.32	9.45	6.25	6.77
2	10.67	6.25	5.14	9.15	6.80
3	6.58	9.48	7.67	6.66	4.79
4	7.78	7.80	9.33	8.04	5.77
5	4.74	8.09	10.45	6.49	10.27
6	5.30	6.33	4.52	7.39	7.19
7	8.27	6.62	6.15	3.80	9.53
8	5.65	8.04	6.80	7.34	8.99
9	6.88	8.54	3.75	4.49	6.98
$average$	6.92	7.83	7.03	6.62	7.45
std	$\pm$ 1.70	$\pm$ 1.14	$\pm$ 2.23	$\pm$ 1.57	$\pm$ 1.69

B.5 Community Analysis with modified Louvain Algorithm

Table B.6: Median number of communities communities extracted from fMRI and EEG frequency bands over time using the modified Louvain algorithm, for all subjects.

Subject	fMRI — EEG delta	fMRI — EGG theta	fMRI — EEG alpha	fMRI — EEG beta	fMRI — EEG gamma
1	7 — 9	6 — 10.5	6 — 9	6 — 10	6 — 9
2	6 — 9	7 — 10	7 — 8.5	6.5 — 9	7 — 8
3	7 — 9	6 — 9	6 — 11	6 — 12	7 — 12
4	6 — 10	6 — 10	6 — 9	6 — 12	6 — 11
5	6 — 9	6 — 9.5	6 — 9	6 — 12	6 — 10
6	6 — 8	6 — 9	6 — 10	6 — 9	6 — 10
7	6 — 9	7 — 9	6 — 10	6 — 10.5	7 — 14
8	7 — 8	6 — 8	6 — 9	7 — 10	7 — 9
9	6 — 9	6 — 10	6 — 10	6 — 11	6 — 10

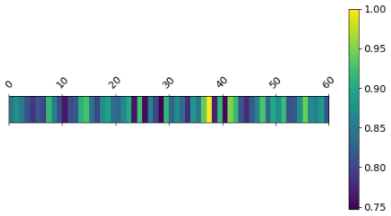

(a) fMRI (for time points obtained with EEG delta)

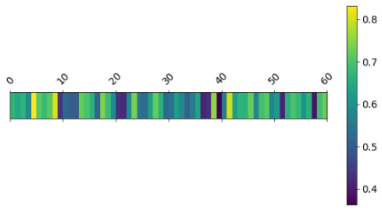

(b) EEG delta

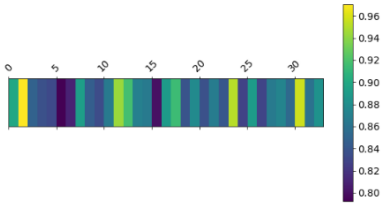

(c) fMRI (for time points obtained with EEG theta)

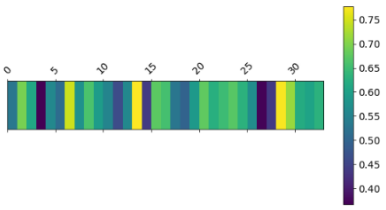

(d) EEG theta

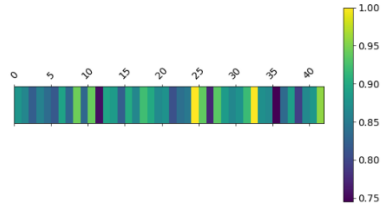

(e) fMRI (for time points obtained with EEG alpha)

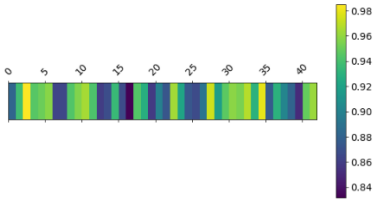

(f) EEG alpha

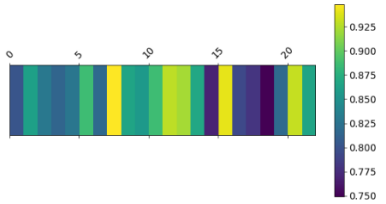

(g) fMRI (for time points obtained with EEG beta)

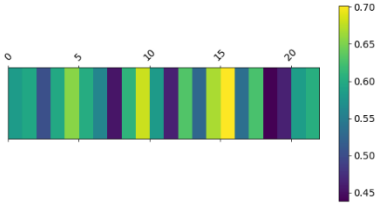

(h) EEG beta

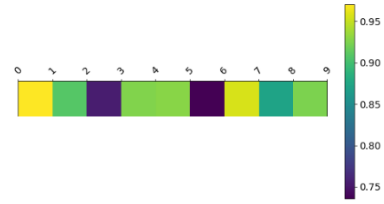

(i) fMRI (for time points obtained with EEG gamma)

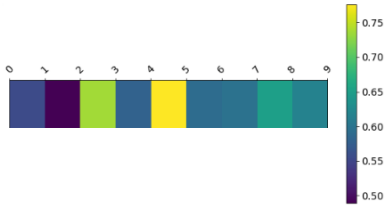

(j) EEG gamma

Figure B.13: NMI coloured arrays regarding the comparison of the communities obtained for each time point with the regular and modified version of the Louvain algorithm, for fMRI and EEG frequency bands, for subject 7.

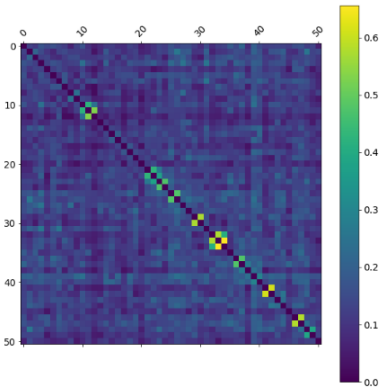

(a) fMRI (for time points obtained with EEG delta)

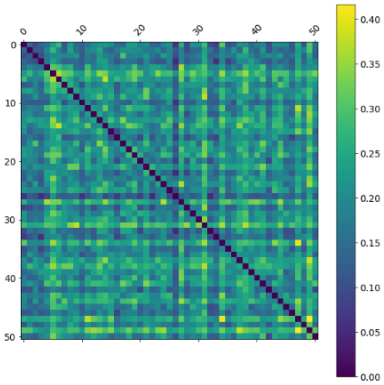

(b) EEG delta

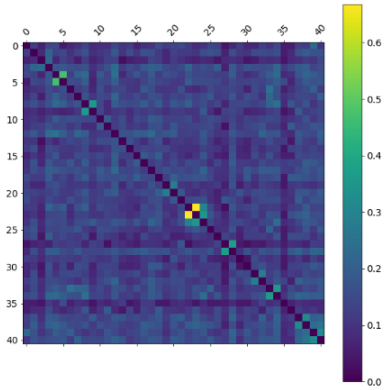

(c) fMRI (for time points obtained with EEG theta)

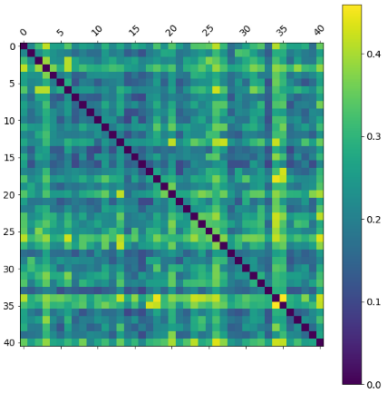

(d) EEG theta

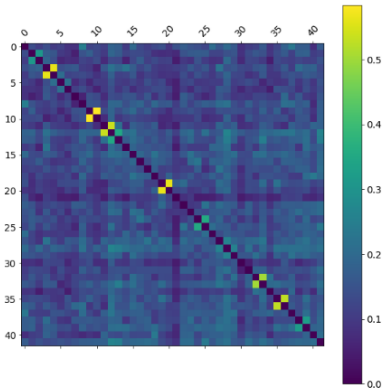

(e) fMRI (for time points obtained with EEG alpha)

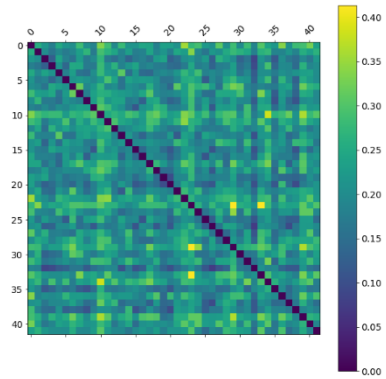

(f) EEG alpha

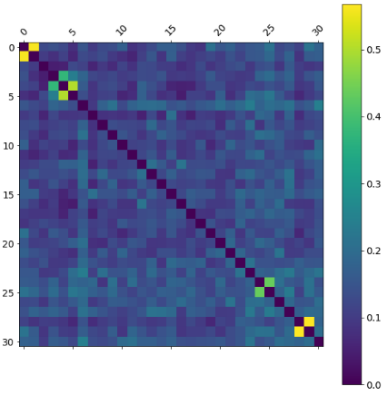

(g) fMRI (for time points obtained with EEG beta)

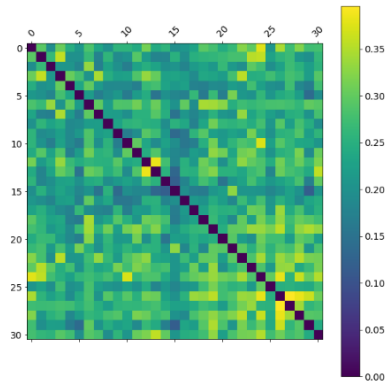

(h) EEG beta

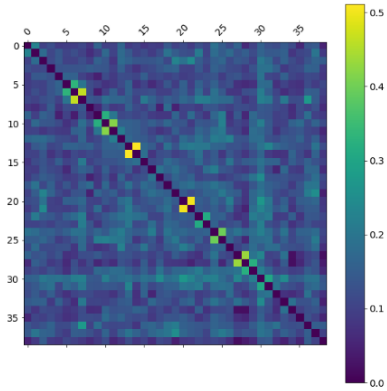

(i) fMRI (for time points obtained with EEG gamma)

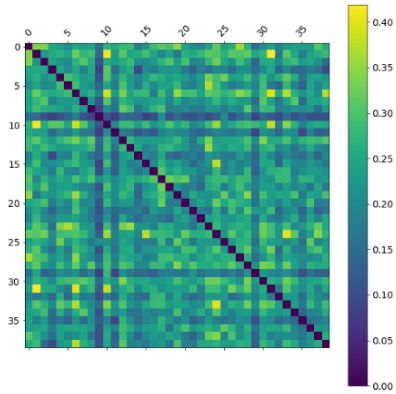

(j) EEG gamma

Figure B.14: NMI matrices regarding the temporal comparison of the communities obtained with the modified Louvain algorithm, for fMRI and EEG frequency bands, for subject 9.

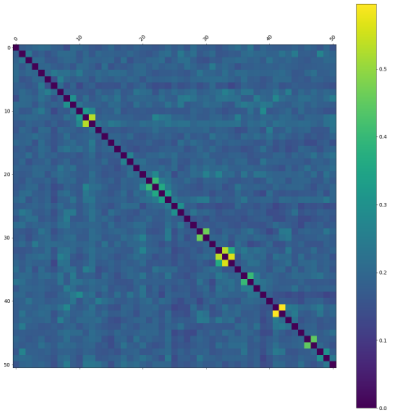

(a) fMRI (for time points obtained with EEG delta)

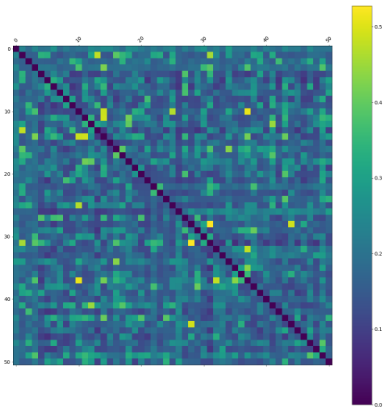

(b) EEG delta

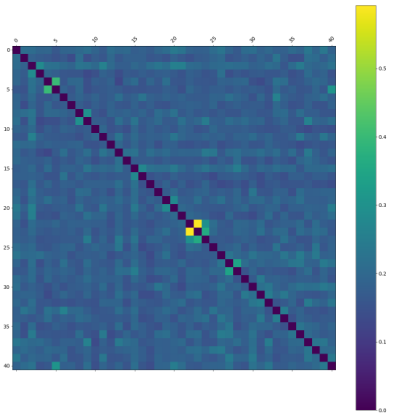

(c) fMRI (for time points obtained with EEG theta)

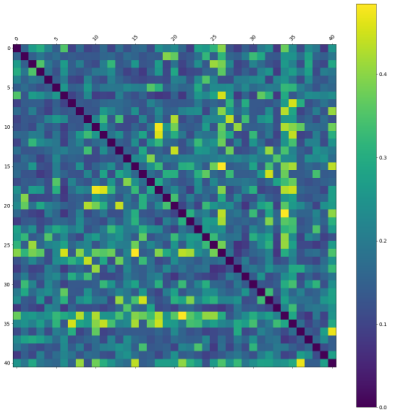

(d) EEG theta

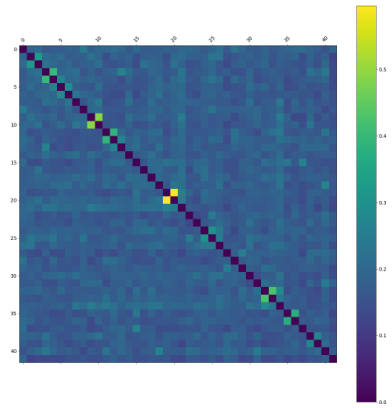

(e) fMRI (for time points obtained with EEG alpha)

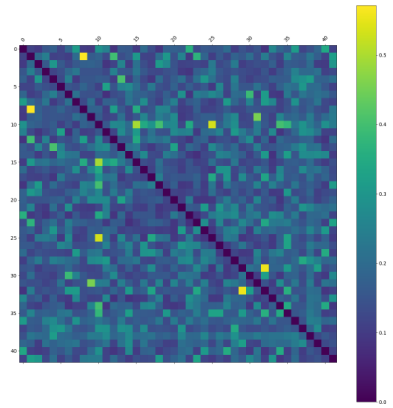

(f) EEG alpha

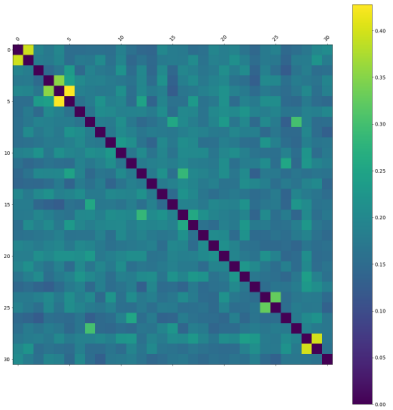

(g) fMRI (for time points obtained with EEG beta)

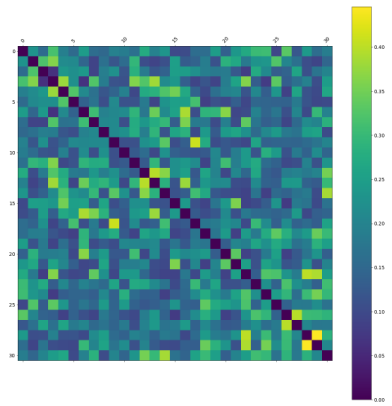

(h) EEG beta

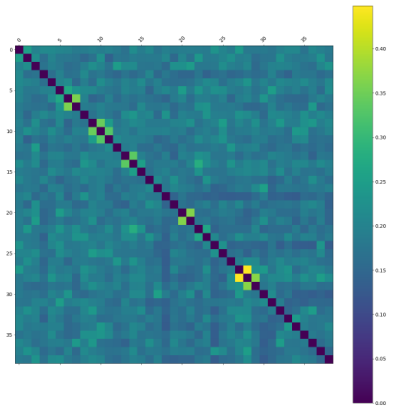

(i) fMRI (for time points obtained with EEG gamma)

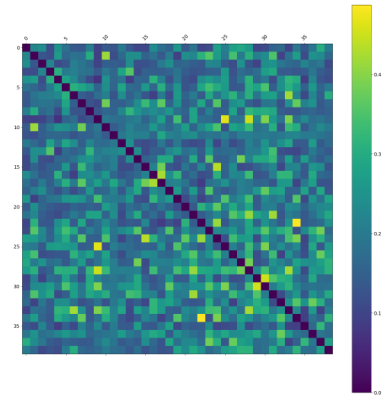

(j) EEG gamma

Figure B.15: Jaccard Index matrices regarding the temporal comparison of the communities obtained with the modified Louvain algorithm, for fMRI and EEG frequency bands, for subject 9.

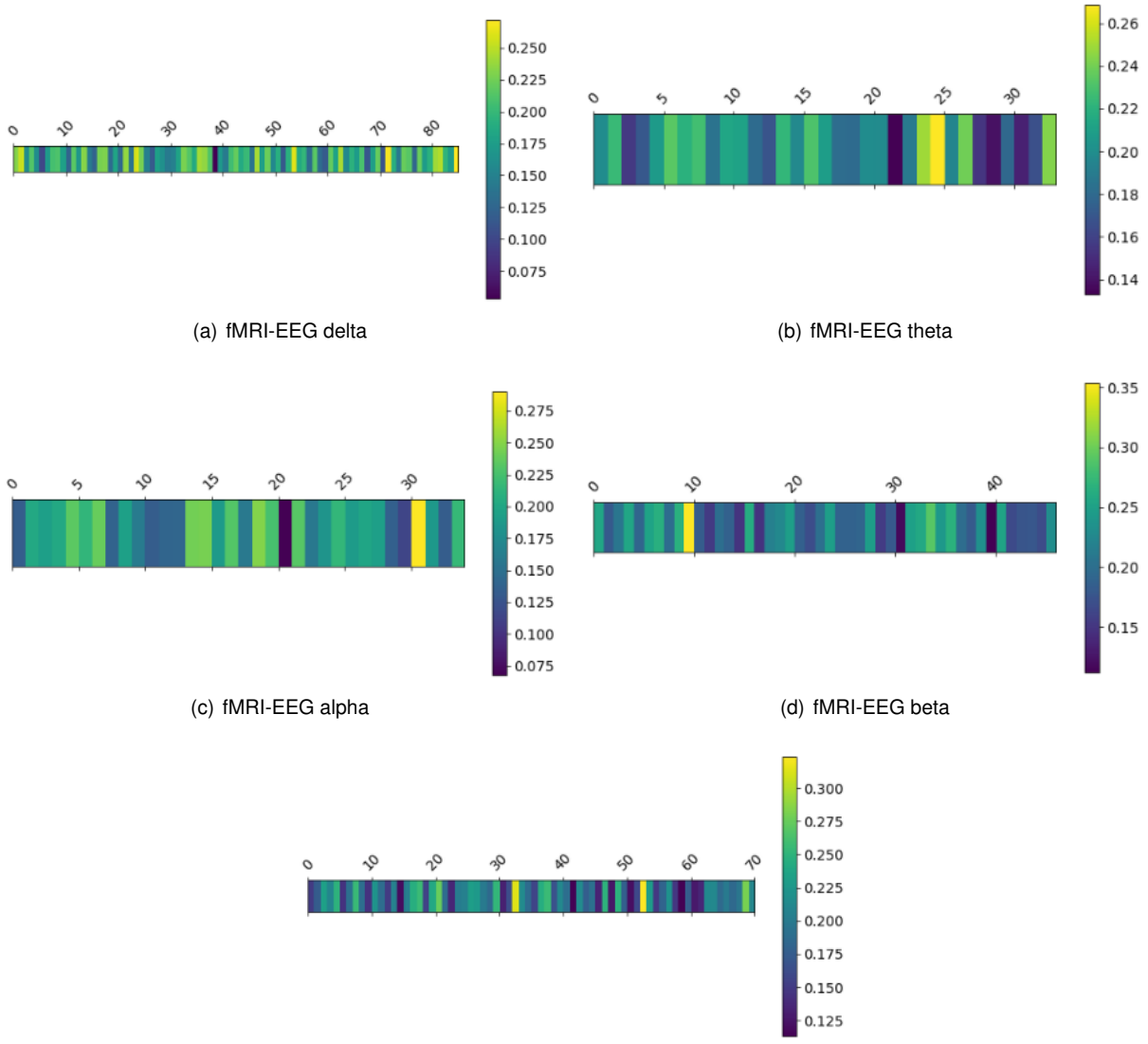

(a) fMRI-EEG delta

(b) fMRI-EEG theta

(c) fMRI-EEG alpha

(d) fMRI-EEG beta

(e) fMRI-EEG gamma

Figure B.16: NMI coloured arrays regarding the comparison of the communities obtained over time with the modified Louvain algorithm, between fMRI and EEG frequency bands, for subject 2.

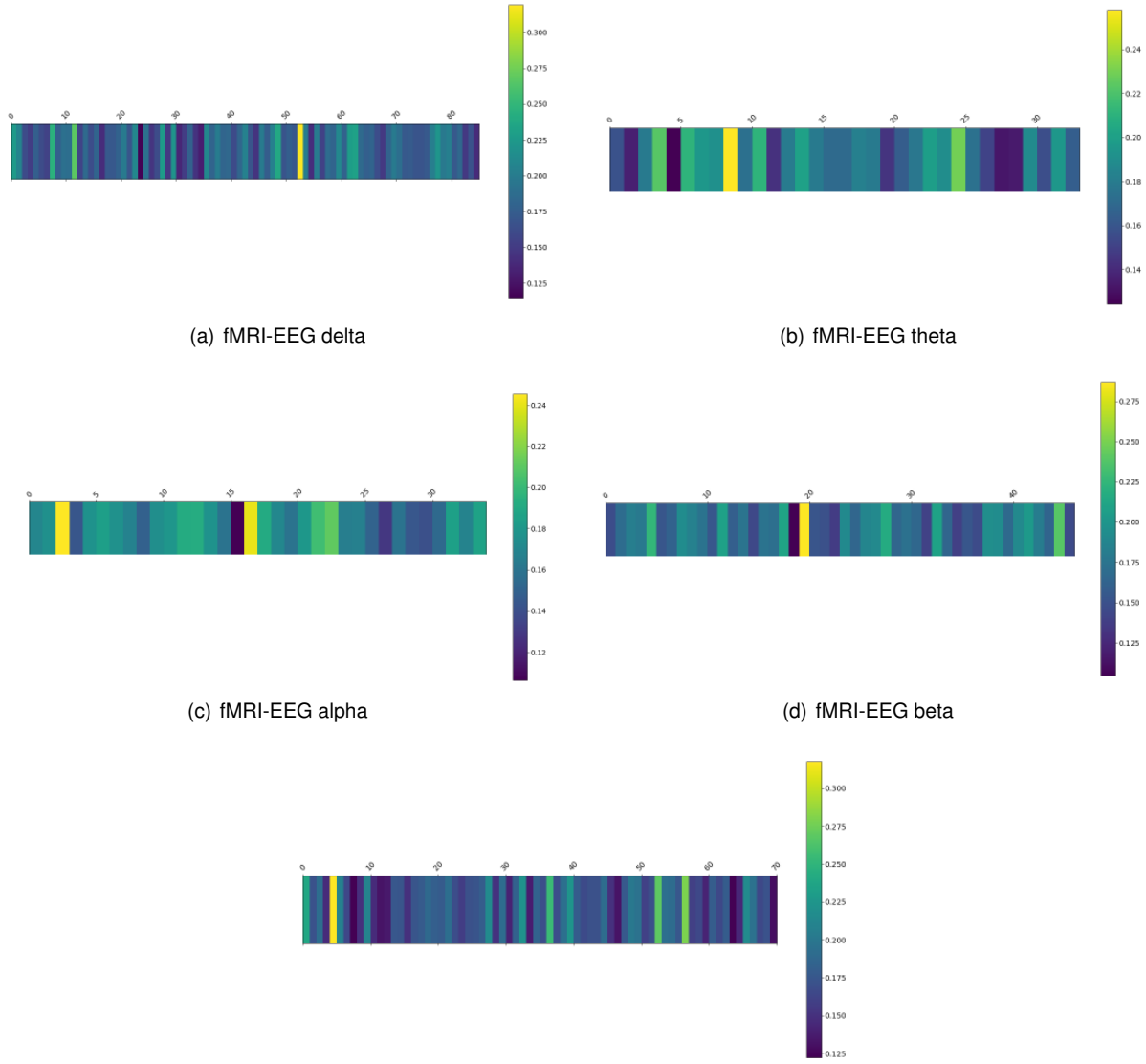

(a) fMRI-EEG delta

(b) fMRI-EEG theta

(c) fMRI-EEG alpha

(d) fMRI-EEG beta

(e) fMRI-EEG gamma

Figure B.17: Jaccard Index coloured arrays regarding the comparison of the communities obtained over time with the modified Louvain algorithm, between fMRI and EEG frequency bands, for subject 2.

B.6 Community Analysis with multiplex Louvain Algorithm

Table B.7: Median number of communities communities extracted from the combined functional networks over time using the multiplex version of Louvain algorithm, for all subjects.

Subject	fMRI-EEG delta	fMRI-EGG theta	fMRI-EEG alpha	fMRI-EEG beta	fMRI-EEG gamma
1	5	5	5	6	5
2	4	5	5	5	4
3	5	5	5	5	4
4	6	5	5	5	6
5	6	5	5	6	7
6	6	6	6	7	5
7	5	5	5	5	5
8	6	6	6	4	5
9	5	7	6	5	6

Appendix C

Motif Analysis Results

The following figures and tables summarize the results regarding the motif analysis.

C.1 Motif Analysis with Rewiring Null Model

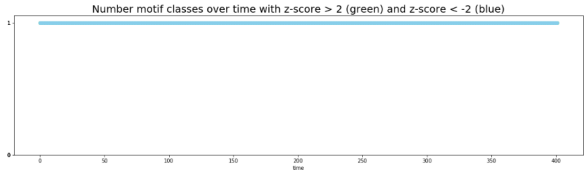

(a) fMRI - subgraphs of size 3

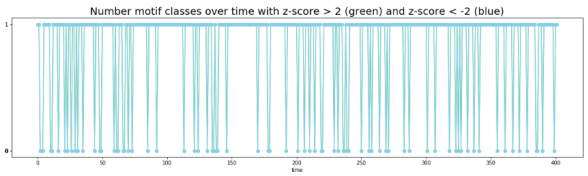

(b) EEG delta - subgraphs of size 3

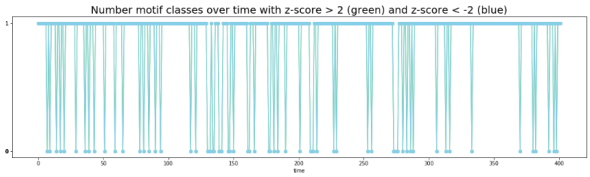

(c) EEG theta - subgraphs of size 3

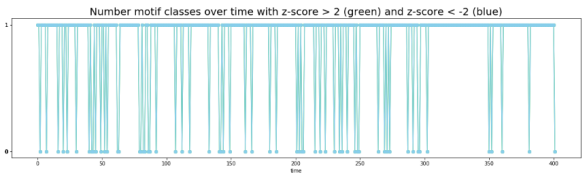

(d) EEG alpha - subgraphs of size 3

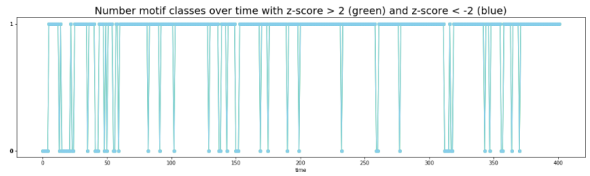

(e) EEG beta - subgraphs of size 3

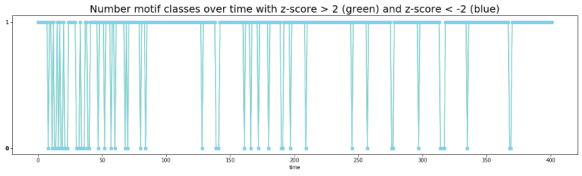

(f) EEG gamma - subgraphs of size 3

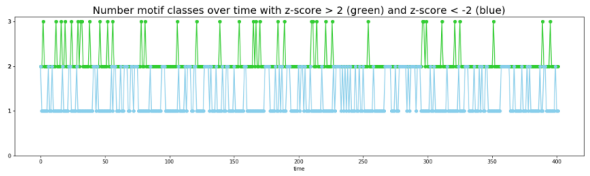

(g) fMRI - subgraphs of size 4

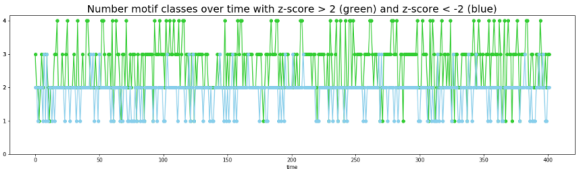

(h) EEG delta - subgraphs of size 4

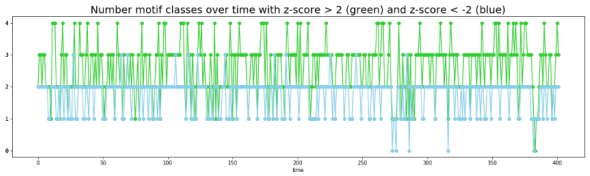

(i) EEG theta - subgraphs of size 4

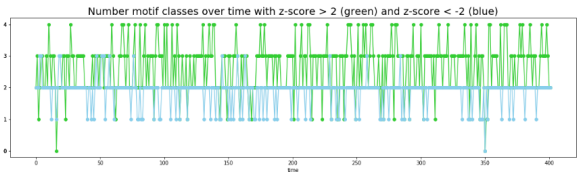

(j) EEG alpha - subgraphs of size 4

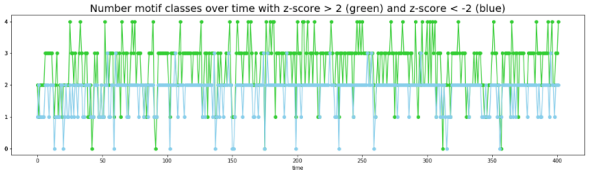

(k) EEG beta - subgraphs of size 4

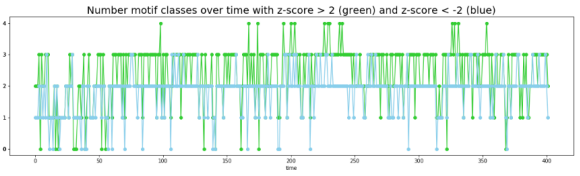

(l) EEG gamma - subgraphs of size 4

Figure C.1: Variation of number of motif classes over- (in green) and under-represented (in blue), for subgraphs with 3, 4 and 5 nodes, for fMRI and EEG frequency bands, for subject 3.

Table C.1: Average percentage of time points for which each motif class was the one (top-1) with highest positive z-score and with lowest negative z-score, corresponding to the over- and under-represented motifs, respectively, considering the subgraphs with 3 nodes, for all subjects - for fMRI and EEG functional networks, against the rewiring null model. The values with an * symbol correspond to the motif class selected as the most recurring one with highest (+) or lowest (-) z-score, across time, for at least 1 subject.

Motif	in top-1 (+) (%)	in top-1 (-) (%)
$fMRI$		
1	-	100.0*
2	100.0*	-
$no \quad motif$	-	-
$EEG \quad delta$		
1	6.5	74.0*
2	74.0*	6.5
$no \quad motif$	19.5	19.5
$EEG \quad theta$		
1	2.2	77.4*
2	77.4*	2.2
$no \quad motif$	20.4	20.4
$EEG \quad alpha$		
1	2.9	83.3*
2	83.3*	2.9
$no \quad motif$	13.8	13.8
$EEG \quad beta$		
1	0.7	88.8*
2	88.8*	0.7
$nomotif$	10.5	10.5
$EEG \quad gamma$		
1	0.2	94.1*
2	94.1*	0.2
$no \quad motif$	5.7	5.7

Table C.2: Average percentage of time points for which each motif class was the one (top-1) or second one (top-2) with highest positive z-score and with lowest negative z-score, corresponding to the over- and under-represented motifs, respectively, considering the subgraphs with 4 nodes, for all subjects - for fMRI and EEG functional networks, against the rewiring null model. The values with an * symbol correspond to the motif class selected as the most recurring one at each top position, (+) or (-), across time, for at least 1 subject.

Motif	in top-1 (+) (%)	in top-2 (+) (%)	in top-1 (-) (%)	in top-2 (-) (%)
$fMRI$				
1	-	-	100.0*	-
2	-	-	-	31.3
4	-	100.0*		
5	100.0*	-	-	-
$no\ \ motif$	-	-	-	65.7*
$EEG\ \ delta$				
1	-	-	87.7*	6.9
3	-	9.5	-	62.2*
4	35.1*	47.4*	-	1.4
5	22.6	22.8	-	2.0
6	42.2*	13.6	-	-
$no\ \ motif$	0.1	5.8	0.2	17.0
$EEG\ \ theta$				
1	-	-	94.1*	2.7
3	-	3.5	-	60.0*
4	36.5*	45.8*	-	0.4
5	21.7	21.7	-	0.5
6	40.9*	16.3	-	-
$nomotif$	0.5	10.6	0.6	31.1
$EEG\ \ alpha$				
1	-	-	92.0*	4.9
3	-	3.6	-	69.7*
4	39.8*	47.6*	-	0.4
5	30.1	26.1	-	1.1
6	30.3*	13.6	-	-
$no\ \ motif$	0.4	6.6	0.3	19.7
$EEG\ \ beta$				
1	-	-	92.2*	3.2
3	-	-	2.8	75.6*
4	38.8*	48.5*	-	0.3
5	43.3*	23.8	-	0.1
$no\ \ motif$	1.3	10.6	2.8	20.0
$EEG\ \ gamma$				
1	-	-	94.0*	2.8
3	-	0.4	2.5	84.9*
4	30.7	61.1*	-	0.1
5	60.3*	21.0	-	0.1
$no\ \ motif$	1.3	8.0	2.3	11.5

Table C.3: Average percentage of time points for which each motif class was the first one to fifth one (top-1-4) with highest positive z-score, corresponding to the over- -represented motifs, considering the subgraphs with 5 nodes, for all subjects - for fMRI and EEG functional networks, against the rewiring null model. Only shown the motifs with highest percentages per position in the top. The values with an * symbol correspond to the motif class selected as the most recurring one at each top position, across time, for at least 1 subject.

Motif	in top-1 (+) (%)	in top-2 (+) (%)	in top-3 (+) (%)	in top-4 (+) (%)	in top-5 (+) (%)
$fMRI$					
8	-	-	-	100.0*	-
9	-	-	-	-	73.2*
11	-	-	100*	-	-
12	-	-	-	-	19.4
15	0.2	99.8*	-	-	-
20	99.8*	0.2	-	-	-
$no\ \ motif$	-	-	-	-	1.5
$EEG\ \ delta$					
9	-	-	-	-	9.2
10	-	-	-	-	9.8
11	-	-	9.5	11.8	11.9*
15	13.9*	16.8	8.1	7.4	10.8
16	7.6	13.5	17.9*	26.1*	14.9*
18	7.9	31.0*	22.9*	14.3	8.0
19	27.2*	18.5*	20.8*	13.5	8.2
20	12.7	-	-	-	-
21	30.3*	9.3	9.3	8.5	6.1
$no\ \ motif$	-	-	-	-	4.8*
$EEG\ \ theta$					
9	-	-	-	-	9.5
11	-	-	10.2*	11.4*	12.5*
15	14.5	13.5	-	-	7.9
16	9.8	13.4	17.8*	21.6*	12.1*
18	13.2	33.9*	18.8*	13.2	-
19	24.7*	18.1	19.4*	12.7	-
20	8.8	-	-	-	-
21	27.5*	10.0	11.9	9.7	-
$no\ \ motif$	-	-	-	4.2	10.6*
$EEG\ \ alpha$					
11	-	-	13.3	14.6	14.8*
15	18.5*	19.0*	-	-	-
16	-	13.0	18.9*	21.6*	12.8*
18	13.1	27.3*	18.5*	13.0	9.1
19	25.6*	19.1*	19.5*	12.1	-
20	13.5	-	-	-	-
21	20.1*	9.2	9.6	8.4	-
$no\ \ motif$	-	-	-	-	7.5*

Table C.4: Continuation of table C.3.

Motif	in top-1 (+) (%)	in top-2 (+) (%)	in top-3 (+) (%)	in top-4 (+) (%)	in top-5 (+) (%)
$EEG\ \ beta$					
8	-	-	-	8.7	9.6
9	-	-	-	8.8	12.5*
11	-	14.0	22.7*	12.8*	8.1
15	24.9*	19.6*	-	-	-
16	10.1	11.9	12.1	14.4*	11.4
18	11.9	19.3*	12.9	10.7	8.9
19	17.4*	13.9	14.9*	11.4	7.7
20	16.1*	-	-	-	-
21	10.9	-	-	-	-
$no\ \ motif$	-	-	-	6.6	11.8*
$EEG\ \ gamma$					
8	-	-	-	16.9*	13.0*
9	-	-	-	8.3	12.6*
11	-	16.9	33.0*	13.3*	8.0
15	27.4*	31.0*	8.9	-	-
16	8.9	8.7	10.7	14.3*	12.5*
18	-	11.8	8.9	-	-
19	11.3	13.2	11.8	12.7*	11.2*
20	31.0*	6.5	-	-	-
$no\ \ motif$	-	-	-	4.2	7.2*

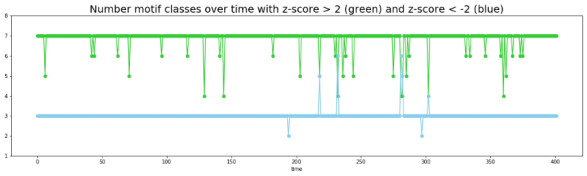

(a) fMRI - subgraphs of size 5

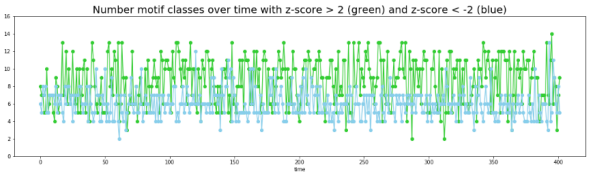

(b) EEG delta - subgraphs of size 5

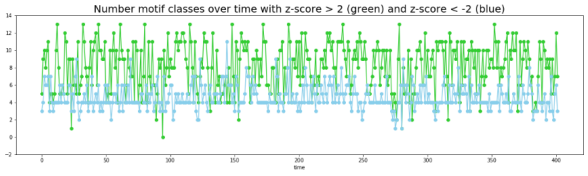

(c) EEG theta - subgraphs of size 5

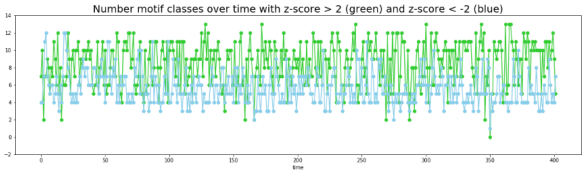

(d) EEG alpha - subgraphs of size 5

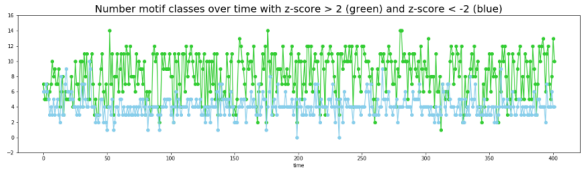

(e) EEG beta - subgraphs of size 5

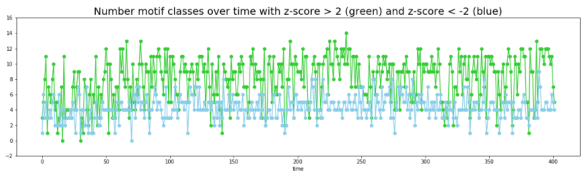

(f) EEG gamma - subgraphs of size 5

Figure C.2: Continuation of figure C.1.

Table C.5: Average percentage of time points for which each motif class was the first one to fifth one (top-1-5) with lowest negative z-score, corresponding to the under-represented motifs, respectively, considering the subgraphs with 5 nodes, for all subjects - for fMRI and EEG functional networks, against the rewiring null model. Only shown the motifs with highest percentages per position in the top. The values with an * symbol correspond to the motif class selected as the most recurring one at each top position, across time, for at least 1 subject.

	Motif	in top-1 (-) (%)	in top-2 (-) (%)	in top-3 (-) (%)	in top-4 (-) (%)	in top-5 () (%)
	$fMRI$					
	1	99.4*	0.6	-	-	-
	3	-	-	99.5	-	-
	4	0.6	99.4*	-	-	-
	5	-	-	-	0.6	0.3
	12	-	-	-	0.6	0.3
	$no\ \ motif$	-	-	0.5	98.8*	99.3*
EEG	$delta$					
	1	64.5*	8.6	6.3	-	-
	2	-	50.5*	14.5	7.5	-
	3	-	-	8.2	-	7.0
	4	22.6	9.9	6.8	19.1*	11.4
	6	6.4	11.6	9.2	11.6	18.0*
	13	-	-	-	27.7*	6.4
	17	-	11.8	49.0*	15.5	10.3
	$no\ \ motif$	-	-	-	-	18.6*
EEG	$theta$					
	1	72.3*	11.1	5.1	-	-
	2	5.2	54.9*	19.0	-	-
	4	12.9	7.8	7.7	18.3*	7.9
	6	4.8	6.1	6.2	8.7	10.9
	13	4.4	-	-	27.3*	4.6
	17	3.5	16.6	50.7*	11.9	7.3
	$no\ \ motif$	-	-	-	15.9	49.8*
EEG	$alpha$					
	1	70.0*	11.5	6.5	-	-
	2	4.8	52.9*	17.4	-	-
	4	16.2	7.1	7.2	15.1	9.1
	6	4.9	7.5	8.2	9.9	11.8
	10	-	-	-	-	6.0
	13	-	-	4.9	29.8*	6.1
	17	2.3	14.4	48.3*	13.9	10.5
	$no\ \ motif$	-	-	-	10.9*	39.1*

Table C.6: Continuation of table C.5.

	Motif	in top-1 (-) (%)	in top-2 (-) (%)	in top-3 (-) (%)	in top-4 (-) (%)	in top-5 (-) (%)
EEG	$beta$					
	1	82.4*	8.1	-	-	-
	2	5.4	69.5*	11.0	-	-
	4	6.0	-	-	-	-
	6	-	-	-	-	4.4
	10	-	-	-	-	11.7
	13	-	-	25.3	32.1*	-
	17	-	10.9	43.0*	23.6	-
	$no\ \ motif$	-	3.0	9.1	27.9*	69.5*
EEG	$gamma$					
	1	82.9*	9.6	-	-	-
	2	4.6	70.1*	13.4	-	-
	6	-	-	-	4.7	9.8
	10	-	-	-	5.3	27.7*
	13	-	-	27.1	37.1*	13.2
	17	2.7	11.4	41.4*	26.8	13.2
	$no\ \ motif$	-	-	4.3	14.5	44.6*

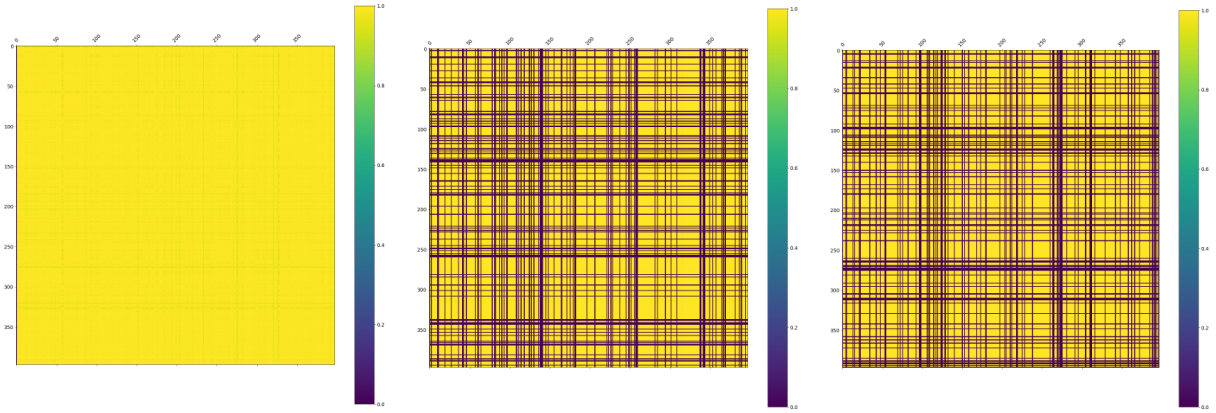

(a) fMRI - subgraphs of size 3 (b) EEG delta - subgraphs of size 3 (c) EEG theta - subgraphs of size 3

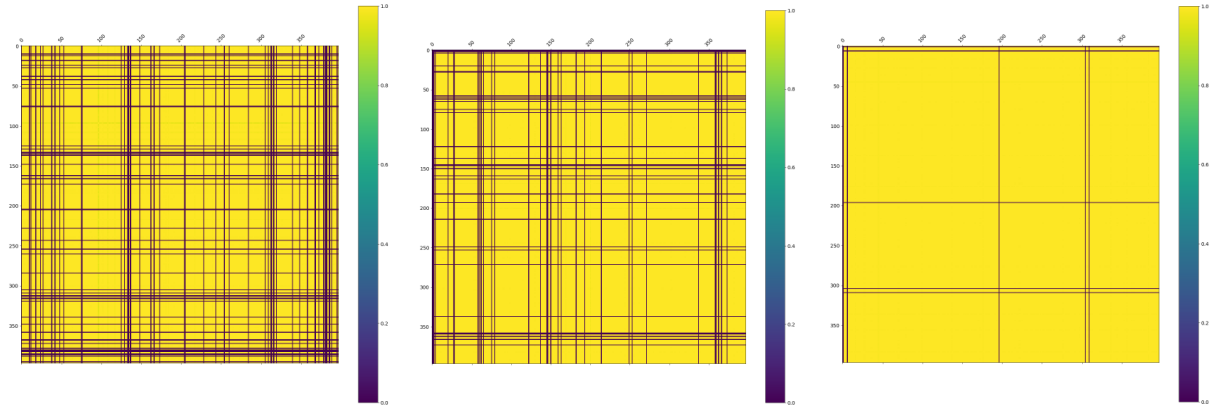

(d) EEG alpha - subgraphs of size 3 (e) EEG beta - subgraphs of size 3 (f) EEG gamma - subgraphs of size 3

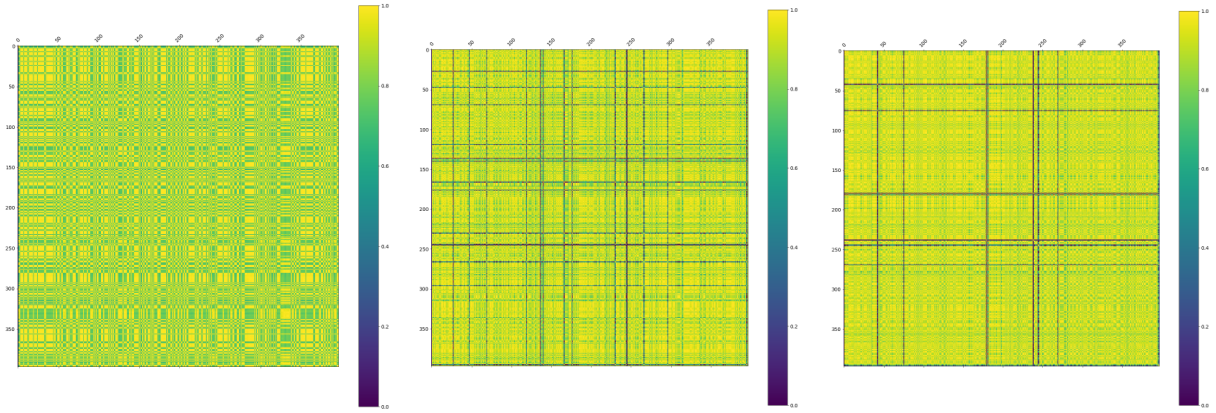

(g) fMRI - subgraphs of size 4 (h) EEG delta - subgraphs of size 4 (i) EEG theta - subgraphs of size 4

Figure C.3: Cosine similarity matrices, resulting from the comparison of the network fingerprints between all pairs of time points, for subgraphs with 3, 4 and 5 nodes, for fMRI and EEG frequency bands, for subject 1.

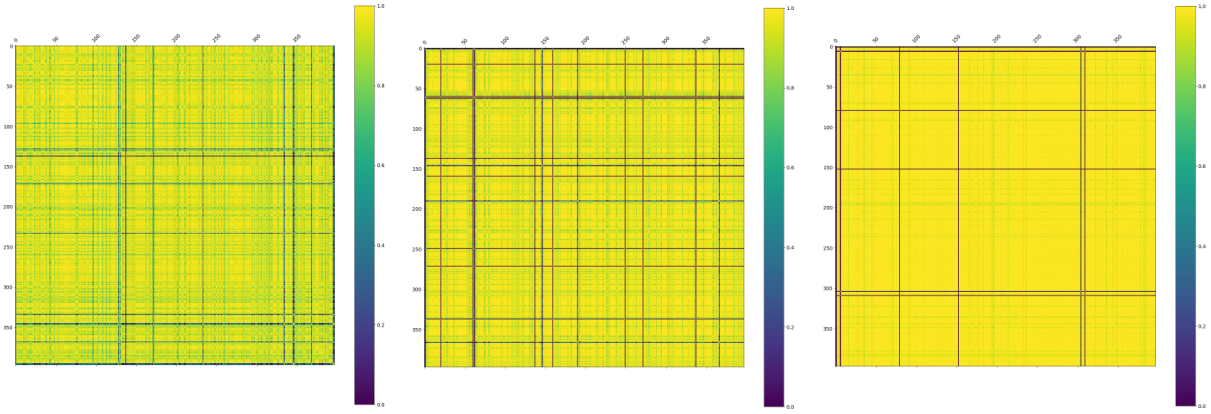

(a) EEG alpha - subgraphs of size 4 (b) EEG beta - subgraphs of size 4 (c) EEG gamma - subgraphs of size 4

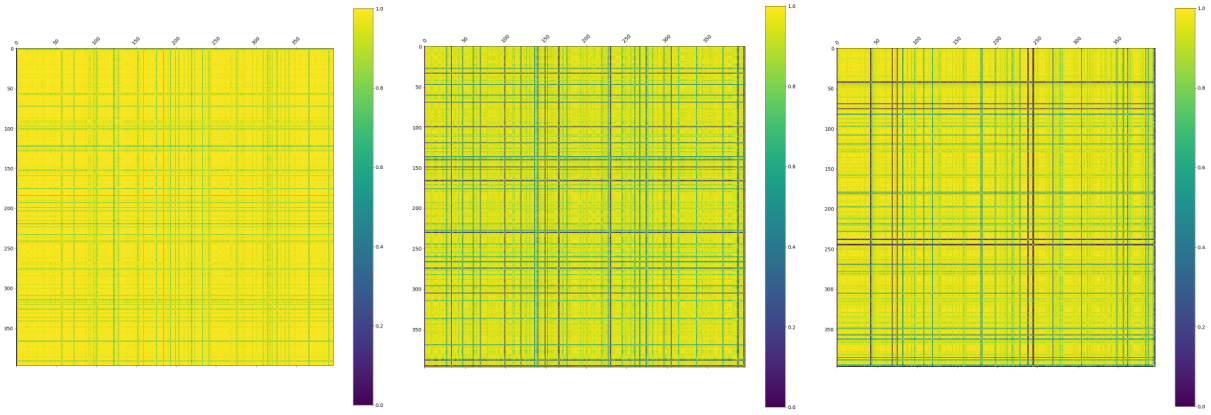

(d) fMRI - subgraphs of size 5 (e) EEG delta - subgraphs of size 5 (f) EEG theta - subgraphs of size 5

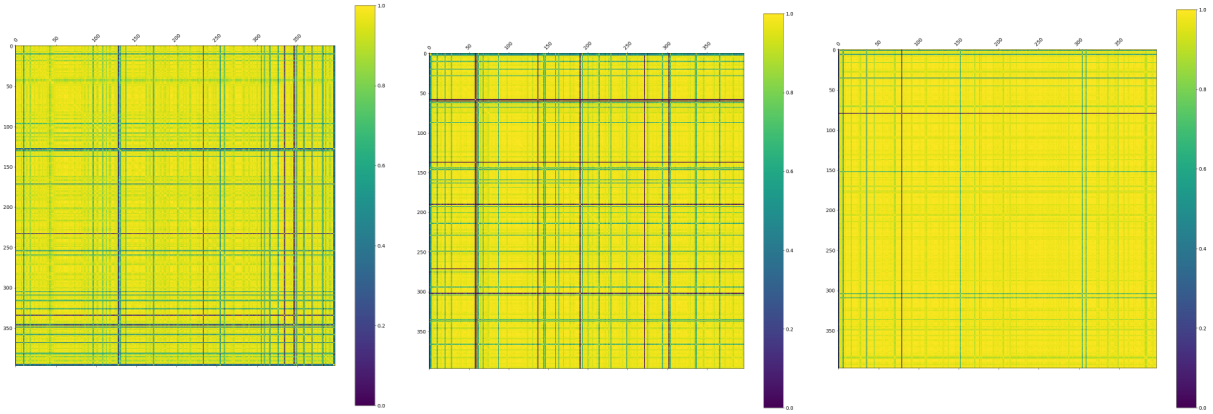

(g) EEG alpha - subgraphs of size 5 (h) EEG beta - subgraphs of size 5 (i) EEG gamma - subgraphs of size 5

Figure C.4: Continuation of the figure C.3.

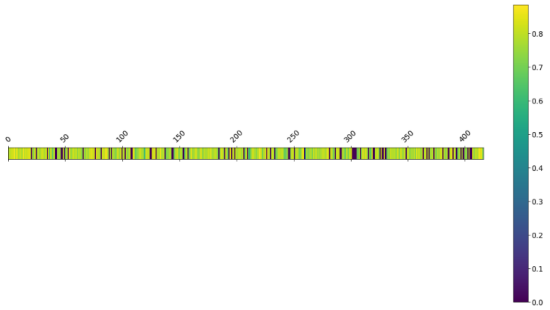

(a) fMRI- EEG delta - subgraphs of size 3

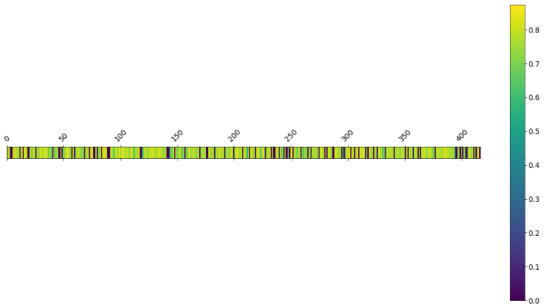

(b) fMRI- EEG theta - subgraphs of size 3

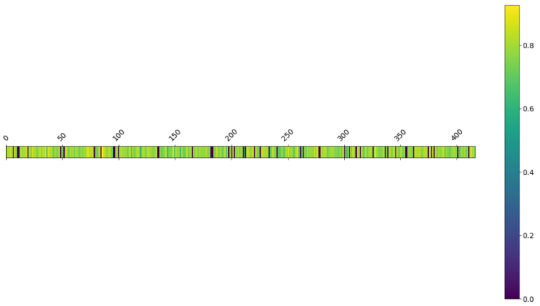

(c) fMRI- EEG alpha - subgraphs of size 3

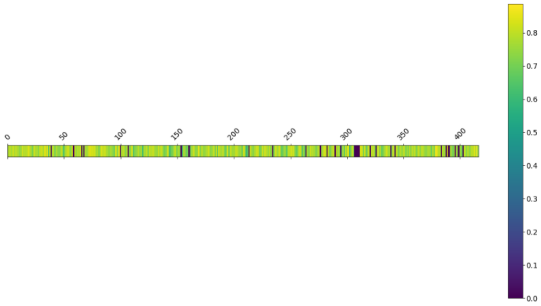

(d) fMRI- EEG beta - subgraphs of size 3

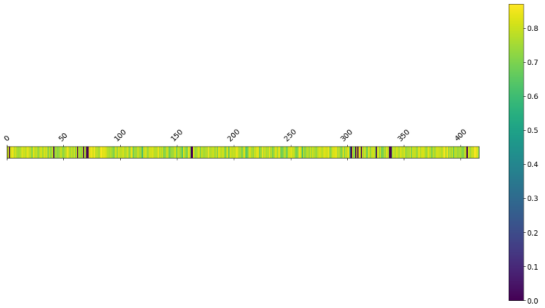

(e) fMRI- EEG gamma - subgraphs of size 3

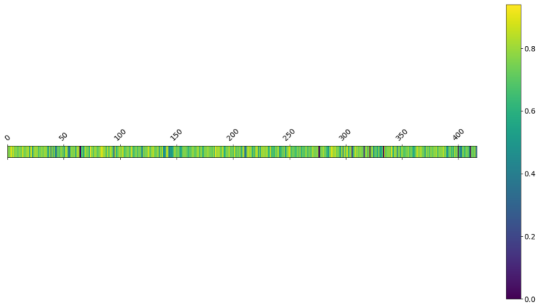

(f) fMRI- EEG delta - subgraphs of size 4

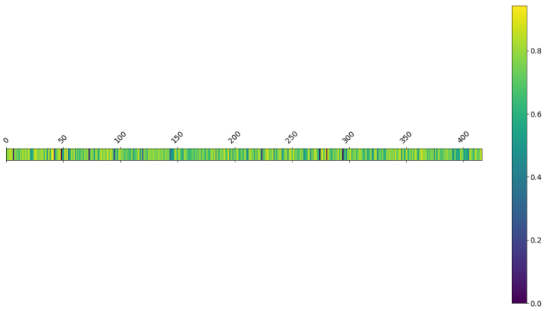

(g) fMRI- EEG theta - subgraphs of size 4

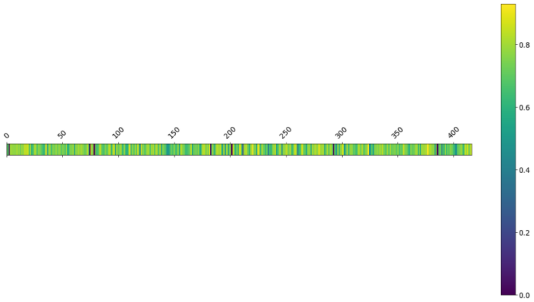

(h) fMRI- EEG alpha - subgraphs of size 4

Figure C.5: Cosine similarity matrices, resulting from the comparison of the network fingerprints between fMRI and EEG for all time points, for subgraphs with 3, 4 and 5 nodes, for subject 6.

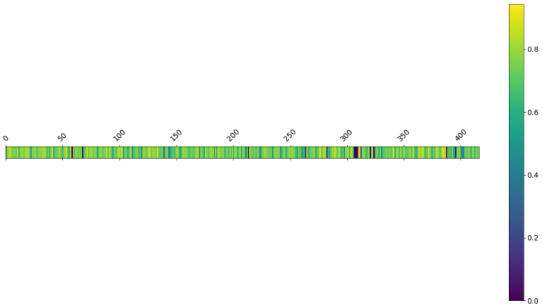

(a) fMRI- EEG beta - subgraphs of size 4

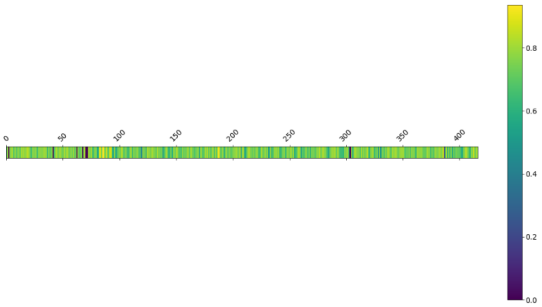

(b) fMRI- EEG gamma - subgraphs of size 4

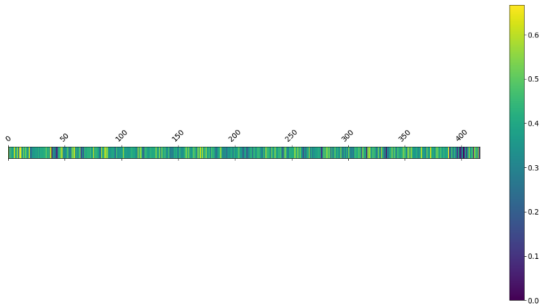

(c) fMRI- EEG delta - subgraphs of size 5

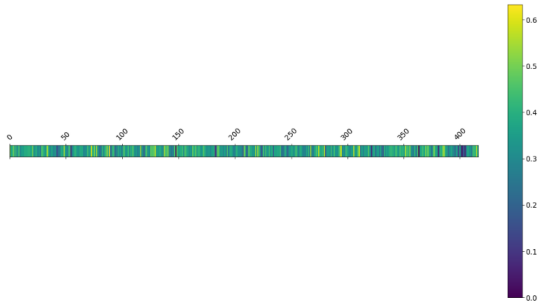

(d) fMRI- EEG theta - subgraphs of size 5

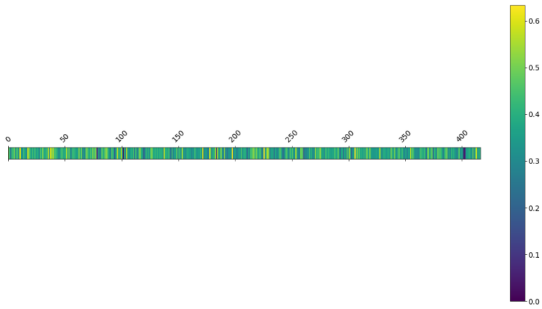

(e) fMRI- EEG alpha - subgraphs of size 5

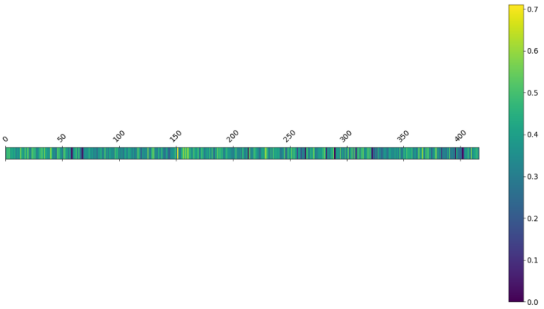

(f) fMRI- EEG beta - subgraphs of size 5

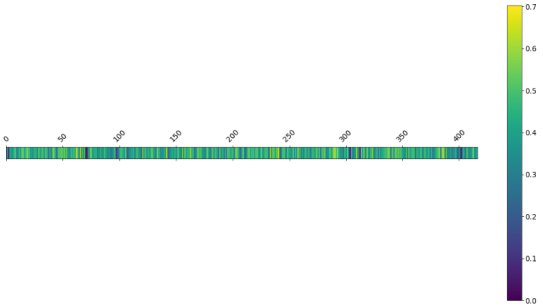

(g) fMRI- EEG gamma - subgraphs of size 5

Figure C.6: Continuation of figure C.5.

C.2 Motif Analysis with Degree Constrained Spatial Null Model

Table C.7: Average percentage of time points for which each motif class was the one (top-1) with highest positive z-score and with lowest negative z-score, corresponding to the over- and under-represented motifs, respectively, considering the subgraphs with 3 nodes, for all subjects - for fMRI and EEG functional networks, against the degree constrained spatial null model. The values with an * symbol correspond to the motif class selected as the most recurring one with highest (+) or lowest (-) z-score, across time, for at least 1 subject.

Motif	in top-1 (+) (%)	in top-1 (-) (%)
$fMRI$		
1	-	100.0*
2	0.2	-
$no\ \ motif$	99.8*	-
$EEG\ \ delta$		
1	1.9	-
2	2.0	-
$no\ \ motif$	95.9*	100*
$EEG\ \ theta$		
1	-	-
2	0.1	-
$no\ \ motif$	99.9*	100*
$EEG\ \ alpha$		
1	3.4	-
2	8.1	-
$no\ \ motif$	88.9*	100.0*
$EEG\ \ beta$		
1	-	-
2	-	-
$nomotif$	100.0*	100.0*
$EEG\ \ gamma$		
1	-	-
2	0.07	-
$no\ \ motif$	99.3*	100.0*

Table C.8: Average percentage of time points for which each motif class was the one (top-1) or second one (top-2) with highest positive z-score and with lowest negative z-score, corresponding to the over- and under-represented motifs, respectively, considering the subgraphs with 4 nodes, for all subjects - for fMRI and EEG functional networks, against the degree constrained spatial null model. The values with an * symbol correspond to the motif class selected as the most recurring one at each top position, (+) or (-), across time, for at least 1 subject.

Motif	in top-1 (+) (%)	in top-2 (+) (%)	in top-1 (-) (%)	in top-2 (-) (%)
$fMRI$				
1	-	-	26.9	72.6*
2	-	-	72.6*	26.7
5	0.4	-	-	-
$no\ \ motif$	99.6*	100.0*	-	-
$EEG\ \ delta$				
3	-	10.6	-	-
4	9.1	17.8	-	-
5	13.8	4.0	-	-
6	28.2*	6.1	-	-
$no\ \ motif$	42.7*	59.7	100.0*	100.0*
$EEG\ \ theta$				
3	3.3	2.4	-	-
4	1.8	4.4	-	-
5	5.4	0.8	0.1	-
6	10.8	1.6	-	-
$nomotif$	78.7*	90.6*	99.9*	100.0*
$EEG\ \ alpha$				
1	-	-	0.1	-
2	-	-	0.1	-
3	-	4.9	0.1	0.1
4	4.9	12.1	-	-
5	14.7	2.8	-	-
6	10.7	4.2	0.1	-
$no\ \ motif$	65.4*	73.3*	99.6*	99.9*
$EEG\ \ beta$				
3	-	0.3	-	-
4	-	2.1	-	-
5	7.4	-	-	-
6	1.5	-	-	-
$no\ \ motif$	89.8*	96.9*	100.0*	100.0*
$EEG\ \ gamma$				
2	-	0.9	-	-
3	-	-	-	-
4	-	7.1	-	-
5	19.7	-	-	-
6	1.2	-	-	-
$no\ \ motif$	76.5*	90.0*	100.0*	100.0*

Table C.9: Average percentage of time points for which each motif class was the first one to fifth one (top-1-4) with highest positive z-score, corresponding to the over- -represented motifs, considering the subgraphs with 5 nodes, for all subjects - for fMRI and EEG functional networks, against the degree constrained spatial null model. Only shown the motifs with highest percentages per position in the top. The values with an * symbol correspond to the motif class selected as the most recurring one at each top position, across time, for at least 1 subject.

Motif	in top-1 (+) (%)	in top-2 (+) (%)	in top-3 (+) (%)	in top-4 (+) (%)	in top-5 (+) (%)
$fMRI$					
12	0.5	-	-	-	-
20	0.3	-	-	-	-
$no\ \ motif$	96.6*	100.0*	100.0*	100.0*	100.0*
$EEG\ \ delta$					
9	-	-	-	-	4.4
10	-	-	7.0	5.4	5.6
11	-	-	-	4.5	-
13	6.1	7.4	-	3.8	3.6
14	-	-	-	-	3.9
15	5.0	7.8	-	-	-
16	6.6	8.3	7.7	8.9	4.9
18	-	10.5	12.1	8.4	5.8
19	11.0	10.2	8.7	-	4.5
20	9.8	-	-	-	-
21	32.7*	8.9	-	-	-
$no\ \ motif$	22.7*	30.6*	37.0*	42.8*	48.1*
$EEG\ \ theta$					
10	-	-	3.6	-	-
11	-	-	-	-	1.0
13	8.7	4.2	-	-	-
16	-	3.6	3.6	3.0	2.0
18	-	4.8	4.4	3.1	1.9
19	4.5	3.7	3.3	2.1	1.7
20	4.8	-	-	-	-
21	19.4	5.1	-	-	-
$no\ \ motif$	53.7*	68.2*	74.5*	79.6*	83.2*
$EEG\ \ alpha$					
11	-	-	-	2.2	1.4
15	-	4.2	-	-	-
16	-	-	1.8	2.26	1.3
18	-	-	-	-	1.8
19	4.4	2.5	3.8	-	-
20	5.4	-	1.6	-	-
21	7.18	2.3	-	-	-
$no\ \ motif$	70.5*	78.1*	81.7*	84.3*	86.6*

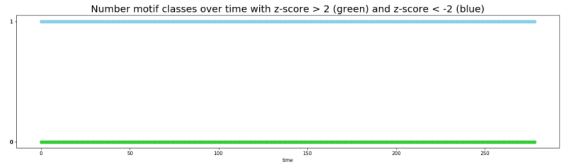

(a) fMRI - subgraphs of size 3

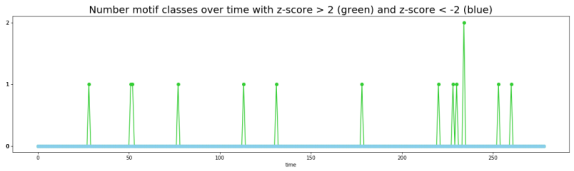

(b) EEG delta - subgraphs of size 3

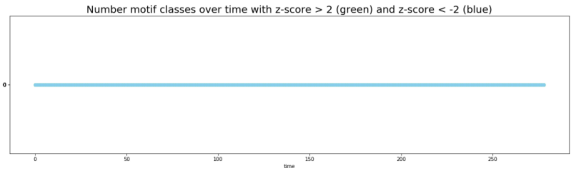

(c) EEG theta - subgraphs of size 3

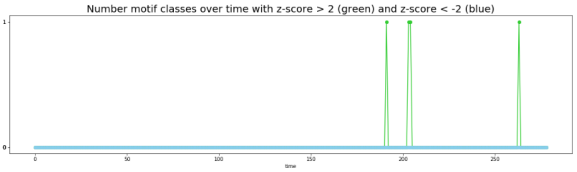

(d) EEG alpha - subgraphs of size 3

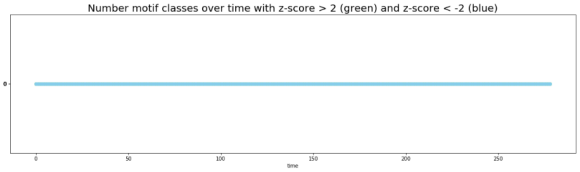

(e) EEG beta - subgraphs of size 3

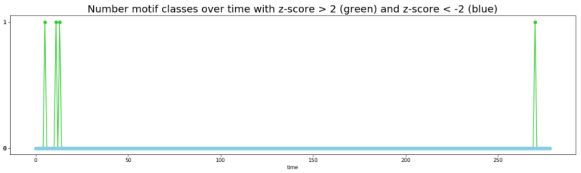

(f) EEG gamma - subgraphs of size 3

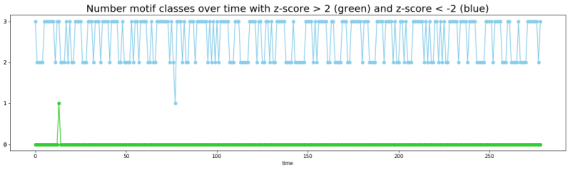

(g) fMRI - subgraphs of size 4

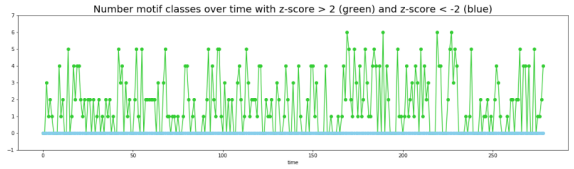

(h) EEG delta - subgraphs of size 4

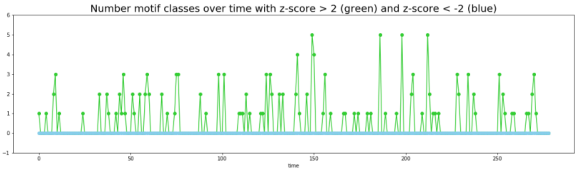

(i) EEG theta - subgraphs of size 4

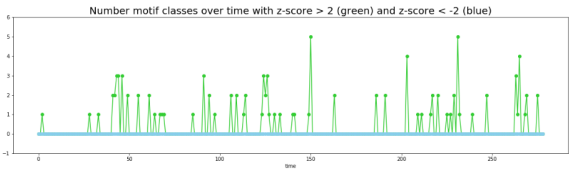

(j) EEG alpha - subgraphs of size 4

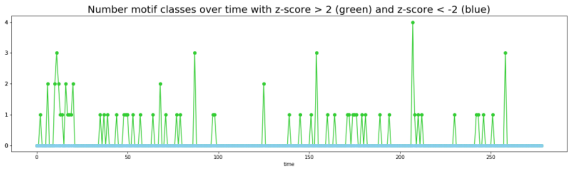

(k) EEG beta - subgraphs of size 4

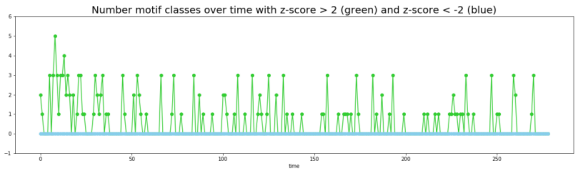

(l) EEG gamma - subgraphs of size 4

Figure C.7: Variation of number of motif classes over- (in green) and under-represented (in blue), for subgraphs with 3, 4 and 5 nodes, with respect to the degree constrained spatial null model for fMRI and EEG frequency bands, for subject 5.

Table C.10: Continuation of table C.9.

	Motif	in top-1 (+) (%)	in top-2 (+) (%)	in top-3 (+) (%)	in top-4 (+) (%)	in top-5 (+) (%)
EEG	$beta$					
	8	-	-	1.9	2.0	-
	9	-	-	-	-	1.0
	11	-	-	2.7	1.8*	-
	15	3.1	4.6	-	-	-
	16	-	-	-	-	1.1
	18	-	1.2	-	-	-
	20	9.5	-	-	-	-
	21	2.9	-	-	-	-
	$no\ \ motif$	77.0*	84.6*	88.9*	91.1*	93.6*
EEG	$gamma$					
	8	-	4.7	5.4	4.9	-
	11	-	3.0	6.3	5.1	-
	12	3.2	-	-	-	-
	13	2.8	-	-	-	-
	15	3.5	9.8	-	-	-
	17	3.4	8.7	10.7	14.3*	12.5*
	20	20.4*	-	-	-	-
	$no\ \ motif$	55.3*	66.7*	71.8*	75.2*	79.5*

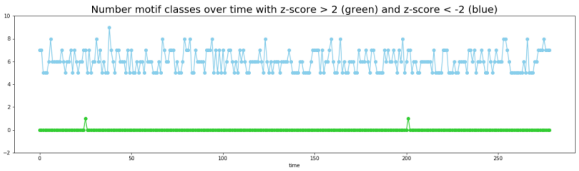

(a) fMRI - subgraphs of size 5

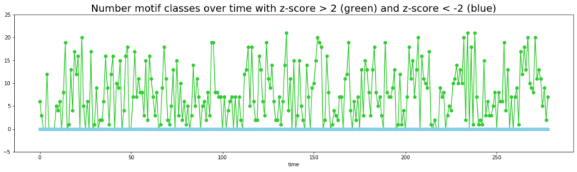

(b) EEG delta - subgraphs of size 5

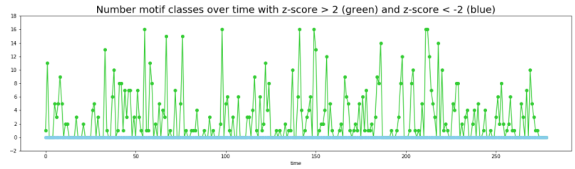

(c) EEG theta - subgraphs of size 5

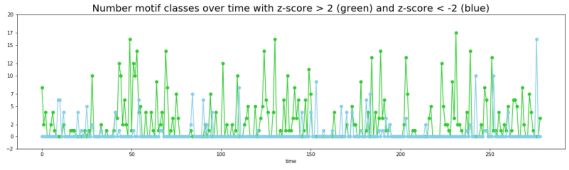

(d) EEG alpha - subgraphs of size 5

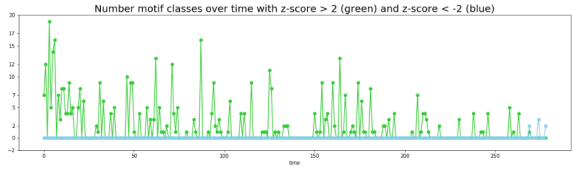

(e) EEG beta - subgraphs of size 5

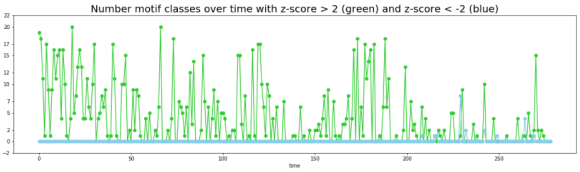

(f) EEG gamma - subgraphs of size 5

Figure C.8: Continuation of figure C.7.

Table C.11: Average percentage of time points for which each motif class was the first one to fifth one (top-1-5) with lowest negative z-score, corresponding to the under-represented motifs, respectively, considering the subgraphs with 5 nodes, for all subjects - for fMRI and EEG functional networks, against the degree constrained spatial null model. Only shown the motifs with highest percentages per position in the top. The values with an * symbol correspond to the motif class selected as the most recurring one at each top position, across time, for at least 1 subject.

Motif	in top-1 (-) (%)	in top-2 (-) (%)	in top-3 (-) (%)	in top-4 (-) (%)	in top-5 () (%)
$fMRI$					
1	-	19.1	33.0	42.6*	4.1
3	90.3*	8.6	-	-	-
4	-	19.2	47.3*	28.2	-
5	-	-	-	6.1	86.1*
8	6.4	52.9*	15.9	22.6	3.1
$no\ \ motif$	-	-	-	-	-
$EEG\ \ delta$					
8	0.2	-	-	-	-
17	0.4	0.1	-	-	-
$no\ \ motif$	99.0	99.9	99.9	100.0*	100.0*
$EEG\ \ theta$					
1	0.9	0.5	-	-	-
2	-	0.4	-	-	-
3	0.6	0.4	-	-	-
4	-	-	-	0.2	0.1
17	0.8	0.5	0.2	0.1	0.1
$no\ \ motif$	96.1	97.4	98.7	99.0	99.3
$EEG\ \ alpha$					
1	11.1*	7.5	4.2	3.2	2.5
2	3.5	6.1	5.3	5.1	3.6
3	8.1	7.8	6.9	5.2	3.3
4	-	4.1	5.8	6.5	9.1
5	-	-	-	-	3.8
6	-	-	-	-	3.1
10	-	-	-	-	2.7
14	2.7	-	-	-	-
17	3.0	-	-	2.6	2.7
$no\ \ motif$	51.9*	55.9	57.7	59.0	60.4

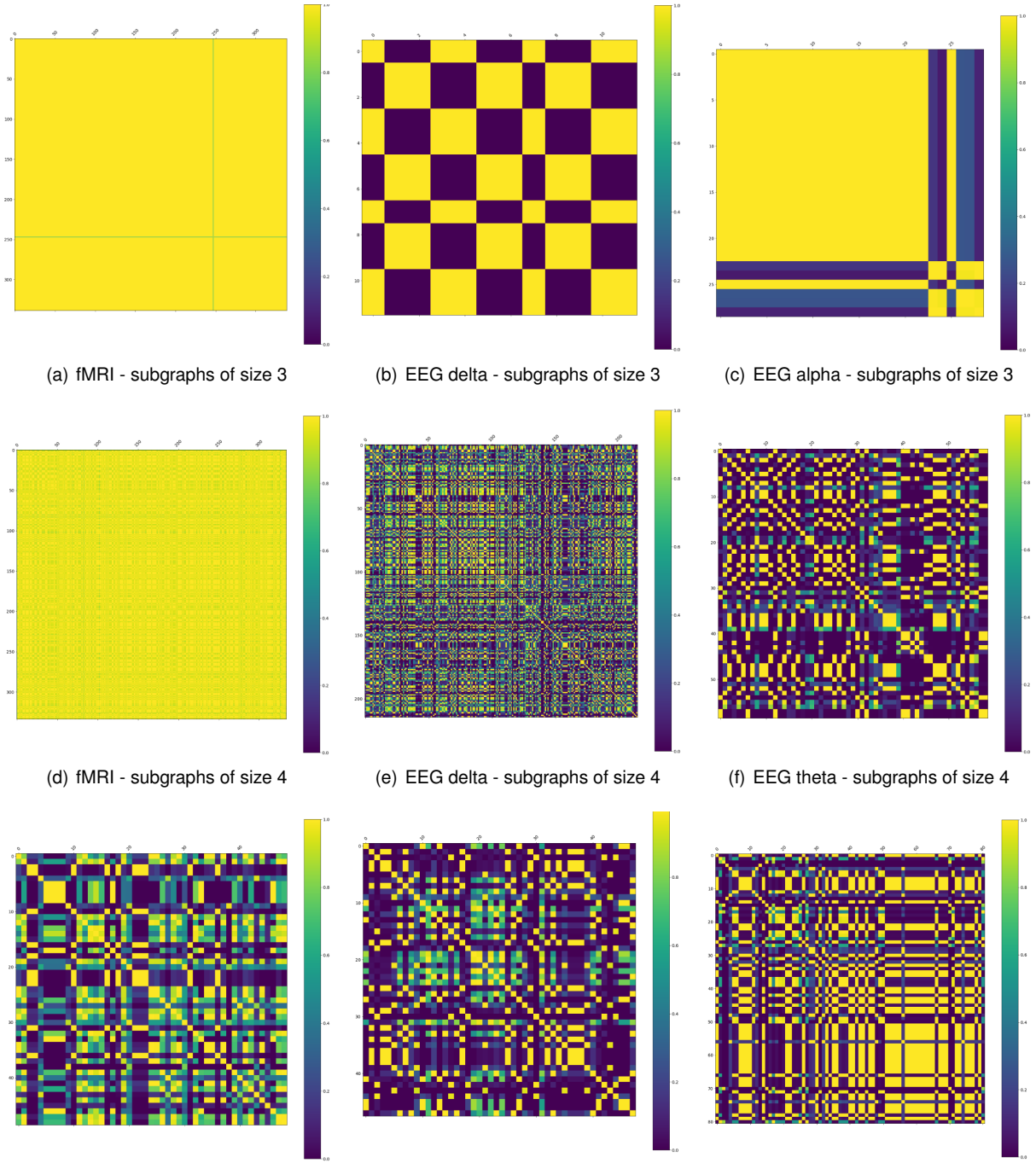

(a) fMRI - subgraphs of size 3 (b) EEG delta - subgraphs of size 3 (c) EEG alpha - subgraphs of size 3

(d) fMRI - subgraphs of size 4 (e) EEG delta - subgraphs of size 4 (f) EEG theta - subgraphs of size 4

(g) EEG alpha - subgraphs of size 4 (h) EEG beta - subgraphs of size 4 (i) EEG gamma - subgraphs of size 4

Figure C.9: Cosine similarity matrices resulting from the comparison of the network fingerprints between time points that present over- or under-represented motifs, with respect to the degree constrained spatial null model, for subgraphs with 3, 4 and 5 nodes, for fMRI and EEG frequency bands, for subject 4. The frequency bands with no time point deviating from this spatial null model are not represented.

Table C.12: Continuation of table C.11.

Motif	in top-1 (-) (%)	in top-2 (-) (%)	in top-3 (-) (%)	in top-4 (-) (%)	in top-5 (-) (%)
$EEG\ \ beta$					
1	2.8	1.0	-	-	-
2	-	1.1	-	-	-
3	1.0	1.1	-	-	-
4	-	-	0.9	0.3	0.4
14	-	-	-	-	0.3
17	-	-	0.5	0.3	0.3
$no\ \ motif$	83.0	93.5	95.0	96.3	97.4
$EEG\ \ gamma$					
1	0.3	-	-	-	-
2	0.6	0.2	-	-	-
10	0.5	0.4	-	-	-
13	0.4	-	-	-	-
19	0.4	0.2	-	-	-
21	0.8	-	-	-	-
$no\ \ motif$	95.4*	97.6*	98.4*	99.1*	99.3*

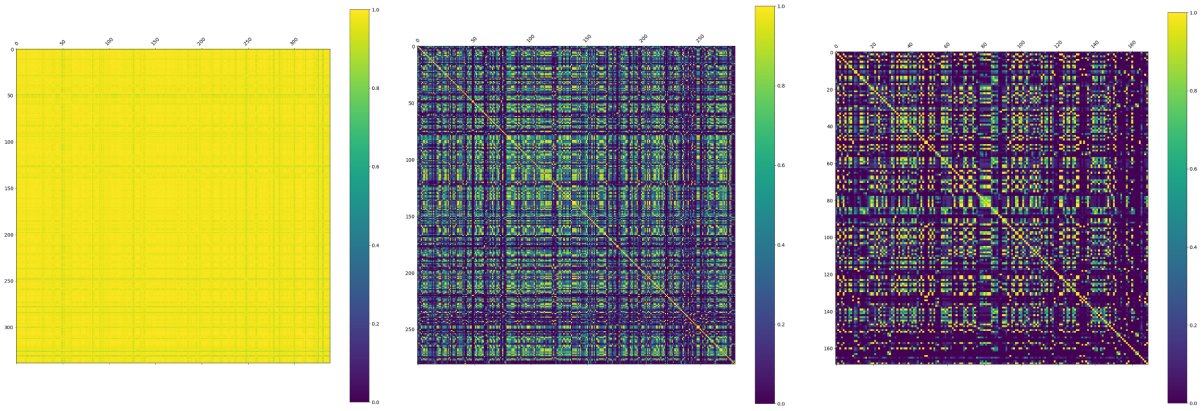

(a) fMRI - subgraphs of size 5 (b) EEG delta - subgraphs of size 5 (c) EEG theta - subgraphs of size 5

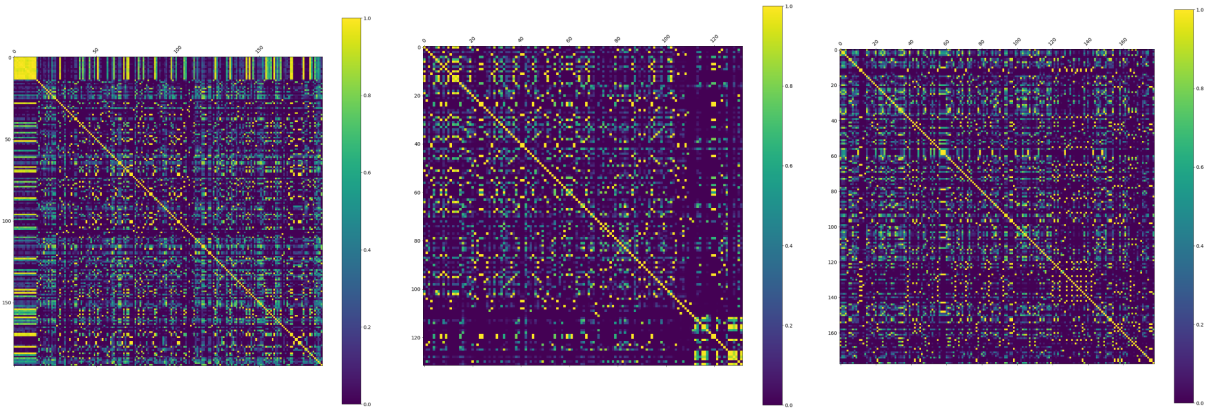

(d) EEG alpha - subgraphs of size 5 (e) EEG beta - subgraphs of size 5 (f) EEG gamma - subgraphs of size 5

Figure C.10: Continuation of figure C.9.

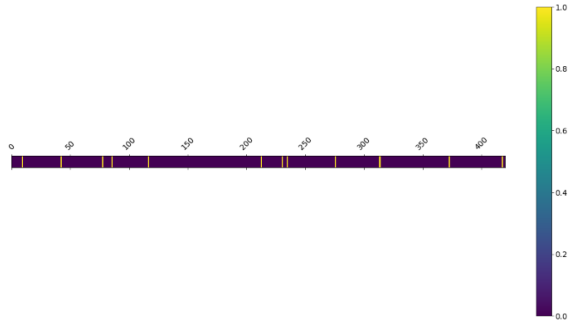

(a) fMRI- EEG delta - subgraphs of size 3

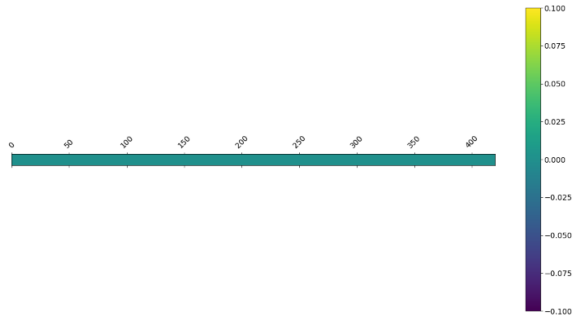

(b) fMRI- EEG theta - subgraphs of size 3

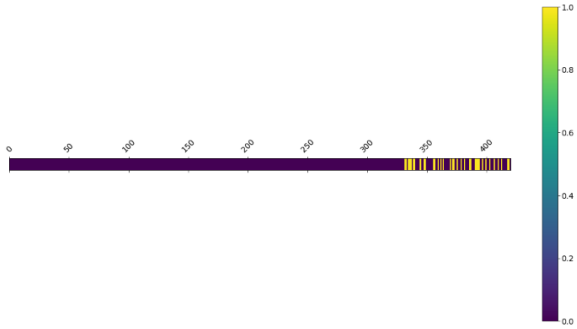

(c) fMRI- EEG alpha - subgraphs of size 3

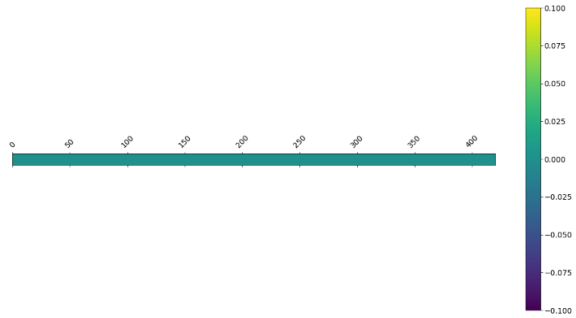

(d) fMRI- EEG beta - subgraphs of size 3

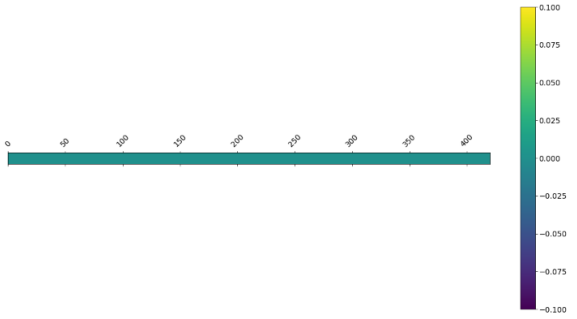

(e) fMRI- EEG gamma - subgraphs of size 3

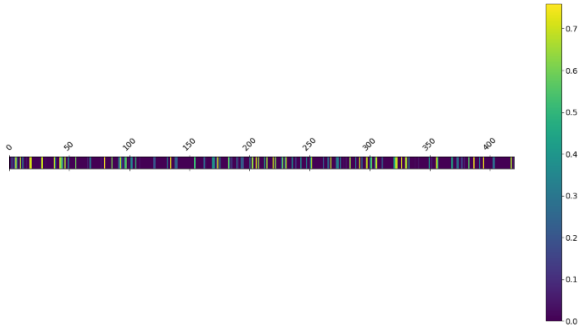

(f) fMRI- EEG delta - subgraphs of size 4

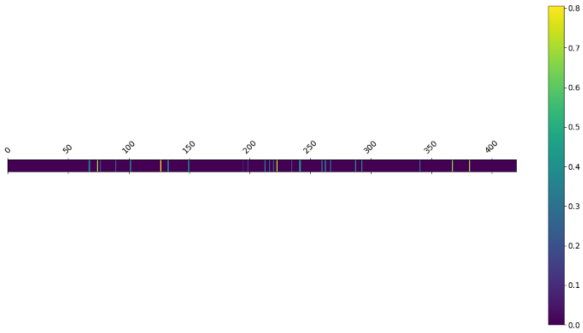

(g) fMRI- EEG theta - subgraphs of size 4

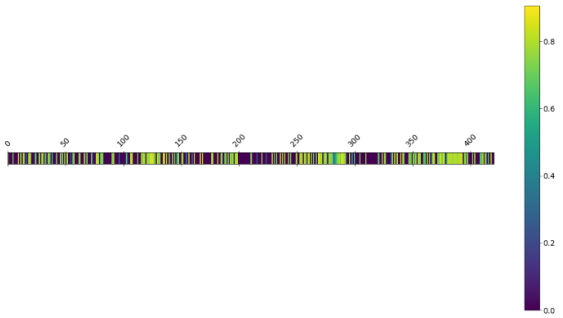

(h) fMRI- EEG alpha - subgraphs of size 4

Figure C.11: Cosine similarity matrices, resulting from the comparison of the network fingerprints between fMRI and EEG for all time points, with respect to the degree constrained spatial null model, for subgraphs with 3, 4 and 5 nodes, for subject 9.

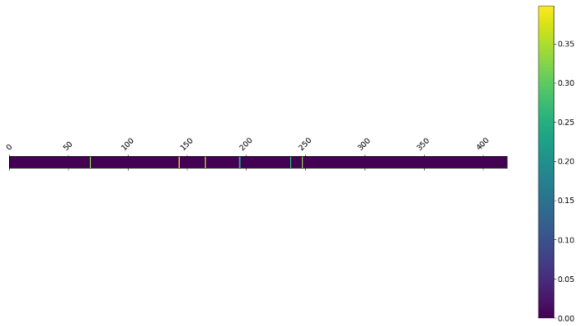

(a) fMRI- EEG beta - subgraphs of size 4

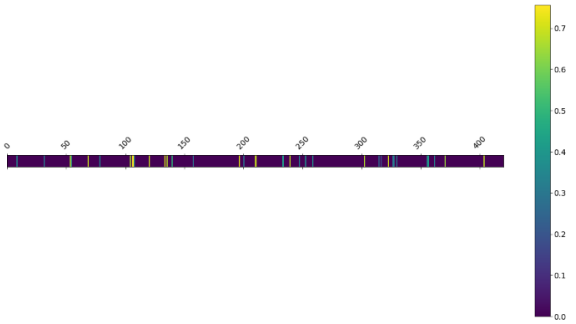

(b) fMRI- EEG gamma - subgraphs of size 4

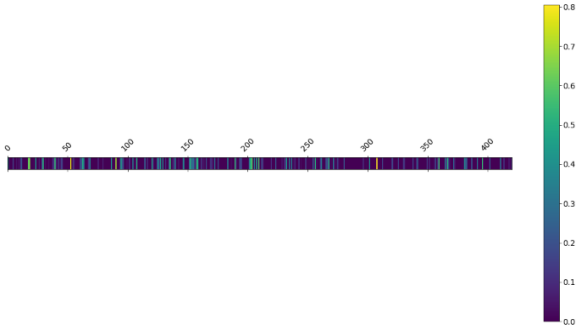

(c) fMRI- EEG delta - subgraphs of size 5

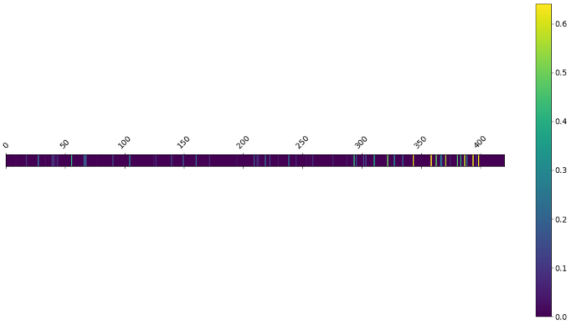

(d) fMRI- EEG theta - subgraphs of size 5

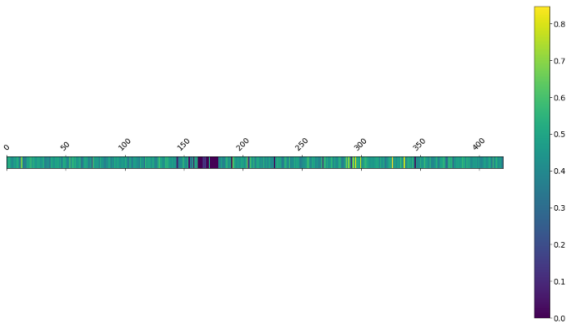

(e) fMRI- EEG alpha - subgraphs of size 5

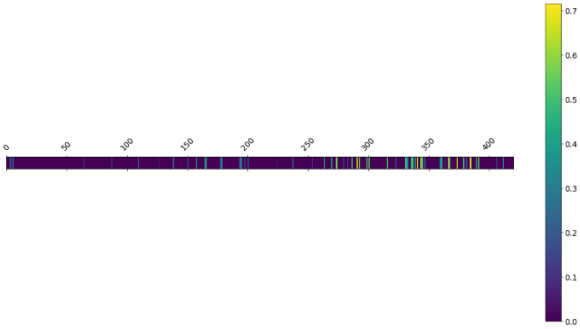

(f) fMRI- EEG beta - subgraphs of size 5

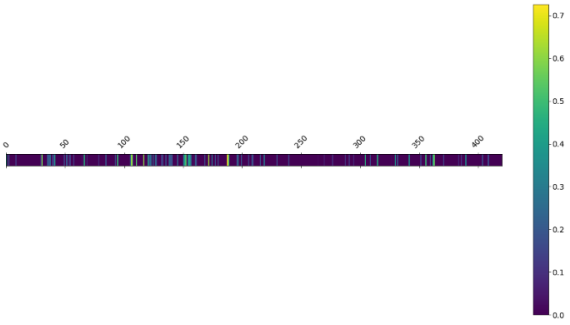

(g) fMRI- EEG gamma - subgraphs of size 5

Figure C.12: Continuation of figure C.11.